



## Additive manufacturing of metallic components – Process, structure and properties



T. DebRoy<sup>a,\*</sup>, H.L. Wei<sup>a</sup>, J.S. Zuback<sup>a</sup>, T. Mukherjee<sup>a</sup>, J.W. Elmer<sup>b</sup>, J.O. Milewski<sup>c</sup>, A.M. Beese<sup>a</sup>, A. Wilson-Heid<sup>a</sup>, A. De<sup>d</sup>, W. Zhang<sup>e</sup>

<sup>a</sup> Department of Materials Science and Engineering, The Pennsylvania State University, University Park, PA, United States

<sup>b</sup> Materials Engineering Division, Lawrence Livermore National Laboratory, Livermore, CA, United States

<sup>c</sup> APEX3D LLC, Santa Fe, NM, United States

<sup>d</sup> Department of Mechanical Engineering, IIT Bombay, Mumbai, India

<sup>e</sup> Department of Materials Science and Engineering, Ohio State University, Columbus, OH, United States

### ARTICLE INFO

#### Article history:

Received 3 July 2017

Received in revised form 18 September 2017

Accepted 6 October 2017

Available online 7 October 2017

#### Keywords:

Additive manufacturing

3D printing

Powder bed fusion

Directed energy deposition

Laser deposition

Printability

### ABSTRACT

Since its inception, significant progress has been made in understanding additive manufacturing (AM) processes and the structure and properties of the fabricated metallic components. Because the field is rapidly evolving, a periodic critical assessment of our understanding is useful and this paper seeks to address this need. It covers the emerging research on AM of metallic materials and provides a comprehensive overview of the physical processes and the underlying science of metallurgical structure and properties of the deposited parts. The uniqueness of this review includes substantive discussions on refractory alloys, precious metals and compositionally graded alloys, a succinct comparison of AM with welding and a critical examination of the printability of various engineering alloys based on experiments and theory. An assessment of the status of the field, the gaps in the scientific understanding and the research needs for the expansion of AM of metallic components are provided.

© 2017 Elsevier Ltd. All rights reserved.

### Contents

1. Introduction .....	115
2. Process .....	116
2.1. Manufacturing processes for alloys .....	116
2.2. Feedstock materials .....	119
2.3. Heat source characteristics .....	121
2.4. Interaction between heat source and feedstock materials .....	122
2.5. Principles of heat and mass transfer and fluid flow .....	123
2.5.1. Boundary conditions .....	125
2.6. Temperature and velocity distributions and cooling rates .....	126
2.7. Non-dimensional numbers .....	128
2.8. Process stability .....	132
2.8.1. Kelvin Helmholtz hydrodynamic instability .....	132
2.8.2. Plateau Raleigh capillary instability .....	132

\* Corresponding author.

E-mail address: [rt1@psu.edu](mailto:rt1@psu.edu) (T. DebRoy).

2.9.	Defects . . . . .	133
2.9.1.	Loss of alloying elements . . . . .	133
2.9.2.	Porosity and lack of fusion defects . . . . .	135
2.9.3.	Surface roughness . . . . .	137
2.9.4.	Cracking and delamination . . . . .	139
2.10.	Residual stresses and distortion . . . . .	139
2.10.1.	Origin of residual stresses . . . . .	140
2.10.2.	Directed energy deposition versus powder bed AM . . . . .	142
2.10.3.	Thermal-stress analysis approach . . . . .	142
2.10.4.	Computational codes for thermal-stress analysis . . . . .	143
2.10.5.	Results of calculated residual stresses and distortion . . . . .	143
2.10.6.	Measurement of residual stresses and distortion . . . . .	145
2.10.7.	Mitigation strategy to reduce residual stresses . . . . .	147
2.10.8.	Future research needs . . . . .	148
2.11.	Process control . . . . .	148
3.	Structure . . . . .	149
3.1.	Solidification structure . . . . .	149
3.1.1.	Nucleation . . . . .	150
3.1.2.	Growth . . . . .	150
3.1.3.	Key parameters in determining the solidification structure . . . . .	152
3.2.	Grain structure . . . . .	154
3.2.1.	Grain growth direction . . . . .	154
3.2.2.	Grain growth rate . . . . .	158
3.2.3.	Grain size and morphology . . . . .	159
3.2.4.	Grain structures in miscellaneous conditions . . . . .	161
3.3.	Texture . . . . .	161
3.3.1.	Texture in PBF system . . . . .	161
3.3.2.	Texture in DED system . . . . .	162
3.3.3.	Influential factors . . . . .	163
3.4.	Phase transformations . . . . .	164
3.4.1.	Non-heat treatable alloys . . . . .	165
3.4.2.	Heat treatable alloys . . . . .	165
3.4.3.	Microstructures of AM fabricated alloys . . . . .	166
4.	Properties . . . . .	172
4.1.	Ferrous alloys . . . . .	173
4.1.1.	Austenitic stainless steel . . . . .	173
4.1.2.	Precipitation hardening (PH) stainless steel . . . . .	175
4.2.	Nickel base alloys . . . . .	177
4.3.	Titanium alloys . . . . .	178
4.4.	Lightweight alloys . . . . .	182
4.4.1.	Aluminum alloys . . . . .	182
4.4.2.	Magnesium alloys . . . . .	184
4.5.	Fatigue in AM . . . . .	185
4.6.	Creep in AM . . . . .	187
4.7.	Discussion . . . . .	188
5.	AM of special materials . . . . .	188
5.1.	Refractory alloys . . . . .	188
5.2.	Precious metals . . . . .	190
5.3.	Compositionally graded alloys . . . . .	190
6.	Welding vs AM . . . . .	191
6.1.	Processes and applications . . . . .	191
6.2.	Deposition rates and surface finish . . . . .	192
6.3.	Localized heat sources . . . . .	193
6.4.	Microstructure and macrostructure . . . . .	195
6.5.	Mechanical properties . . . . .	197
6.6.	Summary . . . . .	200
7.	Printability of alloys . . . . .	201
7.1.	Printability of PBF AM processes . . . . .	201
7.2.	Printability of DED AM processes . . . . .	204
7.3.	Theoretical calculations of printability . . . . .	204
8.	Concluding remarks . . . . .	207
	Acknowledgements . . . . .	208
	References . . . . .	208

## Nomenclature

Symbol	Description
$C_p$	specific heat
$D$	width of deposit
$D^{EP}$	elastic-plastic stiffness matrix
$D^E$	elastic stiffness matrix
$d$	secondary dendrite arm spacing
$d\varepsilon$	total strain increment
$d\varepsilon^E$	elastic strain increment
$d\varepsilon^P$	plastic strain increment
$d\varepsilon^{Th}$	thermal strain increment
$d\varepsilon^V$	volumetric strain increment
$E$	elastic modulus
$E_v$	volumetric heat input
$f$	distribution factor
$f_n$	height of a surface peak or valley
$F_o$	Fourier number
$g$	acceleration due to gravity
$G$	temperature gradient
$h$	sensible heat
$H$	heat input per unit length
$h_s$	hatch spacing
$h_c$	convective heat transfer coefficient
$I$	moment of inertia
$J_i$	evaporative flux of element $i$
$k$	thermal conductivity
$L$	length
$LF$	lack of fusion index
$Ma$	Marangoni number
$M_i$	molecular weight of element $i$
$N$	number of measurement locations along a profile
$P$	total power of heat source
$P_d$	power density
$Pe$	Peclet number
$P_i$	equilibrium vapor pressure of element $i$
$P_R$	reference heat source power
$Q^*$	non-dimensional heat input
$r$	radial distance from heat source axis
$R$	solidification rate
$R_a$	average surface roughness
$r_b$	radius of heat source
$Ri$	Richardson number
$S_j$	source term for the momentum equation
$t$	time
$T$	temperature
$T_0$	initial temperature
$T_a$	ambient temperature
$t_f$	local solidification time
$t_l$	layer thickness
$T_p$	peak temperature
$u$	velocity of material flow
$U$	characteristic velocity
$U_g$	velocity of shielding gas
$U_l$	velocity of liquid metal in molten pool
$v$	scanning speed
$V_{hkl}$	growth velocity of the dendrite tip along crystallographic direction [ $h k l$ ]
$V_R$	reference scanning speed
$V_n$	normal solidification velocity at the solid-liquid interface
$V_b$	beam velocity vector
$x$	distance

$\alpha$	thermal diffusivity
$\beta$	volumetric coefficient of thermal expansion
$\gamma$	surface tension
$\Delta H$	latent heat
$\Delta T$	temperature difference
$\Delta T_c$	undercooling contribution from solute diffusion
$\Delta T_K$	undercooling contribution from solid-liquid interface curvature
$\Delta T_R$	undercooling contribution from thermal diffusion
$\Delta T_T$	undercooling contribution from attachment kinetics
$\Delta T_{tot}$	total undercooling
$\varepsilon$	emissivity
$\varepsilon^*$	thermal strain parameter
$\varepsilon_C$	cooling rate
$\varepsilon_e$	elastic strain
$\varepsilon_m$	maximum elastic strain
$\varepsilon_o$	inelastic strain caused by creep and phase transformations
$\varepsilon_p$	plastic strain
$\eta_l$	absorption coefficient of deposit
$\eta_P$	fraction of energy absorbed by powder during flight
$\theta$	angle
$\lambda$	laser absorptivity
$\lambda_c$	positive fraction accounting for condensation of vaporized atoms
$\mu$	dynamic viscosity
$\rho$	density
$\sigma_{SB}$	Stefan-Boltzmann constant
$\sigma$	stress
$\sigma_f$	flow stress
$\tau$	characteristic time scale
$\tau_M$	Marangoni stress
$\varphi$	nickel equivalent expression
$\psi$	angle between normal to solidification interface and preferred $[hkl]$ direction

## 1. Introduction

Additive manufacturing (AM) processes build three-dimensional (3D) parts by progressively adding thin layers of materials guided by a digital model. This unique feature allows production of complex or customized parts directly from the design without the need for expensive tooling or forms such as punches, dies or casting molds and reduces the need for many conventional processing steps. Intricate parts, true to their design can be made in one-step without the limitations of conventional processing methods (e.g. straight cuts, round holes) or commercial shapes (e.g., sheet, tubing). In addition, a significant reduction in the part count can be realized by eliminating or reducing the need to assemble multiple components. Furthermore, parts can be produced on demand, reducing the inventory of spares and decreasing lead time for critical or obsolete replacement components. For these reasons, AM is now widely accepted as a new paradigm for the design and production of high performance components for aerospace, medical, energy and automotive applications. Aerospace examples include complex fuel injector nozzles that previously required assembly of multiple parts and lightweight engineered structures that result in significant cost savings. Medical and dental implants produced by AM offer significant improvements in integration, biocompatibility and the possibility of patient-matched devices derived from the patient's own medical imaging. Mixing and swirling burner tips made from high temperature materials in complex shapes save energy, extend component lifetime and reduce system repair and downtime. Automotive applications include prototyping and the rapid fabrication and repair of industrial hardware such as punches, dies and custom tooling.

Significant advances over the past twenty years in the constituent technologies of AM metal processing, including lower cost reliable industrial lasers, inexpensive high performance computing hardware and software, and metal powder feedstock technology have enabled it to become a state-of-the-art processing method. It has now reached a critical acceptance level, as evidenced by the rapid growth in sales of commercial systems. AM metal technology, developed in national laboratories, universities and industrial research laboratories, is now being demonstrated and adopted by industry. While certain applications have reached technology readiness levels of fully certified production, most have done so through brute force certification of each individual part type, material and process. A more thorough understanding of the feedstock materials, processes, structures, properties and performance are desirable to produce defect-free, structurally-sound and reliable AM parts.

Additive manufacturing has grown from the field of rapid prototyping, which was developed more than 30 years ago for producing non-structural components largely for design purposes. The newer field of metal AM has the ability to produce hard to manufacture components in complex structural shapes that are difficult or impossible to fabricate by conventional means, as a direct replacement of conventionally manufactured components. Metal AM is now finding acceptance for critical applications such as medical implants, aerospace, and in many other fields with a clearly demonstrated ability to produce complex shapes [1]. There are however some metallurgical differences between conventional and AM components such as mechanical anisotropy, residual stress, and defects unique to AM processes that must be addressed for critical aerospace applications, particularly those components that require exposure to high temperature fatigue [1]. Application such as fuel injectors and other highly complex components are now beginning to make their way to certification, while other high performance components such as turbine blades for example are at an earlier stage of development.

The AM of alloys has its origins in metal powder technology, high-energy beam welding, cladding and prototyping. The existing knowledge base in these technologies is helpful but does not address many of the important features of AM. If the many decades of research efforts that have resulted in a relatively mature knowledge base of welding and cladding is any clue, the path forward for the research and development of AM of metallic materials is going to be a long and tortuous road. The journey has already begun with a growing interest for research, particularly of metallic materials. The increasing number of publications and several reviews [2–11] on processes, microstructure and properties of AM parts are available in the literature. Since AM is relatively new and rapidly evolving, a periodic critical assessment of our understanding is necessary and this review seeks to fulfill this need.

The review focuses on the AM of metallic materials, particularly the processes, structure and properties of parts. Solid-state processes such as sheet lamination or those that rely primarily on cold compaction, binders or infiltration and brazing are not within the scope of this review. Apart from its comprehensive coverage of important engineering alloys, this review includes AM of special materials including refractory alloys, precious metals and compositionally graded alloys. Also, a succinct comparison of AM with welding is presented to highlight the similarities in physical processes. The mature knowledge base of welding and metallurgy can provide powerful synergistic benefit for deeper scientific understanding of AM. Furthermore, the review seeks to critically examine the printability of various engineering alloys based on the current knowledge base of AM, metallurgy and fusion welding. Where possible, this review emphasizes quantitative understanding in a form that can be used for back-of-the-envelope calculations to obtain reusable insights. It is hoped that this work will be helpful to understand the current state of the technology, the gaps in scientific work and the research needs most beneficial for the advancement and expansion of AM of metallic materials.

## 2. Process

The AM processes consolidate feedstock materials such as powder, wire or sheets into a dense metallic part by melting and solidification with the aid of an energy source such as laser, electron beam or electric arc, or by the use of ultrasonic vibration in a layer by layer manner. Table 1 indicates the commonly used alloys and their various applications in additive manufacturing [1]. Manufacture of a structurally sound, defect free, reliable part requires an understanding of the available process options, their underlying physical processes, feedstock materials, process control methods and an appreciation of the origin of the various common defects and their remedies. This section provides an introduction to AM processes with a particular emphasis on the reusable process fundamentals for engineers and researchers.

### 2.1. Manufacturing processes for alloys

The AM processes fall into two categories defined by ASTM Standard F2792 [12] as Directed Energy Deposition (DED) and Powder Bed Fusion (PBF). A further distinction is provided as a function of the primary heat source; we will use the nomenclature for laser (L), electron beam (EB), plasma arc (PA), and gas metal arc (GMA) heat sources as PBF-L, PBF-EB,

**Table 1**  
Common additive manufacturing alloys and applications [1].

Alloys ⇌ Applications ↓	Aluminum	Mangaging steel	Stainless steel	Titanium	Cobalt chrome	Nickel super alloys	Precious metals
Aerospace	X		X	X		X	
Medical			X	X			X
Energy, oil and gas			X				
Automotive	X		X				
Marine			X				
Machinability and weldability	X		X				
Corrosion resistance			X	X			
High temperature			X	X			
Tools and molds		X	X				
Consumer products	X		X				X

DED-L, DED-EB, DED-PA and DED-GMA. An additional distinction can be made between direct-to-metal AM processes, which begin with a computer model and directly produce a net shaped part and indirect processes that begin with a computer model, print an intermediate part, and then require additional intermediate processing steps such as casting, bulk sintering or machining to attain a net shaped part. While nearly all applications of AM fabricated metal part require some degree of post processing, heat treatment, and finishing, PBF AM processes, and in many cases DED processes, may be considered direct-to-metal. DED processes are also often used to produce large rough “blank” shapes requiring extensive machining to create the direct features. Binder jetting and ultrasonic additive manufacturing (UAM) are considered indirect AM metal processes [13–15]. Within this review, we focus primarily on direct to metal DED and PBF AM processes as they share similar fundamentals of high energy density heat sources, localized melting and microstructural evolution based upon solidification of the melt.

Additional nomenclature refers to the feedstock commonly used, either in the form of powder or wires, as powder-bed, powder-feed or wire-feed processes. A critical understanding of the capabilities and complexities of these AM processes is needed for the selection of the right technique for a target application. The current section provides the underlying principles of these AM techniques and their specific features.

**Fig. 1(a)** shows a schematic view of DED-L [16–25] with powder used as the feedstock material. DED-L typically relies upon the feeding of powder into the melt path and molten pool created by a laser beam to deposit material layer-by-layer or feature-by-feature upon a substrate part or build plate. A shielding gas such as argon is used to protect the molten metal from oxidation and to carry the powder stream into the molten pool. DED-EB (**Fig. 1(b)**) uses an electron beam to

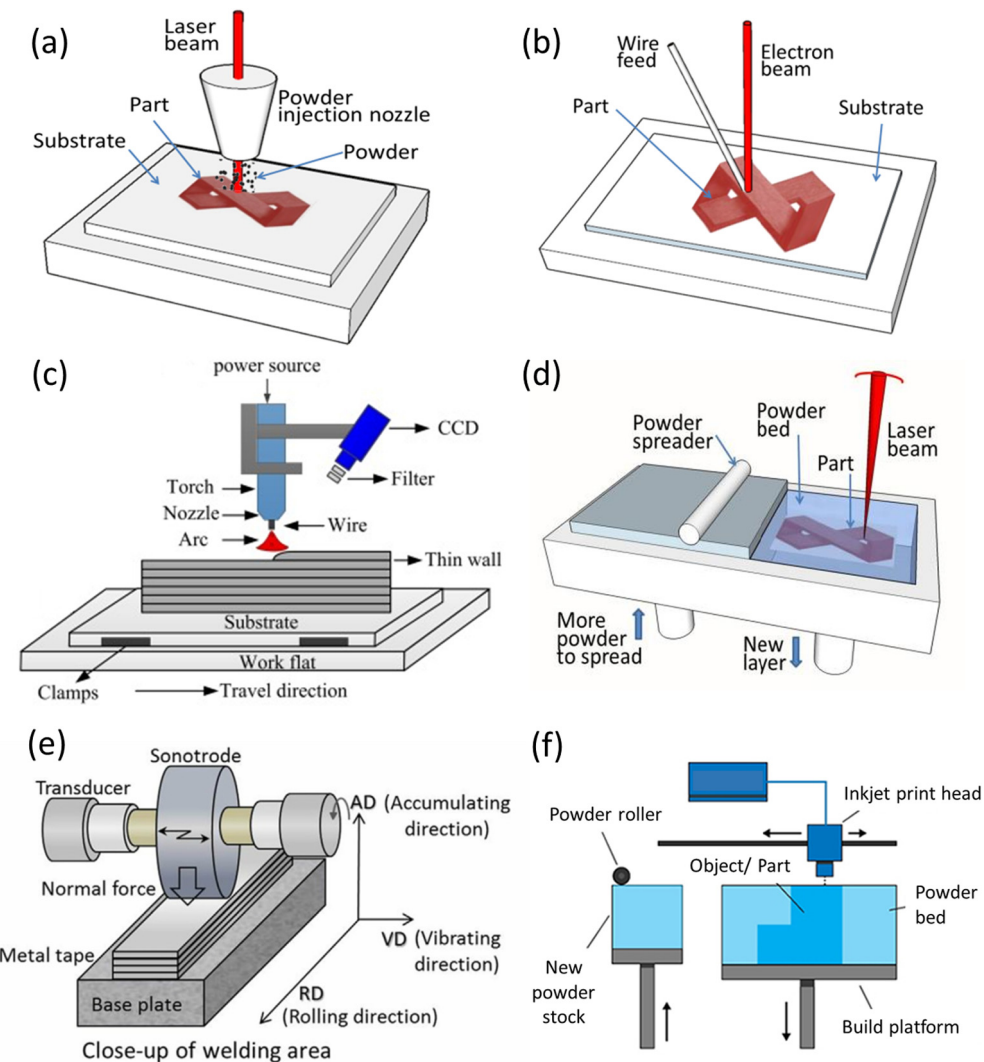


**Fig. 1.** Schematic diagram of (a) DED-L (b) DED-EB (c) DED-GMA [29] (d) PBF-L (e) ultrasonic additive manufacturing (UAM) process [38] and (f) binder jet process [40].

create a deposit by feeding commercial filler wire into the molten pool. A large vacuum chamber provides a high-purity processing environment during the build and cooling. In DED-PA or DED-GMA, an electric arc is used as the heat source with filler wires as feedstock material similar to fusion welding [26–29]. These processes consist of the power source, a wire feeding system, and an integrated multi-axis control system for relative movement of the build and the heat source as shown in Fig. 1(c). In all of these DED processes, a 3D part is fabricated in a layer-by-layer manner following the input of a digitized geometry from a computer aided design (CAD) file. The distance between the focused beam and the build surface is maintained by a synchronized multi-axis movement of the fixture that holds the substrate and the heat source during layer-by-layer deposition. The parts with overhanging features may also require appropriate supporting structure to prevent distortion of hot overhangs induced either thermally or under their own weight [30]. The processing conditions such as scanning speed of the heat source and feed rate of the feedstock material are either pre-set or controlled in-process by appropriate sensors. After the deposition process, the fabricated part is removed from the substrate by machining and often requires further finishing operations to achieve the desired surface quality.

PBF-L [31–35] begins with a solid or surface CAD model, orienting it within a build volume to include support structures, slicing into planar layers, defining a scan path and build-file based upon a pre-specified set of material specific parameters and the specific machine configuration (Fig. 1(d)). The part forms by spreading thin layers of powder and fusing pass-by-pass and layers upon layer of this powder, under computer control, within an inert chamber, incrementally lowering the Z-axis after each layer. Fusion occurs by a raster motion of the laser heat source using galvanometer driven mirrors, resulting in melting and solidification of overlapping melt tracks.

PBF-EB is similar to PBF-L but instead uses an EB heat source within a vacuum chamber. Electromagnetic coils raster the electron beam across each layer of powder. The process relies on two-step sequence, first lightly sintering each layer of powder to prevent electro-static charging and repulsion of the powder particles followed by an additional pass fusing the region defined by the part volume. As the alloy powder is already lightly sintered on a bed which is often held at an overall elevated temperature, the PBF-EB processes usually allow relatively faster scanning speed of the beam but are limited to electrically conductive powder. For PBF processes, the scanning of the beam for each layer can follow different patterns, also referred to as hatching, such as unidirectional, bidirectional, spiral, zigzag and cross-wise.

The UAM process [36,37] involves joining of metallic sheets together by use of ultrasonic vibrations under a constant normal force as shown schematically [38] in Fig. 1(e). Metal sheets are softened by the heat generated by ultrasonic vibration and joined in solid-state. Finally, in binder jet AM process [39], a liquid binder jet is supplied by an inkjet printer head on an alloy powder bed as shown [40] in Fig. 1(f). The binder is cured to hold the powder together to fabricate the component.

The delivery of the feedstock material depends on the specific AM process. In DED-L process, the alloy powder is fed coaxially with the laser beam by a set of nozzles. In PBF based AM processes, solid powders are often reused to avoid wastage that can result in poor surface finish and mechanical properties of the final part, as discussed in a later section. In contrast to the powder based AM processes, the DED-GMA technique is similar to filler wire based fusion welding processes. Gas metal arc welding processes especially with short-circuiting mode of metal transfer is commonly used for DED-GMA process because of lower arc power compared to other modes of metal transfer. For deposition of titanium alloys, a plasma arc (DED-PA by Norsk Titanium) is also attempted as the heat source with titanium filler wire to avoid arc instability [28]. Commercial abundance and low price of the filler wire compared to alloy powders make the DED-GMA or PA processes less expensive. In UAM, the feedstock is supplied as rolled sheet or foil typically in the thickness range of 0.5–1.0 mm [36,37].

The AM processes are also characterized by their production times, maximum size of the component that can be fabricated, ability to produce intricate parts and the product qualities such as defects and dimensional accuracy. The production time of the powder based AM processes is high due to the limitations of powder feeding rate, scanning speed and low layer thickness. In contrast, filler wires allow relatively higher mass flow (deposition) rate in wire based processes. As a result, the powder based processes are considered suitable for relatively smaller parts and the wire based processes are considered suitable for fabrication of large-size components, typically heavier than 10 kg [28].

Good surface finish and ability to produce intricate features are considered to be the special strength of the powder based AM processes due to small size of the powder particles. Use of laser and electron beam further allows controlled melting and solidification with the powder-fed and powder-bed AM processes resulting in good dimensional accuracy. Within this discussion, good surface finish refers to a comparison between AM metal processes. Factors contributing to surface quality for powder-based systems include alloy type, powder shape, size and morphology as well as laser or electron beam focal spot sizes and other process and design parameters. As stated above, wire based processes with high deposition rates and capable of producing large components require large molten pools and feature large layered weld beads with correspondingly rough beaded surfaces. Shapes deposited using wire feedstock often require machining to achieve the desired net shape while powder based processes often produce shapes and feature that require little finishing to achieve a functional form. Section 2.9.3 below provides additional detail regarding the relationship between powder feedstock materials and surface roughness. Section 6.2 below provides additional detail regarding deposition rates and surface roughness for wire based processes.

UAM and binder jetting are still nascent and have found few commercial applications to date [13–15]. The subsequent sections in this article are therefore focused on the powder and wire based AM processes.

**Table 2** shows a comparison of the DED and PBF based AM techniques. In practice, an AM process is selected by considering the desired product size, quality and an overall comparison of cost associated with the candidate processes [14]. As stated above, AM processes with alloy powder as feedstock material are commonly used to fabricate very intricate components with a reasonably good surface finish. However, the fabrication process is very slow and the powder feedstock is

**Table 2**

Comparison of two main categories of additive manufacturing processes for metallic components: directed energy deposition (DED) versus powder bed fusion (PBF).

Process	DED		PBF	
	Powder	Wire	Powder	
Heat source	Laser	E-beam	Electric arc	Laser
Nomenclature	DED-L	DED-EB	DED-PA/DED-GMA	PBF-L
Power (W)	100–3000	500–2000	1000–3000	50–1000
Speed (mm/s)	5–20	1–10	5–15	10–1000
Max. feed rate (g/s)	0.1–1.0	0.1–2.0	0.2–2.8	–
Max. build size (mm × mm × mm)	2000 × 1500 × 750	2000 × 1500 × 750	5000 × 3000 × 1000	500 × 280 × 320
Production time	High	Medium	Low	High
Dimensional accuracy (mm)	0.5–1.0	1.0–1.5	Intricate features are not possible	0.04–0.2
Surface roughness (μm)	4–10	8–15	Needs machining	7–20
Post processing	HIP and surface grinding are seldom required	Surface grinding and machining is required to achieve better finish	Machining is essential to produce final parts	HIP is rarely required to reduce porosity
Refs.	[16–21]	[22–25]	[26–29]	[31–35]

expensive [13,15]. Wire and metallic sheet based AM processes are fast but lack dimensional accuracy and result in defects and poor surface finish especially for parts with complex shapes [13,14].

In summary, several variants of AM techniques have evolved to manufacture parts with complex internal features and external contours and work with alloys that are difficult to cast and process thermo-mechanically, hard to machine or build successfully by powder metallurgy (sintering).

## 2.2. Feedstock materials

Alloy powders are commonly used as feedstock materials in the laser and electron beam assisted AM techniques due to ease of feeding and controlled melting. Feeding of a mixture of multiple alloy powders in a pre-set ratio further allows building a part with composition/property gradient that is otherwise difficult by the contemporary processes. However, the manufacturing of high quality powder remains a critical challenge due to their high surface area and susceptibility to oxidation. An assessment of the manufacturing routes of alloy powders and their respective performances during the AM processes is therefore important.

The qualities of the additively manufactured parts are significantly influenced by the characteristics of the feedstock materials [41,42]. These characteristics include the shape, size distribution, surface morphology, composition and flowability of the powders [2]. Typical particle sizes for PBF-L are in the range of 10–60 μm and 60–105 μm for PBF-EB. Scanning electron microscopy (SEM), X-ray and computed tomography (CT) are used to examine the shape and the surface morphology of the powder particles [43]. Laser diffraction and sieving method are used to ensure the size distribution of the powders [43]. Flowability of the powders is measured by Hall flow meter [43,44].

The qualities of the feedstock materials depend on their manufacturing process. The alloy powders are mainly made in four ways. In gas atomization (GA) process [45], the molten alloy is atomized by the high pressure flow of argon and nitrogen gas. In rotary atomization (RA) process [46], the molten metal is poured on a rotary disk. Fine droplets of molten metal are flung from the disk, solidified and collected as powders. Plasma rotating electrode process (PREP) [47,48] is a method for producing metal powders where the end of a metal bar is melted using an electric arc or plasma. As the bar is rotated about its longitudinal axis, molten metal is centrifugally ejected resulting in fine droplets that are collected as solidified powders. High pressure water jet is used to atomize and solidify the molten metal droplets as powders in water atomization (WA) process [49].

Fig. 2(a)–(e) shows the SEM images of the alloy powders produced by different processes. The PREP powders are perfectly spherical in shape with smooth surfaces. The powder particles from the RA process also exhibit smooth surface but are not spherical in shape. The GA process forms powders with spherical morphology and dimpled surface texture although the presence of the satellite particles increases the surface roughness. The powders from the WA process are usually irregular in shape with coarse surface texture resulting in lower flowability. As a result, these powders lead to deposition of thinner layers in comparison to that with the powders from GA process under the same AM processing conditions [50,51]. Because of the coarse surface texture and irregular shape of the powders from WA process, the components made by these powders exhibit high surface roughness [50]. The PREP and WA processed powders exhibit the most and the least uniform size distributions, respectively [50,52]. The powders with uniform size distribution promote homogenous melting, and good inter-layer bonding, structure, mechanical properties and surface finish [53,54]. In contrast, the GA processed powders often contain entrapped gas bubbles leading to porosity in the component [54]. Fig. 2(f) and (g) shows that a component fabricated using PREP powders exhibits lower porosity than that made by GA powders under the same processing conditions.

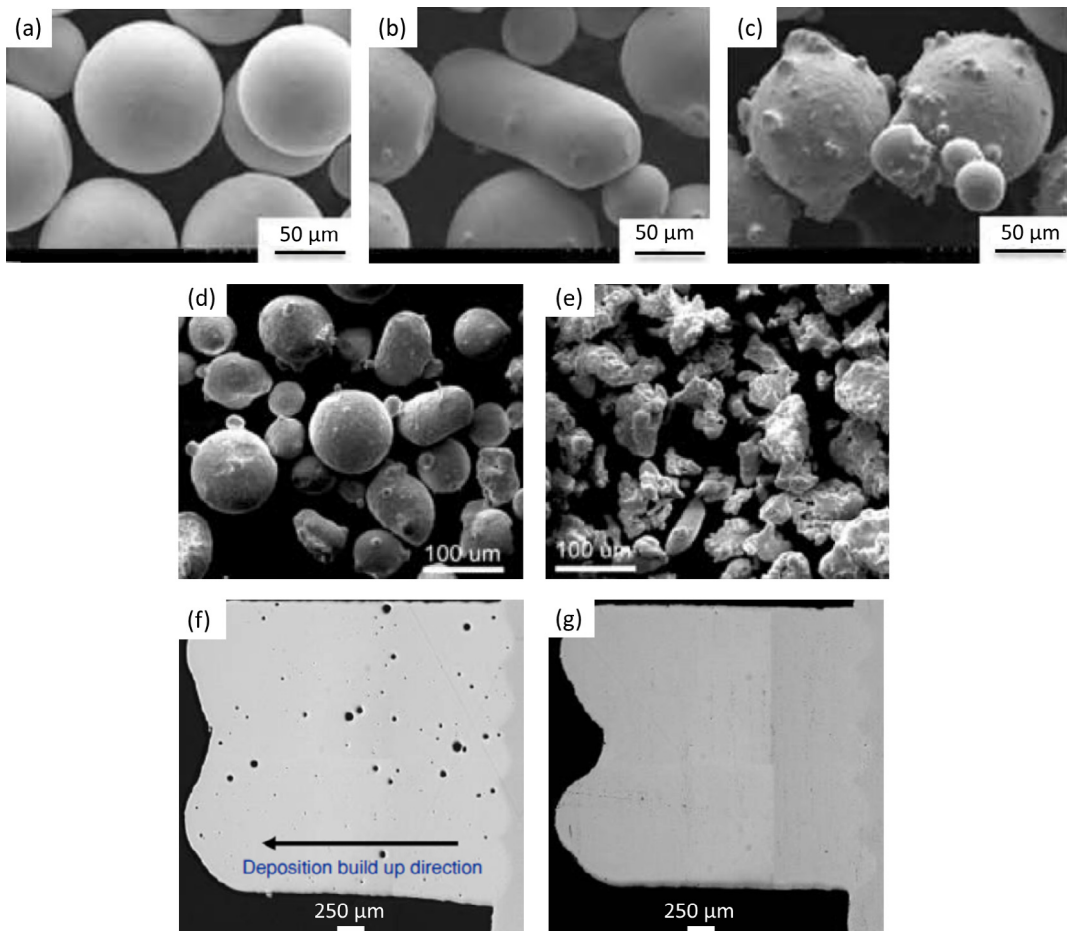


**Fig. 2.** SEM image of the alloy powders manufactured by (a) PREP (b) RA and (c) GA process [52]. Comparison of shape of powders fabricated by (d) GA and (e) WA process [50]. IN 718 component fabricated using (f) GA [54] and (g) PREP powder [54].

Fine powder particles with uniform size distribution and smooth surface are able to provide uninterrupted flow through the feeder nozzles and promote small pool size under the concentrated beam. As a result, both DED and PBF processes prefer the use of alloy powders with good surface finish and size distribution. However, high quality powders are expensive because of the high cost of the fabrication process such as PREP and low yield of the atomization process. In PBF process, the solid powders can be reused to reduce cost although such reuse of powder particles result in irregular shape and poor surface finish of the final part [55]. Therefore, the powders as feedstock materials must be selected by considering both their quality and cost in association with the corresponding AM process. The wires of different alloys and sizes are manufactured by wire drawing and are relatively inexpensive than powders of the same alloy. Filler wires of diameters smaller than 0.8 mm are scarce and thus, wire-fed AM processes require a larger melt pool size resulting in a relatively rougher surface finish of the final part [56,57]. However, the use of filler wires can result in a greater rate of deposition compared to the powder particles.

For PBF AM, the powder packing structure is a critical parameter. Experimental characterization of powder is typically limited to measuring bulk properties (e.g., mean diameter, particle size distribution, and packing density) and is inadequate to resolve the local configuration of individual particles on the powder bed. Alternatively, numerical simulation has been used to obtain the packing structure. Many of the numerical algorithms used stem largely from geometrical considerations (e.g., filling of open space by spheres) and did not consider the particle-to-particle mechanical interactions [58,59]. On the other hand, a group of dynamic simulation algorithms has been applied to simulate the transient packing process where individual particles, roller and their mechanical contact interactions are directly considered based on numerical solution of equations of motion using methods such as Discrete Element Method (DEM) [60,61]. Although it may appear to be large, the number of particles simulated (of the order of 10,000) is still fairly small when compared to that used in the actual build. Moreover, the particles' shape in the simulation is assumed to be perfectly spherical. Hence, validation of the numerical prediction using the experimental data remains a crucial effort in the future.

Alloy wire feedstock materials used in DED AM techniques are melted using electron beam, laser and arc based processes and can increase the mass flow and deposition rate for building a large part or feature. The use of filler wires can result in a greater rate of deposition compared to the powder particles. The wires of different alloys and sizes are manufactured by wire drawing and are relatively less expensive than AM powders of the same alloy. However, the cost savings per kilogram is offset by the material lost to machining process waste as wire based AM processes often require extensive machining allowance to be removed to achieve the desired net shape. In addition remnant material from a partially used spool may not be suitable for reuse unlike the ability to reuse and recycle unfused PBF process powder. On the other hand, the wires are produced for the welding industry and available in spooled form and in a wide range of alloys. The benefits of spooled weld wire include a history of alloy development, well characterized weld metal deposit properties and mature, certified wire production processes. Filler wires of diameters smaller than 0.8 mm are difficult to straighten and feed accurately using conventional welding systems, therefore wire-fed AM processes requiring the use of commercially available weld wire results in a larger melt pool size when compared to powder based processes. This results in large weld beads and a relatively rougher surface finish of the final part [56,57]. As a benefit, wire feedstock has significantly less surface area per kilogram than powder product and is less likely to oxidize and absorb moisture or contaminants. Wire forms are easier to store and handle and pose fewer hazards associated with environment, safety and health when compared to metal powders. Table 3 provides the chemical compositions of the commonly used alloys in AM [62–67]. The differences in their thermo-physical properties result in significant differences in the structure and the properties of the products fabricated using different alloys under same processing conditions. Therefore, all alloys are not equally printable and an appropriate alloy must be selected in order to fabricate a defect free and structurally sound component, as discussed in Section 7 of this review. The selection of a feedstock material, its size and shape directly influence the choice of the right AM technique and processing conditions for a target part and component.

### 2.3. Heat source characteristics

During AM, energy absorption by the feedstock materials affects the temperature profiles, deposit geometry, solidification, microstructure and properties of the part. Energy absorption depends on the heat source characteristics. For lasers, electron beams and plasma arcs the radius and the power density distribution are important properties of the heat source. The power density distributions of these heat sources often follow the following axisymmetric Gaussian profiles.

$$P_d = \frac{fP}{\pi r_b^2} \exp\left(-f \frac{r^2}{r_b^2}\right) \quad (1)$$

where  $f$  is the distribution factor,  $P$  is the total power of the heat source,  $r_b$  is the radius of the heat source and  $r$  is the radial distance of any point from the axis of the heat source. Eq. (1) indicates power density distribution of the heat source on the surface. A higher value of  $f$  indicates higher power density at the heat source axis and vice versa and a larger  $r_b$  indicates lower power density at all radial locations and vice versa.

In Fig. 3, power density is represented as a function of horizontal position relative to the heat source axis for different values of distribution factor. Depending on the nature of the heat source, the power density distribution can also be uniform [68–70]. With the increase of the distribution factor, the energy becomes more focused resulting in a high peak temperature underneath the heat source. Therefore, the power density distribution describes the nature of the heat source and is one of the most important parameters to be controlled in order to fabricate high quality AM components.

There are some commonly used methods for measuring the energy distribution of laser, electron beam, and arc heat sources. Laser beams are a coherent source of photons that can be measured using solid state charged coupled device (CCD) detectors. However, the intensity of a laser beam used for AM will quickly saturate or damage the detector, so means of limiting the beam's intensity are required. A rotating wire apparatus has been used for CO<sub>2</sub> laser beams by spinning a fine wire through the beam and measuring the reflected laser beam intensity to estimate the power density distribution of the beam [71]. More recent devices use a rapidly spinning tube with a small pinhole and mirror to direct the laser to a CCD detector. This method maps the power density of the focused beam of both CO<sub>2</sub> and solid state lasers. Furthermore, by sampling the beam at different locations along its propagation axis, the divergence of the beam can be measured as well as the minimum spot size, allowing for a complete characterization of the laser beam following a standard procedure [72]. Minimum spot sizes used for AM depend on the process. Powder bed typically uses beam diameters on the order of 50–100 μm for fine resolution, while DED powder fed processes use larger, defocused, beams with millimeter sized spots for higher deposition rates.

**Table 3**

Chemical compositions (wt.%) of SS 316 [66], Ti-6Al-4V [65], IN 718 [64], 800 H [67], H 13 steel [63] and AA 6061 [62].

Alloys	Ti	Al	V	Fe	Ni	Cr	Mn	Mg	Si	Mo
SS 316	–	0.005	–	Bal.	8.26	17.2	1.56	–	0.33	–
Ti-6Al-4V	Bal.	6.28	3.97	0.052	–	–	–	–	–	–
IN 718	1.02	0.50	–	Bal.	53.4	18.8	0.07	–	0.12	2.99
800 H	0.35	0.25	–	Bal.	31.0	20.6	0.85	–	0.32	–
H 13	–	–	1.20	Bal.	–	5.50	0.60	–	1.25	1.75
AA 6061	0.15	Bal.	–	0.7	–	–	0.15	1.2	0.8	–

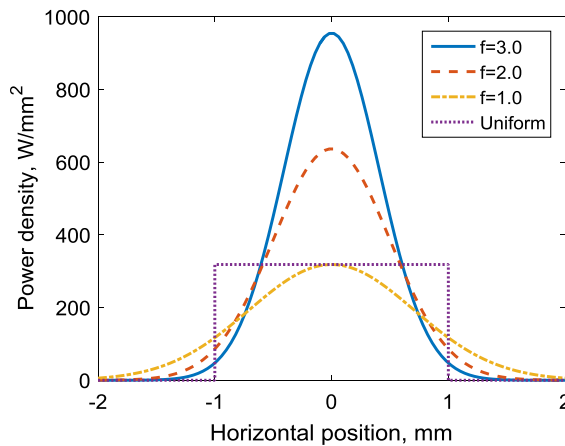


**Fig. 3.** The power density distribution with a power source of 1000 W and 1 mm radius, as a function of horizontal position relative to the heat source axis for different values of the power distribution factor.

Electron beams are focused using magnetic lenses instead of optical lenses used for lasers and interact with materials differently than lasers [73], requiring a different measurement technique. Diagnostic methods for measuring the power distribution in electron beams are variations of the conventional Faraday cup, which is a current measuring device that consists of an electrically conductive trap to capture and measure the beam current. Modifications to the Faraday cup are required for measuring the beam's power distribution so that only a selected portion of the beam is transferred into the cup at any specific time. One type of modified Faraday cup isolates a portion of the beam by placing a slit above the Faraday cup and sweeping the beam over this slit to measure the beam's profile along the sweep direction. This arrangement provides a one-dimensional view of the beam along the sweep direction and is useful for inspecting beams with radial symmetry. However, if the beam is non-circular or has an irregular power distribution then more sophisticated techniques are required to map the power-density distribution in the beam. Pinhole devices [74] and an Enhanced Modified Faraday Cup method that uses computed tomography (CT) with multiple slits [75] are two different methods to measure and map the power distribution of irregular-shaped electron beams. Pinhole measurements are made using a small aperture (<0.10 mm diameter) placed over a Faraday cup, and the electron beam sweeps over the pinhole several times at regularly spaced intervals to provide enough information to map the power distribution in the beam. The CT method uses radial thin slits placed over the Faraday cup to sample the beam. As the beam sweeps over the slits at regularly spaced angles, multiple beam profiles are recorded and CT reconstructed to map the power distribution in the beam [76,77]. High power electron beams cannot be focused as tightly as laser beams and typically have minimum beam diameters on the order of 200 μm [76,77].

In arc sources the power density distribution is affected by the arc length, filler wire diameter, arc current and the nature of the shielding gas and is commonly determined by an appropriate split anode technique [78]. In particular, the pulsed current sources are used for the electric arc assisted wire-fed AM processes. The pulsating nature of current allows high peak pulse for a short duration that helps in superior control on filler wire deposition and heat input.

In conclusion, both laser and electron beams provide high peak power and can be focused to a spot radius on the order of 50 μm (laser powder bed) and 100 μm (EB) resulting in very high power densities. Electron beams and laser beams can further be manipulated to deliver either a uniform, pulsed, or otherwise modulated power distribution over time. In contrast, the focused spot size of an electric arc varies in the range of a few millimeters with the plasma arc being more concentrated than a gas metal arc. The choice of an appropriate heat source for AM will depend on the need for fabrication of parts at high deposition rate or with fine resolution of features.

#### 2.4. Interaction between heat source and feedstock materials

In order to understand the evolution of temperature field during the deposition process in AM, a quantitative assessment of the absorption of heat energy by the feedstock material is needed. In DED processes, a fraction of the total heat is spent to heat the powder particles as they emerge from the nozzle and travel through the beam as shown in Fig. 4(a). The heat absorbed by the particles in-flight depends on their density and thermo-physical properties, shape and size distribution, free flight duration through the beam, and gas velocity [79]. The powder particles are usually heated to a higher temperature although they do not reach their melting temperature [79]. The remaining beam energy impinges on the deposit surface resulting in a small molten pool. The extent of energy absorbed by the deposit surface also depends on beam characteristics, deposit geometry and the shielding gas [79]. The heat source in DED process can be represented by the following volumetric heat source with a modified Gaussian distribution [79].

$$P_d = \frac{fP}{\pi r_b^2 t_l} [\eta_p + (1 - \eta_p)\eta_l] \exp\left(-f \frac{r^2}{r_b^2}\right) \quad (2)$$

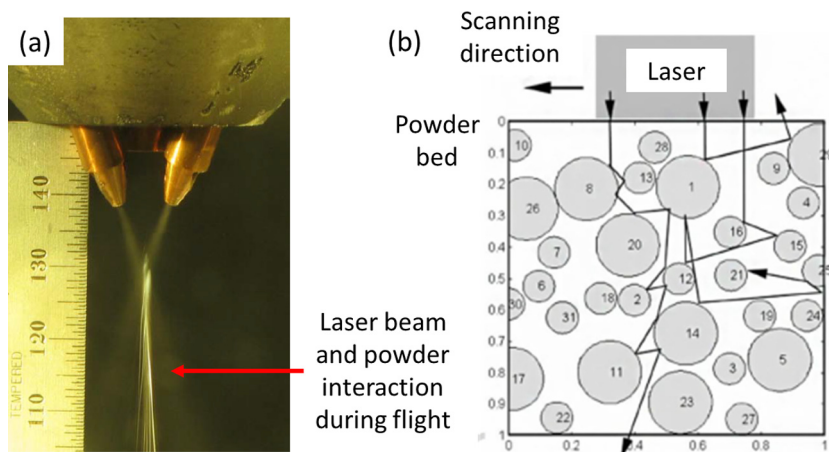


**Fig. 4.** (a) Laser beam and powder interaction during the flight of the powder from the nozzle to the substrate [reproduced with permission, courtesy of Dr. T. A. Palmer] (b) inter-reflection of laser beam and heat absorption by the powder during powder bed fusion process [80].

where  $\eta_p$  is the fraction of energy absorbed by the powder during flight,  $\eta_l$  refers to the absorption coefficient of the deposit, and  $t_l$  is the layer thickness [79]. A higher value of  $f$  indicates higher power density at the heat source axis and vice versa and a larger layer thickness indicates lower power density at all radial locations and vice versa. The value of the absorption is high when the powder is solid, however after a short time (a few milliseconds) the liquid surface absorbs energy by Fresnel absorption [79]. So, the value of  $\eta_l$  is high initially when the liquid layer is forming but reduces once the surface melts. For a laser assisted DED process with Argon as shielding gas, the absorption coefficients for a laser beam of 1064  $\mu\text{m}$  wavelength remain between 0.3 and 0.7 depending on whether the deposit is in liquid or solid state [79].

In case of the PBF processes, the entire amount of heat source energy (as shown in Eq. (1)) is incident on the powder bed. When a laser beam impinges on a particle, part of the energy is absorbed by the particle and the rest is reflected that continues until the beam emerges outside of the powder bed or its intensity becomes negligible as shown in Fig. 4(b) [80]. As the beam undergoes multiple reflections within the powder layers, the coefficient of beam absorption by the powder bed is higher than the Fresnel absorption coefficient of the liquid surface. The heat absorbed by the particles in powder-bed depends on the particle size, packing density of the powder bed and material properties.

The heat absorption mechanism by the wire in DED-GMA process is very similar to that for consumable electrodes in fusion welding processes. However, due to higher surface to volume ratio of the powder, the powder based AM processes have higher melting efficiency [81] than that for DED-GMA. Sometimes, to enhance the melting efficiency the wire is pre-heated by resistive or inductive heating or using a secondary heat source [82].

At high power densities the powder particles or the molten droplets may be ejected from the molten pool resulting in spatter formation. The molten pool experiences significant recoil pressure due to local vaporization of alloying elements and the molten droplets may be ejected when the recoil pressure is higher than the surface tension force at the periphery of the liquid pool. [83,84]. During PBF-EB powder particles may also be ejected due to the high repulsive electrostatic force [85,86].

## 2.5. Principles of heat and mass transfer and fluid flow

Because of the rapid heating, melting and solidification of an alloy by a moving heat source such as a laser or an electron beam, different regions of the build experience repeated heating and cooling which affect its local structure and properties. The spatially variable thermal cycles result in location dependent, inhomogeneous microstructure and properties. Because of the additive nature of the process, experimental measurements of temperatures are only possible on easily accessible surfaces of the build and not at the interior locations. Transient, three dimensional (3D), temperature fields are prerequisites for understanding the most important parameters that affect the metallurgical quality of the components such as the spatially variable cooling rates, solidification parameters, microstructures and residual stresses and distortion of the components.

AM has more similarities with welding than casting. Moving heat source, formation of a fusion zone with recirculating liquid metal that travels along with the heat source are important physical processes that are shared by both welding and most AM processes. There are also differences between welding, DED and PBF-L because the heat source interacts very differently with a powder bed, a falling stream of powder and solid metal. Furthermore, the scanning speeds and heat source powers are very different. In addition, solid metal surrounds the fusion zone on both sides of the weld but not so for the AM processes. Interaction of the feedstock material with the heat source, progressive build-up of the layers, multiple thermal cycles at any specific location as new layers are added on the previously deposited layers, transient changes in the geometry are some of the features that are necessary for the understanding of AM.

Simulation of the 3D transient temperature field is computationally intensive because of the complex physical processes involved in AM and many of the previous calculations involved simplifications to make the calculations tractable. For example, idealized two-dimensional calculations have been undertaken [87,88], and in some instances, heat sources have been simplified as a line source or double ellipsoid heat source [89] that are contrary to the measured power density distribution data for heat sources. Another common simplification is to totally ignore the convective heat transfer which is often the main mechanism of heat transfer within the liquid pool. The benefit of two dimensional calculation is to save computational time. Similarly, the double ellipsoidal heat source model provides elongated fusion zone shape with rapid calculations. Ignoring convective heat transport is appropriate in special cases where no fusion of the powder occurs.

Convective heat transfer simulations require calculation of velocity fields which is a fairly difficult and computationally intensive task. However, there are many convincing evidences in the literature demonstrating that this simplification can lead to highly inaccurate temperature fields and cooling rates. For example, Svensson et al. [90] noted that the heat conduction equation was inadequate in representing experimental cooling curves for welding. Manvatkar et al. [79] showed that the cooling rates from heat conduction calculations in AM were about twice the correct values.

The convective flow mixes the liquid metal from different regions and enhances the transport of heat within the molten pool as shown in Fig. 5. The circulation pattern has a major effect on the temperature distribution in the liquid alloy, heating and cooling rates, solidification pattern, and the microstructure and properties of the build [91]. Therefore, the accurate calculations of 3D temperature fields require fully-coupled solution of both heat transfer and fluid flow equations. In most calculations some simplifications are made to make the calculations tractable. For example, the densities of the solid and liquid metals are assumed to be constant since this assumption saves computational time but does not degrade accuracy of the results. The surfaces of the deposited layers are often considered to be flat. This assumption does not significantly affect the temperature fields and cooling rates in many cases. The thermal effects due to vaporization of alloying elements are also ignored since the effect is generally small compared with the input energy from the heat source.

The 3D transient temperature fields in the parts are commonly obtained by solving the following equations of conservation of mass, momentum and energy [79,92–94].

$$\frac{\partial(\rho u_i)}{\partial x_i} = 0 \quad (3)$$

$$\frac{\partial(\rho u_j)}{\partial t} + \frac{\partial(\rho u_j u_i)}{\partial x_i} = \frac{\partial}{\partial x_i} \left( \mu \frac{\partial u_j}{\partial x_i} \right) + S_j \quad (4)$$

$$\rho \frac{\partial h}{\partial t} + \frac{\partial(\rho u_i h)}{\partial x_i} = \frac{\partial}{\partial x_i} \left( \frac{k}{C_p} \frac{\partial h}{\partial x_i} \right) - \rho \frac{\partial \Delta H}{\partial t} - \rho \frac{\partial(u_i \Delta H)}{\partial x_i} \quad (5)$$

where  $\rho$  is the density,  $u_i$  and  $u_j$  are the velocity components along the  $i$  and  $j$  directions, respectively, and  $x_i$  is the distance along the  $i$  direction,  $t$  is the time,  $\mu$  is the dynamic viscosity,  $S_j$  is a source term for the momentum equation,  $h$  is the sensible heat,  $C_p$  is the specific heat,  $k$  is the thermal conductivity, and  $\Delta H$  is the latent heat content. The source term  $S_j$  considers buoyancy and electromagnetic forces (the latter is applicable when an arc or electron beam is used). Buoyancy force plays a minor role in molten pool convection and does not affect heat transfer and fluid flow in AM. For the electric arc assisted AM, electromagnetic force is also responsible for the molten metal flow and is considered for the calculations of heat transfer and fluid flow in the melt pool.

The solutions of these equations provide the transient temperature fields in the entire build and velocity fields within the liquid region, cooling rates, solidification parameters which are the most important parameters that determine the structure and properties of parts. These equations are solved using appropriate boundary conditions discussed below.

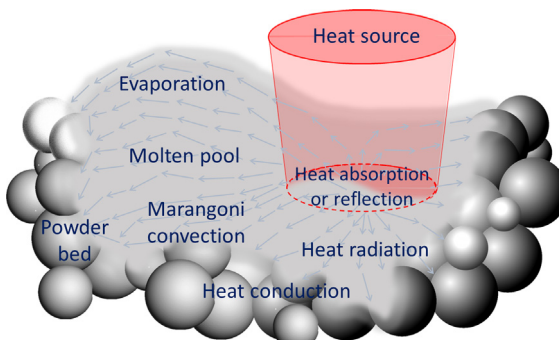


**Fig. 5.** Heat transfer and molten pool dynamics during powder based additive manufacturing.

### 2.5.1. Boundary conditions

The convective flow of molten metal inside the pool is primarily driven by Marangoni flow, i.e., the surface tension gradient on the top surface of the molten pool resulting from the spatial variation of temperature [95,96]. The Marangoni shear stress on the surface of the molten pool can be expressed as:

$$\tau_M = \frac{d\gamma}{dT} \frac{dT}{dr} = -\mu \frac{du_i}{dx_k} \quad (6)$$

where  $T$  is the temperature,  $\gamma$  is the surface tension,  $\tau_M$  is the Marangoni stress,  $r$  is the radial distance from the axis of the heat source,  $u_i$  is the velocity component in the  $i$  direction and  $x_k$  is the distance along  $k$  direction which is the vertical direction. Eq. (6) indicates that the spatial gradient of interfacial tension is a stress, known as the Marangoni stress. It is this stress that drives the flow of liquid metal within the fusion zone.

The surface tension of metals and alloys depends on temperature and composition. The concentrations of surface active elements in alloys, i.e., the elements that have a tendency to migrate to the surface of the liquid, affect the surface tension of alloys significantly. Examples of these elements include common alloying elements such as oxygen, sulfur, selenium, tellurium and nitrogen in steels. For pure metals and alloys containing no surface active elements, the temperature coefficient of surface tension,  $d\gamma/dT$  is negative. As a result, the hot packets of liquid metal carry heat from the middle of the liquid pool to its periphery, and the molten pool becomes wide and shallow. However, when an alloy contains a surface active element, the value of the temperature coefficient of surface tension may become positive except at very high temperatures close to the boiling point of the alloy [97,98]. The variation of surface tension of steels containing low concentrations of sulfur which is often present in steels is shown in Fig. 6. In those cases, the liquid metal flows in a direction opposite to that in the absence of sulfur. Specifically, the convective heat flow carries heat downward in the middle of the liquid pool making the liquid pool deep and narrow [99,100]. It is well known in the welding literature that the presence of low concentrations of surface active elements often results in change in the shape of the molten pool. The effect of these elements on the geometry of the molten pool in AM needs to be investigated.

The velocity component perpendicular to the free surface and all velocity components at the solid-liquid interface are taken as zero. The boundary condition for the heat exchange between the top surface of the build and the surroundings involves consideration of both convective and radiative heat transfer:

$$-k \frac{\partial T}{\partial z} = \sigma_{SB}\varepsilon(T^4 - T_a^4) + h_c(T - T_a) \quad (7)$$

where  $\sigma_{SB}$  is the Stefan-Boltzmann constant ( $5.67 \times 10^{-8} \text{ W m}^{-2} \text{ K}^{-4}$ ),  $\varepsilon$  is the emissivity,  $T_a$  is the ambient temperature and  $h_c$  is the convective heat transfer coefficient. Significant variations in the heat transfer rates can occur depending on the specific experimental conditions. Since the accuracy of the computed temperature field is affected by the value of the heat transfer coefficient, the uncertainty in the heat transfer coefficient can significantly affect the reliability of the computed temperature field. Michaleris [101] reported a heat transfer coefficient of  $1.0 \times 10^{-6} \text{ W m}^{-2} \text{ K}^{-1}$  for free convection and  $21.0 \times 10^{-6} \text{ W m}^{-2} \text{ K}^{-1}$  for forced convection for DED-L of Ti-6Al-4V based on a combination of heat conduction calculations and experiments. Convective heat transfer within the liquid pool was ignored in the estimation [101]. The boundary conditions for other walls are also convective and radiative heat transfer with the surroundings.

In all numerical calculations of temperature and velocity fields, the computational domain is subdivided into many small control volumes or cells and appropriate temperature dependent thermo-physical properties are assigned to each of these cells. Properties of these cells change with time as temperature changes or new materials are added to the build. Additions of mass may be simulated either by changing properties of existing cells or by adding new cells with appropriate

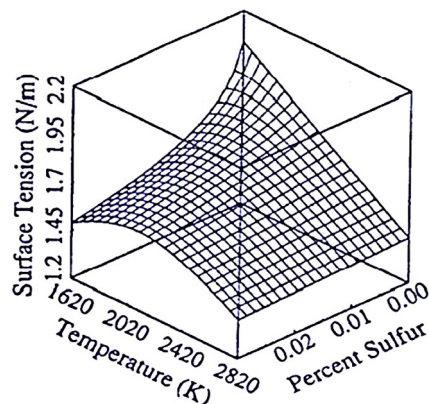


**Fig. 6.** Surface tension of Fe-S alloys as a function of temperature and composition [98].

thermo-physical properties. The commonly used feedstock materials for AM are stainless steel, nickel-base superalloys, Ti-6Al-4V, tool steels and aluminum alloys. Table 4 presents the thermo-physical properties for these alloys [102,103].

Different analytical and numerical approaches have been used to understand the heat transfer and the flow of molten metal. Table 5 provides a summary of the important features of the various methods used to understand heat transfer and materials flow. These include analytical approach [104–106], heat conduction models [107–116], heat transfer and fluid flow models [79,92,93,117–119], level set method [120–123], volume of fluid method [124,125], Lattice Boltzman and arbitrary Lagrangian Eulerian methods [59,126–130]. Many of the previous studies have considered temperature dependent thermal conductivity and specific heat for the work-piece [27,131,132].

In AM processing, heating, melting, solidification, and cooling can occur very rapidly. The melt pool shape [129] changes drastically due to coalescence and the movement induced by surface tension. Therefore, the dimensions of the molten pool and hence the consolidated build depend not only on the amount of heat supplied by the heat source but also controlled by the heat transfer and flow of molten metal within the liquid pool. Several attempts are also made to quantitatively explain how the heat transfer and fluid flow govern the molten pool shape, size and final microstructures and properties of the component using non-dimensional numbers. These non-dimensional numbers and their significance are described in detail in Section 2.7.

## 2.6. Temperature and velocity distributions and cooling rates

The peak temperature in the molten pool can be several hundred degrees above the liquidus temperature of the alloy, sometimes as high as the boiling point of the alloy for the keyhole mode depositions. In AM the measurement of the temperature field is difficult because the heat source moves rapidly and the temperature field is highly transient. The most commonly used method of measuring temperature is by placing thermocouples at monitoring locations in the solid away from the molten region [133–135]. However, the thermocouples need to be very thin to avoid significant errors in measurements. Also, thermocouples can measure temperatures locally at monitoring locations and it is difficult to get a complete temperature field even with multiple thermocouples. Infrared thermography [136–140] is also used to measure the temperature distribution on the surface of the build during AM. However, this method is capable of measuring only the surface temperatures and is unable to provide a 3D transient temperature distribution. Therefore, an alternative way is to estimate the temperature profiles and the cooling rates using a computational model after the model has been properly validated with experimental data of temperature versus time at multiple monitoring locations.

Fig. 7(a) and (b) shows the computed temperature distribution for the 1st and 10th layers, respectively, during a 10-layer-high DED-L of IN 718 powder [141]. The different colors in these figures indicate different temperature bands. In AM, the substrate acts as a heat sink. Therefore, conduction heat loss through the substrate decreases progressively with the deposition of layers. As a result, the peak temperature for the upper layers increases. Because of the rapid scanning of laser beam the temperature contours are elongated behind the heat source and compressed in front of the beam. Fig. 7(c) shows the molten pool shape and size at the mid length of the build while depositing the 10th layer. Only one half of the molten pool is presented to show the temperature and velocity fields both on the surface and in the interior on the longitudinal symmetry plane. Inside the molten pool, the temperature is the highest near the heat source axis and the lowest near the boundary of the pool. This non-uniform temperature results in a surface tension gradient inside the molten pool. Fig. 7(d) shows that inside the molten pool the flow of molten metal is driven by the surface tension gradient.

**Table 4**  
Thermo-physical properties of commonly used alloys in AM [102,103]

Alloy	Liquidus temperature (K)	Solidus temperature (K)	Density (kg/m <sup>3</sup> )	Viscosity (kg/m s)	dγ/dT (N/m K)	Thermal conductivity <sup>a</sup> (W/m K)	Specific heat <sup>a</sup> (J/kg K)
SS316	1733	1693	7800	$7 \times 10^{-3}$	$-0.40 \times 10^{-3}$	A = 11.82 B = 0.0106	A = 330.9 B = 0.563 C = $-4.015 \times 10^{-4}$ D = $9.465 \times 10^{-8}$
Ti-6Al-4V	1928	1878	4000	$4 \times 10^{-3}$	$-0.26 \times 10^{-3}$	A = 1.57 B = $1.6 \times 10^{-2}$ C = $-10^{-6}$	A = 492.4 B = 0.025 C = $-4.18 \times 10^{-6}$
IN 718	1609	1533	8100	$5 \times 10^{-3}$	$-0.37 \times 10^{-3}$	A = 0.56 B = $2.9 \times 10^{-2}$ C = $-7 \times 10^{-6}$	A = 360.4 B = 0.026 C = $-4 \times 10^{-6}$
H13 steel	1725	1585	7900	$7 \times 10^{-3}$	$-0.43 \times 10^{-3}$	A = 18.29 B = $7.5 \times 10^{-3}$	A = 341.9 B = 0.601 C = $-4.04 \times 10^{-6}$
AA6061	925	855	2700	–	–	A = 2.52 B = $0.4 \times 10^{-2}$ C = $-7.36 \times 10^{-6}$	A = 929.0 B = $-0.627$ C = $-1.48 \times 10^{-3}$

<sup>a</sup> Properties are expressed in terms of a polynomial with the form A + BT + CT<sup>2</sup> + DT<sup>3</sup> where T is temperature in K.

**Table 5**

Comparison among the current approaches for heat and fluid flow calculations in AM.

Approaches	Features	Refs.
Analytical approach	<ul style="list-style-type: none"> <li>Analytically solves Rosenthal's heat conduction equation.</li> <li>Outputs are temperature fields, build dimensions and cooling rates.</li> <li>Computationally less expensive, simplified and easy to use.</li> <li>Ignores the dominant mechanism of heat transfer and known to produce large errors.</li> </ul>	[104–106]
Heat conduction models using finite element method (FEM)	<ul style="list-style-type: none"> <li>Solves steady state or transient energy conservation equation with convective and radiative boundary conditions.</li> <li>Outputs are 3D steady state or transient temperature distribution and build shape and size.</li> <li>Many existing software packages, easy to implement, can handle intricate geometries.</li> <li>Does not consider the effects of convective flow of liquid metal inside molten pool on the temperature field, therefore severely overestimates the peak temperature and cooling rate.</li> </ul>	[107–116]
Heat transfer and fluid flow models using finite difference method (FDM)	<ul style="list-style-type: none"> <li>Solves 3D transient conservation equations of mass, momentum and energy.</li> <li>Outputs are 3D transient temperature and velocity distributions, build shape and size, solidification parameters.</li> <li>Considers the effects of molten pool flow inside pool and therefore provides accurate temperature distribution.</li> <li>Often assumes flat top geometry of the deposit to make the calculations tractable.</li> </ul>	[79,92,93,117–119]
Level set method (LSM)	<ul style="list-style-type: none"> <li>Tracks the free surface of the molten pool.</li> <li>Outputs are 3D temperature and velocity distribution of the deposit with free curved surface.</li> <li>The calculated deposit shape and size agree well with experiments.</li> <li>Computationally intensive and tends to suffer from non-conservation of mass.</li> </ul>	[120–123]
Volume of fluid (VOF) using finite difference method (FDM)	<ul style="list-style-type: none"> <li>Tracks the free surface of the molten pool.</li> <li>Outputs are 3D temperature and velocity distribution of the deposit with free curved surface.</li> <li>Computationally intensive.</li> <li>Mass conservation maintained but at less sharp interface than LSM.</li> </ul>	[124,125]
Lattice Boltzmann method (LBM) and arbitrary Lagrangian–Eulerian (ALE)	<ul style="list-style-type: none"> <li>2D and 3D numerical methods involving cellular automaton modeling of discrete particle kinetics by discrete space, time, and particle velocities.</li> <li>It involves free surface boundary conditions treating thermodynamics, surface tension, phase transitions, and wetting.</li> <li>Outputs are molten pool geometry and build shape and size.</li> <li>Can predict the build geometry accurately. Also, the balling phenomenon and surface roughness can be simulated.</li> <li>Computationally intensive however, suitable for massive parallel computing.</li> </ul>	[59,126–130]

The computed motion of liquid metal in the molten pool at the various locations of the build is shown by arrows in Fig. 8 [79]. Since the molten pool moves with the heat source, snapshots of the molten pool at different locations are shown. Velocities shown by the black arrows range from several hundred mm/s up to about one m/s depending on the location. Velocities of similar magnitudes were also reported in laser and electron beam welding. The progressive growth of the size of the melt pool in a nine-layer structure is contributed by the spatial variation of the heat transfer rates. Heat transfer from the molten pool into the substrate becomes more difficult with increasing distance from the substrate. The reduction of heat loss results in larger melt pool and higher peak temperatures in the upper layers.

Fig. 9(a) represents the temperature variation as a function of time for different locations along the deposit width (y-distance) starting from the pool center ( $y = 0$ ) for IN 718 deposit [141]. The peak temperature is the highest at the pool center and decreases gradually with distance away from the center. Unlike most other materials processing operation, in AM each location of the part experiences multiple temperature peaks and thermal cycles. For example, Fig. 9(b) [79] shows the computed thermal cycles at three monitoring locations inside a part. Temperatures at the mid-height and mid-length of the first three layers are shown as a function of time. The first and the strongest peak corresponds to a position of the laser beam just above the monitoring location. The weaker peaks occur during the deposition of the subsequent layers.

The local solidification growth rate,  $R$ , and the temperature gradient,  $G$ , at the solid-liquid interface are the most important parameters that affect the solidification structure. The ratio of the parameters,  $G/R$ , affects the morphology of the solidification structure and  $GR$ , the cooling rate, affects the scale of the microstructure. The shape of the fusion zone and the temperature field affect both  $G$  and  $R$ . The rapid heating and cooling of AM processes leads to sharp peaks in time-temperature plots that result in steep slopes, i.e. high heating and cooling rates. Depending on the alloy system and the location of the build where measurements are taken, cooling rates may vary significantly. It is important to note that it is meaningless to specify one unique cooling rate value for AM thermal cycles as cooling rate is a strong function of the temperature

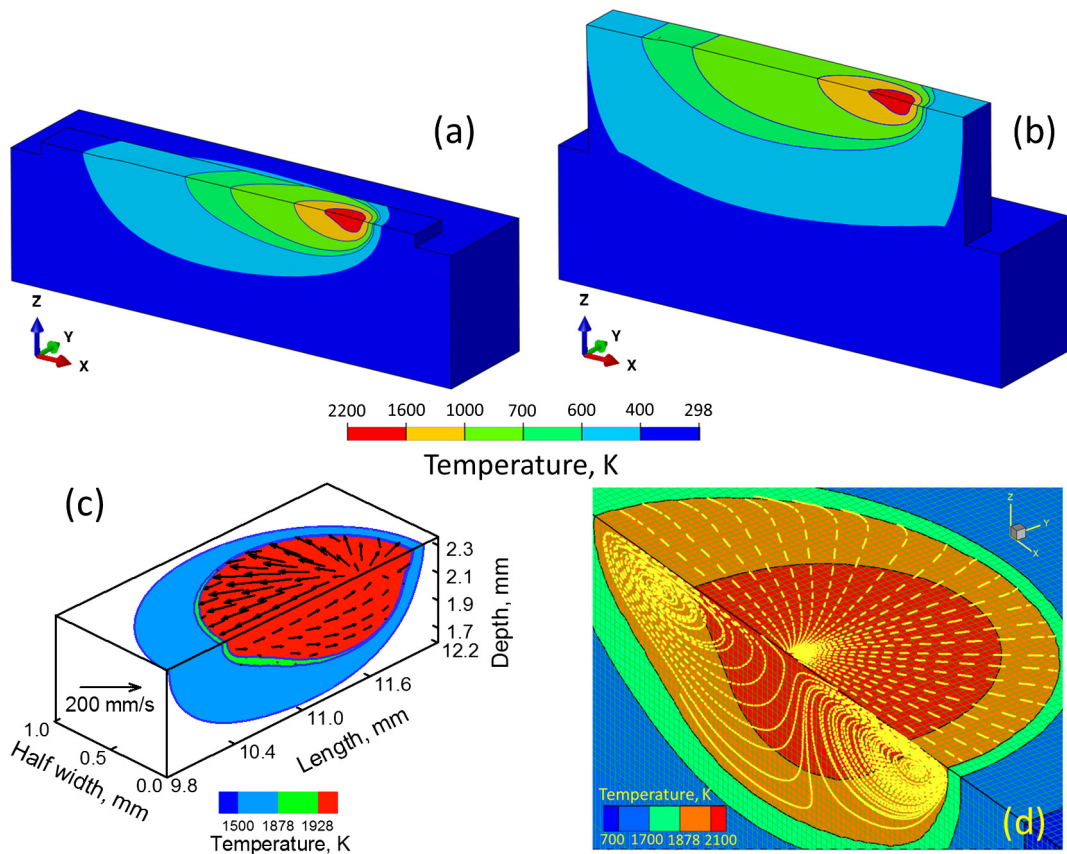


**Fig. 7.** Temperature distribution during the deposition of (a) 1st and (b) 10th layer of IN 718 powder on IN 718 substrate using 300 W laser power and 15 mm/s scanning speed. Laser beam scanning direction is along the positive x-axis [141] (c) pool shape and size at 10th layer [141] and (d) circulation of molten metal inside the pool driven by the surface tension gradient.

and location at which it is measured. Table 6 compares the cooling rates of common manufacturing processes [142] with that for AM [79,131,143–148]. In Table 6, the data can be compared because a temperature range between which cooling rate was calculated or measured was established. However, a single value of cooling rate is often reported in the literature without specifying any temperature range. Typically, there are two useful temperature ranges for which cooling rates are most important. First, cooling rates from the liquidus to solidus temperature are often used for determining the features of solidification microstructure such as cells and dendrites [149]. Second, the thermal history can be important for determining the extent of solid state transformations which vary significantly from one alloy system to another. Perhaps the most well-known range for steels is the 800–500 °C where the cooling rate significantly affects the microstructure. In AM, the cooling rate below the beta transus temperature in Ti-6Al-4V is important for understanding the alpha/beta morphology within prior beta grains [150].

Generally, the molten pool in AM is smaller than that of welding. Small pools cool and solidify rapidly resulting in a higher cooling rate than welding. Among the common AM processes, the fastest cooling is observed for the powder bed fusion owing to its very rapid scanning. However, preheating also affects the cooling rate. During AM, for the upper layers the heat transfer into the substrate is reduced resulting in a lower cooling rate and G/R ratio as shown in Fig. 10 [79]. These variations result in inhomogeneous microstructures and properties in different regions of a part. At each location within a part, the microstructure and the grain structure of the alloy that forms after the first thermal cycle is often changed by the subsequent thermal cycles. Reliable transient 3D temperature fields are thus a prerequisite for understanding microstructure and properties of parts based on physical principles.

## 2.7. Non-dimensional numbers

Several non-dimensional numbers have been used to understand the effects of various AM process variables and material properties on microstructure, properties and defects of the additively manufactured components [143,151]. Non-dimensional numbers are beneficial because they reduce the total numbers of variables to be studied and provide important understanding that a single process variable is unable to provide [143]. Their effectiveness for providing insight about the AM process originates from the fact that very often a group of variables, rather than a single variable, affect the performance

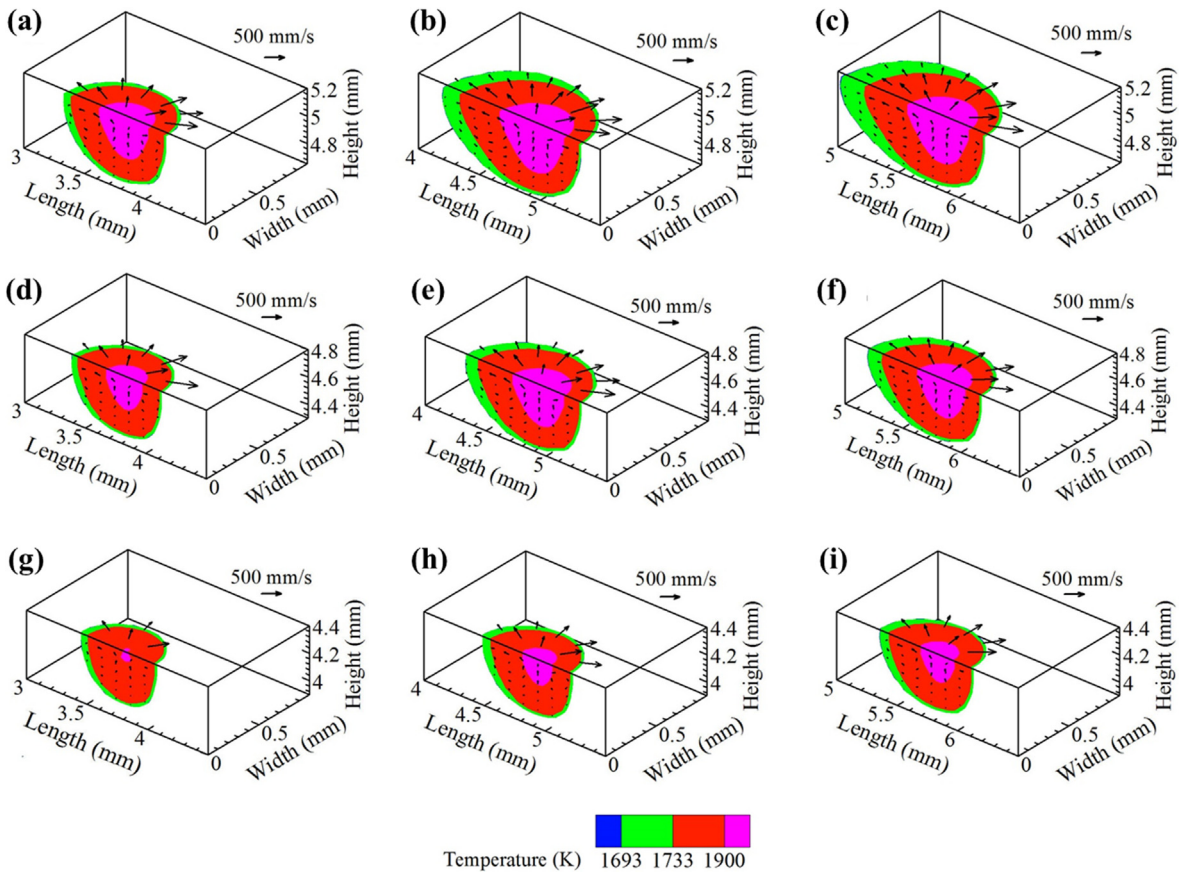


**Fig. 8.** Computed melt pool shape, temperature and velocity fields in the (a) first, (b) second, (c) third, (d) fourth, (e) fifth, (f) sixth, (g) seventh, (h) eighth and (i) ninth layers at mid-length for a laser assisted multi-layer deposition of 316 stainless steel at a laser power of 210 W and scanning speed of 12.7 mm/s [79].

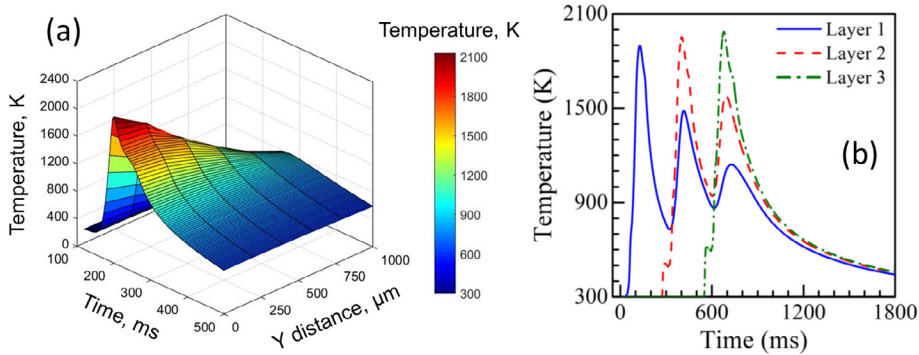


**Fig. 9.** (a) Temperature variation with time at different locations on the top surface of the deposit during a single layer laser assisted deposition of IN 718 powder on IN 718 substrate using the power of 250 W and 15 mm/s scanning speed [141]. (b) Thermal cycles at three monitoring locations in the first three layers in a laser assisted DED of 316 stainless steel at a laser power of 210 W and 12.7 mm/s speed. The monitoring locations are at the mid height and mid-length of each layer [79].

and outcome of a complex process such as AM. Therefore, the commonly used non-dimensional numbers in AM are discussed in this section.

The relative importance of heat transfer by convection and conduction in the molten pool in AM can be determined from the Peclét number,  $Pe$ :

$$Pe = \frac{UL}{\alpha} \quad (8)$$

**Table 6**

Comparison of cooling rates of AM with other common manufacturing processes.

Process	Cooling rate [K/s]	Remarks	Ref.
<i>AM cooling rates</i>			
DED-L	$3 \times 10^3$ – $7 \times 10^3$	SS 316 deposit, speed is 12.7 mm/s	[79]
DED-L	$1 \times 10^3$ – $4 \times 10^3$	SS 316 deposit, speed is 15 mm/s	[143]
DED-L	$5 \times 10^3$ – $3 \times 10^4$	IN 718 deposit, speed is 25–40 mm/s	[144]
DED-GMA	$10^2$ – $10^3$	Ti-6Al-4V deposit, other details are unknown	[145]
PBF-EB	$5 \times 10^4$	IN 718 deposit, speed is 500 mm/s, 750 °C preheat	[146]
PBF-EB	$5 \times 10^4$	Ti-6Al-4V deposit, speed is 1500 mm/s, 600 °C preheat	[147]
PBF-L	$5 \times 10^5$	Ti-6Al-4V deposit, speed is 1000 mm/s	[131]
PBF-L	$1 \times 10^6$ – $6 \times 10^6$	Al alloy deposit, speed is 100–400 mm/s	[148]
<i>Common manufacturing processes</i>			
Casting	$10^0$ – $10^2$		[142]
Arc welding	$10^1$ – $10^3$		
E-beam welding	$10^2$ – $10^4$		
Laser welding	$10^2$ – $10^6$		

Note: The cooling rates are either specified in the literature or approximately estimated from the thermal cycle provided. All cooling rates specified here are measured or calculated between the liquidus and the solidus temperatures of the corresponding alloy at a location directly below the central axis of the heat source.

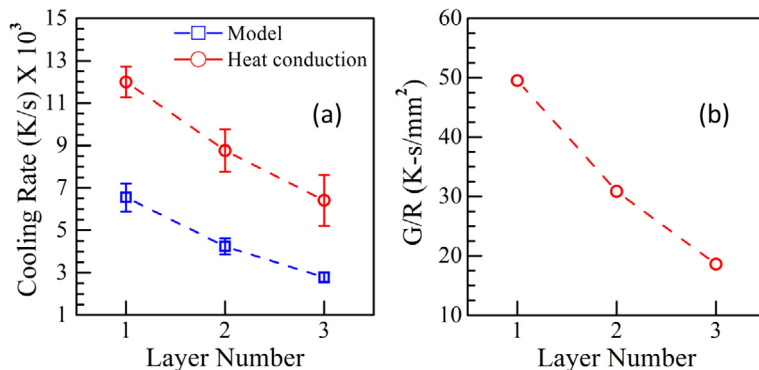


**Fig. 10.** (a) Variation of cooling rate between peak temperature and liquidus temperature and (b) G/R ratio at three monitoring locations in the three layers in a laser assisted DED of 316 stainless steel at a laser power of 210 W and 12.7 mm/s speed [79].

where  $U$  is the characteristic velocity,  $\alpha$  is the thermal diffusivity of the alloy and  $L$  is the characteristic length, generally considered as pool length. A high value of Peclet number ( $Pe \gg 1$ ) indicates that convective heat transfer is the main mechanism of heat transfer within the molten pool.

The shape and size of the deposit depends on the convective flow of the molten metal inside the pool driven by the surface tension gradient in the pool. Marangoni number represents the ratio of the surface tension force to viscous force and is a measure of the strength of the convective flow of liquid metal within the molten pool.

$$Ma = -\frac{d\gamma}{dT} \frac{L\Delta T}{\mu\alpha} \quad (9)$$

where  $\mu$  is the viscosity,  $\alpha$  is the thermal diffusivity of the alloy,  $L$  is the characteristic length of the molten pool, which is taken as the width of the molten pool,  $\Delta T$  is the difference between the maximum temperature inside the pool and the solidus temperature of an alloy, and  $\frac{d\gamma}{dT}$  is the sensitivity of surface tension with respect to temperature.

Fourier number ( $F_o$ ) is used to obtain a relative measure of heat dissipation rate to heat storage rate during AM processing.

$$F_o = \alpha\tau/L^2 \quad (10)$$

where  $\alpha$ ,  $\tau$  and  $L$  refer to thermal diffusivity, characteristic time scale and length, respectively. The characteristic time can be expressed as  $L/v$ , where  $L$  and  $v$  are the pool length and scanning speed respectively [135]. So, Eq. (10) can be re-written as,

$$F_o = \alpha/vL \quad (11)$$

Higher  $F_o$  means faster dissipation of heat which helps in faster cooling of the build and more refined microstructure. A non-dimensional thermal strain parameter ( $\varepsilon^*$ ) represents the effects of common process parameters and material properties on the susceptibility of a component to thermal distortion [152]. The parameter is represented as:

$$\varepsilon^* = \frac{\beta\Delta T}{EI} \frac{tH^{3/2}}{F_o\sqrt{\rho}} \quad (12)$$

where  $\beta$  is the volumetric coefficient of thermal expansion,  $\Delta T$  is the maximum rise in temperature during the process,  $E$  is the elastic modulus and  $I$  is the moment of inertia of the substrate, the product,  $EI$ , is the flexural rigidity of the structure,  $t$  is the characteristic time,  $H$  is the heat input per unit length,  $F_o$  is the Fourier number and  $\rho$  is the density of the alloy powder.

A non-dimensional heat input ( $Q^*$ ) is used as a measure of the energy deposited per unit length of the deposit. It is represented as,

$$Q^* = (P/v)/(P_R/v_R) \quad (13)$$

where  $P$  and  $v$  refer to the laser power and the scanning speed, respectively.  $P_R$  and  $v_R$  represent the reference laser power and scanning speed, respectively. Higher heat input per unit length reduces cooling rate and makes the microstructure coarser. For most alloys the hardness decreases with higher heat input.

There are many examples where experimental data clearly indicate the utility of the non-dimensional numbers. Irrespective of the processing conditions and the material systems, non-dimensional numbers can be used to obtain a comprehensive understanding of the structures and the properties of the additively manufactured components. For example, Fig. 11(a) indicates larger secondary dendritic arm spacing and coarsening of Laves phases at high non-dimensional heat input because of slow cooling that coarsens microstructures. Similarly, high Marangoni numbers exhibit strong circulation of molten metal inside the liquid pool and results in larger pools [143]. A high Fourier number implies faster heat dissipation that results in faster cooling rate and higher G/R ratio [143], both of which are known to influence microstructure and properties of builds. Slow cooling at high non-dimensional heat input [143] results in large grain size and low hardness as shown in Fig. 11(b).

Non-dimensional numbers can also be used to mitigate defects such as porosity, lack of fusion and dimensional inaccuracy due to distortion. Fig. 11(c) shows that an AM component fabricated using higher non-dimensional heat input has lower voids. In addition, higher non-dimensional heat input results in larger pool that ensures good interlayer bonding. High Fourier number indicates rapid heat dissipation and low heat storage. Therefore, high Fourier number results in low thermal strain and distortion as shown in Fig. 11(d).

In summary, the dimensionless variables allow understanding of the underlying physical phenomena in AM processes and the fabricated parts and are useful to prevent defects in AM parts with easy to use, rapid, back of the envelope calculations. Table 7 summarizes the significance of several important non-dimensional numbers in AM. A more complete discussion of the non-dimensional numbers in AM is available in a recent paper [143].

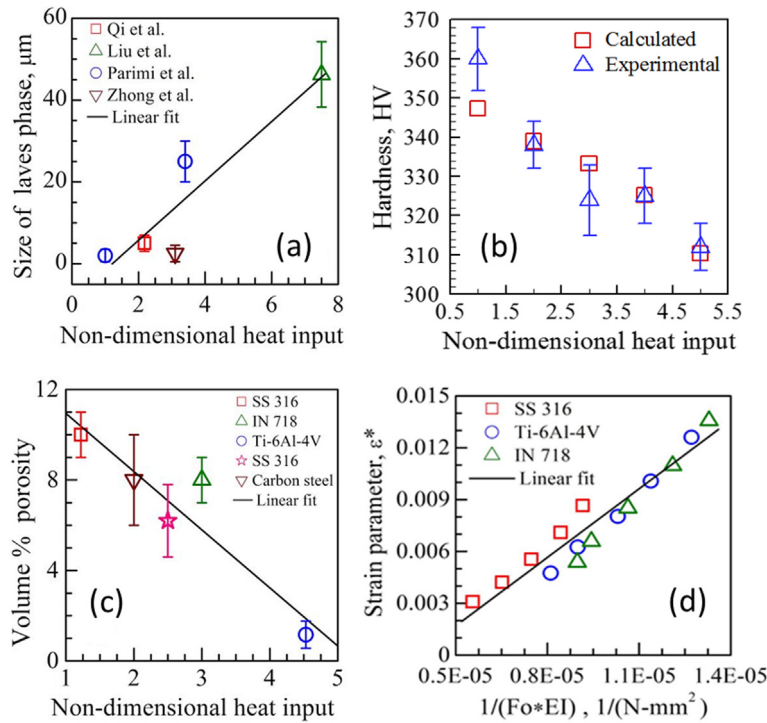


**Fig. 11.** Effects of non-dimensional heat input on (a) size of Laves phase, (b) Vickers hardness, (c) volume fraction of porosity and (d) relation between thermal strain and Fourier number [143].

**Table 7**

Important non-dimensional numbers and their significance [143,151].

ND numbers	Significance
Non-dimensional heat input ( $Q^*$ )	<ul style="list-style-type: none"> <li>Represents the relative magnitude of linear heat input</li> <li>Higher non-dimensional heat input results in higher peak temperature and pool dimensions and slow cooling</li> </ul>
Marangoni number ( $Ma$ )	<ul style="list-style-type: none"> <li>Signifies the convective flow of the molten metal inside the pool driven by surface tension gradient</li> <li>Higher Marangoni number results in larger pool with high aspect ratio, which in turn, help ensures proper interlayer bonding and hence low porosity</li> </ul>
Peclet number ( $Pe$ )	<ul style="list-style-type: none"> <li>Indicates the relative importance of convective heat transfer over heat transfer by conduction</li> <li>If <math>Pe &gt; 1</math>, convective heat transfer is dominant</li> </ul>
Fourier number ( $F_o$ )	<ul style="list-style-type: none"> <li>Represents the ratio of heat dissipation rate to heat storage rate</li> <li>Higher Fourier number indicates high rate of heat dissipation hence faster cooling</li> <li>Higher Fourier number results in low heat storage hence low thermal distortion</li> </ul>
Strain parameter ( $\varepsilon^*$ )	<ul style="list-style-type: none"> <li>Embody all important process parameters and alloy properties that affect the thermal strain and distortion</li> <li>Linearly correlated with thermal strain during AM</li> <li>Does not consider the plastic strain generated during the fabrication</li> </ul>

## 2.8. Process stability

Rapid production of AM parts is often achieved by increasing the scanning speed. As a result, the molten pool becomes elongated and depending on the scanning speed, the liquid pool may become unstable as evidenced by break-up of the single molten pool into isolated puddles of liquid resulting in a discontinuity of the deposited geometry and non-uniform deposit thickness. The origin of the defects is often caused by the Kelvin-Helmholtz hydrodynamic instability or the Plateau Raleigh capillary instability. This section provides a basic introduction of these two instabilities.

### 2.8.1. Kelvin Helmholtz hydrodynamic instability

A continuous increase in the scanning speed may result in a bead-like appearance, commonly known as humping [153,154]. Humping is caused by the hydrodynamic instability of the molten pool known as Kelvin-Helmholtz (KH) instability. The velocity of the liquid metal at the top of the molten pool is lower than the shielding gas velocity. This difference in velocities may result in hydrodynamic instability of the liquid metal surface. KH instability occurs when Richardson number,  $Ri$ , which is the ratio of buoyancy force to shear force, is less than 0.25.

$$Ri = \frac{gL}{(U_g - U_l)^2} \quad (14)$$

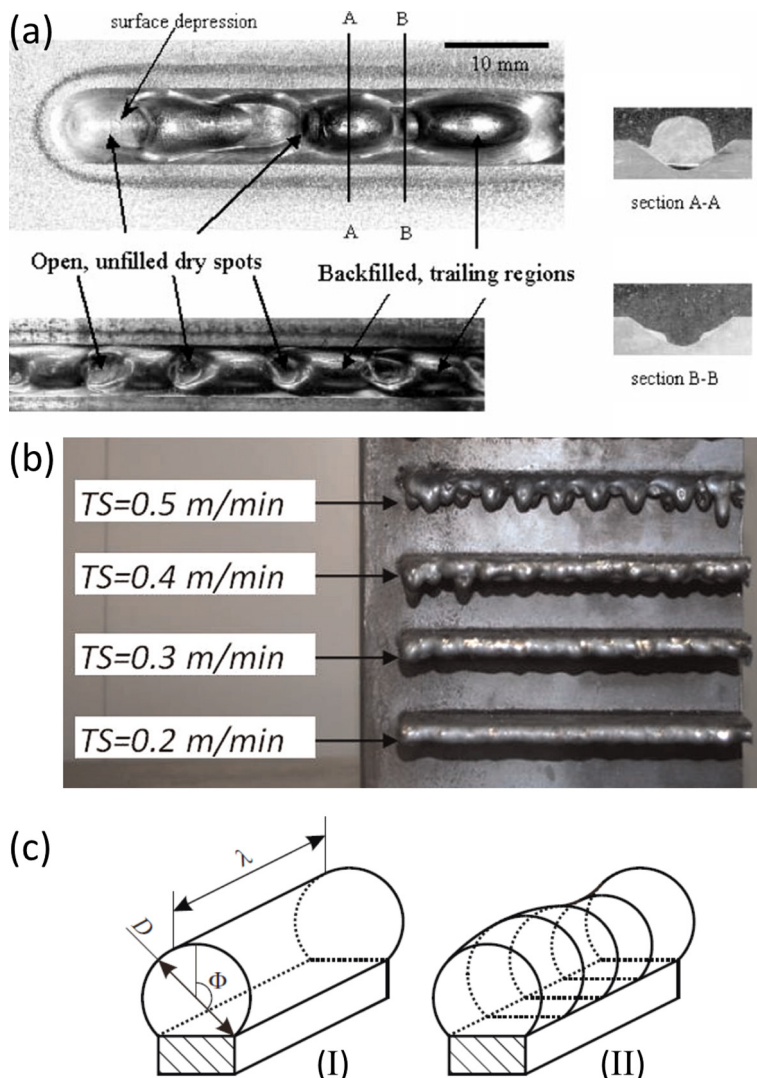
where  $g$  is the acceleration due to gravity,  $L$  is the characteristic length which can be taken as the one half of the layer thickness, and  $U_g$  and  $U_l$  are the velocities of the shielding gas and the liquid metal in the molten pool, respectively. The main factors for the KH instability are the layer thickness and the velocities of the shielding gas and the molten metal, the latter being affected by the thermo-physical properties of the alloy and the AM variables.

Fig. 12(a) shows the hump formation in a high speed arc welding [154]. The humping morphology is characterized by open, unfilled spots in between the humped beads. The front of the molten pool exhibits a large depression known as the gouging region [154]. The trailing region, consisting of bulk of the molten metal resides in the back of the melt pool. Humping in arc welding has been explained on the basis of KH instability [155]. The wavelength of the humping beads was calculated by solving the wave propagation equation on the molten pool surface for various welding parameters [155]. Although, the mechanism of formation of humping due to the KH instability in AM is expected to be similar to that in welding, the literature is scarce. However, the formations of humping beads have been reported for various AM processes, such as, DED-GMA [156,157], DED-PA [158,159] and DED-L [160]. Fig. 12(b) shows the effect of scanning speed on the formation of the humping beads in DED-GMA process. It has been found that humping tends to occur when the scanning speed exceeds a certain critical value. Further research is needed to understand the effects of KH instability on humping defects in AM for various process parameters such as power, speed, layer thickness, hatch spacing and feed rate.

### 2.8.2. Plateau Raleigh capillary instability

During AM, the deposited material sometimes tends to form half-cylindrical shape. This phenomenon depends on variables such as the scanning speed and the surface tension, viscosity and density of the alloy [119,161]. Fig. 12(c-I) schematically shows the cylindrical single track deposit on the substrate during DED-L process. At very high scanning speeds, the molten pool tends to elongate, becomes unstable and separates in small spherical balls to maintain the uniform capillary pressure inside the pool [119]. This phenomenon is called ‘balling effect’ as shown in Fig. 12(c-II). The maximum allowable length of the molten pool that prevents this instability can be obtained from the following relation based on Plateau Raleigh capillary instability [119]:

$$L/D \geq \pi \quad (15)$$



**Fig. 12.** (a) Humping in arc weld [154] (b) effect of scanning speed on humping in DED-GMA [156] and (c) mechanism of ball formation due to the capillary instability [119].

where  $L$  and  $D$  are the length of the molten pool and width of the deposit, respectively. The small spherical balls formed due to the balling effect are accumulated at the sides of the deposit and result in rough surfaces, as described further in Section 2.9.3.

## 2.9. Defects

### 2.9.1. Loss of alloying elements

During AM of many important engineering alloys, pronounced vaporization of alloying elements takes place when the molten pool temperatures are very high. Since some elements are more volatile than others, selective vaporization can occur causing changes in the overall composition of the alloy [152]. Changes in composition can affect solidification microstructure, corrosion resistance and mechanical properties and can be a serious problem in producing high quality components.

In AM, the rapid scanning speeds and complexity of equipment can make in-situ experimental measurements of vaporization very complex. One way to mitigate this issue is by measuring mass both before and after deposition. For example, Klassen et al. [59] validated a numerical model by measuring the mass before and after the PBF-EB of Ti-6Al-4V powder. In addition, compositions of metal vapors have been determined by collecting condensates from the interior surface of a both end open quartz tube mounted co-axial with the laser beam during welding of AISI 202 stainless steel [162].

A method to study vaporization of alloying elements during AM experimentally is to measure the compositions of both the metal powder and the final part. Since most AM parts do not have microstructural homogeneity and often exhibit ele-

mental segregation, accurate and reliable measurements of composition via non-destructive methods such as energy dispersive spectroscopy (EDS) or electron probe microanalysis (EPMA) require an ample volume of data and statistical analysis. However, if a sample can be destructively tested, methods such as inductively coupled plasma (ICP) mass spectrometry [163] can provide excellent accuracy in composition measurements. Although there is a lack of literature reporting changes in composition, some studies have shown significant changes in composition. Brice and coworkers [164,165] have shown that there is a decrease of about 0.9 wt% Al and 0.4 wt% Mg during the PBF-EB of Ti-6Al-4V and AA2139, respectively. Gaytan et al. [166] have reported a 10–15% reduction in aluminum content under optimized parameters in PBF-EB of Ti-6Al-4V, which corresponded to about a 0.6–1.0 wt% decrease for a nominal composition. This finding is consistent with that reported by Taminger [167] as shown in Fig. 13.

An expression for understanding alloying element vaporization is the Langmuir equation [168] in which the vapor flux,  $J_i$ , of element  $i$  is calculated as:

$$J_i = \frac{\lambda_c P_i}{\sqrt{2\pi M_i T}} \quad (16)$$

where  $P_i$  and  $M_i$  are the equilibrium vapor pressure and molecular weight of element  $i$ , respectively,  $T$  is temperature and  $\lambda_c$  is a positive fraction accounting for the condensation of some vaporized atoms. The Langmuir equation was derived for condition under vacuum and previous literature shows that it over-predicts vaporization rates up to an order of magnitude when used at atmospheric pressure unless an appropriate value of the constant  $\lambda$  is used [169]. Modeling work by Semiatin et al. [170] reported a detailed analysis of evaporative losses during PBF-EB of Ti-6Al-4V. Since PBF-EB occurs under vacuum, vaporization fluxes were assumed to obey Eq. (16). Temperature calculations were based on a simple lump-parameter approach assuming the process consisted of continuous melting and laminar flow within the molten pool.

Since the vapor flux is proportional to equilibrium vapor pressure, which has an exponential dependence on temperature, the accuracy of calculations is highly dependent on the computed temperature distribution. Fig. 14(a)–(c) shows the calculated equilibrium vapor pressures of alloying elements over three common AM alloys as a function of temperature [152]. It can be clearly observed that temperature calculations are crucial in determining vaporization fluxes because a small error in temperature can result in a relatively large error in vapor pressure, especially at higher temperatures.

During laser processing the alloying elements vaporize from the surface of the molten pool although the alloying elements are depleted from the entire volume of the liquid pool which is well mixed. As a result, the surface area-to-volume ratio is one of the controlling factors for determining the magnitude of composition change [96]. Therefore, estimations of both temperature field and the geometry of the molten pool are important for understanding the change in composition during AM. There have been many reports in welding literature that deal with the prediction of composition change during various types of fusion welding through rigorous mathematical modeling [168,169,171–175]. The models collectively use an

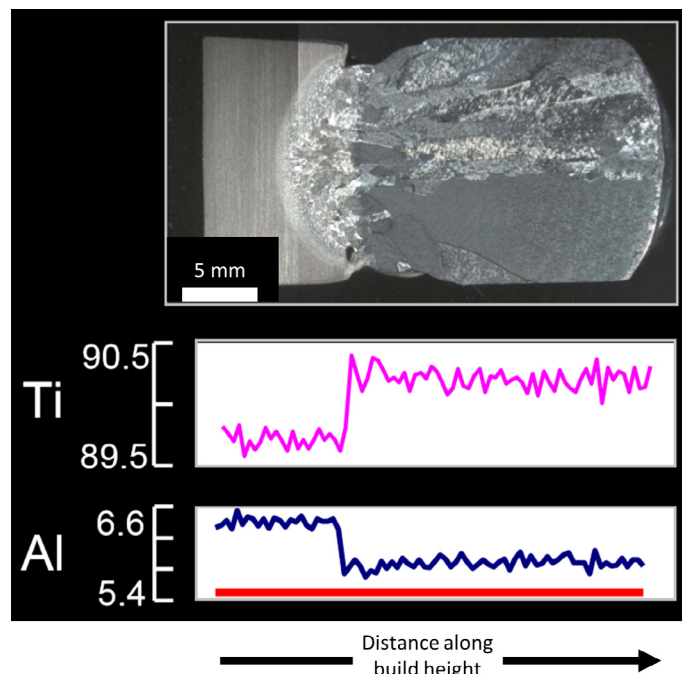


**Fig. 13.** Measured chemical composition along the build height for a Ti-6Al-4V sample fabricated by PBF-EB showing a depletion in Al concentration and an increase in Ti concentration [167].

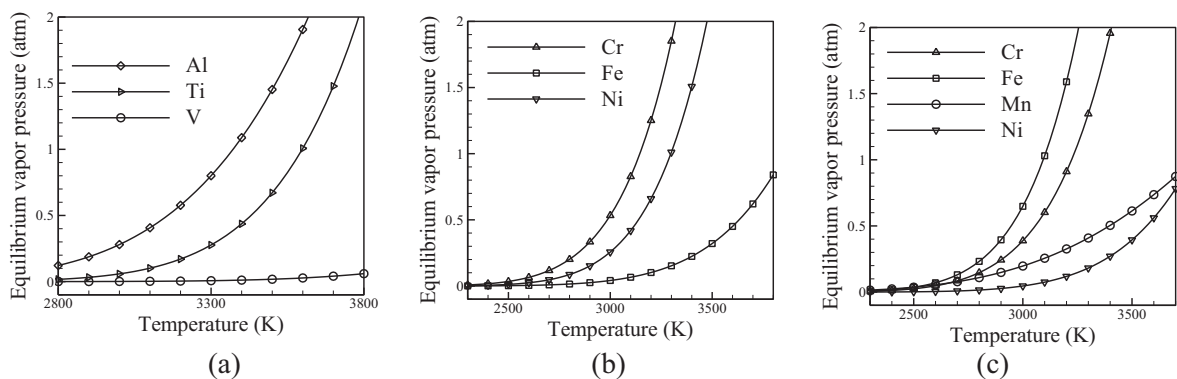


**Fig. 14.** Equilibrium vapor pressures of alloying elements over the liquid alloy for (a) Ti-6Al-4V (b) IN625 and (c) SS 316 [152].

approach for vaporization calculations where contributions from both concentration gradients and pressure gradients determine the overall vaporization flux. Due to the similarities between fusion welding and AM, these models offer an attractive framework for the calculation of vaporization rates in AM processes. Other than a few reported cases in which a keyhole is formed during AM [34,176], the melting process typically remains in conduction mode as the penetration into the previously deposited layer only needs to be a small fraction of the layer height to ensure interlayer bonding.

It was found that during DED of Ti-6Al-4V under different process parameters, the “slow and hot” conditions yielded the highest aluminum contents [177]. Although counterintuitive at first, this finding can be explained by the competition between temperature and the surface to volume ratio. Higher temperatures do indeed facilitate more vaporization, but also increase the size of the molten pool which causes less compositional variation due to the increased volume. Once mathematical models are developed and well tested, parametric studies can be undertaken to better understand the importance of process variables. It is expected that the most important AM variables that influence the vaporization of alloying elements are those that affect molten pool geometry and temperature distributions. These variables include power, scanning speed, feedstock feed rate and beam diameter, which can be lumped into larger parameters such as heat input per unit length or power density.

### 2.9.2. Porosity and lack of fusion defects

Porosity and lack of fusion voids are common defects in AM [178–180] that need to be minimized or eliminated due to their adverse effects on mechanical properties [181]. Researchers have suggested three main mechanisms by which these defects are produced. First, when some AM processes are operated at very high power density, deposition or melting may be performed in keyhole mode [182]. Without careful control of keyhole mode melting, keyholes can become unstable and repeatedly form and collapse, leaving voids inside the deposit that consist of entrapped vapor [182]. Therefore, those porosities are almost spherical in shape [183]. Fig. 15(a) shows keyhole porosity formed during laser assisted AM of 316L stainless steel. The size of keyhole porosity can vary depending on the shape and size of the keyhole. Second, gas can be entrapped inside the powder particles during the powder atomization process [184]. These entrapped gases result in microscopic spherical gas pores as shown in Fig. 15(b). In addition, gas pores may also be formed due to the entrapment of the shielding gas or alloy vapors inside the molten pool. Third, lack of fusion defects can be caused by inadequate penetration of the molten pool of an upper layer into either the substrate or the previously deposited layer [52,152,185] as shown in Fig. 15(c).

Laser AM methods often employ an inert shielding gas such as argon to prevent contamination of the molten pool or hot solidified metal, whereas electron beam AM is performed in vacuum or under an inert gas such as He. It is known that inert gasses are insoluble in liquid metals [186], so that any pores that are created will remain in the solidified pool unless they can escape by floating out of the molten pool. Non-inert shielding gas such as nitrogen has been shown to reduce and/or eliminate porosity in stainless steel welds by dissolving into the liquid melt pool before it solidifies [186], but cannot be used on all metals due to adverse reactivity with some metals. Eliminating the shielding gas and performing laser welding under vacuum has also been shown to reduce or eliminate porosity in porosity prone metals, however this practice has not yet been attempted for laser AM [187]. Inadequate penetration can cause elongated voids to form in the final product which are typically larger than 10 μm in equivalent diameter [152,188]. These macro-pores are much larger than the gas pores and can be distinguished by sharp edges that act as stress concentrators under applied loads. The following “lack of fusion index” (LF) was shown to correlate well with the extent of voids [152]:

$$\text{LF} = \text{Molten pool depth}/\text{Layer thickness} \quad (17)$$

A larger pool with sufficient penetration into the previously deposited layer ensures proper bonding and minimizes lack of fusion voids [152]. Therefore, voids are reduced for an AM process with a high LF value as shown in Fig. 15(c). Fig. 15(d) shows that higher heat input per unit length, defined as the ratio of laser power to scanning speed, can effectively minimize

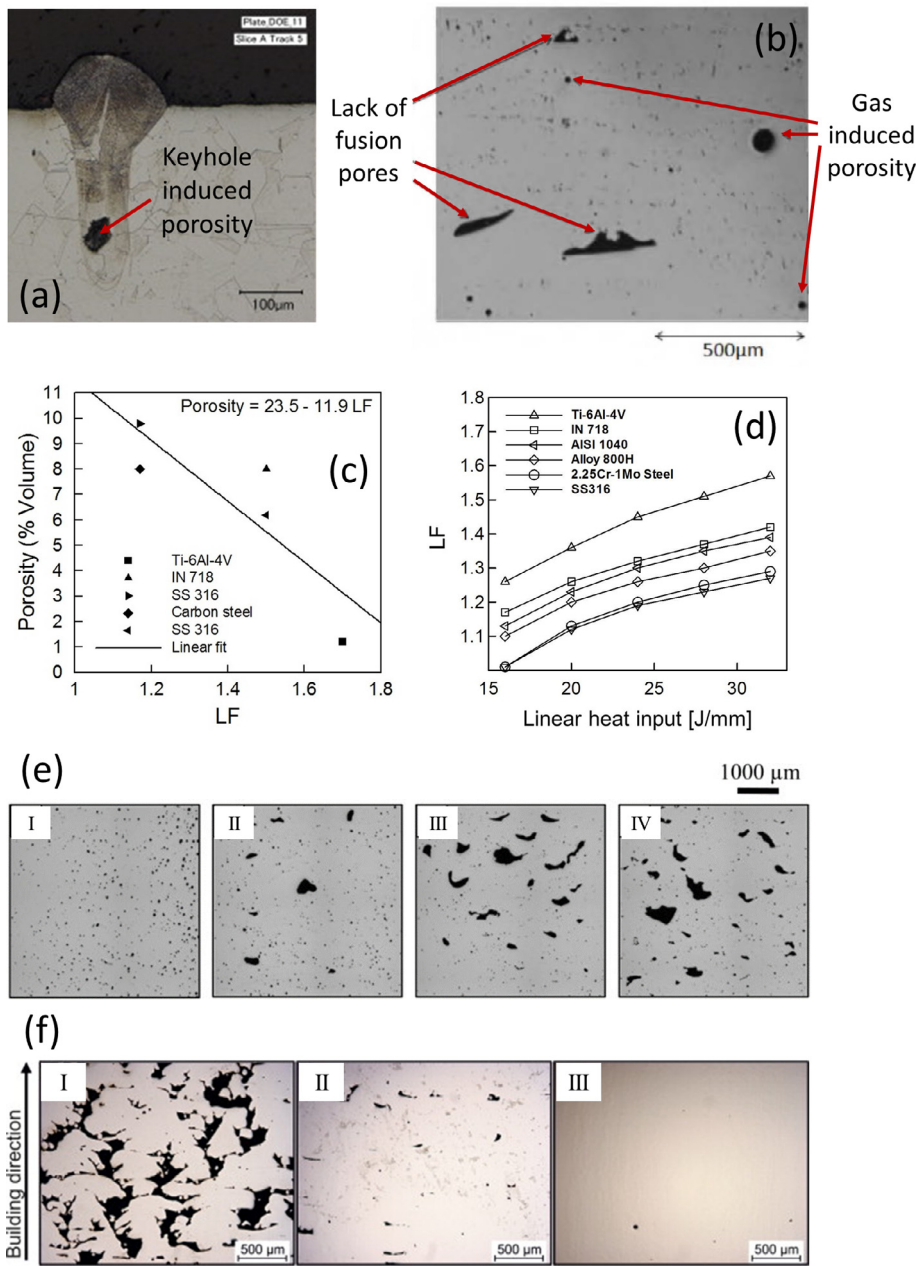


**Fig. 15.** (a) Keyhole porosity [182] (b) lack of fusion pores and gas induced porosity [52] (c) relation between volume% of porosity and lack of fusion index [152] (d) relation between lack of fusion index and heat input [152] (e) effect of scanning speed on porosity (I) 250 (II) 500 (III) 750 and (IV) 1000 mm/s [189] (f) effect of laser power on porosity (I) 90 (II) 120 and (III) 180 W [190].

the amount of the lack of fusion pores by increasing the pool depth. Rapid scanning reduces the pool size and enhances susceptibility of forming lack of fusion porosity [189] as shown in Fig. 15(e). In contrast, increasing laser power can reduce porosity by increasing the pool size [190] and ultimately increasing penetration depth as shown in Fig. 15(f).

There are several techniques available to measure porosity. The Archimedes method [191] is the simplest non-destructive method for measuring porosity of an entire specimen. The volume percentage of porosity is estimated from the density of the component calculated using this method [191]. However, the details of the shape, size and distribution of the pores cannot be determined using this method. Optical microscopy [188] is a widely used destructive method to measure porosity. A major drawback of this method is that 3D porosity can only be measured as an area fraction in a certain 2D plane [188]. Therefore, the volume of the pores cannot be accurately measured using this technique. Also, this method is not suitable for measuring very small pores (<50 μm). Fig. 16(a) shows an optical micrograph of a PBF made Ti-6Al-4V sample used to

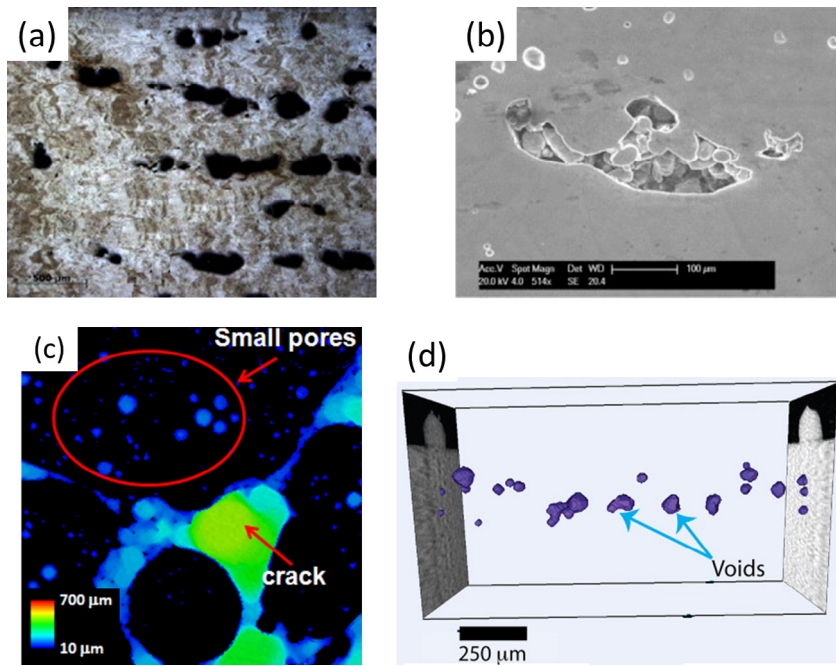


**Fig. 16.** Measurements of porosity and lack of fusion defects using (a) optical microscopy [188] (b) SEM [189] (c) X-ray CT [192] and (d) SRμT [182].

measure lack of fusion defects. Fig. 16(b) shows a scanning electron microscope (SEM) [189] image of a lack of fusion defect that is about 100 μm in size. X-ray computer tomography (X-ray CT) [192] can measure pores as small as 10 μm as shown in Fig. 16(c), and has been used to study porosity formation in laser welds as well [186,187]. Fig. 16(d) shows keyhole porosity measured using Synchrotron Radiation micro-Tomography (SRμT) [182]. This method can be used to measure in-situ formation of porosity. SEM, X-ray CT and SRμT can accurately measure shape, size and distribution of very small pores. However, these methods are expensive because of the high capital cost of the equipment. Internal pores may be closed by hot isostatic pressing (HIP) [193] after the process, although these post processing operations are time consuming and expensive. In addition, surface cracks (see Section 2.9.4) are difficult to be closed by HIP. Therefore, it is often desirable to reduce porosity and lack of fusion defects by controlling process parameters such as laser power, scanning speed, and layer thickness.

### 2.9.3. Surface roughness

Surface roughness or the surface character of AM fabricated parts results from a number of interdependent input parameters resulting in several observable or measureable output conditions that can ultimately affect part performance. These input parameters are related to material feedstock, part design, process selection, process parameters, post processing and finishing. Output conditions can range from partially fused powder particles (or weld beads), improper melting such as balling, lack of fusion of layers or striations due to build conditions, melt track or scan path strategy. Material feedstock conditions include the alloy type, powder PSD (particle size distribution) and powder morphology. Wire feedstock conditions include alloy type, wire diameter and process parameters related to wire feed rate. Part and process design conditions relate to down skin surfaces, feature geometry, part orientation within the build volume, and support structures. Process parameters related to surface roughness include heat source power, travel speed, layer height, overhang angles, scan strategy or path planning such as profile paths. Post processing conditions include support removal, machining polishing, peening, tumbling and chemical treatment. Additional detail regarding surface defects related to roughness such as porosity, lack of fusion, cracking or delamination is provided above in Section 2.9 (Defects). Further detail of roughness associated with powder feedstock is provided in Section 2.2 (Feedstock materials).

Surface roughness is one of the most important features of intricate components fabricated using AM. Surface roughness is measured using a profilometer or analyzing the surface morphology using SEM [194]. On the surface the height of a peak or the depth of a valley ( $f_n$ ) is measured at  $N$  locations along the profile length  $L$ . The average surface roughness ( $R_a$ ) is numerically calculated as [194]:

$$R_a = \frac{1}{N} \sum_{i=1}^N |f_n| \quad (18)$$

Additively manufactured components for high end applications require an average surface roughness less than 1 μm [195]. However, as-deposited parts often exhibit rough surfaces and require post processing such as surface machining, grinding,

chemical polishing, post HIP and shot peening to attain the required finish [196,197]. These operations are time consuming and expensive [198]. Therefore, it is important to understand the root causes of surface roughness in order to alleviate this problem.

There are two main causes of surface roughness. The surface roughness caused by 'stair step effect' [199] is due to the stepped approximation by layers of curved and inclined surfaces as shown in Fig. 17(a). The average surface roughness ( $R_a$ ) depends on the layer thickness ( $t_l$ ) and the build angle ( $\theta$ ) and can be represented by the following equation [199]:

$$R_a = 1000t_l \sin\left(\frac{90 - \theta}{4}\right) \tan(90 - \theta) \quad (19)$$

where  $R_a$  is the arithmetic mean of the surface roughness of a region with a particular build angle. Surface roughness increases with the increase in layer thickness [200] as shown in Fig. 17(b). Therefore, the common AM obstacle of balancing the tradeoff between intricacy and build time arises in the case of surface roughness. Building a part with small layer thickness can effectively reduce the surface roughness. However, it takes more time to build parts with thin layers. Alternative way is to avoid a sharp build orientation angle by properly selecting the building direction for complex parts [199].

A second mechanism for forming rough surfaces is improper melting of powder particles and balling phenomenon [201–203]. When a low heat input is used, the energy delivered is insufficient to completely melt the powder particles. The solid powder particles stick at the surfaces of the build [203]. Fig. 17(c) shows an SEM image [203] of the solid powder particle on the surface of the build. The average surface roughness caused by improperly melted particles is on the same order of magnitude as the powder diameter. At high laser scanning speeds, the molten pool becomes elongated, which can break into small islands due to the aforementioned Raleigh instability [125,204]. This process is often described as

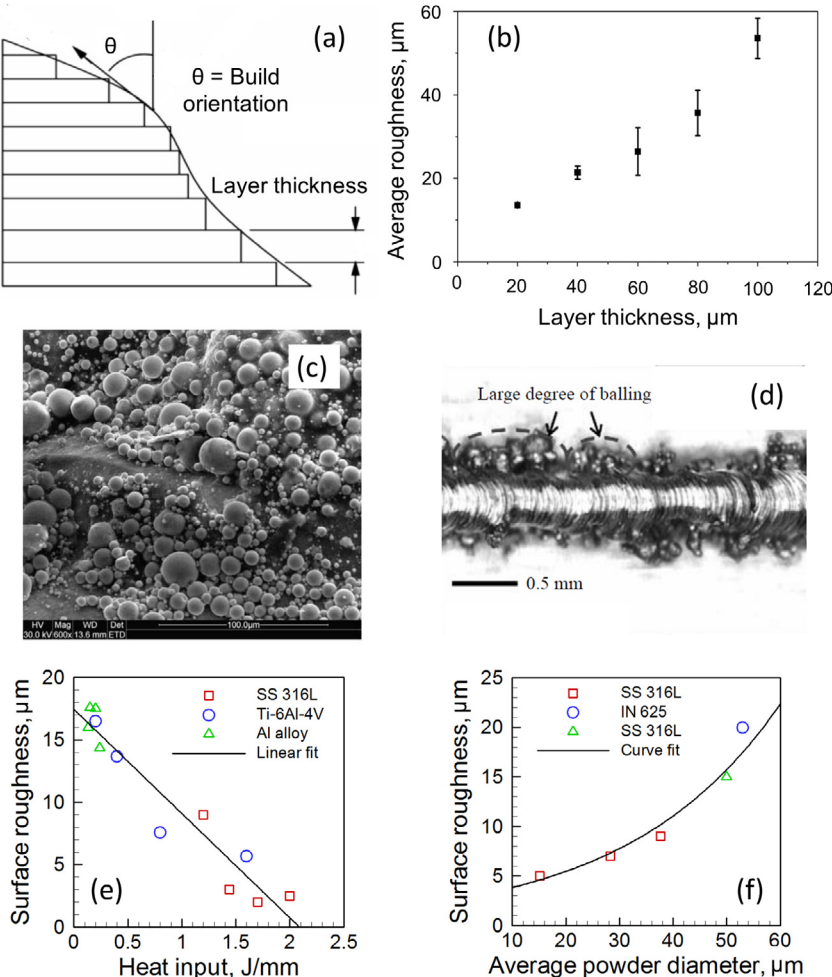


**Fig. 17.** (a) Stair case effect causing surface roughness [199] (b) relation between surface roughness and layer thickness [200] (c) SEM image of solid powders on build surface [203] (d) balling effect [195] (e) effect of heat input on surface roughness [205,206] (f) effect of powder diameter on surface roughness [195,205,207].

balling phenomenon [203]. Due to the surface tension gradient driven flow inside the molten pool, these small balls are dragged to the outer edges of the molten pool [125,195]. Therefore, small balls can be found at the side edges of the solidified track as shown in Fig. 17(d). High heat input achieved by high laser power and low scanning speed can completely melt all the powder particles and reduce the balling phenomenon. Therefore, it is expected that surface roughness can be reduced with an increase in the heat input. Fig. 17(e) shows a collection of surface roughness data from independent literature [205,206] for three alloys plotted against linear heat input. From this figure it can be confirmed that surface roughness of AM components can be minimized by increasing heat input independent of the alloy systems. However, very high heat input can be detrimental for surface finish due to high thermal stresses and non-uniform solidification rate [53]. Finally, larger powder particles are difficult to melt. Therefore, components fabricated with coarser powders may exhibit poor surface finish. Larger solid particles on the build surface also result in higher surface roughness. Fig. 17(f) shows the relation between the average powder diameter and the surface roughness using the data from independent literature [195,205,207]. It is shown that smoother surface can be achieved by fabricating components using finer powder particles.

Optimization and the reduction of surface roughness depends the interaction of a large number of input parameters and processing conditions. As an example for PBF-L, depending on the material type and process used to produce the powder (10–60  $\mu\text{m}$  powder), powder flow and spreading by roller or blade, the surface roughness may be adversely effected at the lower range of PSD. In another example, the PBF-EB process uses powder sizes in the range of 45–105  $\mu\text{m}$  to reduce the effects of electrostatic charging, repulsion and floating of powder and disturbance of the spread powder layer. In this example, the tradeoff between increased surface roughness due to larger PSD vs process disturbance due to electrostatic charging result in a slightly rougher surface when comparing PBF-EB to PBF-L.

Wire fed systems feature similar input parameters and output conditions related to surface roughness but at a much larger scale due to large molten pool sizes and deposit bead widths and layer heights. Surface features associated with roughness are referred to using welding terms such as lack of sidewall fusion, undercutting, irregular top bead and crater formation. Further detail of roughness associated with wire fed processes related to weld processing (Section 6, Welding vs AM) is provided in Section 6.2 (Surface finish).

#### 2.9.4. Cracking and delamination

There are three main types of cracking observed in additively manufactured components [208]. First, similar to welding, solidification cracking in AM [209] can be observed along the grain boundaries of the build [210]. The solidifying deposit tends to contract due to both solidification shrinkage and thermal contraction. However, the temperatures of the substrate or the previously deposited layers are lower than those of the depositing layer. Therefore, the contraction of the depositing layer is more than that of the lower layer and the contraction of the solidifying layer is thus hindered by the substrate or the previously deposited layer. That results in the generation of a tensile stress at the solidifying layer. If the magnitude of this tensile stress exceeds the strength of the solidifying metal, cracking may be observed along those grain boundaries [210]. The cracking in two  $\gamma'$ -strengthened nickel superalloys (CM247LC and CMSX486) fabricated by selective laser melting was studied over a wide range of process parameters by Carter et al. [211]. It was found that although the void fraction decreased with an increase in the energy density, the cracking density did not correlate directly with the energy density. Their findings underscore the need to understand the effect of metallurgical (e.g., solidification temperature range) and mechanical (e.g., residual stress) factors [210] on hot cracking in additively manufactured materials.

Second, liquation cracking [209] is observed in the mushy zone or partially melted zone (PMZ) of the build [210]. In PMZ rapid heating below the liquidus temperature of the alloy causes melting of certain grain-boundary precipitate phases such as low melting point carbides. During the cooling of the build, the PMZ suffers a tensile force due to the solidification shrinkage and thermal contraction of the deposit. Under this force, the liquid films around those grain boundary phases or carbides may act as cracking sites [210]. The alloys exhibiting wide mushy zone (large difference between the liquidus and the solidus temperature, such as nickel base superalloys), large solidification shrinkage (large molten pool, such as Ti-6Al-4V) and large thermal contraction (high coefficient of thermal expansion, such as aluminum alloys) are the most susceptible to liquation cracking [210]. In AM components cracking can be very long [212] spreading over several layers (Fig. 18(a)) or small with a maximum length equal to the layer thickness (Fig. 18(b)).

Finally, delamination is basically the separation of two consecutive layers as shown in Fig. 18(c), which is caused by the residual stresses at the layer interfaces exceeding the yield strength of the alloy [141].

#### 2.10. Residual stresses and distortion

An inherent consequence of the deposition of liquid alloy powder on a relatively cooler substrate or prior deposited layers is the steep temperature gradient, thermal strain and residual stresses [213,214]. The residual stresses can lead to the part distortion, loss of geometric tolerance and delamination of layers during depositing (see Fig. 18(c)), as well as deterioration of the fatigue performance and fracture resistance of the fabricated part [213,214]. A quantitative knowledge of the evolution of thermal stresses during AM is essential to understand and consequently control/mitigate the aforementioned issues. For instance, for powder bed AM, the part distortion may be large enough to prevent the rake (or levelling system) from spreading a fine layer of powder across the target area. An understanding of thermal stresses can help optimize the placement of support structures to minimize the distortion.

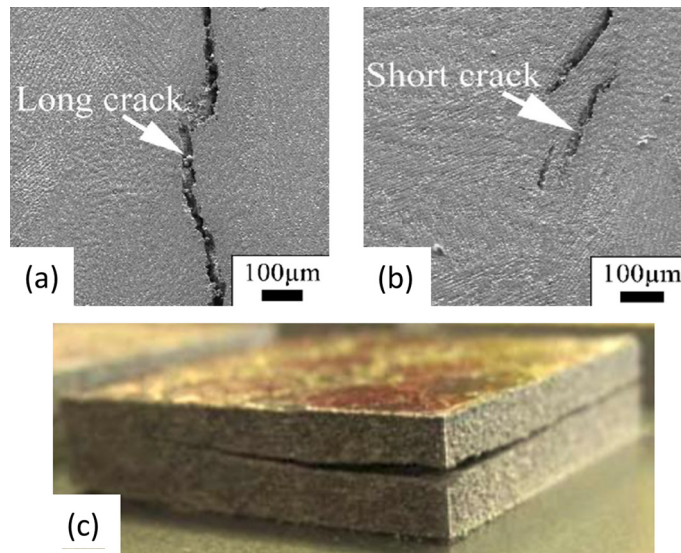


**Fig. 18.** (a) Long crack [212] (b) short crack [212] and (c) delamination in additive manufacturing [208].

Similar to those in fusion welding, the residual stresses in AM are highly spatially non-uniform and vary with time during building. Experimental measurement of residual stresses is typically limited to a few discrete points in 3D volume or 2D contours on selected planes of the part after the fabrication is completed. On the other hand, computational models, based on the numerical solution to thermal-stress equilibrium equations, can provide the evolution of stresses and displacements in the 3D geometry as a function of time. Due to the complexities of modeling (to be discussed in detail later), it is crucial for the computational models to be validated using high-quality experimental data.

This section is organized as follows. First, the origin of residual stresses is discussed using a simple bar-frame problem. Second, the current status of AM residual stress modeling is examined, followed by a review of several experimental measurement techniques. Finally, the existing mitigation strategies to reduce residual stresses are discussed.

#### 2.10.1. Origin of residual stresses

Key physical factors responsible for the origin of AM residual stresses include (1) spatial temperature gradient due to localized heating and cooling by the traveling heat source, (2) thermal expansion and contraction of material due to such heating and cooling, and (3) strain compatibility (uneven distribution of inelastic strains), force equilibrium and stress-strain constitutive behavior especially with respect to cyclic plastic flow. The AM and fusion welding share many of the same physical phenomena especially those key physical factors governing the formation of residual stresses and distortion [6,69,210,215]. Hence, the classic bar-frame problem, established to illustrate the origin of residual stresses in fusion welding [216], is adapted to explain that in AM. Special treatments needed for AM vs. welding residual stress modeling are discussed later.

As shown in Fig. 19, a solid bar is connected to a rigid box frame; both are set at temperature  $T_0$  initially. The middle bar experiences heating to a peak temperature  $T_p$  and cooling back to  $T_0$ . This situation is analogous to a line deposit made on a substrate where the hot metal deposited in the center is surrounded by the cold base metal. For this simple problem, only the stress/strain along the length or Y direction (analogous to the longitudinal stress/strain) is analyzed.

Since the middle bar is fully constrained by the rigid box frame, the following strain compatibility equation can be written:

$$\varepsilon_e + \varepsilon_p + \varepsilon_o + \alpha(T - T_0) = 0 \quad (20)$$

where  $\varepsilon_e$  is the elastic strain,  $\varepsilon_p$  is the plastic strain,  $\alpha$  is the coefficient of thermal expansion (CTE),  $T$  is the local temperature, and  $T_0$  is the initial temperature defined previously. In addition,  $\varepsilon_o$  includes the other inelastic strain such as that from phase transformation and creep; it is set to zero in this simple analysis. The elastic strain is described by 1D Hooke's law of linear elasticity, i.e.,  $\varepsilon_e = \sigma/E$ , where  $\sigma$  is the stress, and  $E$  is the Young's modulus. The maximum elastic strain ( $\varepsilon_m$ ) that the material can endure before the plastic deformation takes place is  $\varepsilon_m = \sigma_f/E$ , where  $\sigma_f$  is the flow stress. The last term in the left hand side of Eq. (20) represents the thermal strain.

To facilitate the analysis, the box frame and middle bar are assumed to be made of a nickel alloy whose properties have the following typical values:  $E = 200$  GPa,  $\sigma_f = 800$  MPa, and  $\alpha = 1.25 \times 10^{-5} \text{ K}^{-1}$ . Moreover, the properties are treated as temperature-independent, and  $\sigma_f$  does not change with plastic strain (i.e., perfect plasticity). Using those property values,  $\varepsilon_m = \pm 0.4\%$ , where  $+0.4\%$  and  $-0.4\%$  indicate the elastic strain limits in tension and compression, respectively. The initial temperature  $T_0 = 300$  K, and the peak temperature of the middle bar  $T_p = 1500$  K.

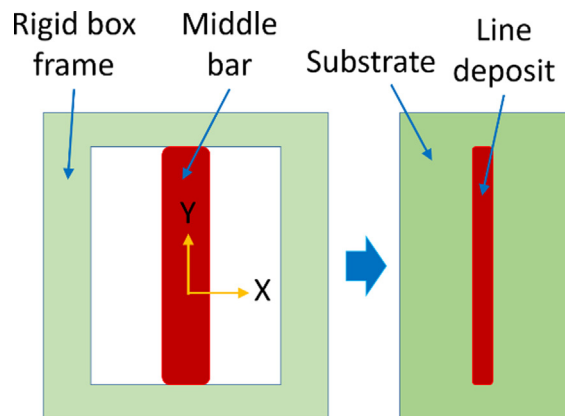


**Fig. 19.** Schematics of a simple bar-frame problem to illustrate the origin of AM residual stresses.

The evolution of stress in the middle bar as it is heated up and cooled down can be divided into four stages. *Stage 1* is the elastic compression at the beginning of heating, during which the thermal expansion is accommodated by the elastic deformation and there is thus zero plastic strain:  $\varepsilon_e = -\alpha(T - T_0)$ . The compressive elastic strain limit ( $-0.4\%$ ) is reached when  $T = 620$  K (i.e.,  $T - T_0 = 320$  K). Further heating leads to *Stage 2* – plastic compression in the middle bar:  $\varepsilon_p = -\alpha(T - T_0) - \varepsilon_m = -\alpha(T - T_0) + 0.4\%$ . At  $T_p = 1500$  K, the compressive plastic strain formed in the middle bar is  $-1.1\%$ . In other words, the middle bar is plastically shortened by  $1.1\%$  at the end of heating.

*Stage 3* corresponds to elastic tensioning that starts as the middle bar is cooled down. The drop in thermal strain (contraction) is first compensated by the release of compressive elastic strain:  $\varepsilon_e = -\alpha(T - T_0) - \varepsilon_p = -\alpha(T - T_0) + 1.1\%$ . When  $T$  decreases to 1180 K, the elastic strain in the middle bar becomes zero (and thus zero stress as  $\sigma = E\varepsilon_e$ ). Further decrease in temperature causes a tensile elastic strain in the middle bar, and the tensile elastic strain limit ( $+0.4\%$ ) is reached when  $T$  decreases to 860 K. Finally, *Stage 4* when plastic tensioning takes place as the middle bar cools down further to  $T_0$ :  $\varepsilon_p = -\alpha(T - T_0) - \varepsilon_m = -\alpha(T - T_0) - 0.4\%$ . Although it is plastically deformed in tension during *Stage 4*, the middle bar still has a compressive plastic strain of  $-0.4\%$  after cooling down to  $T_0$ . However, since it has a tensile elastic strain of  $+0.4\%$ , the middle bar experiences a tensile stress of  $+800$  MPa (same as  $\sigma_f$ ). This is the residual stress formed in the middle bar. Considering the force balance, the two vertical sides of the box frame experience a compressive stress at the end of cooling.

From the above analysis, the following key factors for residual stresses can be identified:

- [1] **Spatial temperature gradient**: If the two are uniformly heated and cooled, the box frame and middle bar would expand and contract freely. As a result, there would be no elastic and plastic strains and thus residual stress in the middle bar.
- [2] **Thermal expansion**: Structural metals commonly used in AM (e.g., stainless steels, and nickel, aluminum and titanium alloys) have a CTE above  $1 \times 10^{-5}$  K $^{-1}$ . With only a few hundred Kelvins rise/drop in temperature, the thermal strain can exceed the elastic strain limit, resulting in accumulation of plastic strain upon further heating/cooling. Moreover, when dissimilar metals are used, the difference in CTE between two metals (i.e., CTE mismatch) can result in the formation of residual stresses even when they are heated and cooled down uniformly.
- [3] **Plasticity and flow stress**: The above analysis purposefully did not account for the heating and cooling rates. This is because the AM stress modeling is commonly formulated as a quasi-static problem (as opposite to a dynamic problem) as the speed of stress wave in metals is several orders of magnitude faster than that of heat conduction. In other words, whenever a new temperature field is established, the stresses are redistributed “instantaneously” to reach a new static equilibrium state. Rate-independent but temperature-dependent flow stress is typically used in the quasi-static stress analysis.

In the weld stress modeling literature, metal plasticity (i.e., hardening) was identified as a crucial parameter for the accuracy of predicted residual stresses [217]. Particularly, Qiao et al. linked the annealing of plastic strain to the microscopic dislocation recovery and recrystallization in cold-worked 304 stainless steel exposed to a simulated weld thermal cycle [218]. They found that incorporating constitutive (hardening) behavior with temperature-dependent annealing improved the accuracy of predicted residual stresses when compared to the conventional rate-independent hardening behaviors. The temperature- and time-dependent constitutive behavior is expected to be important for AM stress modeling as well, especially considering electron beam melting where the entire powder bed can be preheated to a high temperature (e.g., approximately 1273 K).

Finally, for welding of ferritic steels, the large volume expansion due to martensitic transformation upon cooling was found to markedly influence the residual stresses and distortion [215,219]. Incorporation of transformation-induced plastic-

ity (which is both temperature- and time-dependent) is also expected to be essential for accurate simulation of residual stresses in additively manufactured ferritic steels exhibiting martensitic transformation.

### 2.10.2. Directed energy deposition versus powder bed AM

Residual stresses and distortion in AM is a global phenomenon. Simulating the entire part build-up on the substrate (as opposite to a local region) is essential to accurately calculate these quantities. Due to the relatively coarse spatial and temporal resolutions mandated for the calculation of global distribution of stresses and displacements, the AM stress model is not suitable to directly simulate the material addition (e.g., powder particles fusing into the molten pool). Instead, it relies prescribing the material addition via meshing. In other words, a mesh for the entire part is created following the deposition or melting path where the bead shape and size have to be known *a priori*. The bead typically has a rectangular cross section to facilitate the filling of the 3D volume by individual passes. This simplification of material addition in AM stress modeling has an important implication on how the different AM processes are treated, as discussed in the following.

As discussed in Section 2.1, there are various types of AM processes depending on the feedstock materials (powder or wire) and heat sources (laser, electron beam or arc) used. From the perspective of AM stress modeling, the AM process can be divided into two main categories: directed energy deposition and powder bed AM. The former category includes both powder blown and wire feed AM. The approach of stress modeling for directed energy deposition is essentially the same as that of fusion welding. Particularly, the solution domain is meshed to include only the solid substrate and deposited layers and no powder [69]. On the other hand, the presence of the pre-placed powder layer in powder bed AM requires special treatment since the powder particles have a different thermal and mechanical response than the consolidated solid metal [6]. Despite of the need to handle powder material, the standard approach of solving temperature, stresses and strains remains the same for both powder bed and directed energy deposition AM. This standard approach is discussed in the next section.

### 2.10.3. Thermal-stress analysis approach

The sequentially-coupled heat conduction analysis in transient mode followed by elastic-plastic small displacement analysis has been the standard approach to numerically solve thermal distortion and residual stresses in AM [220]. In other words, the transient temperature field in AM is calculated first by the numerical solution of heat conduction equation. The temperature field as a function of time is then imported into the stress model as “thermal loads” to calculate the stresses and strains. Fully-coupled analysis, which solves the heat conduction and stress equilibrium equations “simultaneously”, was used by some researchers [221]. For the same model, the fully-coupled analysis would require much more computational resources to run than the sequentially-coupled one.

As discussed in Sections 2.5 and 2.6, the temperature distribution can be significantly influenced by the molten metal convection. However, given its complexity, the molten metal fluid flow phenomenon is not directly simulated but approximated via a heat flux distribution from energy beam when solving the heat conduction problem in a typical AM thermal-stress model. A departure from the conventional use of heat conduction analysis was attempted in a recent study by Mukherjee et al. [141], where a well-tested 3D heat transfer and fluid flow model was used to compute the temperature field. The temperature field was then inputted into a stress model based on Abaqus, a commercial finite element analysis (FEA) code, to calculate the residual stresses and distortion in laser powder blown AM of Ti-6Al-4V and IN718. The sequential coupling of two models took advantage of similar meshes used, in which the material addition was prescribed by pre-placed elements in both models. Despite of such limitation, the results showed an improved accuracy of predicted residual stresses by considering the molten pool fluid flow than the heat conduction analysis alone.

For the solution of stress equilibrium equations, the stress-strain constitutive behavior is considered in an incremental manner to account for steep temperature gradient, sharp change in thermal strains and consequent stresses as [222–224]:

$$d\sigma = D^{EP} \cdot d\varepsilon - D^E \cdot (d\varepsilon^{Th} + d\varepsilon^V) \quad (21)$$

where  $d\varepsilon$  is the total incremental strain that is composed of elastic ( $d\varepsilon^E$ ), plastic ( $d\varepsilon^P$ ), thermal ( $d\varepsilon^{Th}$ ) and other volumetric ( $d\varepsilon^V$ ) strain increments, and  $D^{EP}$  and  $D^E$  are the elastic-plastic and elastic stiffness matrices, respectively. The thermal strain is computed from the local temperature field [222–224] and the strain associated with change in volume due to solid-state phase transformation is deemed as the volumetric strain [225].  $D^E$  is computed as function of Young's modulus and Poisson's ratio, while  $D^{EP}$  requires a knowledge of elastic-plastic response of the selected alloy in terms of yielding criterion and the plastic modulus [222–224]. The overall analysis becomes further complicated as the properties of the alloys can vary significantly with temperature. It is noted that the stresses and strains are solved together in Eq. (21), which yields both quantities in the solution domain.

Accounting for pass-by-pass and layer-by-layer deposition of alloy powder (or filler wire) as it occurs during building remains the most challenging aspect in numerical modeling of AM residual stresses and distortion. As discussed earlier, the material addition is handled by pre-placed elements. The addition of new materials appends stiffness to an existing structure and requires progressive attachment of a large number of new elements to a solution domain. The three commonly used methods for handling material deposition are the so-called (1) element birth, (2) quiet element, and (3) hybrid activation [69,101]. In the element birth method, elements for the yet to be deposited material are deactivated (and thus not included in the solution domain) at the beginning and then gradually activated or born into the solution domain. In the quiet element method, all elements are present at the beginning and assigned to artificial properties with very little stiffness. The

properties for those quiet elements are then gradually switched to the physical properties based on the build path. Finally, the hybrid activation method combines the element birth and quiet element methods, where only the current deposition layer is activated and set to quiet and all the subsequent layers to be deposited are deactivated [101].

For AM with a relatively small number of passes, analysis of individual passes to build a final part can be computationally affordable [109,226]. In such individual pass approach, the heat input from the energy beam is typically applied as a volumetric heat flux whose center moves according to the deposition path, thus representing a moving heat source. This individual pass approach with moving heat source was applied to both powder blown [226] and powder bed AM [109]. However, the power bed AM typically has a large number of melting layers and passes, making it impractical to simulate the individual passes for building a full-sized part. For computational efficiency, a lumped pass approach, where successive melting passes and even successive layers are grouped together with elements for those layers being activated at once [2,112], is utilized. For this lumped pass approach, a stationary heat flux is assigned to the lumped region over a user-specified time period. Clearly, the way that the material is deposited and the way that the heat input is applied in the individual pass approach are more “physical” (albeit at the cost of higher computational time) than the lumped pass approach.

An alternative to the lumped pass approach was applied by Song et al. to evaluate residual stresses in thin walls of C263 nickel base superalloy fabricated by laser powder bed AM [227]. Taking advantage of the thin wall geometry, two 2D thermal-stress models were established. One was a plane strain model where the computational domain was the cross-section perpendicular to the laser scan direction, while the other was a plane stress model where the domain was the longitudinal section parallel to the scan direction. In addition to the moving heat source analysis, they also attempted rapid residual stress evaluation via a thermal contraction model, although it was also limited to 2-D and thus thin-wall geometry. On the other hand, Fergani et al. developed an analytical assessment of residual stresses in a homogeneous semi-infinite medium [228]. The temperature field was first calculated using an equation similar to Rosenthal solution of a traveling point source of heat. Analytical equations formulated based on McDowell theory were then used to compute the thermal-stresses and subsequently residual stresses by considering the temperature field and cyclic plastic flow for laser powder bed AM of 316L stainless steel.

#### 2.10.4. Computational codes for thermal-stress analysis

Several multi-physics FEA codes, available either commercially or through research institutions, have been customized or enhanced for AM stress modeling. Some of the commercial codes include 3DSim (<http://3dsim.com/>), ESI (<http://www.esi-group.com/>), Additive Works (<https://additive.works/>), Abaqus (<http://www.3ds.com/>), and Ansys (<http://www.ansys.com/>). Diablo is a research code from Lawrence Livermore National Laboratory that has been used for powder bed AM [109]. The extent of user customizations for AM simulation varies from code to code. Generally, it includes meshing the deposited geometry according to the build path where different groups of elements are created to represent individual passes and/or layers. These element groups are then used to prescribe the sequence of element activation to account for the material addition. The same mesh is typically used in both the thermal and stress models to facilitate transferring the temperature field from the former to the latter. In the thermal model, the heat input from energy beam (e.g., power and traveling speed) is applied via a volumetric heat flux, which may require coding a user subroutine if such function is not implemented in the FEA code. The computed temperature field as a function of time is transferred into the stress model as thermal loads. Key mechanical properties that need specified in the stress model include: Young's modulus, Poisson's ratio, stress-strain curves, and coefficient of thermal expansion, all of which are a function of temperature. Property data is needed over a wide range from room temperature to close to melting temperature. User materials may need to be developed to incorporate the metal plasticity at high temperatures and the phase transformation induced plasticity described previously.

#### 2.10.5. Results of calculated residual stresses and distortion

A large volume of research has been published for powder blown AM of various materials ranging from stainless steels [88,229–233], carbon steels [68,234–239], nickel-based alloys [27,141,152,158,240–244] and Ti-6Al-4V [6,27,141,152,158,213–221,244,245]. A detailed list and some of the significant features of these reported models are presented in Table 8. The predominant presence of the longitudinal and the normal residual stresses, and nearly negligible transverse stresses was highlighted by all the model calculations. In particular for typical thin-wall structures, the longitudinal residual stress appeared tensile towards the mid-length and compressive near the free end while the normal component of the residual stress tended to be exactly opposite in nature as shown in Fig. 20 [232,233]. Typically, the ratio of the maximum residual stress to the alloy yield strength at room temperature appeared to be the highest in deposits of nickel-based alloy powder compared to that for Ti-6Al-4V and stainless steel. For example, the maximum computed residual stresses in an IN718 deposit was found to be around  $1.5\sigma_y$  in comparison to around  $1.0\sigma_y$  for Ti-6Al-4V as shown in Fig. 21 [141]. In case of AISI 304 stainless steel, the computed residual stresses were found to remain in a range of  $0.6\sigma_y$  to  $0.9\sigma_y$  [88,230] and further lower in deposits of H13 tool steel [236–238] within permissible range of process conditions.

Wire arc additive manufacturing (WAAM) is suitable for fabricating parts requiring large volume of deposition [27,158,246]. Ding et al. applied a 3D sequentially-coupled heat conduction analysis followed by elastic-plastic structural analysis. It was found that the pattern of residual stresses was similar to that in fusion welding with filler wire deposition [27,246]. The longitudinal residual stress was tensile and maximum at the mid-length of a layer while the transverse and normal stresses were found negligible for typical thin wall builds of mild steel, which was expected due to small transverse cross-section and multiple thermal cycles [27,246].

**Table 8**

A summary of thermal and structural analysis in additive manufacturing of alloys.

Powder/Substrate	Process	Remarks	Refs.
MONEL 400/AISI 1006	LENS	3D sequential thermal and elastic-plastic analysis using ANSYS, higher equivalent stresses at upper layers.	[220]
Low-C steel	Micro-casting	1D & 2D axisymmetric sequential thermal and elastic-plastic analysis using ABAQUS, single and a few adjacent drops added to a large substrate with arbitrary boundary conditions, lower residual stress with substrate preheating.	[667–669]
Low-C steel SS 308/Low-C steel	Micro-casting Micro-casting	3D, rest same as in [667–669] 1D & 2D generalized plastic strain, rest same as in [667–669], lower residual stress with deposition pathway & substrate preheating.	[670] [671]
SS 304 SS 304	LADMD LENS	1D, considered solidification rate Review of [667–671], showed normalized maximum residual stress as function of power, scanning speed and substrate preheating in thin wall build	[231] [88,230]
SS 304	LSFF	3D sequential thermal & elastic analysis using COMSOL & MATLAB, equivalent stress higher towards edge, little effect of layer height, lower residual stress with substrate preheating	[229]
SS 410	LENS	3D sequential thermal & elastic-plastic analysis by SYSWELD, $\sigma_z$ found dominant, remained compressive at interior and tensile towards the edge, $\sigma_x$ found tensile at mid-length and mid-height, but compressive at top and bottom of the walls.	[232,233]
H13/Mild steel	LADMD	3D, used ABAQUS for a sequential thermal and elastic-plastic analysis, considered strain due to change in phases	[236–238]
AISI 4140	LPD	3D sequential thermal & elastic-plastic analysis using ANSYS, lower stresses with short bead & spiral-in deposition pattern	[672]
Low-C steel/Structural steel	WAAM	Same as [236] while strain due to phase change not considered, high tensile longitudinal stress at mid-length as in welding.	[68,234]
H13/ASTM A36	LPD	Same as [672], multi-track cladding, strain due to phase change considered, high tensile residual stress at clad-substrate interface	[68]
H13 Dental Ni-alloy & porcelain Waspaloy, IN718/IN 718	LHW MMLD LADMD	Same as [68], tensile residual stress maximum at substrate-layer interface 2D, used ANSYS, bi-metallic deposition, higher stresses with Ni-alloy deposit Used ANSYS [242] and ABAQUS [243], high tensile residual stress at substrate-layer interface, examined effect of deposition pattern on lowering residual stress and overall distortion	[239] [235] [242,243]
IN718	SMD	Used finite element method and “element activation”, not clear if a commercial code was used, rest as [242]	[240]
Ti-6Al-4V	EBAM	3D sequential thermal and elastic-plastic analysis in CUBIC, stress relaxation temperature of 690 °C to improve prediction	[241,244]
Ti-6Al-4V	EBAM	3D sequential thermal and elastic-plastic analysis in ABAQUS, lower distortion and residual stress with substrate preheating	[221]
SS 316, Ti-6Al-4V, IN 718	LENS	Used computed temperature history from a 3D heat transfer & fluid flow model for elastic-plastic analysis in ABAQUS, a python script imported geometry & temperature field in ABAQUS	[141]
Mild steel (wire)	WAAM	3D sequential thermal and elastic-plastic analysis in ABAQUS	[27,158]

LADMD: Laser assisted direct metal deposition, MMLD: Mixed-material laser densification, LSFF: Laser solid freeform fabrication, LENS: Laser engineered net shaping, LPD: Laser powder deposition, WAAM: Wire-arc additive manufacturing, LHW: Laser hot wire additive manufacturing, SMD: Shaped metal deposition - same as WAAM, EBAM: Electron beam additive manufacturing (with wire); [ $\sigma_x$ ,  $\sigma_y$  &  $\sigma_z$  refer respectively to longitudinal, transverse and normal components of stresses w.r.t. scanning velocity].

There are fewer published works on modeling residual stresses and distortion in powder bed AM than powder blown AM. Some model for powder bed AM took the same standard approach as that for powder blown AM where the presence of pre-placed powder was ignored [112]. On the other hand, Hodge et al. developed a thermomechanical model for selective laser melting, a powder bed AM process [109]. Their model considered both the consolidated and powder phases by using phase-dependent material properties (e.g., thermal conductivity) and a volumetric contraction from the melting consolidation of powder particles, as shown in Fig. 22.

For improved computational efficiency, Li et al. [247] proposed a method that mapped the local residual stress field calculated in the meso-scale layer hatch model to the macro-part model for fast prediction of part distortion. However, the validity of such an approach for complex part geometry is yet to be demonstrated. Another approach being adopted for efficient distortion modeling in AM is that based on the inherent-strain method developed by Yuan and Ueda for weld distortion of large-scale structures [248]. The method directly applies a known inherent-strain to calculate the distortion and does not require the computationally-intensive thermal and elastic-plastic analysis. Although its accuracy is demonstrated for distortion modeling of welded structures, the application of inherent-strain method for AM distortion modeling requires further validation especially considering the diverse scanning patterns that can be employed in building a part.

Finally, as shown in Eq. (12), Mukherjee et al. [152,244] defined an analytical expression of strain parameter for estimation of maximum distortion as function of linear heat input, substrate stiffness, peak temperature, coefficient of thermal expansion of the depositing alloy, and the Fourier number that manifested a ratio of the rate of heat dissipation to storage. The strain parameter was shown to provide a fair correlation to the maximum thermal distortion in layer-wise deposition of alloy powder for a number of alloys including stainless steel, Ti-6Al-4V and IN 718 [152,244].

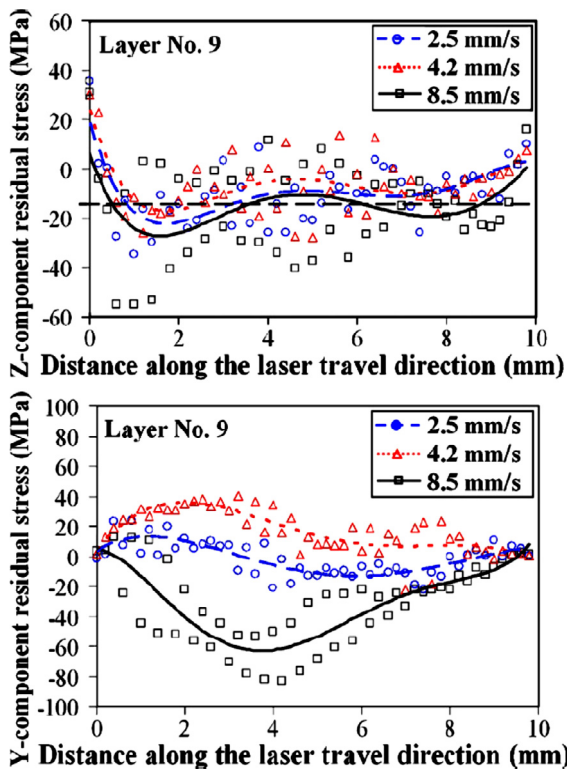


**Fig. 20.** Computed residual stresses along the laser travel or scanning direction at the surface of the ninth layer at different scanning speeds in deposition of SS 410. Y- and Z- component corresponds to longitudinal and normal residual stresses. Computed results are shown by points [233].

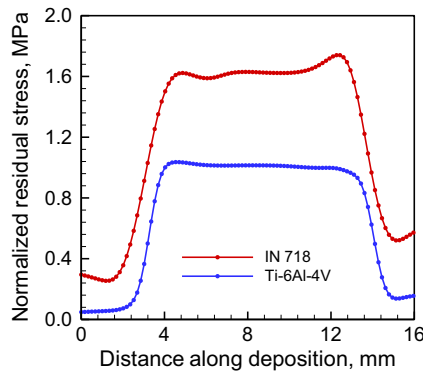


**Fig. 21.** Longitudinal component of normalized residual stress along the laser travel or scanning direction for a laser power of 250 W and scanning speed of 15 mm/s in deposits of IN 718 and Ti-6Al-4V [141].

#### 2.10.6. Measurement of residual stresses and distortion

A variety of techniques have been used to measure the residual stresses ex-situ post fabrication. Many of the techniques are the same as those used for welding residual stress measurement. Several excellent reviews of residual stress measurement are available in the literature for general techniques [249] and those applied to AM [250] and welding [251]. For completeness, a brief overview of residual stress measurement for AM is provided as follows, where recent advances in measurement techniques such as in-situ distortion measurement during fabrication and high spatial-resolution stress measurement are highlighted.

The residual stresses in additively manufactured parts were measured indirectly by Vickers micro-indentation [252,253], and directly by destructive means such as hole-drilling combined with laser holography [254] as well as using strain gauges [255–257], and non-destructive methods such as X-ray [258,259] and neutron diffraction techniques [260–267]. Table 9 presents a summary of some of the significant studies reported in literature on measurement of residual stresses and distortion

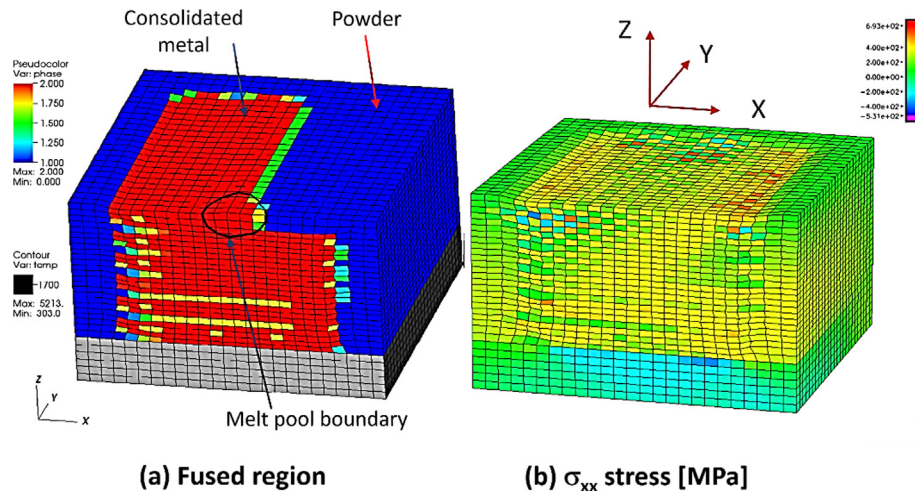


**Fig. 22.** Computed fused region and  $\sigma_{xx}$  stress when building the 12th layer of a solid cube. Other stress components are not shown for brevity and they are available in the reference (Hodge et al. [109]).

in AM of alloys. In LENS deposited thin-walled hollow and solid samples of H13, Griffith et al. measured tensile and compressive stresses respectively along and perpendicular to the deposition [254]. The maximum values of stresses were only around  $0.5\sigma_y$  and a possible transformation of austenite to martensitic phases was considered responsible for such low values of residual stress. In PBF-L of AISI 300 maraging steel, Casavola et al. [255] used standard hole-drilling method and reported the maximum tensile stress of around  $0.7\sigma_y$  near the free surface (0.1 mm hole depth), its sharp drop to around 85% at a depth of 0.5 mm and a plateau at 1.5 mm irrespective of processing conditions. Although the nature of the measured stresses remained nearly the same, the latter studies augmented clarity to the pattern of stresses along the plane of deposited layer. In multi-layer deposits of stainless steel (SS) 316L prepared by PBF-L, X-ray diffraction based measurement showed the residual stress parallel to the scanning direction much higher compared to that normal to the scanning direction [258]. Lower energy input and shorter scanning strips reduced the magnitude of residual stresses that were always higher towards the free edges, i.e., at the beginning and end of the scanning lines making the parts susceptible to bowing [258].

Hole-drilling techniques for residual stress measurement usually suffers from lower resolution and greater likelihood of uncertainties. X-ray diffraction based techniques, although superior to the hole-drilling methods, can only penetrate little into the surface (3–10  $\mu\text{m}$ ) for the measurement of residual stresses. In contrast, the neutron beam penetrates to a greater depth into most of the metallic materials and is increasingly considered as a suitable technique for more reliable measurement of residual stresses in parts for critical use. Rangaswamy et al. [264,265] used neutron diffraction and contour methods to measure residual stresses in LENS deposited thin walls [265] and, solid pillars of rectangular and square cross-sections of SS 316 [264,265] and IN718 [265]. These authors found the stress predominantly aligned in the axial or growth direction with its nature compressive at the center and tensile towards the edges as shown in Fig. 23, and magnitude around 50% and 80% of the nominal yield strength respectively in thin wall and solid pillar deposits. All these measurements showed very little presence of the longitudinal and transverse residual stresses that was interesting. It is noted that neutron diffraction requires a precise knowledge of the stress-free lattice spacing ( $d_0$ ) in order to calculate the lattice strain. In the welding literature, the  $d_0$  value was found to significantly influence the accuracy of the residual stresses as it was strongly dependent on local chemical composition in dissimilar metal weld [268]. The same issue can become critical for AM as it is increasingly used for site-specific properties in metals and alloys [269].

In powder bed fused and built wedge, prism and L-shaped parts, Wu et al. [267] used neutron diffraction and a digital image correlation (DIC) based method to measure residual stresses. The latter method involved a digital comparison of images acquired before and after localized stress relief during sectioning to obtain a measure of surface residual stresses without surface conditioning or a numerical model. The results obtained were found to be in good agreement with the near-surface neutron diffraction measurements. The authors reported reduction in residual stresses by decreasing scan island size and increase in energy per unit length that was unexpected. Vrancken et al. [266] employed the contour method to measure residual stresses and relate the same to mechanical behavior of parts in PBF-L of Ti-6Al-4V. The two dimensional mapping of residual stresses showed a direct influence on the anisotropic behavior of the part while the maximum stress was close to yield point of Ti-6Al-4V that was also reported earlier [141] for this alloy. Preheating of powder also reduced the thermal stress induced distortion in sample cantilever parts of AlSi10Mg built by PBF-L process [270]. Finally, Dunbar et al. developed an interesting technique to measure the distortion in-situ in PBF-L utilizing differential variable reluctance transducer (DVRT) displacement sensor [271]. Such in-situ data provides history profiles that are crucial to validate the accuracy of thermal-stress models of AM.

**Table 9**

Significant efforts to measure distortion and residual stresses in AM of alloys.

Powder/Substrate	Process	Remarks	Refs.
IN 718	LRF, SLM	Vickers micro-indentation and empirical relations assuming equal bi-axial stress state; layer-wise tensile stresses with high values towards the edge; smaller size deposition island reduced stresses.	[252,253]
H13	LENS	Hole drilling with strain measured by laser light interferences on a hologram, ( $\sigma_x$ ) and ( $\sigma_z$ ) respectively tensile and compressive; maximum tensile stress around $0.3\sigma_y$ ; austenite transforming to martensite at low temperature considered responsible for reduced residual stresses.	[254]
AISI Marage 300 steel	SLM	Hole drilling with standard strain gauges; use of high laser power, low scanning velocity and appropriate deposition strategy suggested; irrespective of layer height and processing conditions, maximum tensile stress at free surface (0.1 mm hole depth).	[255]
Ti-6Al-4V	LSF	Hole drilling with strain gauges; both ( $\sigma_x$ ) and ( $\sigma_z$ ) compressive in the middle and tensile at free edges; annealing reduced $\sigma_x$ by 60% and $\sigma_z$ by 72%; solution annealing reduced both $\sigma_x$ and $\sigma_z$ by around 65%.	[257]
Ti-6.5Al-1V-2Zr	LRF	Hole drilling with strain gauges; laser power and powder feed rate increased residual stresses; scanning speed and staggered scanning reduced residual stresses.	[256]
SS 316L, Ti-6Al-4V	SLM	X-ray diffraction; both $\sigma_x$ and $\sigma_z$ were tensile from top to bottom with a depth-wise wavy nature, $\sigma_x > \sigma_z$ and higher values toward the layer-substrate interface; examined 5–25 layer samples.	[259]
SS 316L	SLM	X-ray diffraction, $\sigma_x \gg \sigma_z$ ; stresses compressive in the middle and tensile at free edges; Lower $\sigma_x$ and $\sigma_z$ with shorter strips.	[258]
SS 316	LENS	Neutron diffraction, $\sigma_x$ and $\sigma_z$ nearly insignificant compared to $\sigma_y$ that depicted a parabolic variation in through-thickness direction with tensile at the surface and compressive in the interior.	[265]
SS316, IN718	LENS	Neutron diffraction and contour methods; same as [258]; “negligible $\sigma_x$ ” was different from all other studies.	[264]
SS 410/SS 410	LENS	Neutron diffraction; 25 layered thin wall samples; $\sigma_z$ found dominant, remained mostly compressive and tensile towards the edge.	[263]
Waspaloy/IN 718	LDMD	Neutron diffraction and contour methods; $\sigma_x$ tensile at mid-length and zero towards the edges - maximum $\sigma_x$ reduced from around 420 MPa to 245 MPa near substrate; $\sigma_z$ insignificant at vertical free surface & increasingly compressive towards the substrate; consistent results measured by the two methods.	[262]
AA2319/AA2219-T8	EBAM	Thin-walled build with filler wire; neutron diffraction; $\sigma_x$ and $\sigma_y$ became tensile with intermediate annealing otherwise compressive along build-substrate interface; $\sigma_z$ remained insignificant; maximum tensile stress remained low around 25 MPa only	[260]
H13	DMD	Wedge shaped deposition; neutron diffraction; compressive stresses at the top up to a depth of 4 mm - attributed to transformation of austenite to martensite at low temperature; this is in contrast to other alloys; the same considered beneficial for dies and molds of H13.	[261]
SS 316L	SLM	Neutron diffraction and digital image correlation (DIC) which digitally compared images acquired before and after localized stress relief from sectioning; wedge, prism and L shaped specimens.	[267]
Ti-6Al-4V	SLM	Contour method; maximum stress close to yield stress.	[266]
IN 718	EBM, DLMS	Neutron diffraction; tested prism shaped parts; parts built by EBM showed smaller stresses that was attributed to preheating of powder.	[673]
AISI10Mg	SLM	Measured thermal stress induced distortion; a preheating temperature of 250 °C resulted in minimum distortion in cantilever shaped parts.	[270]
IN 625, Ti-6Al-4V	DMD	Hole drilling method; both distortion and residual stress measured, distortion and residual stress reduced with dwell time for IN 625 deposit but increased in Ti-6Al-4V built.	[284]
IN 718	DLF	Measured 3D warpage; maximum in normal to the substrate; reduced warpage with shorter bead.	[273]

LSF: Laser solid forming (similar to LENS), LRF: Laser rapid forming, DLF: Direct laser fabrication, DLMS: Direct laser metal sintering, DMD: Direct metal deposition, [ $\sigma_x$ ,  $\sigma_y$  and  $\sigma_z$  refer respectively to longitudinal, transverse and normal components of stresses w.r.t. scanning velocity].

Shot peening is a common post-fabrication process to introduce compressive residual stresses for improving fatigue life. Salvati et al. measured the residual strain distribution in IN718 compressor blade that was fabricated by laser DED (blown powder) and subsequently subjected to shot peening treatment [272]. The measurement was performed using both the focused ion beam and digital image correlation (FIB-DIC) ring core milling method and the synchrotron X-ray powder diffraction (SXRPD) in transmission mode.

#### 2.10.7. Mitigation strategy to reduce residual stresses

Identifying appropriate strategies to mitigate residual stresses and/or stress induced distortion remains the main underlying driver for both the computational and experimental studies. The substrate preheat temperature, shorter deposition length or scanning in smaller islands, effective deposition strategy such as spiraling-in as against spiraling-out, increase in scanning speed and decrease in layer height were found significant recourses to reduce or mitigate both distortion and residual stresses [273]. It is noted that the substrate preheat temperature can not only reduce the final residual stresses post fabrication but also the stresses during building. As shown in Eq. (20), a high preheat can reduce the temperature difference and thus the thermal strain, which in turn, can lower the stresses. The use of high preheat can also be important to mitigate solidification cracking of additively manufactured nickel-base superalloys. Although change in beam power and scanning speed could control the residual stresses, together they influenced the size of melt pool and hence, were not suggested as desirable ways to mitigate residual stress. Mechanical tensioning of substrate as well as intermediate rolling of deposits

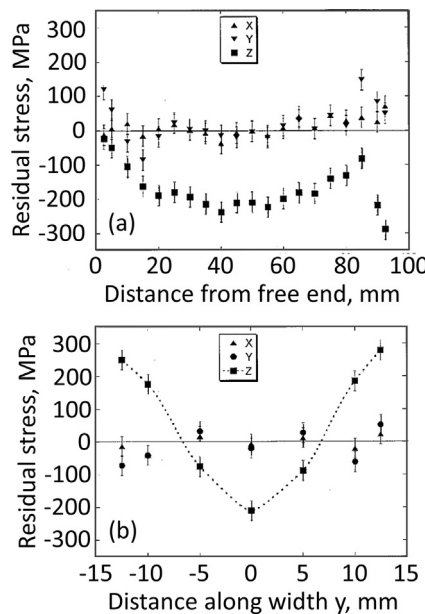


**Fig. 23.** Measured components (x - transverse, y - longitudinal, z - normal) of residual stresses in thin-wall deposits of SS 316 using neutron diffraction - (a) from free surface to substrate along the mid-length, and (b) along the layer at a height of 22.5 mm [265].

by shaped rollers were found to reduce residual stress and distortion in wire-arc additively manufactured parts similar to in arc welding [274–276].

#### 2.10.8. Future research needs

First, an important prerequisite for AM thermal-stress modeling is a database of temperature dependent thermo-physical properties for important engineering alloys. Mechanical properties are needed at high temperatures but typically at low strain rates. Incorporation of volumetric change due to solid-state phase transformation and creep strain can be important to improve the accuracy of predicted residual stresses. This need is expected to become even greater as various compositionally-graded parts are increasingly fabricated by AM, in which the properties can vary from location to location over a short distance.

Second, as discussed previously, the need to know the deposit profile *a priori* remains a major shortcoming of the AM thermal-stress model that relies on element activation for adding material. Enhancing the coupling of the heat transfer and fluid flow model with the stress model is a potential solution for improved accuracy of predicted temperature field and better handling of material addition.

Finally, computationally efficient models for predicting residual stresses and distortion must be scalable to full size parts with complex geometry. This is a significant challenge as the length-scale for the phenomena that affect the residual stresses and distortion varies from tens of microns (e.g., melt flow) to centimeters (e.g., support structures). As discussed earlier, several simplified approaches have shown their potential in fast prediction. However, rigorous validation of those models using high-quality experimental data is still necessary.

#### 2.11. Process control

In industrial applications, it is often desirable or even necessary to monitor the process with *in-situ* measurements and adjust process parameters as needed to ensure part quality. Recent attention has been given to monitoring AM to acquire feedback from the process with the overall goal of achieving full process control. The most important and widely reported types of measurements are temperature and molten pool geometry. In this section, a brief overview of the different types of thermal and molten pool measurement techniques, advantages and disadvantages and implications are discussed.

Temperature is by far the most common variable measured for process monitoring and control [15]. A particularly popular device for temperature measurements is a pyrometer, which is a broad term that encompasses different types of devices. Digital cameras and photodiodes are the most common devices that fall into the category of pyrometers. Both convert light to electrical signal and the intensity of the light is proportional to the temperature. A major benefit of pyrometry is that it is a non-contact measurement that has no adverse effects on the process itself. In the DED process, the sensor is typically placed near-coaxially with the moving heat source. This allows the device to be as close as possible to the region of interest for the entire process. A disadvantage is that pyrometers are only capable of providing surface temperatures, which

is only a minor part of the complete 3D molten pool shape and does not give any data below the surface. Perhaps the biggest drawback of pyrometry is the dependence on accurate physical properties to relate the emitted radiation to temperature, which are sometimes very difficult to obtain especially when working with uncommon alloys. Despite these disadvantages, pyrometers have been the choice for temperature measurements for many reported studies [15,104,277–283].

As discussed in Section 2.6, thermocouples are another type of device commonly used for temperature measurements [245,271,284,285]. A benefit of using thermocouples for temperature measurements is that they are fairly inexpensive when compared to pyrometers. Also, the spatial accuracy and the ability to measure internal temperatures of a build provide advantages over pyrometry. However, a major drawback of using thermocouples is that they are usually placed in the substrate prior to deposition, therefore only coming in contact with the first deposited layer. Measurements in higher layers therefore are not possible with thermocouples during a continuous AM process.

Another important parameter to control during AM processes is the molten pool geometry. Ideally, each part fabricated would be built with a uniform melt pool throughout the entire process time. However, geometries often dynamically change due to non-uniform heating and cooling cycles as well as heat accumulation. Overall part quality, especially during the fabrication of complex features, can be diminished if the melt is not carefully controlled. Molten pool geometries are most commonly monitored with the use of high speed cameras to capture many successive images in a short amount of time. The large amounts of data for accurate measurements require highly efficient and powerful computing for real-time feedback of the process. Also, digital cameras are only capable of offering a view of the surface geometry of the molten pool, which is often insufficient when attempting to control the process.

Other possible monitoring techniques involved the detection and measuring of process features other than temperature and pool geometry. For example, Barua et al. [286] used a camera setup calibrated to measure surface temperatures with a goal to detect defects such as porosity, lack of fusion or cracking. The idea was based on a predicted reference cooling curve for a defect-free build and any temperature deviation from the reference curve indicated a type of defect. The user was then notified of the possible defect, which could help to halt the process saving time and cost. Another measurement technique is through the use of laser displacement sensor which calculates distance from the sensor to a surface based on the time between sending and receiving a signal. Heigel et al. [285] used a laser displacement sensor for *in-situ* distortion measurements and coupled their readings with thermal measurements and a thermo-mechanical FEA model. Other works [287–289] have used displacement sensors to monitor layer height during laser-based DED.

Complete process control can be broken down into process monitoring and dynamic responses to changing conditions. Alone, process monitoring can provide invaluable data to be analyzed after deposition to validate models and establish trends in response to different variables. However, to fully control the AM process, monitoring techniques need to be coupled with appropriate models to utilize the data and accurately change process parameters to compensate for the dynamically changing measurements [290]. Significant efforts [291,292] have already been made using closed-loop feedback to control certain process variables. However, often these studies are limited to the effect of only one process parameter. There is a need for a comprehensive capability of reading and interpreting useful process related feedback in order to adjust process variables for achieving high quality parts. As computing capabilities rise and the understanding of the physical processes of AM is advanced, the feasibility of such a model will become within reach.

### 3. Structure

Since many AM methods use heat sources identical to traditional welding processes such as arcs, lasers and electron beams, they often produce structures closely resembling those in multipass welds. Process-structure-property relationships are available for the welding of several alloys [210,293,294], and these are of interest in the AM of metallic materials. However, there are occasions whereby AM produced structures differ from traditional welds due to the precision and flexibility provided by rapid beam scanning that some AM processes possess, allowing additional layer-by-layer control of the structures that form. In the following sections, the variables that control the solidification structure, the grain structure, the macroscopic texture, and the microstructure of AM components are discussed in detail and compared with conventional welding methods where appropriate. Other important structure-related aspects of AM, such as residual stresses and distortion, are addressed in a previous section of this review.

#### 3.1. Solidification structure

The grain structure and crystallographic texture of a component depend on the melting and solidification of the melt pool. The melt pool dissipates heat into the substrate, creating a curved melt pool shape. The shape varies with processing parameters and can be oval or tear-dropped on the top surface, and semicircular or keyhole in cross section depending on the heat source intensity and scanning speed [210,293–295]. The geometric features of the melt pool are important as they affect the shape of the subsequent grains that form in the fusion zone and the local solidification rate. In keyhole mode operation, which is often desirable in welding, the beam penetrates deeply into the metal substrate with minimal heat input to the part [295]. This geometry is known to change to conduction mode at high speeds for both electron beam [73,296] and laser beam processes [181,182]. The conduction mode is more desirable for AM since unstable keyhole can produce unwanted porosity in AM components. The importance of the geometric shape of melt pools to create effective AM builds is often overlooked,

and is an important consideration when developing AM processes to create the desired structural features [297,298]. In this section, nucleation and growth of solidification structures during AM are reviewed. Additionally, key parameters in determining the solidification microstructure are discussed including the important effects of temperature gradient  $G$ , solidification rate  $R$ , and undercooling  $\Delta T$  on the resulting AM microstructures.

### 3.1.1. Nucleation

In most AM processes, the layer-by-layer process deposits metal that has the same chemical composition as the previous layer. Under these circumstances nucleation of a new phase is not required for the metal to epitaxially regrow from the existing substrate since both will have the same crystal structure [210,293]. AM fabrication with identical or similar metals, and welding, require only epitaxial growth from the substrate. This eliminates the need for nucleation and allows growth to occur spontaneously with no activation energy barrier as long as the temperature drops below the liquidus. However, there are times when dissimilar metals may be deposited by AM, such as laser surface cladding [299–301] or fabrication of functionally graded composites [302,303], where nucleation at the melt pool boundary may be required. This may also be the case when producing the first AM layer on a dissimilar metal support structure. In these circumstances, nucleation of a new phase may be required before growth of this new phase can occur in the melt pool, depending on the similarities in the depositing metal and the substrate metal crystal structures [304,305]. If nucleation is required at the liquid/solid interface, the new phase will have to overcome an energy barrier which may ultimately affect the microstructure and mechanical properties of the component [304,305].

### 3.1.2. Growth

Growth occurs during solidification from previously deposited AM layers, and ultimately determines the crystallographic nature of the AM structure through partial or complete melt-back of the previously formed underlying layer [306]. Increased heat intensity will penetrate further into previous layers, and the remelting of previous layers is necessary to fabricate high quality AM components because it removes surface contaminants, breaks down oxide films, and provides a clean solid-liquid interface at the atomic level [307].

During solidification, the structure near the melt pool boundary is dominated by the base metal [188,210,308]. However, further away from the melt boundary, the microstructure is dominated by competitive growth [210,309]. Fig. 24 shows the competitive growth during DED-L of an aluminum alloy with unidirectional scanning pattern for thin wall deposition [310]. Competitive growth phenomena have also been observed in many other alloy systems such as iron based alloys [311,312], nickel based alloys [304,305], titanium based alloys [25] and tantalum [313].

Competitive growth occurs among dendrites with various crystallographic orientations in the polycrystalline materials [210,308]. Dendrites with easy-growth directions aligned closely with the maximum heat flow direction at the solid-liquid interface achieve competitive growth during the solidification process. The easy growth directions for materials with various crystal structures are presented in Table 10 [210]. It shows that the preferred crystallographic directions for solid-

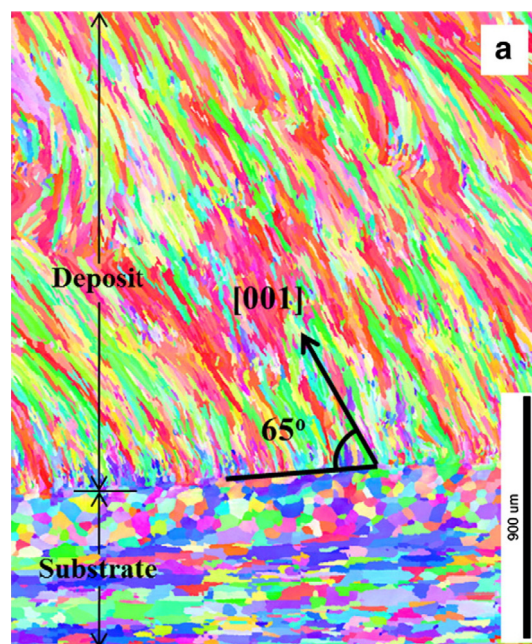


**Fig. 24.** Competitive growth shown in the longitudinal plane of the sample made by DED-L with Al-11.28 Si deposited on Al 7475 substrate [310].

**Table 10**

Easy growth directions for materials with various crystal structures [210].

Crystal structure	Easy-growth direction	Examples
Face-centered-cubic (fcc)	$\langle 1\ 0\ 0 \rangle$	Aluminum alloys, austenitic stainless steels
Body-centered-cubic (bcc)	$\langle 1\ 0\ 0 \rangle$	Carbon steels, ferritic stainless steels
Hexagonal-close-packed (hcp)	$\langle 1\ 0\ \bar{1}\ 0 \rangle$	Titanium, magnesium
Body-centered-tetragonal (bct)	$\langle 1\ 1\ 0 \rangle$	Tin

ification are  $\langle 1\ 0\ 0 \rangle$  for face centered and body centered cubic materials. Therefore, in such polycrystalline specimens containing randomly oriented grains, preferred growth during solidification occurs when the base metal grains oriented along  $\langle 1\ 0\ 0 \rangle$  directions grow along the maximum heat flow direction. The heat flow direction at the solid/liquid interface is dependent on the local curvature of the boundary of the melt pool. Columnar structures are developed when dendrites that are more aligned with the temperature gradient outgrow slower growing misaligned dendrites [95,96,297,298].

The competitive growth among dendrites with various crystallographic orientations can be quantitatively examined as well. The angular relationships between the scanning velocity, the solidification interface normal and the dendrite growing direction are schematically represented in Fig. 25 [314]. The direction of heat flow at any point on the solidification surface is normal to the surface, which can be given by [315]:

$$\nabla T = \frac{\partial T}{\partial x} i + \frac{\partial T}{\partial y} j + \frac{\partial T}{\partial z} k \quad (22)$$

where  $T$  is temperature and  $i, j$  and  $k$  are unit vectors in the scanning, width and vertical directions, respectively. The temperature gradient,  $G$ , can be calculated by [315]:

$$G = \|\nabla T\| \quad (23)$$

which is the magnitude of  $\nabla T$ . The angle,  $\theta$ , between the heat flow direction and the scanning direction can be calculated from the following relation [315]:

$$\cos \theta = \frac{\frac{\partial T}{\partial x}}{\sqrt{\left(\frac{\partial T}{\partial x}\right)^2 + \left(\frac{\partial T}{\partial z}\right)^2}} \quad (24)$$

The normal solidification velocity  $\vec{V}_n$  at the solid-liquid interface is geometrically related to beam velocity  $\vec{V}_b$  [315–317]:

$$|\vec{V}_n| = |\vec{V}_b| \cdot \cos \theta \quad (25)$$

The relationship between the growth velocity  $V_{hkl}$  of the dendrite tip along a specific crystallographic direction  $[h\ k\ l]$  and the normal solidification velocity  $V_n$  is given by [315–317]:

$$|\vec{V}_{hkl}| = \frac{|\vec{V}_n|}{\cos \psi} = |\vec{V}_b| \cdot \frac{\cos \theta}{\cos \psi} \quad (26)$$

where  $\psi$  is the angle between the normal to the solidification interface and the preferred  $[h\ k\ l]$  crystallographic direction. Eq. (26) indicates that the dendrites may have a misorientation  $\psi$  between its crystallographic direction and the maximum

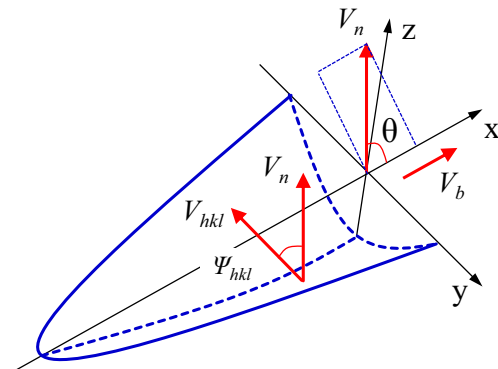


**Fig. 25.** Schematic representation of the angular relationships between the scanning velocity  $V_b$ , the solidification interface normal  $V_n$  and the dendrite growing direction  $V_{hkl}$ .

heat flow direction which is represented by  $\vec{V}_n$ . The misorientated dendrite trunks must have a velocity  $V_{hkl}$  higher than  $\vec{V}_n$  in order to keep up with the solidification interface of the melt pool. Therefore, they are characterized by a slightly larger undercoolings and thus lie behind the better orientated dendrites. This small lag will cause the misorientated dendrites to be out-grown by those having a better orientation [308].

In summary, the growth direction and velocity of the solidification structure of the AM component are dependent on both crystallographic orientation and local heat flow direction. The competitive growth among dendrites with various crystallographic orientations plays an important role in demining the final solidification structure.

### 3.1.3. Key parameters in determining the solidification structure

AM is a complex process with numerous processing parameters involved such as the scanning speed, the power, spot size of the heat source, powder size distribution, and powder flow rate (DED) or powder layer thickness (PBF), etc. In addition, for powder bed AM processes, the scanning strategy, or melt pool path, is an important and often underappreciated variable that affects the final integrity of the component [318]. The solidification microstructure of various depositing materials for a given set of AM parameters is determined by several critical parameters, which are the temperature gradient G, solidification rate R and undercooling  $\Delta T$  [319].

**3.1.3.1. Solidification map.** A solidification map is constructed using G and R in their combined forms of GR and G/R. The ratio G/R determines the mode of solidification while the product GR governs the scale of the solidification microstructure [319]. Fig. 26 illustrates the effect of G/R and GR on the solidification microstructure [210]. The solidification microstructures can be planar, cellular, columnar dendritic or equiaxed dendritic with decreasing G/R values. The dimension of all the four solidification microstructures decreases with increasing cooling rate GR. Solidification maps for particular alloys can be used to judge what structures can form during solidification. Fig. 27 presents solidification maps for Inconel 718, Inconel 690, and Ti-6Al-4V [320–322].

Significant effort has been made to study the evolution of solidification structure guided by the solidification maps, especially for single crystal nickel based alloys [299,317,323–341]. The targeted solidification microstructures during AM of single crystal alloys are aligned columnar dendrites epitaxially growing from the single crystal substrate, without the formation of equiaxed dendrites. A single crystal deposit formed through an additive process can be characterized by several microstructural parameters such as the solidification growth rate and temperature gradient. Depending on the values of these parameters, the solidification structure may change from columnar to equiaxed, undergo the oriented-to-misoriented transition or form stray grains [306,307,326,333,334,338–342]. Desired solidification microstructures can be obtained by referring to the solidification maps with known temperature gradient G and solidification rate R.

The most widely observed solidification microstructures in the AM components are columnar and equiaxed structures. Under certain solidification conditions, the growth of columnar structure is terminated with the formation of equiaxed structure. The CET occurs when nucleation of sufficiently numerous equiaxed dendrites takes place in the constitutionally undercooled liquid adjacent to the columnar dendritic front [343]. Efforts have been made to quantitatively predict CET for various alloys [317,323–325,344]. For example, a microstructure selection map of superalloy CMSX-4 for a nuclei density  $2 \times 10^{15}/\text{m}^3$  was built to predict the formation of columnar and equiaxed structure [343]. It should be noted that CET is critical to the quality of the single crystal deposit because it limits the height of columnar dendrites growth.

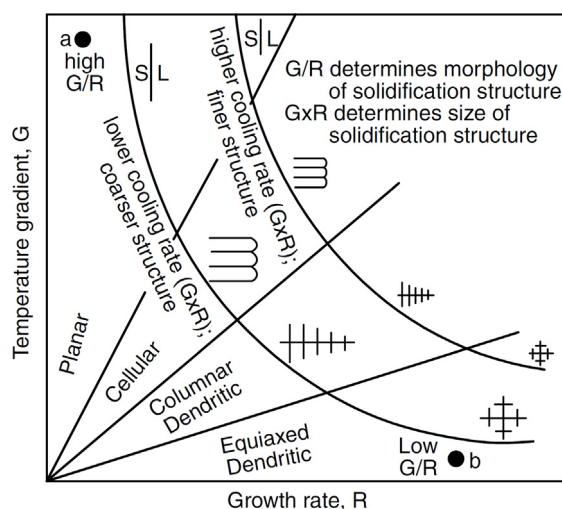


**Fig. 26.** Effect of temperature gradient G and growth rate R on the morphology and size of solidification microstructure [210].

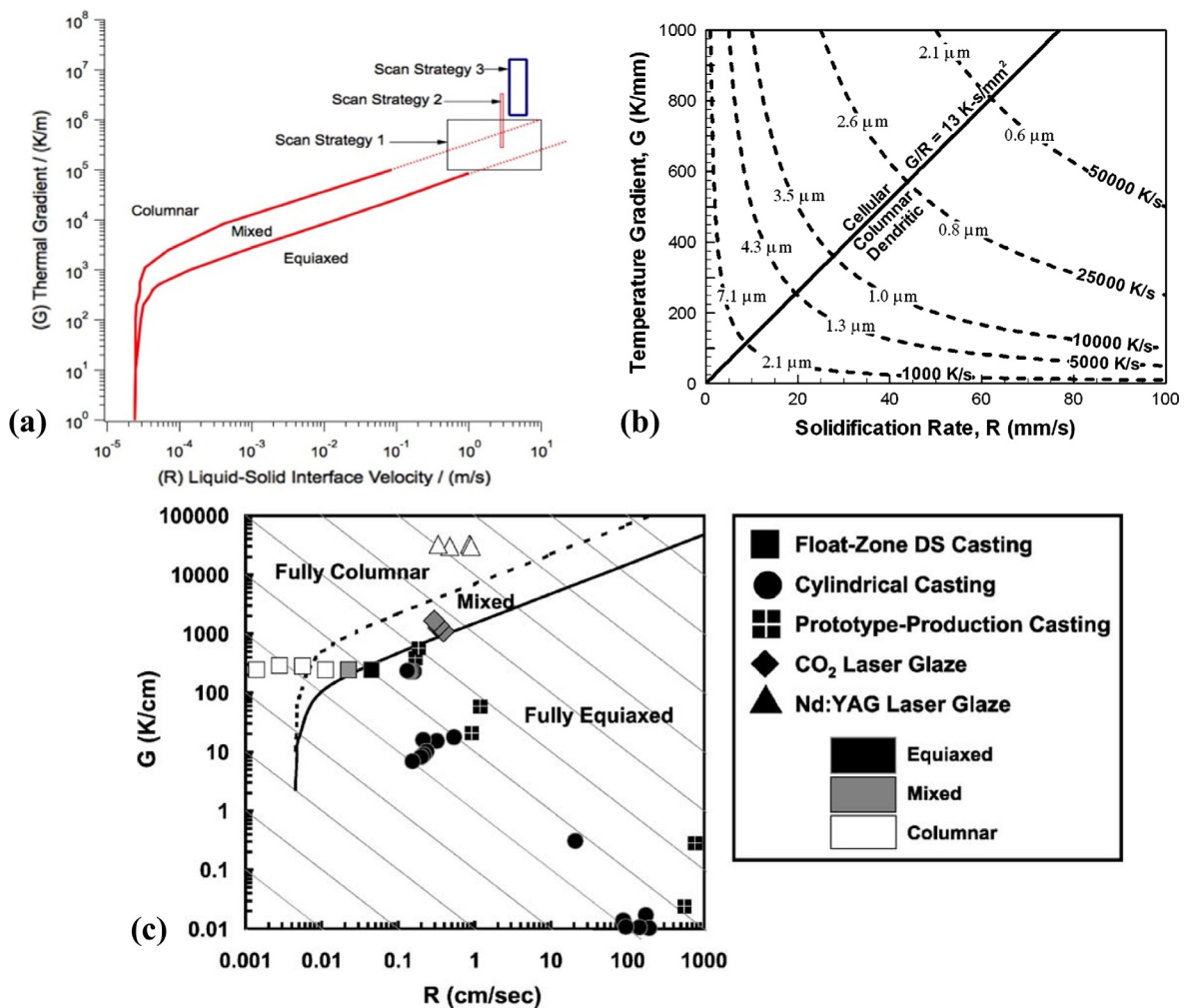


Fig. 27. Solidification maps for several widely used alloys, (a) IN 718 [379], (b) IN 690 [321], (c) Ti-6Al-4V [320].

The scale of the solidification structure can be predicted in terms of the cooling rate GR. For example, the secondary dendrite arm spacing of the columnar and equiaxed dendrites can be correlated with the cooling rate or solidification time, which can be expressed as [210,345]:

$$d = at_f^n = b(\varepsilon_c)^{-n} \quad (27)$$

where  $t_f$  is local solidification time,  $\varepsilon_c$  is cooling rate, and  $a$ ,  $b$  and  $n$  are material specific constants. Eq. (27) indicates that coarser dendritic structures are produced by lower cooling rate and longer growth time. Since smaller dendrite arms have more surface area per unit volume, the total surface energy of the solidifying material can be reduced if larger dendrite arms grow at the expense of the smaller ones [210]. The slower the cooling rate during solidification, the longer the time available for coarsening and the larger the dendrite arm spacing. Similarly, the higher the cooling rate, the finer the cellular structure [210].

**3.1.3.2. Undercooling.** The driving force for dendrite growth is provided by undercooling. The difference between the equilibrium liquidus temperature and local dendrite tip temperature is the total undercooling, which can be divided into four parts [96,210]:

$$\Delta T_{tot} = \Delta T_C + \Delta T_T + \Delta T_K + \Delta T_R \quad (28)$$

where  $\Delta T_C$ ,  $\Delta T_R$ ,  $\Delta T_T$  and  $\Delta T_K$  are the undercooling contributions associated with solute diffusion, thermal diffusion, attachment kinetics and solid-liquid interface curvature, respectively. For most metallic alloys, when solidified under normal solidification conditions,  $\Delta T_T$ ,  $\Delta T_K$  and  $\Delta T_R$  are small and solute undercooling  $\Delta T_C$  predominates. Solute undercooling is also expressed as constitutional supercooling in the literature. The variation of solidification microstructure from planar to cel-

lular, columnar dendritic or equiaxed dendritic is essentially due to the increase in constitutional supercooling at the solidification interface.

The growth kinetics of both columnar and equiaxed morphologies can be calculated using the KGT model [319] or Hunt's model [346]. Fig. 28 shows the correlation between undercooling and dendrite growth velocity for IN718 [347] calculated from the KGT model. It can be observed that undercooling significantly increases with dendrite growth velocity. The undercooling is about 50 K/s for the dendrite growing at the heat source scanning velocity of 20 mm/s.

In summary, despite the complexities of AM, the solidification structure is mainly determined by a few key parameters which are the temperature gradient  $G$ , solidification rate  $R$ , and undercooling  $\Delta T_{\text{tot}}$ . Efforts to correlate the processing parameters with these key solidification parameters can efficiently promote the understanding of the relationship between process and structure.

In addition to the dendritic microstructure discussed above, the solidification microstructure can consist of a substantial amount of precipitates especially for those precipitation-strengthened alloys (e.g., Ni-base superalloys). This is largely due to the rapid cooling in the highly localized melt pool, resulting in a non-equilibrium solidification condition during AM. Unlike equilibrium solidification conditions, diffusion in the solid is rather limited under non-equilibrium solidification conditions. In other words, there is insufficient time for solute alloying elements such as Nb and C, partitioned into the liquid, to re-diffuse back into the solid. As the concentration of these alloying elements rises in the remaining liquid, eutectic solidification can occur near the terminal stage of solidification, forming precipitates such as NbC and Laves ( $\text{Ni}_2\text{Nb}$ ). For instance, Laves phase and Nb-rich MC carbides are commonly observed at the interdendritic regions due to micro-segregation of these solute elements during various AM processing of nickel alloy IN718 [348–351]. Finally, the solidification sequence and products under the non-equilibrium condition can be readily described by the Scheil theory [210], which is implemented in several commercial computational thermodynamics codes such as Thermo-Calc<sup>®</sup> and Pandat<sup>TM</sup>.

### 3.2. Grain structure

The grain structure formed during solidification significantly affects its resistance to solidification cracking and mechanical properties. Grains are the coarsest microstructural features that need to be considered [8]. Significant effort has been made to study the evolution of grain structure during AM [4,25,34,300,315,324,325,329,352–380]. In this section, the direction and velocity of grain growth, as well as the size and morphology of grains are discussed. Furthermore, the evolution of grain structure in various conditions is briefly described.

#### 3.2.1. Grain growth direction

**3.2.1.1. Experimental observations.** The direction of grain growth may closely align with the  $\langle 0\ 0\ 1 \rangle$  build direction, especially in the powder bed system which has fast scanning speed [180,376,381–383]. Nearly vertically oriented columnar grains in several alloy systems produced by PBF are shown in Fig. 29 [311,373,376]. In contrast, the direction of grain growth may significantly deviate from the build direction, which typically appears in DED process with low scanning speed [305,310,312,357]. Fig. 30 shows several examples of inclined columnar grains in various alloys by DED [305,312,351,384,385]. Curved columnar grains with a variety of orientations can be observed. In addition, these columnar grains do not align uniformly and grow through multiple layers like those in Fig. 29.

The orientation of the grain structure is affected by the shape and size of the melt pool. As discussed in a previous section, the geometry of the melt pool is determined by the process parameters, material properties, and cooling conditions. Fig. 31

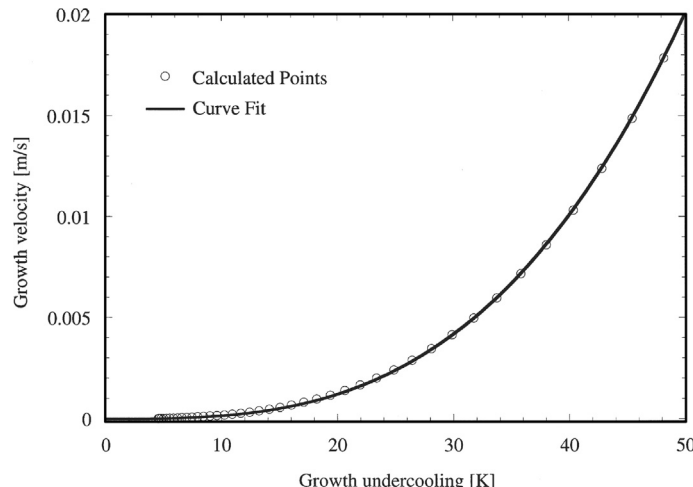


**Fig. 28.** Dendrite growth velocity as a function of undercooling for IN 718 [347].

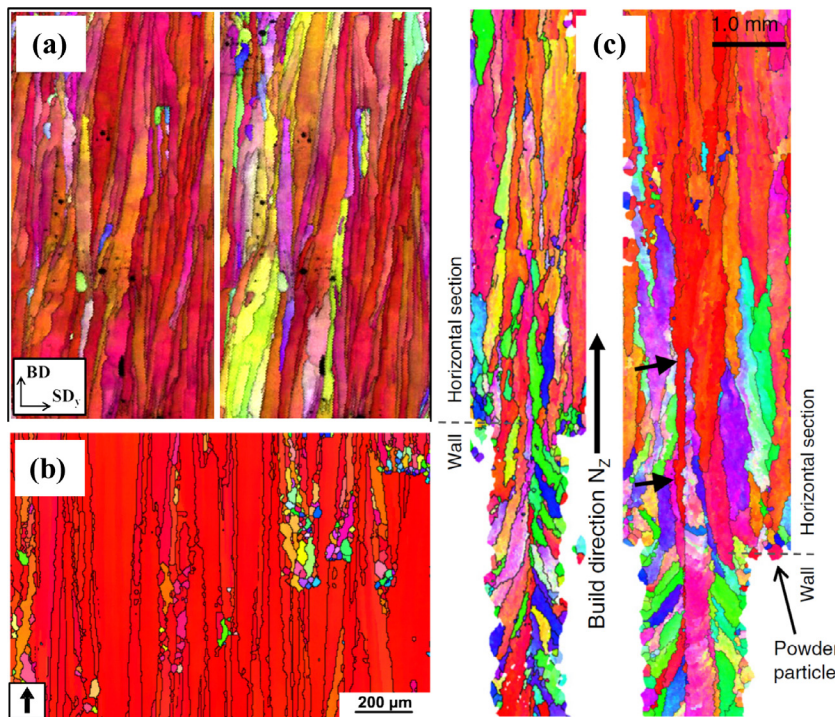


**Fig. 29.** Grain orientations closely aligned with the  $\langle 0\ 0\ 1 \rangle$  build direction in samples made by PBF. (a) high-silicon steel (6.9%wt Si) [311], (b) IN 718 [376], (c) Ti-6Al-4V [373].

shows the comparison of the shapes of the melt pools produced by PBF and DED, respectively [310,386]. It can be observed from Fig. 31(a) and (b) that the shape of the melt pool during PBF resembles the appearance of a “long river” with high length to depth ratio. The grains that grow at high melt pool speeds in this process are fairly straight. On the contrary, the melt pools produced during DED generally resembles the shape of a “localized puddle”, as shown in Fig. 31(c) and (d), which has comparable length and depth. This shape of the melt pool creates longer and more curved columnar grains as a result of the geometric curvature of the weld pool itself [297,298,387].

**3.2.1.2. Mechanism.** The striking differences in the shapes of the melt pools produced by PBF and DED result in the significantly different grain orientations demonstrated in Figs. 29 and 30. Typically, columnar grains grow from the boundary towards the center of the melt pool along location dependent directions during solidification. For polycrystalline materials, the grain growth direction is parallel to the maximum heat flow direction which is normal to the solidifying surface of the melt pool [210,297].

The melt pool is long and shallow during PBF, which indicates that the solidification involves downwards heat flow at the melt pool boundary, opposite to the build direction. In contrast, the comparatively short and deep melt pool during DED is characterized by an obvious curvature at its trailing edge. The heat flow directions in such a case are significantly affected by the local positions at the melt pool boundary. Fig. 32(b) and (c) schematically illustrate the development of columnar grains in the central longitudinal plane of the melt pool in these two significantly different melt pools.

Fig. 32(a) shows that for the case shown in Fig. 31(a) and (b), the bottom of the melt pool is nearly horizontally oriented due to the fast scanning speed. Thus, the columnar grains epitaxially grow from the previously deposited layer, along the build direction which is perpendicular to the bottom of the melt pool. The columnar grains grow as the bottom of the melt pool moves upwards during the subsequent cooling process. Therefore, the grain structure attained in the central longitudinal plane is analogous to that by directional solidification [388].

Unlike the location independent direction of grain growth shown in Fig. 32(a), the local growth direction shown in Fig. 32(c) is spatially variable with the movement of the weld pool, depending on the 3D temperature gradients which affects the local curvature of the solidification interface [297]. The columnar grains grow continually by shifting their direction of growth to align with the temperature gradient [309]. Thus macroscopically, it appears that the curved columnar grains are “pulled” by the curvature of the trailing edge of the melt pool [297]. Geometrically in the 3D space, the columnar grains appear perpendicular to the local curvature of the melt pool boundary. The grain structure attained in this process is similar to that formed in the fusion welded component [297].

The melt pool shape illustrated in Fig. 32(a) is an extreme condition in which very fast scanning speed, 1.4 m/s, was used. There are intermediate melt pool shapes, e.g. Fig. 32(b), between the melt pools shown in Fig. 32(a) and (c) when slower

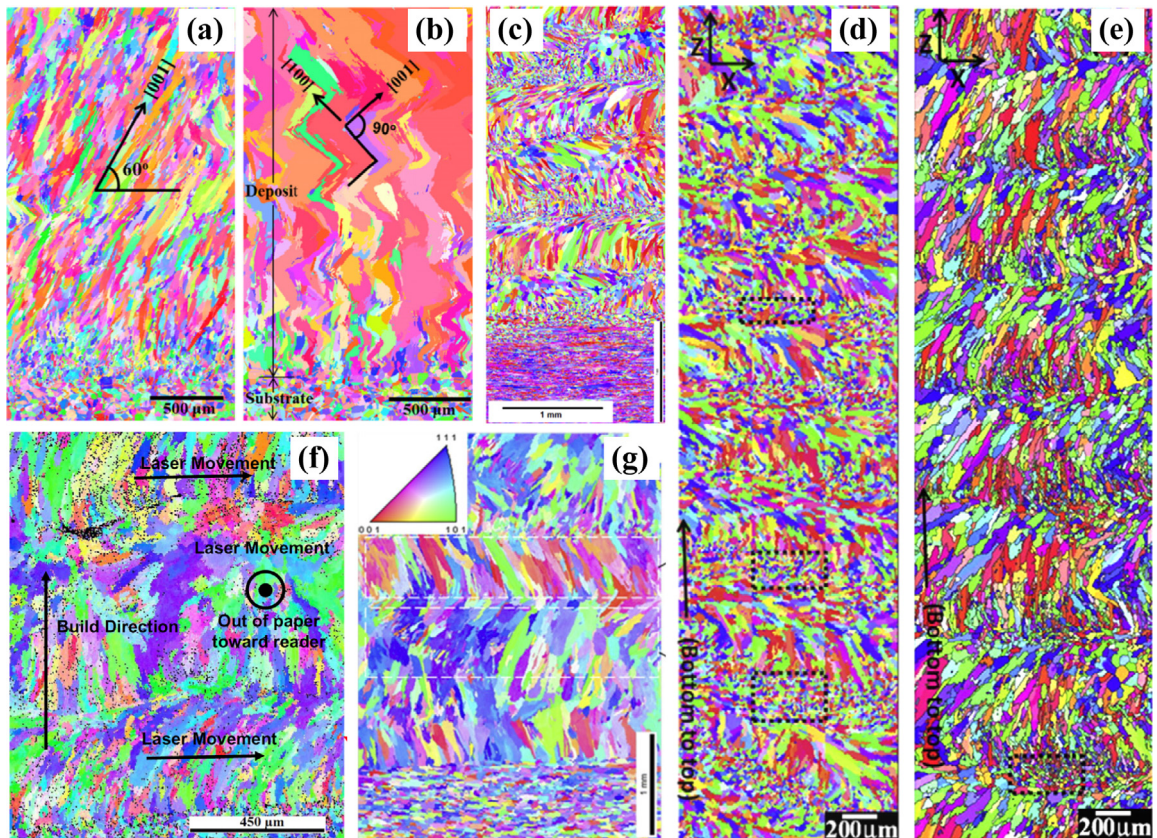


**Fig. 30.** Grain orientations significantly deviated from the  $\langle 0\ 0\ 1 \rangle$  build direction in samples made by DED. (a) IN 718 by unidirectional laser scanning [305], and (b) IN 718 by bidirectional laser scanning [305]. (c) Cu-38Ni alloy [439], (d) IN 718 by unidirectional laser scanning [351], (e) IN 718 by bidirectional laser scanning [351], (f) 316L stainless steel [312], (g) Al 4047 alloy [384].

scanning speeds are used. The maximum heat flow direction at the melt pool boundary is close to the build direction for the conditions shown in Fig. 32(b), which may have a deviation angle less than 10°. The grain growth directions in such case follow the maximum temperature gradient and tilt in the laser scanning direction, with an example found for Ti-6Al-4V by PBF [188].

The selection of the cross section, i.e. longitudinal, transverse and horizontal planes, matters for the observation of melt pool shape and grain structure. An example is shown in Fig. 33 for the predicted melt pool shape of Ti-6Al-4V by PBF-EB [373]. In this process, the high scanning velocity ( $\sim 1$  m/s) and small beam diameter ( $\sim 100$   $\mu$ m) lead to highly elongated melt pools typically with length to width aspect ratio of the order 5:1 and length to depth ratio of 20:1 [188,373,389]. Although the melt pools shown in Fig. 31(a) and (b) are highly elongated in the horizontal and longitudinal sections, the transverse section of the melt pool still shows highly localized hemisphere shape. The melt pool shape and the grain structure in the transverse section are shown in Fig. 34 [386]. The resulting directions of the columnar grains are perpendicular to the boundary of the melt pool.

Note that the subgrain structure such as the columnar dendrites grows only along several easy growth directions. As indicated in Table 10, the easy growth directions are the  $\langle 1\ 0\ 0 \rangle$  directions for cubic materials such as stainless steels, aluminum and nickel based alloys and the  $\langle 1\ 0\ \bar{1}\ 0 \rangle$  directions are for hexagonal close packed materials such as magnesium and titanium based alloys. In other words, the growth direction of a selected columnar dendrite try to follow the temperature gradient as shown in the pattern illustrated in Fig. 32(c).

The shape of the melt pool is typically depicted by the liquidus isotherm. As discussed in the previous section, undercooling plays an important role in crystal growth as the driving force during solidification. Thus theoretically, the solid/liquid interface represented by the dendrite tips deviates from that determined by the liquidus isotherm of the bulk alloy due to microsegregation of alloying elements, constitutional undercooling, and by dendrite tip undercooling which is a function of growth velocity. However, as the temperature gradient is high during AM, on the order of 500 K/mm [79,92], the segregation of alloying elements is limited to locations close to the L/S interface and the influence of undercooling on the exact position of the solidification front may be neglected. In addition, columnar grains closely align to the normal of the melt pool boundary in systems where no significant undercooling occurs such as pure metal.

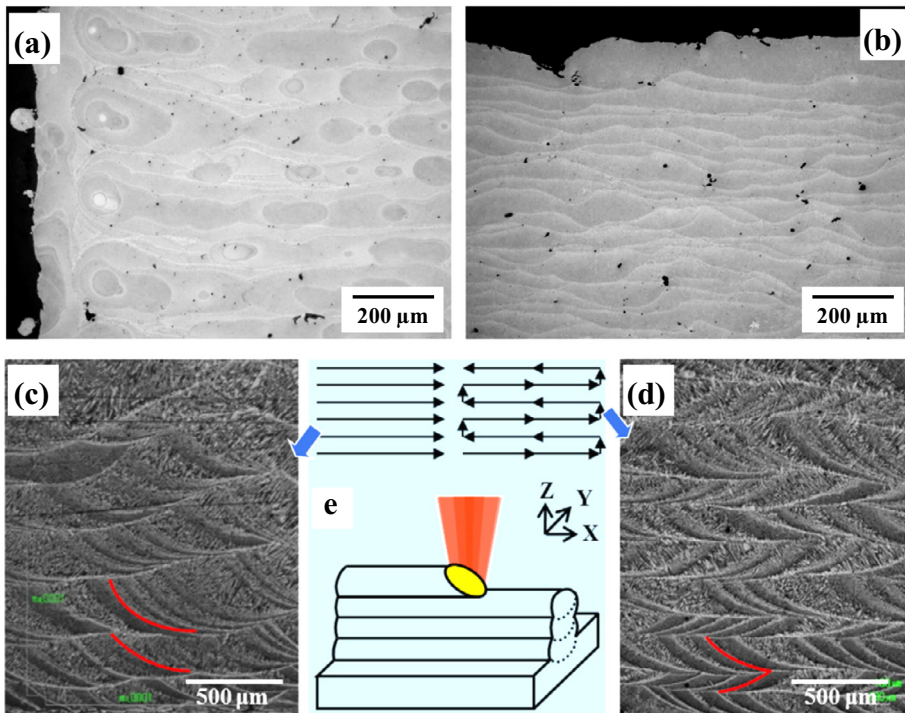


**Fig. 31.** Comparison of the shapes of the melt pools produced by PBF-L and DED. (a) and (b): top and side views of a AlSi10Mg sample produced by PBF-L, respectively [386]. (c) and (d): side view of two Al4047 samples made by DED-L with unidirectional and bidirectional scanning strategy, respectively [310].

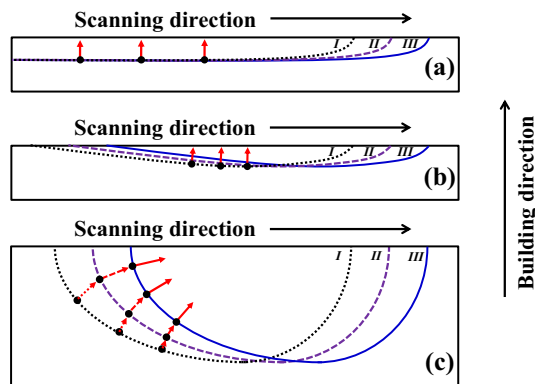


**Fig. 32.** Schematic illustration of the growth direction of the columnar grains in the longitudinal plane of the melt pool. (a) vertical grain orientation which is location independent typically in PBF, mimic shape of the melt pool shown in Fig. 33(a) and (b), (b) nearly vertical grain orientation originates from the long and shallow melt pool, typically in PBF, (c) inclined grain orientations which are location dependent typically in DED. The curves marked with I, II and III represent the melt pool boundaries at three different locations along the scanning direction.

The incremental development of the columnar grains may not always follow the normal to the curved surface determined by the liquidus isotherm when the actual solidifying surface significantly deviates from the liquidus isotherm due to the influence of undercooling. Fig. 35 shows an example of the effect of undercooling on the grain growth directions [390] where noticeable discrepancies exist between the actual solidifying surface and the liquidus isotherm in systems where significant undercooling occurs. Prominent deviation of the actual solidifying surface from the liquidus isotherm can be observed, which further increases with scanning speed. However, the extent of the deviation caused by undercooling needs to be carefully examined for the specific solidification conditions.

In summary, the orientations of the grains in polycrystalline materials are dependent on the shape of the melt pool which is determined by the AM process parameters and the thermo-physical properties of the material being deposited.

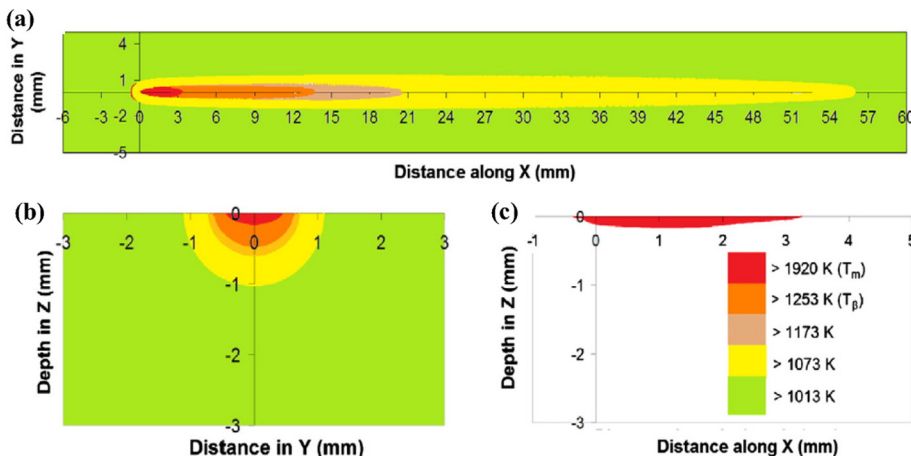


**Fig. 33.** The melt pool shape predicted for the PBF-EB [373]. (a) temperature field of the horizontal top surface, (b) temperature field of the transverse cross section at the maximum melt pool width, with (c) melt pool shape in the central longitudinal plane.

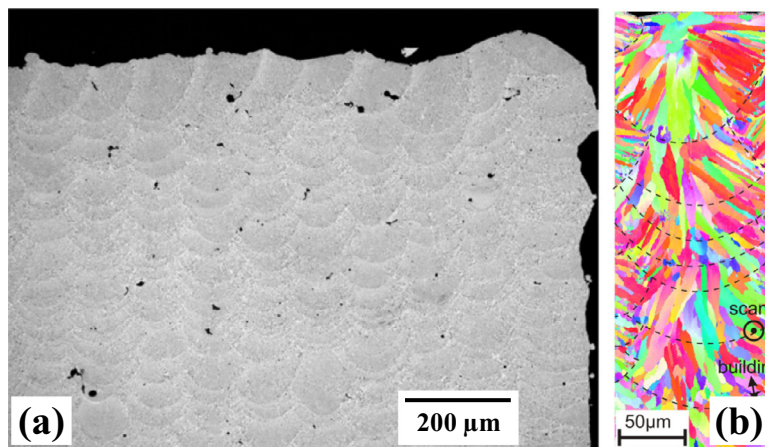


**Fig. 34.** Shape of the melt pool and the corresponding grain structure in the transverse section of a AlSi10Mg sample produced by PBF-L [386].

### 3.2.2. Grain growth rate

The motion of the melt pool determines the grain growth rate which depends on both the scanning speed and the location at the melt pool boundary. The local grain growth speed can be expressed by Eq. (25). Fig. 36 shows that the local grain growth rate,  $R$ , depends on the location and scanning speed [297]. It can be observed that  $R$  is zero on the edge of the melt pool, and that  $R$  increases as the grains grow towards the centerline of the melt pool. In addition,  $R$  increases as the scanning speed is increased [297].

For AM processes operated at low and moderate scanning speeds, the shape of the melt pool is close to elliptic [305,310]. The maximum rate of grain growth appears at the centerline of the melt pool where the angle between the scanning direction and solidification direction,  $\theta$ , is 0 according to Eq. (25). Thus,  $\cos \theta$  equals to 1 and the maximum rate of grain growth equals to the scanning speed. However, the shape of the melt pool may be substantially elongated at high scanning speeds [309]. The typical scanning speed for PBF is on the order of 1 m/s which is much faster than DED with typical scanning speed of 10 mm/s. The maximum rate of grain growth in PBF occurs at the centerline of the melt pool, is smaller than the scanning speed because  $\theta$  is greater than 0 and  $\cos \theta$  is smaller than 1. Therefore, the progress of the solidification front cannot match the scanning speed, which results in significantly elongated melt pool. When comparing welds to AM processes, welds typically operate at slower speeds, and have oval or slightly tear-dropped shape fusion boundaries on the top surface of the plate. This is also the case with DED AM and wire-based AM processes. However, the molten pool in PBF based processes tends to be much more elongated to avoid keyholing that can create AM defects and to reduce processing time for economic reasons. Therefore, the extent of the deviation of the solidification rate along the centerline of the melt pool from the scanning speed is strongly dependent on the thermo-physical properties of the material [309] and the AM processing parameters.

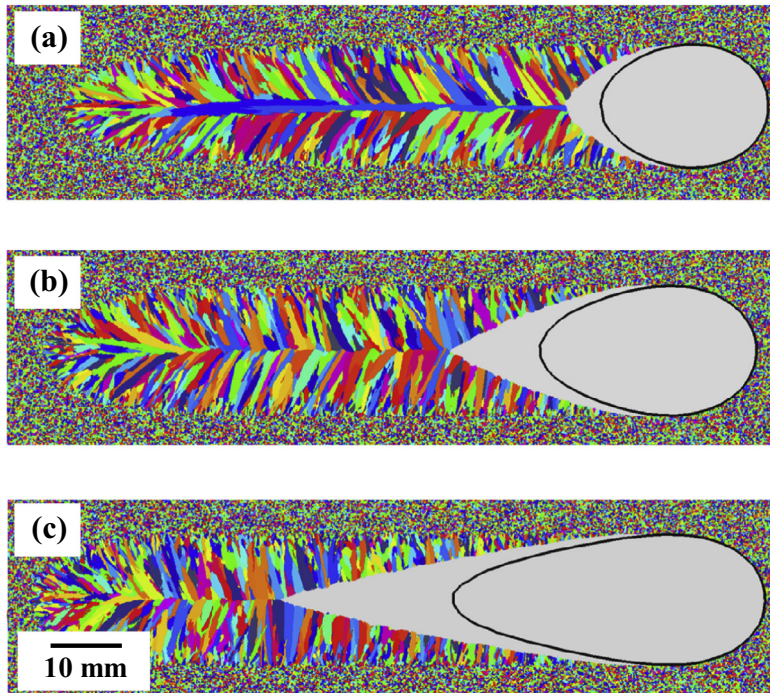


**Fig. 35.** Effect of undercooling on the grain structure [390]. Scanning speed (a) 1 mm/s, (b) 2 mm/s, and (c) 5 mm/s.

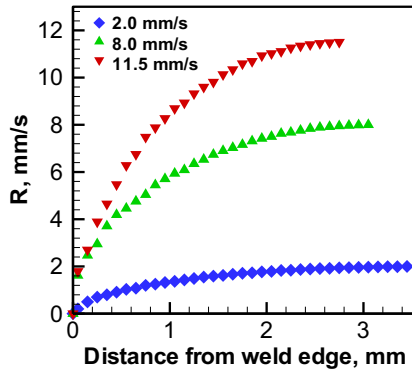


**Fig. 36.** Grain growth rate  $R$  as function of scanning speed and location at the melt pool boundary [297].

### 3.2.3. Grain size and morphology

**3.2.3.1. Grain size.** The size of the grains in the additive manufactured components is affected by several factors. Cooling rate is one of most important variables in determining the grain size. Finer grain structure is obtained from higher cooling rates because shorter growth times are available for the growth of the grains, and vice versa. As discussed in the process section, cooling rate decreases as the layer height increases [79,92]. Thus, grain structure becomes coarser in the upper layers due to lower local cooling rate than those in the lower layers [357]. Another important factor affecting the grain size is the scanning strategy. As mentioned before, epitaxial growth and competitive growth of the columnar dendrites occur during solidification of AM. The result from continuously competitive growth is fewer number and larger size of the grains [305,373].

**3.2.3.2. Grain morphology.** Columnar grains and equiaxed grains have been widely observed in the solidified region of components made of titanium-based, iron-based and nickel-based alloys [25,312,351,354]. The columnar grains are generally coarse and characterized by anisotropic mechanical properties. In contrast, equiaxed grains are usually small and with more uniform mechanical properties [297]. Profound anisotropy of mechanical properties originates from the aligned columnar grains oriented along certain directions. The anisotropy in mechanical behavior is detrimental for applications involving multidirectional stresses. Thus, attaining only aligned columnar grain structure is an inappropriate choice for fabricating

components with isotropic mechanical properties. On the other hand, the anisotropy can be significantly reduced with equiaxed grain structure or a mixture of equiaxed and columnar grain structures. Tensile strength and ductility decrease significantly when there are just columnar grains with their grain boundaries being perpendicular to the tension during tensile testing. The deposited metal is susceptible to solidification cracking when the orientation of the columnar grains near the track centerline is nearly parallel to the scanning direction. In contrast, the formation of equiaxed grains in the deposit can help reduce solidification cracking. Fine equiaxed grains can enhance mechanical properties such as improving the ductility and fracture toughness of the deposit.

As previously discussed, CET is unwanted during solidification of single crystal superalloy and the formation of equiaxed grains in AM components have been investigated [25,352,354,376,377,379,391–402]. However, in polycrystalline materials equiaxed grains are desired for obtaining isotropic structure and property. CET occurs under certain conditions [343,344]. Columnar grains commonly have planar, cellular or columnar dendritic substructures and equiaxed grains have equiaxed dendritic substructures [297,403]. Thus, equiaxed grains can be generated by promoting the formation of equiaxed dendrites. Similar to the CET for dendrites, CET for grains could be predicted using the solidification parameter, G/R, with solidification maps [297,354,379]. The G/R value decreases with higher scanning speed and the distance away from the melt pool boundary [297]. Furthermore, G/R decreases towards the upper layers, which indicates increasing instability of the solidification interface with progressive deposition of the build [79].

Generally, equiaxed grains are rare in polycrystalline materials processed by PBF due to the extremely high temperature gradient which is on the order of  $10^6$  K/m [79,92,313,373,386]. However, equiaxed grains may still form owing to constitutional supercooling near the solidification front [351,354] and heterogeneous nucleation on partially melted powders [25,373] or added refractory particles [159]. Fig. 37(a) and (b) shows the prediction of solidification parameters for grain morphology of IN718 in PBF-EB using point heat sources [354]. Highly misoriented equiaxed grains and oriented columnar grains in the same layer were produced through rapidly changing the scan strategy between continuous and pulsed heat sources by controlling the motion of the electron beam. It can be observed from Fig. 37(b) that the grain morphology is columnar as the melt pool begins to solidify and it moves towards the mixed region for columnar and equiaxed grains during solidification and results in a pure equiaxed region at the end of solidification. Fig. 30(d) shows the electron backscatter diffraction (EBSD) characterization results in the longitudinal plane where both columnar and equiaxed grains form during DED of IN718 [351]. These results show that equiaxed grains can be promoted in both the DED and PBF systems under appropriate processing conditions.

Fig. 38 shows a mixture of columnar and equiaxed grains in a Ti-6.5Al-3.5Mo-1.5Zr-0.3Si sample processed by DED [25]. The mixed grain structure results from the heterogeneous nucleation on partially melted powders for equiaxed grains and the epitaxial growth from the bottom of the melt pool for columnar grains [25]. Deep melt pool associated with low mass deposition rate favors the formation of large full columnar prior grains growing epitaxially from bottom of the melt pool. High mass deposition rate results in insufficient powder melting which leads to heterogeneous nucleation within the melt pool and thus promotes fine equiaxed prior grains.

Note that the most widely used titanium alloy, Ti-6Al-4V, does not produce equiaxed grains during AM. Typically planar growth is dominant in Ti-6Al-4V during AM, although the alloying elements are nearly 10 wt% and the solidification rates are extremely high [404]. This is because of the high partition coefficients of Al and V in Ti which are close to one [405]. It was suggested that the narrow solidification range from liquidus to solidus temperatures limits the degree of constitutional supercooling and nucleation of equiaxed grains ahead of the solidification front becomes very difficult [373].

In summary, the scale and morphology of the grain structure are highly dependent on the processing parameters of AM. Tailoring of the grain structure can be achieved by controlling the solidification parameters for specific alloys.

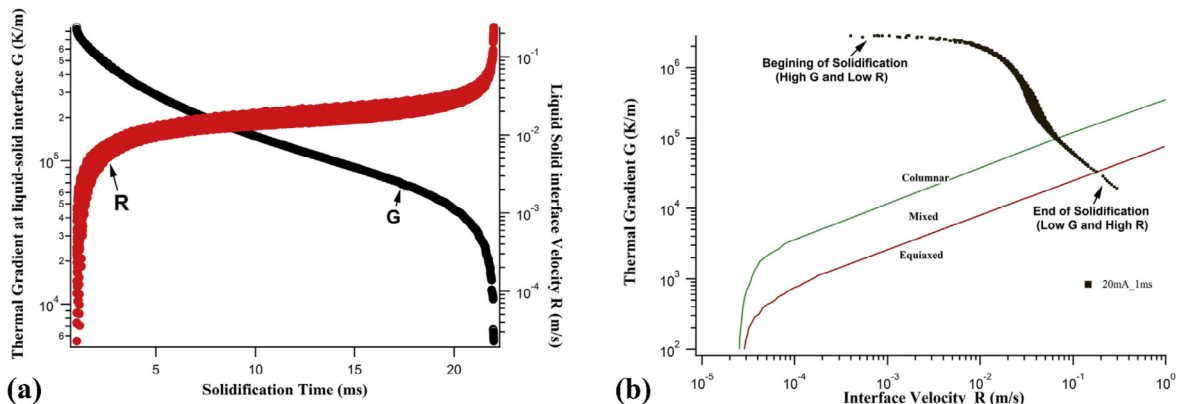


**Fig. 37.** Calculated solidification parameters for grain morphology of IN 718 in PBF-EB [354]. (a) Variation of temperature gradient  $G$  and liquid-solid interface velocity  $R$  with solidification time. (b) Solidification map of IN 718 with  $G$  and  $R$  superimposed, indicating the formation of columnar and equiaxed grains.

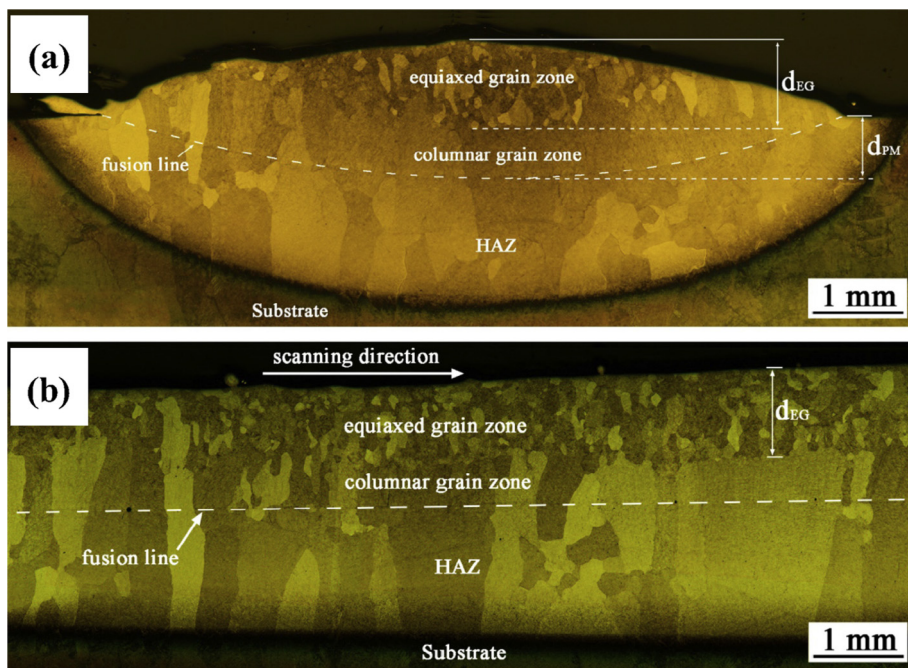


**Fig. 38.** Mixture of columnar and equiaxed grains in a DED sample of a Ti-based alloy in (a) transverse section and (b) longitudinal section [25].

### 3.2.4. Grain structures in miscellaneous conditions

Grain growth in high entropy alloys during AM [406] also follows the principles discussed above. Due to the similarities in the physical processes of welding and AM, solidification microstructures of high entropy alloy welds can be helpful [407]. Efforts have been made to further improve the grain structure by using additional processing steps such as hot isostatic pressing (HIP) and rolling [408,409]. HIP processing is designed to reduce pores and other defects present within the AM components. Sometimes HIP can also be combined with a post processing heat treatment schedule to do both at the same time. Flaws and defects at or open to the part surface will not close when using HIP and may contribute to the degradation of mechanical properties.

Additionally, microstructure refinement through recrystallization for various alloys has been studied [24,363,410–413]. Recrystallization through post processing heat treatment can promote the formation of refined equiaxed grain structure from the oriented grain structure of the as-deposited part. Unlike in plastically deformed specimens where the relief of stored internal strain energy causes recrystallization, the residual thermal stress accumulated from the repeated thermal cycles is the driving force for recrystallization in the AM component in the absence of cold work. Thus, the extent of recrystallization is dependent on the processing conditions such as heat input and overlap rate which affect the residual thermal stresses.

## 3.3. Texture

Components having the same shape and size made by different processing parameters may have strikingly different textures [188,305,310,351,386,412]. Since texture affects mechanical and chemical properties of the additively manufactured components, its control based on scientific principles is important for the serviceability of the fabricated parts [315]. Texture of various alloys processed by DED and PBF and the mechanisms for their formation are discussed in this section [8,117,365,414–437]. In addition, the influential factors for the formation of texture are also discussed.

### 3.3.1. Texture in PBF system

Strong  $\langle 0\ 0\ 1 \rangle$  fiber texture which is parallel to the build direction were observed for various alloys [311,318,373,376,383,386,421,431,438]. Fig. 39(a) shows the reconstructed  $\beta$ -textures for Ti-6Al-4V by PBF-EB [373]. Fig. 39(b) schematically illustrates the different surface  $\beta$ -grain structures generated by the contour pass and in-fill hatching within bulk sections [373]. The grain structures consist of coarse columnar grains parallel to the build direction, rather than being aligned with the curvature of the melt pool solidification front in individual beam tracks as shown in Fig. 29(c).

The formation of the texture shown in Fig. 39(a) originates from the fact that in bulk sections the grains grow up through many layers, which favors the development of a coarse grain structure that has a texture more optimized with the average growth conditions. The optimum grain growth direction is the build direction after several layers because the beam is scanned backwards and forwards and rotated by  $90^\circ$  each alternate layer [373].

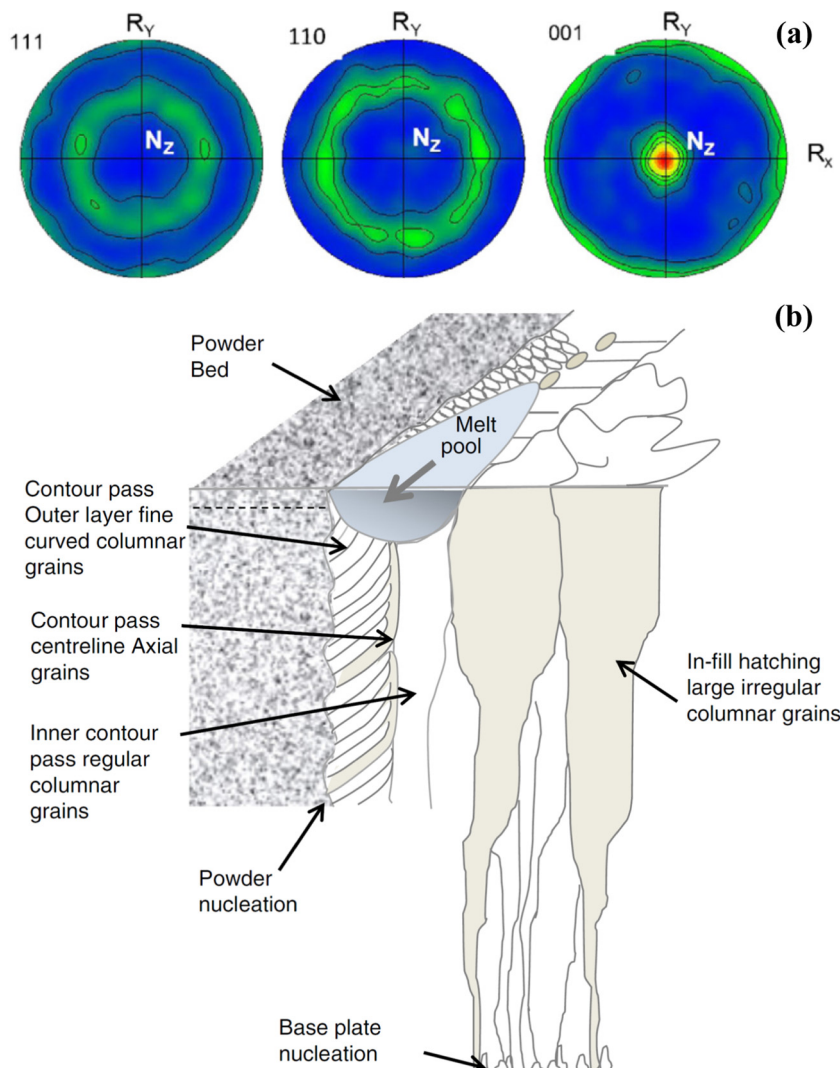


**Fig. 39.** (a) Pole figures depicting reconstructed  $\beta$ -textures for Ti-6Al-4V by PBF-EB [373]. (b) Schematic illustration showing the different surface  $\beta$ -grain structures generated by the contour pass and in-fill hatching within bulk sections [373].

The formation of the strong  $\langle 0\ 0\ 1 \rangle$  fiber texture is a compromised result of grain growth. If a grain grows in any one layer with an  $\langle 0\ 0\ 1 \rangle$  direction normal to the inclined melt pool surface it will be tilted away from the build direction by an angle  $\alpha$ . When the beam direction is reversed in the next layer it will be aligned further away from the maximum growth direction by  $2\alpha$  and thus less favorably orientated. Although grains with orientations closer to the maximum temperature gradient at the trailing edge of the melt pool may have a growth advantage in individual beam passes, they will be poorly aligned when the beam travel direction reverses or rotates. Thus, over many layers, grains aligned with  $\langle 0\ 0\ 1 \rangle$  direction parallel to the build direction will on average be more closely aligned to the maximum temperature gradient when the raster pattern is altered, and will dominate the texture [373].

### 3.3.2. Texture in DED system

The texture observed in IN718 by DED is shown in Fig. 40 [305]. Unidirectional laser beam scanning pattern developed a fiber texture while a backward and forward bidirectional scanning pattern developed a rotated cube texture in the deposit [305], as shown in Fig. 40(a) and (b), respectively.

The mechanism for the formation of the texture shown in Fig. 40(b) is analogous to that in Fig. 39(a). These textures are both compromised results between the alignment of easy growth directions of the grains and the maximum heat flow directions at the melt pool boundaries. Fig. 40(c) shows the directions of maximum temperature gradient for alternate laser scanning directions [315]. Generally, growth is favored when the maximum heat flow direction aligns closely with one of the easy-growth directions. However, the actual direction of grain growth may deviate considerably from the local maximum temperature gradient for certain laser scanning pattern.

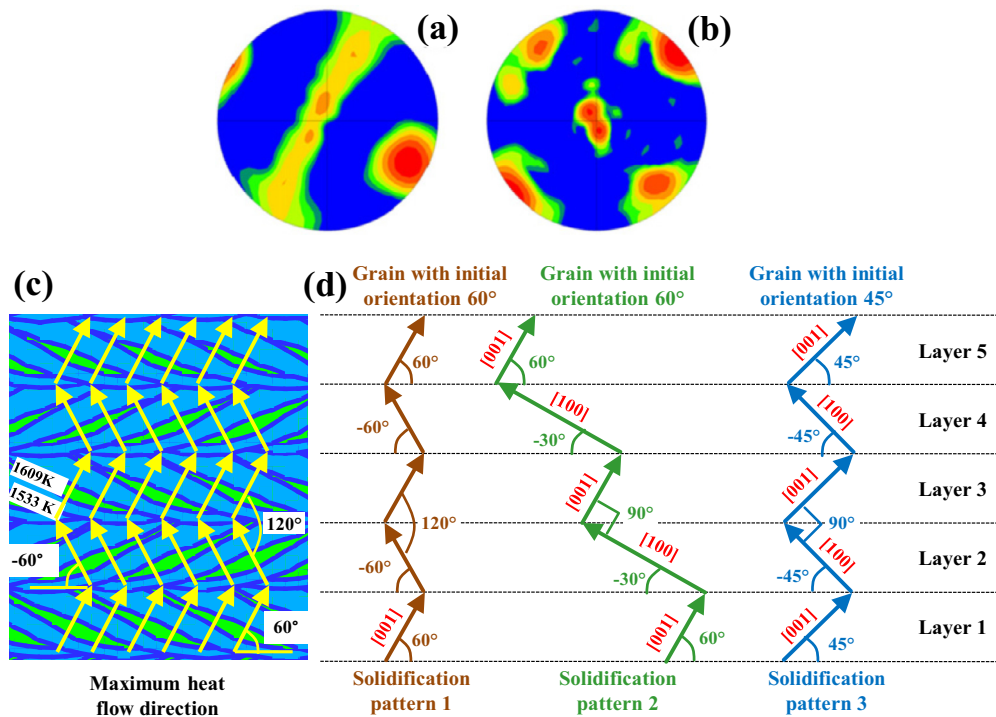


**Fig. 40.** DED-L of IN 718, (a) and (b) pole figures for the texture by unidirectional and bidirectional laser scanning, respectively [305]. (c) Maximum temperature gradient during bidirectional laser scanning [315]. (d) Schematic illustration for primary dendrite growth patterns of grains with different orientations during bidirectional laser scanning [315].

Fig. 40(d) schematically shows possible primary dendrite growth patterns [315]. In the first pattern, the primary dendrite trunks coincide with the directions of maximum heat flow in different layers. This behavior does not occur because the driving force required for nucleation is much higher than that for grain growth. In the second solidification pattern, the primary dendrites of neighboring layers are perpendicular to each other. However, in the second layer the maximum heat flow direction deviates 30° with the primary dendrite growth direction. This pattern is unrealistic because of the large misalignment between the growth direction and the maximum heat flow direction. For solidification pattern 3 the grain orientation in the first layer is at 45° with scanning direction. The primary dendrite in the second layer grows epitaxially from the secondary dendrites in the first layer and makes an angle of  $-45^\circ$  with the horizontal line. As a compromise, there is a deviation of 15° between the maximum heat flow direction and the primary dendrite growth direction in all the layers [315].

In short, the evolution of texture is affected by both the easy growth directions of the grains and the maximum heat flow directions at the melt pool boundaries. Strong fiber texture can be formed when these directions are closely aligned. Cube texture can be formed as compromised results when these directions are significantly misaligned.

### 3.3.3. Influential factors

Solidification texture depends on the local heat flow directions and competitive growth of the grains. Epitaxial growth contributes significantly to the formation of textures in AM fabricated components. The metallurgical challenge associated with processing of metals and alloys using AM techniques is that the material tends to solidify in an epitaxial manner producing columnar grains with  $\langle 0\ 0\ 1 \rangle$  texture oriented along the build direction. Epitaxial growth from the previously deposited layers will not occur if they are insufficiently remelted, in which case strong texture cannot be maintained.

Texture could be adjusted by varying the process parameters, e.g. scanning speed and the layer thickness, since these variables directly determine the extent of remelting of the previously deposited tracks. Higher heat input, reduced beam size and reduced layer thickness and hatch spacing would intensify the morphology and the crystal texture [311,373,386]. An example for the effect of scanning speed on the fiber texture of a cobalt based alloy by laser deposition is shown in Fig. 41 [300]. The texture may also be affected by the scanning strategy [305,310,439], depending on the specific processing conditions and material systems [386]. A strong fibrous  $\langle 1\ 0\ 0 \rangle$  texture was altered into a weak cubic texture along the build and scanning directions when a rotation of  $90^\circ$  of the scanning vectors within or between the layers is applied for Ti-6Al-4V by PBF [386]. The result shown in Fig. 40 is also an example of texture control by changing scanning strategies.

There is another form of texture that can be produced in PBF system using a macroscopic scan strategy. In some AM systems small cubes of metals are built, layer by layer, in an array that fills space. These small cubes can be arbitrarily arranged, i.e., put down in a non-contiguous way and can be created such that the melt pool motion is unidirectional in a layer plane

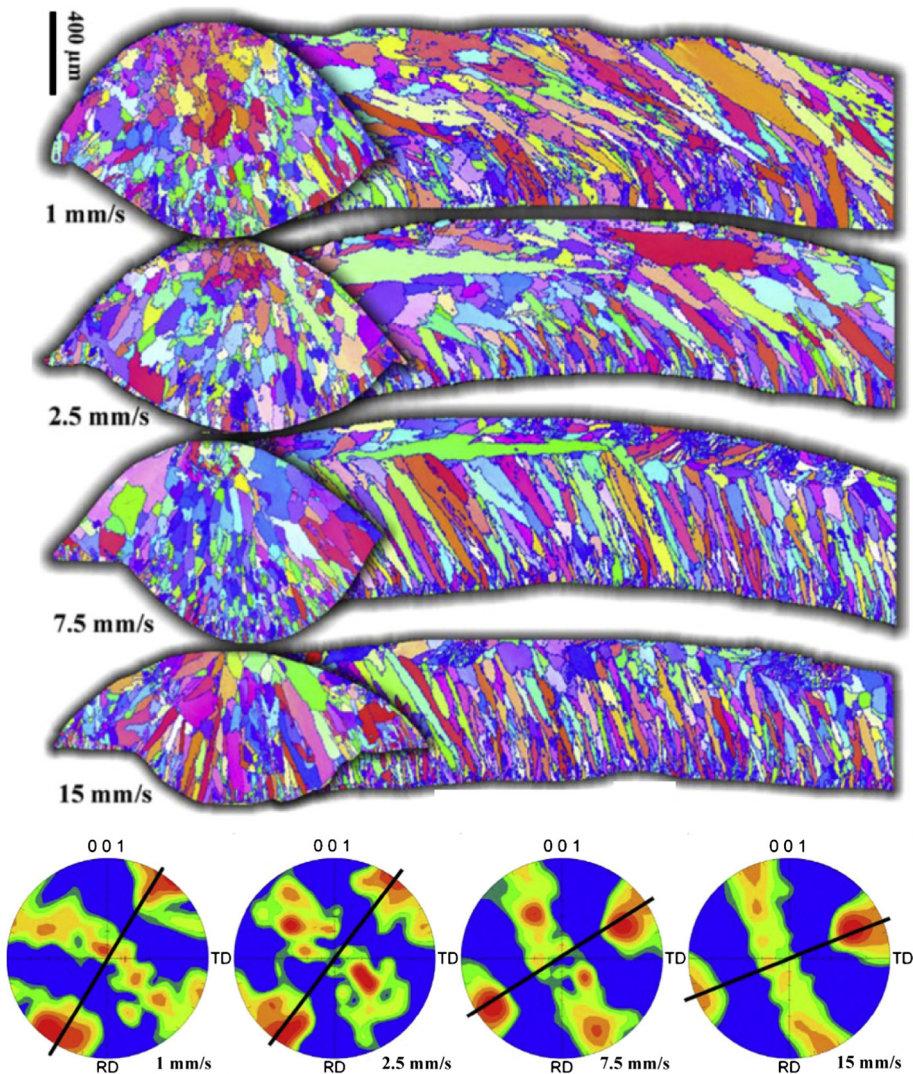


**Fig. 41.** Inverse pole figures with grain boundaries from transverse and longitudinal cuts across single laser tracks formed at four different laser cladding speeds [300]. The fiber solidification texture in longitudinal cross sections shown by the pole figures for different scanning speeds strongly corresponds to the grain shape orientation angle [300].

for all cubes or scanned at different angles for each cube layer. By randomly orienting the scan direction of each cube within a given layer a less textured component can be created and residual stresses are believed to be reduced [386].

In short, fiber texture parallel to the build direction is commonly observed in additively manufactured components. Cube texture can be obtained by manipulating processing parameters such as scanning strategy. Texture is dependent on the evolution of grain structure which is affected by the shape and size of the melt pool that determined by the AM processing parameters. It is important to note that one distinction between welding and AM processes is the ability to control this texture through scanning strategies, which is easily performed in AM but more difficult to accomplish using traditional welding methods.

### 3.4. Phase transformations

The previous sections have discussed the effects of AM processing parameters on the microstructures and macrostructures that form during solidification which is a critical step in the formation of a metal AM part. However, once the metal has solidified and cooled below its solidus temperature, it must still cool to room temperature and can undergo solid state transformations along the way. In addition, reheating of previously deposited AM layers can further result in solid state phase transformations, and alter the residual stress state and distortion of the part being fabricated. In this section, solid state phase transformations that occur during AM processing will be reviewed for both heat treatable, and non-heat treatable alloys.

### 3.4.1. Non-heat treatable alloys

Non-heat treatable alloys are those that achieve their properties largely through solid solution strengthening or cold work by rolling, forging or other methods. Pure metals, such as aluminum and copper; precious metals such as gold, silver, and platinum; and often times refractory metals such as molybdenum, tungsten, and tantalum fall into this category. In addition, metals with low alloy contents, or those that have largely single phase microstructures, or those that do not undergo phase transformations do not require heat treatment. Some common AM examples are the 4000 series aluminum alloys (Al-Si) [310,387,440,441], and austenitic SS (304L and 316L) [312,357,360]. When producing components from these metals by AM, it is important to note that there will be no ability to post process them to increase their strength through cold work since they will be used in the as-solidified state. Hence their properties will be similar to those of the annealed conventional metals, but with modifications to that occur due to microstructural scale refinement, contamination, or defects that are introduced by the AM process. Additive manufacture of refractory metals and precious metals that are non-heat treatable will be discussed in Section 5 of this article.

Components made out of aluminum alloys can be difficult to produce for several reasons since many alloys are also difficult to weld using conventional techniques. The difficulties are related to wide solidification temperature ranges that can lead to weld cracking, high solidification shrinkage that can cause defects and solidification stresses, and high thermal conductivity. Nearly all of the heat treatable aluminum alloys are welded using dissimilar filler metals near the Al-Si eutectic, and these alloys have proven to be popular alloys for AM processing [4,310,384,387,440,441]. Al-Si-Mg is also a commonly used AM aluminum alloy that is often used in the as deposited condition, but can also be heat treated for improved properties [4,387].

Austenitic stainless steels, AISI 304L and 316L, are very important engineering alloys that are readily weldable if the compositions are controlled to prevent solidification cracking [210,293] and have been a popular AM material [4,312,357,380]. Although these alloys do undergo a bcc to fcc phase transformation during cooling, they are considered non-heat treatable since there is little strengthening by means other than cold work. During welding [296], and during AM processing [312,357], there is a strengthening effect over and above the annealed base metal properties, but this strength is often associated with a decrease in ductility. The strengthening effect is related to a refined microstructure that forms during welding and AM, combined with ferrite/austenite interface boundaries. The observed reduction of ductility is often related to defect formation during AM processing [181], and/or higher impurity contents of the AM build.

### 3.4.2. Heat treatable alloys

Heat-treatable alloys are those that undergo phase transformations upon heating and cooling in a way that significantly alter their properties. Conventionally processed alloys may also contain cold or warm work to improve their properties in addition to heat treating. High strength steels and aluminum alloys, nickel based superalloys, and many titanium alloys fall into this category. These alloys are much more complex than non-heat treatable alloys, and can be more difficult to produce through AM techniques for several reasons. One reason is that many of these alloys are specifically designed to have high strength, and this strength often reduces their ductility and can lead to cracking during AM processing [2]. Another reason is that, in order to achieve uniform and high strength properties, the AM builds must undergo post build heat treating (PHT) to achieve the desired properties [2,4]. This additional step is a cost and departure from producing parts ready for direct application from the AM machine, and may cause unwanted distortion of the part undergoing PHT.

Heat-treatable alloys for AM such as Inconel 718 [354,362,368,370,400] and Ti-6Al-4V [374,389,408,417,425,435,442] are often known to have good weldability. It is more difficult to fabricate AM components with desired properties using other alloys such as maraging steel [443], precipitation hardening steels such as 17-4PH [444], and tool steels [445]. The metallurgy of all of these alloys can be complex, and subject to individual AM processing parameters as well as the final heat treating conditions [2,4,444], which can sometimes be incorporated into a hot isostatic press (HIP) treatment to remove residual stress and minimize porosity at the same time [2]. The effects of PHT on as deposited AM builds are discussed elsewhere in this article in the mechanical properties and residual stress sections.

Phase transformations that occur in AM components are often times similar to welding except that at higher cooling rates for the powder bed processes at high scan rates. Understanding the phase transformations and the effects of scanning speed on them requires knowledge of the kinetics of the phase transformations, and this information can be difficult to acquire. In-situ synchrotron-based work has been done to experimentally determine transformation kinetics in arc welds using spatially-resolved X-ray diffraction (SRXRD) and time-resolved X-ray diffraction (TRXRD) [446,447]. The spatially resolved studies can be used to map the phases surrounding a weld in real time, allowing the transformation rates to be calculated from the weld speed. Fig. 42 shows one in-situ SRXRD phase map for an AISI 1045 steel arc weld, where the ferrite phase (blue color) transforms to an austenitic phase (red color) near the weld pool on heating and then back to ferrite on cooling [448]. Comparing these data with the calculated weld isotherms for equilibrium conditions, further indicates non-equilibrium conditions required to create phase transformations both on heating and on cooling and the kinetics of the transformations [448].

Higher cooling rates in excess of  $10^3$  °C/s have been investigated using time-resolved method with 0.05 s resolution under both actual and simulated welding conditions [447]. One such experiment is shown in Fig. 43 for an arc welded Fe-C-Al-Mn steel alloy [448], where the major diffraction peaks for the ferrite and austenite phases are recorded continuously during heating and cooling of a transient spot weld. Fig. 43(a) shows that the phase transformation begins sometime after the arc is established when ferrite (bcc) transforms to austenite (fcc), leaving a small amount of delta ferrite present when

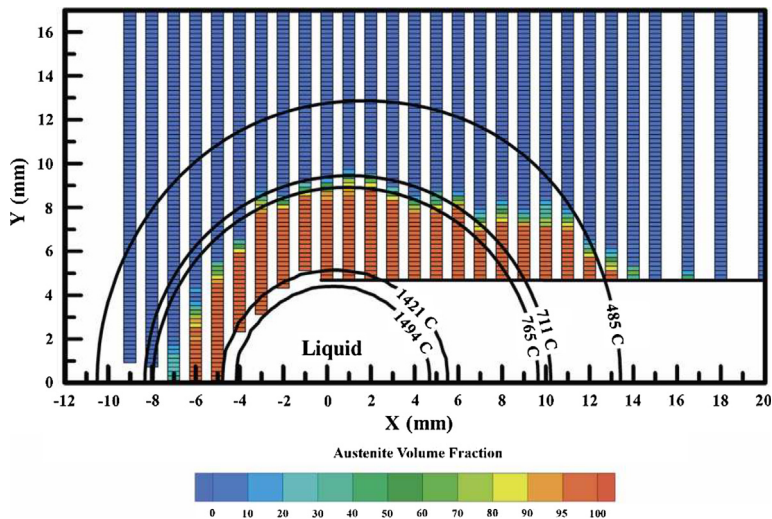


**Fig. 42.** An SRXRD phase map showing the austenite phase fractions measured across the width of the weld HAZ. Weld isotherms, calculated using a coupled thermal fluids weld model, are superimposed over the SRXRD data. In the plot, the shading indicates that the austenite fraction varies from 0% austenite (blue) to 100% austenite (red) [448].

the arc is turned off. Direct observations such as this are important to the understanding of how the microstructure evolves during cooling, and can reveal the formation of non-equilibrium phases that are not easily predicted by other means [449,450]. Fig. 43(b) shows the weld cooling behavior after the arc is extinguished, where a rapid transformation back to the ferrite phase occurs. Analysis of the time-temperature transformation relationships reveals kinetics of how microstructures evolve during welding and can be used directly for AM processes such as wire arc and DED which have cooling rates similar to conventional welds, and can possibly be extrapolated to higher speed AM processes such as PBF.

The phases that form during solidification as well as solid-state phase transformations in AM have also been directly identified with *in situ* synchrotron micro-X-ray diffraction during the rapid cooling process. The sequences of solidification and phase transformation in the rapidly heated and solidified Ti-48Al under AM conditions was observed using *in situ* synchrotron micro-X-ray diffraction with temporal resolution of 10 ms as shown in Fig. 44 [451,452]. Peaks of the intermetallic TiAl  $\gamma$ - and Ti<sub>3</sub>Al  $\alpha_2$ -phases are indicated. The  $\alpha_2$ -phase is the ordered variant of the high-temperature  $\alpha$ -phase. The temporal resolution is 10 ms. The graphs are composed of azimuthally integrated, background subtracted and laterally stacked diffraction spectra [452]. The evolution of the various phases that appear and disappear during fast cooling was tracked by the changes in diffraction peak intensities [451]. The possibility to estimate local temperatures and directly correlate them to diffraction signals gives deeper insights into the processes observed under non-equilibrium conditions and reliable cooling rate measurements [452]. Synchrotron X-ray diffraction was used to obtain the bulk textures of IN718 theta shaped specimens built with PBF-EB [453]. The *in situ* characterizations of solidification and phase transformation are a valuable tool for understanding the alloy behavior and for designing new alloys for AM taking into account the non-equilibrium characteristics of these processes [452].

### 3.4.3. Microstructures of AM fabricated alloys

**3.4.3.1. Microstructures of nickel based alloys.** The formation of precipitates and intermetallic compounds in nickel based alloys is critical to their microstructures. This section reviews the correlation between the AM processing conditions and the microstructural features of nickel based alloys. An overview of the microstructures of different nickel based alloys by various AM processes is presented in Table 11. The chemical composition as well as the thermal histories both affect the microstructure. Some nickel based alloys such as IN 718 do not readily develop the  $\gamma'$  phase during PBF-L [412]. The  $\gamma'$  and  $\gamma''$  phases are precipitated during post processing heat treatment. In contrast, some other alloys such as René 142 by EBM develop a  $\gamma'$  precipitate structure without any post processing heat treatment [454]. The correlations between  $\gamma$ ,  $\gamma'$  and  $\gamma''$  phases including precipitate size, volume fraction, and precipitation sequences determine the build properties. The microstructures of nickel based alloys need to be optimized through compositional variations, process control and post processing heat treatment to achieve comparable or better properties of their counterparts produced by conventional processing.

Different from conventional processes such as casting and welding, AM processes are characterized by rapid cooling rates and repeated heating and cooling cycles which substantially affect the evolution of microstructure. Fig. 45 shows the microstructure of CMSX-4 after PBF-EB [336]. The  $\gamma'$  phase precipitates when the temperature exceeds 1223 K. Different layers are subjected to different thermal cycles during processing, which results in location dependent  $\gamma'$  size within the sam-

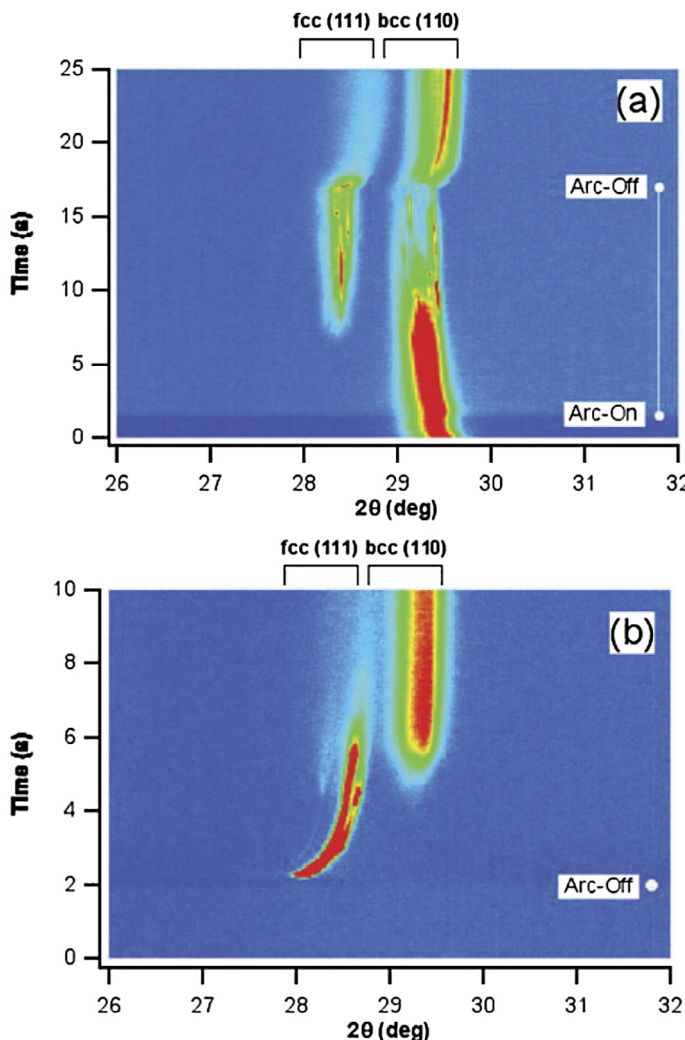


**Fig. 43.** Results from an *in situ* TRXRD arc welding experiment showing the ferrite/austenite phase transformations of an Fe-C-Al-Mn steel on: (a) heating and (b) cooling with 0.050 s time resolution [447,449]. The major diffraction peaks are plotted for each phase where the intensity of each phase increases from blue to red.

ple. The precipitates at the bottom of the sample are exposed to more thermal cycles and longer periods of coarsening than those near the top of the sample. Therefore, larger precipitates are found at the bottom than near the top surface [336]. Significant spatial heterogeneity in microstructure of the as deposited nickel based alloy was reported. The morphologies and distribution of  $\gamma'$  phase are affected by the dendritic structure of the René 41 sample produced by DED [455]. The size of  $\gamma'$  precipitates in the dendrite cores was larger than that in the interdendritic zones due to large supersaturations and fine-segregations of elements in the DED-L process. The eutectic products such as Laves phase and NbC contain higher levels of Nb in the matrix than that close to the interdendritic boundaries due to segregation. Thus, enhanced precipitation occurs in  $\gamma$  regions close to eutectic products during repeated heating and cooling processes [348]. The microstructural heterogeneity in the as-deposited conditions unavoidably leads to mechanical heterogeneity. Thus, post processing heat treatment is necessary to achieve homogeneous microstructures.

Intermetallic compounds such as Laves and delta phases are often observed in nickel based alloys [349,351,401,456–460] and are known to adversely affect mechanical properties. Compounds such as Laves,  $\text{Ni}_3\text{Nb}-\delta$ , Nb-rich MC are all eutectic products and are observed at the interdendritic regions or grain boundaries. Thin oxide films at grain boundaries often serve as potential substrates for the nucleation of the intermetallic phases [456]. Laves phase forms in Nb-rich liquid and the microstructure is influenced by the segregation of Nb and the distribution of Nb-rich liquid in the interdendritic region [349].

The formation of intermetallic compounds is largely affected by the solidification process. The intermetallic compound forms near the final stage of solidification and its size is largely affected by the cooling rate [457,459]. Laves phases are observed in long chain morphology and often induce hot cracking, as shown in Fig. 46 [349,362]. Laves phase has been

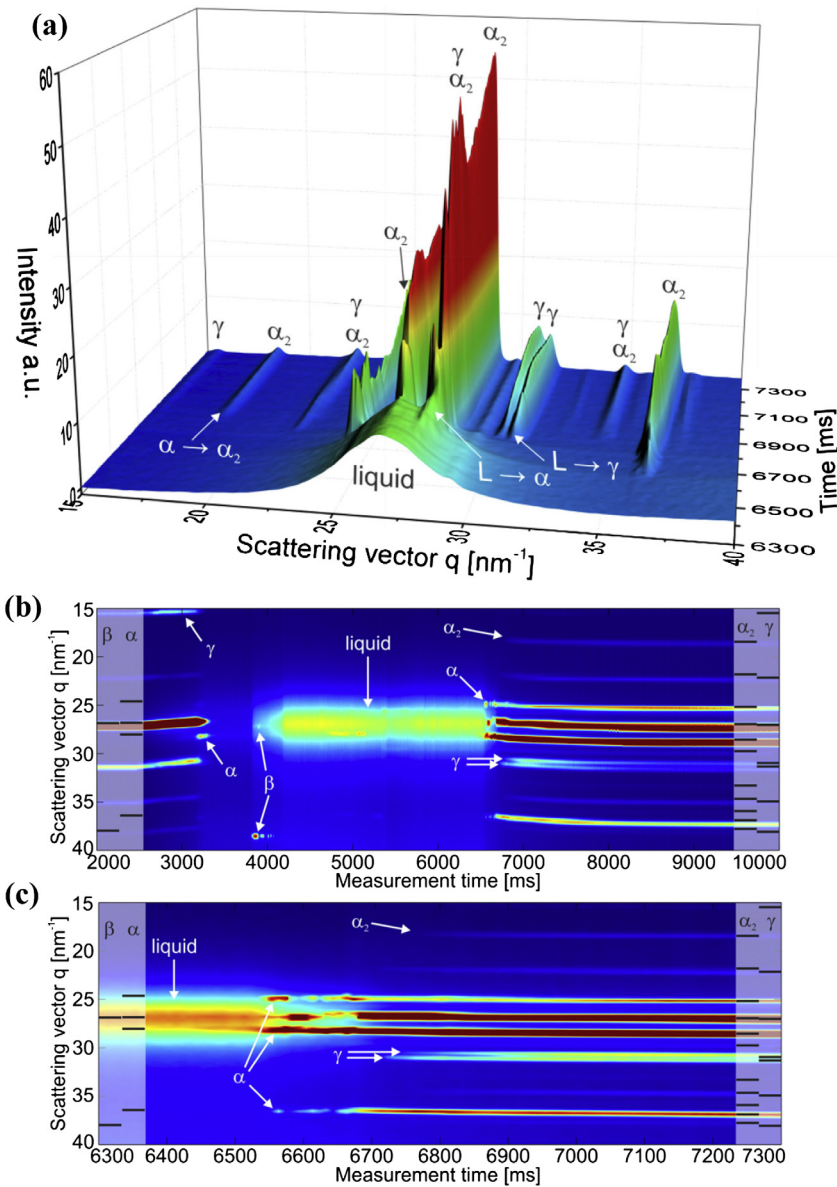


**Fig. 44.** (a) Time evolution of the azimuthally integrated diffraction pattern in Ti-48Al upon rapid solidification. The solidification by  $\alpha$ , followed by  $\gamma$ -formation and  $\alpha$  to  $\alpha_2$  ordering is clearly observed. (b) Intensity map showing the phase evolution in Ti-48Al during a complete melting cycle and (c) a close view on rapid solidification and cooling within 1 s. [452].

observed in various DED processed nickel based alloys as well as the PBF-L processed IN718 [461]. Besides the influence of cooling rate, the formation of Laves phase is also affected by the morphology of the solidification structure which is dependent on the ratio of temperature gradient, G, to growth rate, R. Small equiaxed dendrite arm spacing under a high cooling rate and low G/R ratio is beneficial for forming discrete Laves phase particles. In contrast, large columnar dendrite arm spacing under a low cooling rate and high G/R ratio tends to produce continuously distributed coarse particles of Laves phase [349,459].

**3.4.3.2. Microstructure of titanium alloys.** Ti-6Al-4V is primarily composed of a hexagonal close-packed  $\alpha$  phase and a body-centered cubic  $\beta$  phase at room temperature. In the AM process, the  $\alpha$  phase transforms to the  $\beta$  phase during heating when the temperature exceeds the  $\beta$  transus temperature. Upon cooling, the  $\beta$  phase transforms back to primary  $\alpha$  phase for low cooling rate as shown in Fig. 47 or to a martensitic  $\alpha'$  phase for high cooling rate as shown in Fig. 48. The evolution of  $\beta$  grains during solidification is discussed in Section 3.2.

**Table 11**

Microstructure of nickel based alloys by various AM processing conditions.

Alloy	Process	Condition	Microstructure	Refs.
Inconel 625	DED-L	AD	$\gamma$ -Ni (fcc) solid solution	[304]
		AN (700 °C/1 h/AC)	$\gamma''$ in $\gamma$ -matrix	
		AN (800 °C/1 h/AC)	$\delta$ in $\gamma$ -matrix	
		AN (1100 °C, 1200 °C/1 h/AC)	$\gamma$ solid solution	
Inconel 718	DED-L	AD	Laves phase in interdendritic region of $\gamma$ -matrix	[305,350,503]
		AN (700 °C/1 h/AC)	$\gamma' + \gamma''$ in $\gamma$ -matrix	[305]
		AN (800 °C/1 h/AC)	$\gamma' + \gamma'$ in $\gamma$ -matrix	
		AN (900 °C/1 h/AC)	$\gamma' + \delta$ in $\gamma$ -matrix	
	DED-L	AD	$\gamma'$ in $\gamma$ -matrix	[351]
		AN (1000 °C, 1100 °C, 1200 °C/1 h/AC)	Laves phase + $\gamma'$ with $\gamma$ -matrix	[348]
	DED-L	HT (1080 °C/1.5 h/AC, 980 °C/1 h/AC, 720 °C/8 h/FC, 620 °C/8 h/AC)	$\gamma''$ in interdendritic regions and close to laves phase and NbC in $\gamma$ -matrix	[490]
			Nb-rich MC type carbides along grain boundaries	
Inconel 718	PBF-L	AD	Oblate spheroids/ellipsoids $\gamma''$ in $\gamma$ -matrix	[412]
		AN (1160 °C/4 h/AC)	Spherical $\gamma' + \delta$ in $\gamma$ -matrix	[350]
	PBF-L	ST (980 °C/1 h/AC)	$\delta$ + Laves phase in $\gamma$ -matrix	[503]
		DA (720 °C/8 h/FC, 620 °C/8 h/AC)	$\gamma' + \gamma'', \delta +$ Laves phase in $\gamma$ -matrix	
Inconel 738	DED-L	AD	$\gamma' + \gamma$ , eutectic on the grain boundary	[674]
	PFB-L	AD	Small carbide precipitates	[383]
		HIP (1180 °C/4 h), 1120 °C/2 h, 850 °C/20 h	Duplex-size $\gamma'$ in $\gamma$ -matrix	
René 41	DED-L	AD	$\gamma' + \gamma$ , with $\gamma'$ larger in dendritic cores than in interdendritic zones	[455]
René 80	PBF-L	TSRHT (1082 °C/2 h heating and cooling/FC)	$\gamma' + \gamma$	[326]
René 142	PBF-EB	AD	Cuboidal $\gamma'$ 59 vol%, $\gamma$ 41 vol%	[454]
CMSX-4		AD	Cuboidal $\gamma'$ 72 ± 5 vol% with $\gamma$	[336]
IC221W (Ni <sub>3</sub> Al based single crystal alloy)	DED-L	AD	Mainly Ni <sub>3</sub> Al and some $\gamma$ and Ni <sub>5</sub> Zr	[337]

AD: as deposited, ST: solution treatment, DA: double aging, TSRHT: thermal stress relief heat treatment  $\gamma$ : Ni (fcc) solid solution,  $\gamma'$ : Ni<sub>3</sub>Al and Ni<sub>3</sub>Ti, cubic (ordered face-centered) Li2 crystal structure,  $\gamma''$ : Ni<sub>3</sub>Nb, metastable coherent in  $\gamma$ -matrix, body-centered tetragonal (bct) (DO22) crystal structure,  $\delta$ : Ni<sub>3</sub>Nb, stable incoherent in  $\gamma$ -matrix, orthorhombic crystal structure [412].

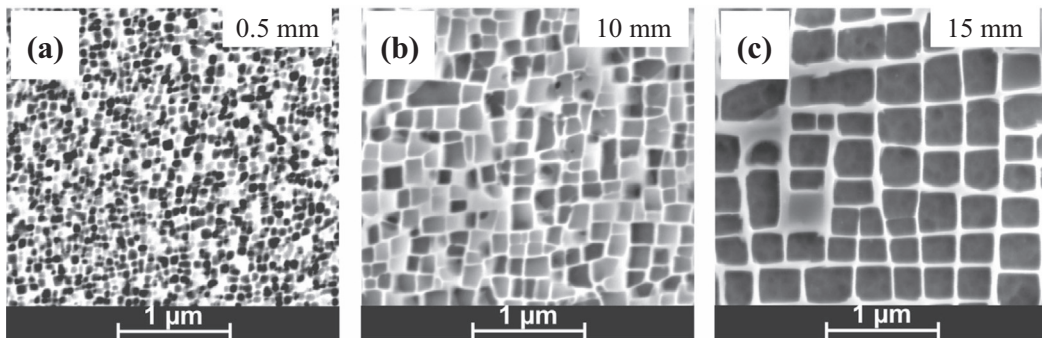


**Fig. 45.** SEM images of the  $\gamma/\gamma'$  microstructure of the nickel based superalloy CMSX-4 by PBF-EB at different sample heights.  $\gamma'$  size and volume as a function of the distance to the top surface [336].

The lamellar spacing of the  $\alpha$  phase decreases with the increase in cooling rate. The  $\alpha$  phase experiences *in situ* growth and its amount depends on the local thermal cycles. Significant variation of the  $\alpha$  phase lamellar spacing has been observed at various locations in a single layer [158]. The spacing is a function of the peak temperature which has to be below the  $\beta$  transus [158]. The thickness of the grain boundary  $\alpha$  is dependent on the cooling rate. The size of the prior  $\beta$  grains determine the largest size of an  $\alpha$  colony developing locally [394].

Ti–6Al–4V fabricated under fast cooling conditions consists of acicular  $\alpha'$  martensite, and usually displays high yield strength but limited ductility. Post processing heat treatment is usually needed to transform the  $\alpha'$  martensite to  $\alpha$  phase in order to achieve improved mechanical properties. The width of the  $\alpha$  plates is mainly dependent on the peak temperature

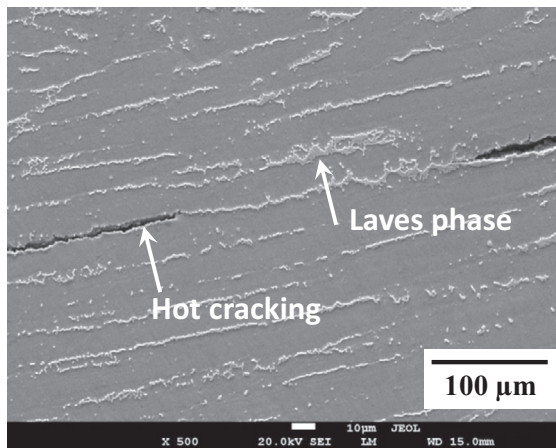


**Fig. 46.** (a) Hot cracking with long chain morphology Laves phase in IN 718 by DED [349].

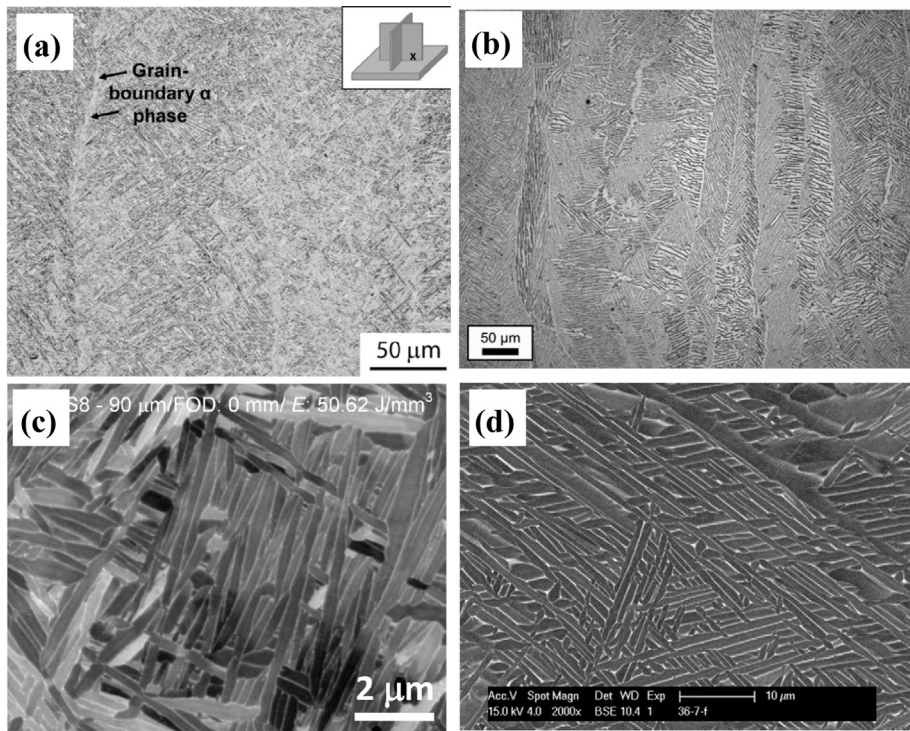


**Fig. 47.** Microstructure of Ti-6Al-4V produced by different processes. (a) DED, fine lamellar Widmanstätten structure and a small amount of grain boundary α phase indicated by arrows [150]. (b) PBF-EB, columnar prior β grains delineated by grain boundary α; within prior β grains, a transformed α + β microstructure with both colony and Widmanstätten morphology is observed [389]. (c) PBF-L, lamellar (α + β) structure [359]. (d) DED-GMA, α phase lamellae in gray shades and a β matrix in white contrast [22].

for sub-transus treatments. Heat treating at temperatures below the β-transus, followed by furnace cooling was optimal for the overall ductility and tensile properties. In contrast, heat treating temperature over β-transus is undesirable. The cooling rate dominates for the super-transus treatments, in which case the β grains transform to lamellar α + β, α-Widmanstätten colonies and α' martensite for furnace cooling, air cooling and water quenching, respectively [394]. The lamellar α + β and α-Widmanstätten colonies result in lower tensile properties while the α' martensite gives poor ductility compared with the structure attained by sub-transus treatment.

Apart from post processing heat treatment, the martensitic α' phase may be decomposed *in situ* during the AM process. The decomposition of martensite was observed during PBF-L where α' martensite transformed into an ultrafine lamellar (α + β) structure [359]. The transformation results from the multiple thermal cycles during the progressive deposition of

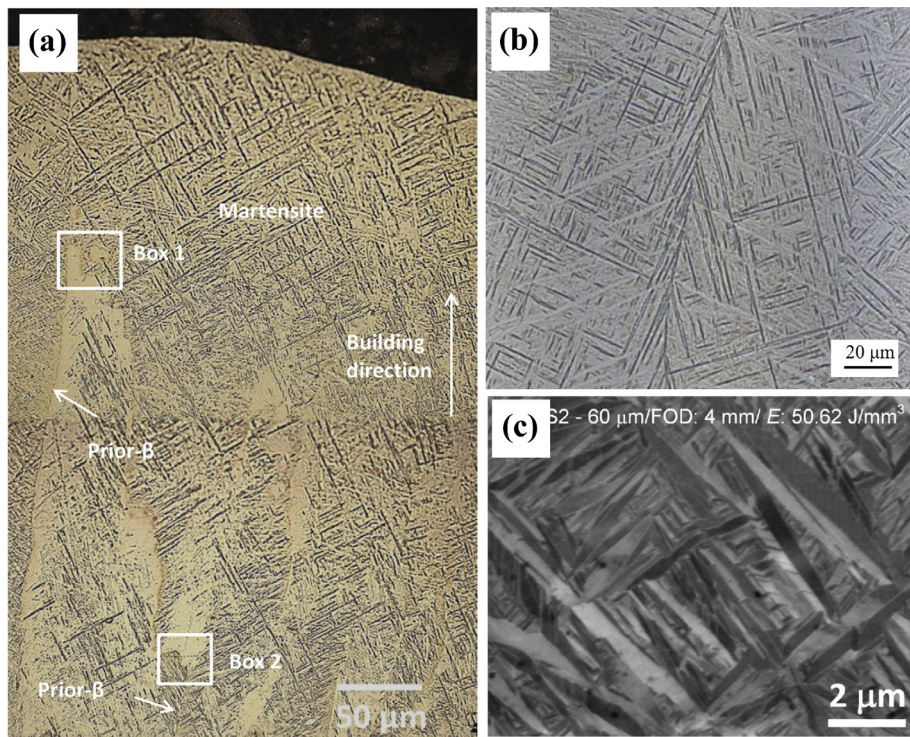


**Fig. 48.** (a) PBF-EB, optical microstructure of the last few layers in the as-built Ti-6Al-4V cylindrical sample showing orthogonally oriented martensitic needles in the top surface layer, followed by a mixture of martensitic needles and featureless patch-like regions. [353]. (b) DED, microstructure composed of  $\alpha'$ -martensite [520]. (c) PBF-L, microstructure predominantly consisted of acicular  $\alpha'$  martensite [359].

upper layers [359,462]. The processing parameters such as the layer thickness, defocus and the energy density of the laser beam need to be carefully controlled [359].

The capability of adding alloying elements in powder form to commercial feedstock materials in AM allows tailoring of microstructures and properties [404]. For example, the addition of 10 wt% Mo to Ti-6Al-4V completely suppressed the transformation from  $\beta$  to  $\alpha'$  martensite during rapid solidification by reducing the  $\beta$ -transus temperature from 995 °C to 900 °C. Thus a combination of high strength and good ductility was achieved through the microstructure of fully  $\beta$  titanium matrix with dispersed Mo particles [404].

**3.4.3.3. Microstructure of aluminum alloys.** The most common aluminum alloys processed by AM are the eutectic Al-Si and the hardenable Al-Si-Mg alloys [4]. The microstructure of Al-Si alloys usually consists of primary aluminum and eutectic, fully eutectic, or mixture of primary silicon and eutectic depending on the composition and solidification condition [384]. The microstructure of the AlSi10Mg part produced by PBF-L is typically cellular with some occasional side branches [386]. The cellular primary Al is decorated with fibrous Si particles. Additionally, Mg<sub>2</sub>Si is precipitated in AlSi10Mg during AM [386,463]. The fine microstructure results in a high hardness even without any post processing precipitation hardening treatment.

The variation of microstructural morphology with the location of the Al 4047 alloy (AlSi 11.28) deposit by DED-L is shown in Fig. 49 [384]. The microstructure consists of columnar dendrites and equiaxed dendrites in different regions depending on local thermal cycles. The bright primary Al dendrites coexist with the gray Al-Si eutectic, which is the typical microstructure of Al-Si alloy [310,384]. Fibrous Si particles were developed in the eutectic phase due to the high cooling rate of the laser deposition process. Equiaxed Si particles were developed from these fibrous Si particles due to the multiple thermal cycles during the deposition of subsequent layers [384].

**3.4.3.4. Microstructure of stainless steels.** A wide range of steels have been processed by AM such as austenitic stainless steels [312,357,464–466], precipitation hardenable steels [467], maraging steels and soft magnetic high silicon steel [311]. The most common microstructures of additively manufactured austenitic stainless steels are cells and columnar dendrites. Equiaxed structure is rarely reported due to the high temperature gradient in the AM process. Fig. 50 shows the typical microstructure at different locations of a nine layer deposit of SS 316L by DED [465]. The solidified structures are primarily cells and the size of the cells increases with depositing height due to the accumulation of heat during the AM process [465].

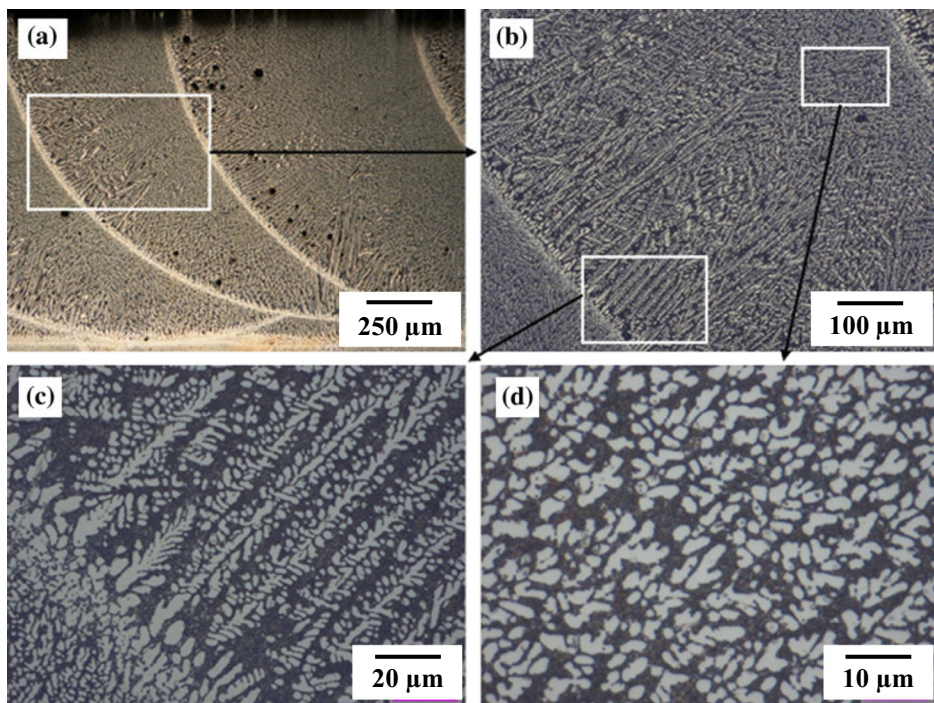


**Fig. 49.** Optical micrographs of the as-deposited Al 4047 sample by DED revealing the columnar dendrites and equiaxed microstructures near the bottom and top of the layer, respectively [384].

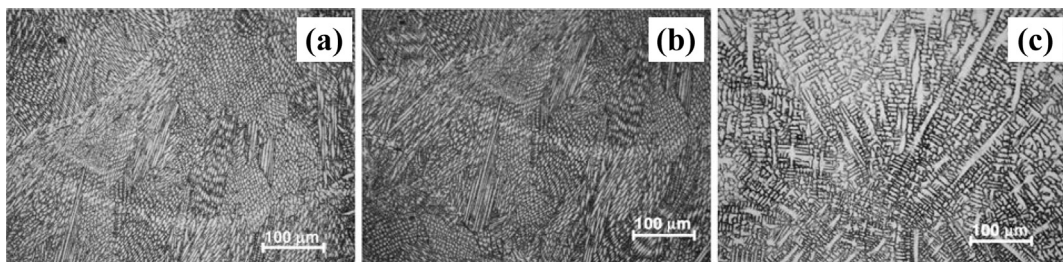


**Fig. 50.** Solidified microstructures with layer height dependent scales. (a) lower, (b) middle, and (c) top layer for a 9-layer structure of austenitic stainless steel 316L by DED-L [465].

Austenitic stainless steels often contain a small amount of ferrite apart from austenite. Columnar δ-ferrite dendrites were observed inside the austenite matrix in SS 304L by DED [357]. Rejection of solute at the solidifying interface enriches the intercellular regions with chromium and molybdenum, which results in the formation of ferrite. The ferrite content decreases with increasing cooling rate because of the reduced time for solute redistribution at high rates [466]. Functional materials such as soft magnetic silicon steel, Fe-6.5%Si, was recently fabricated using PBF-L [311]. Single ferritic phase was obtained in the as deposited near-fully dense component with columnar grains oriented towards the build direction [311].

To summarize, the solidification structure, grain structure, texture and microstructure are highly dependent on the process and the chemical composition of the alloys, which, in turn, significantly affect the properties of the AM components. It is essential to establish the correlations among processing parameters and mechanical properties through controlling the structure in considering the rapid heating and cooling processes in a highly-localized region during AM. The common feature of structure development from a local melt pool of welding and AM makes the fundamentals of heating, cooling, solidification and phase transformation developed in the mature welding field being useful to the emerging AM.

#### 4. Properties

In this section, the strength, ductility, and anisotropy of mechanical properties of metallic AM components are described with an emphasis on the interconnection between structure and properties. As a metric to compare studies, it is first important to note the disparate processes, heat sources, and processing parameters used throughout the literature. While it is not

possible to describe the thermal history in terms of a single parameter, often linear or volumetric heat input is used to compare studies. Linear heat input,  $H$ , is defined as:

$$H = \frac{P}{v} \quad (29)$$

where  $P$  is the laser power, and  $v$  is the laser scanning speed. Volumetric heat input,  $E_v$ , is defined as:

$$E_v = \frac{P}{v \cdot t_l \cdot h_s} \quad (30)$$

where  $t_l$  is the layer thickness and  $h_s$  is the hatch spacing [468]. While much of the reported data do not include sufficient information to compute these heat inputs, they will be used to compare studies where possible. However, it is not possible to directly compare the linear or volumetric heat inputs in studies using different lasers without accounting for differences in laser absorptivity. Results from multiple different processes including PBF-L, PBF-EB, DED-L and DED-EB will be discussed.

#### 4.1. Ferrous alloys

##### 4.1.1. Austenitic stainless steel

The most commonly studied austenitic stainless steels made by AM include AISI type 304 stainless steel (304), AISI type 304L stainless steel (304L), AISI type 316 stainless steel (316), and AISI type 316L stainless steel (316L). All consist of  $\gamma$ -austenite and  $\delta$ -ferrite when processed by AM [357,469], but are generally fully austenitic when conventionally processed [470,471]. These alloys have been primarily deposited using PBF-L and DED-L. In general, as-deposited AM austenitic stainless steels exhibit higher yield strength, ultimate tensile strength and hardness and lower ductility when compared to their traditionally processed counterparts, as shown in Table 12.

The disparate properties in these steels made by AM compared to conventionally processed lies in the inherent microstructural differences discussed in Section 3. The high strengths in AM components can be attributed to a combined effect of refined grain features due to rapid solidification, dendritic and cellular structures as well as a potentially high dislocation density due to rapid solidification and residual stresses [469,472–474]. The low elongation in these materials is also a combination of factors, including the general tradeoff between strength and ductility, higher dislocation density in AM, finer grain features leading to dislocation pileup at grain boundaries or internal defects such as sharp lack-of-fusion defects, which act as stress risers under tensile loading [357,472,475,476].

In austenitic stainless steels made by DED, the yield strength and ultimate tensile strength decrease with increasing linear heat input as shown in Fig. 51, but no clear trend is found in yield or ultimate tensile strengths as a function of volumetric heat input. Lower linear heat inputs result in smaller melt pools, higher thermal gradients, and therefore fast cooling rates and fine microstructures, leading to higher yield and ultimate tensile strengths compared to components made with higher linear heat inputs [7,357,472,474]. Few researchers report hatch spacing and layer thickness, so it is not possible to compute the volumetric heat input for most studies. Therefore, the data is not sufficient to determine general trends for strengths as a function of volumetric heat input.

The scatter in Fig. 51 can be partially attributed to the fact that different laser types were used in the reported studies. The actual energy used to melt previous layers or the substrate depends on the materials' absorptivity of the laser. Both Nd:YAG and CO<sub>2</sub> lasers are used in laser based AM. The Fe absorptivity of a CO<sub>2</sub> laser ( $\lambda = 10.6 \mu\text{m}$ ) is 0.12 at room temperature, which is lower than the Fe absorptivity of 0.25–0.32 of a Nd:YAG laser ( $\lambda = 1.06 \mu\text{m}$ ) [477]. Therefore, for the same linear heat input delivered by the system, the actual absorbed energy is lower when using a CO<sub>2</sub> laser compared to that when using a Nd:YAG laser.

In austenitic stainless steels made by PBF, no clear trend can be identified in yield and ultimate tensile strengths as a function of linear or volumetric heat input. In PBF, the thermal history of the components being fabricated depends on the scan strategy, which cannot typically be prescribed in the closed commercial AM systems and is difficult to capture. However, scan strategies vary between studies based on multiple samples being fabricated on the same build plate and the orientation of the samples [478–481]. The variation in scan strategy, as well as any variation in laser spot size or build preheating, is at least partially responsible for the lack of clear trends.

Slight anisotropy in mechanical properties of austenitic stainless steels is observed among AM specimens. The microstructure in these materials is anisotropic in that elongated grains and dendrites are often oriented along the build direction, as this is roughly the direction of the highest thermal gradient during AM processing [357,472,473,480,482]. In general, the yield and ultimate tensile strengths in austenitic stainless steels is equal to or higher in the longitudinal direction compared to those in the transverse direction as shown in Figs. 52 and 53 and Table 12. In austenitic stainless steels made by DED, the elongation is equal to or lower in the longitudinal direction compared to the transverse direction, whereas the trend is not clear in PBF as shown in Figs. 52(c) and 53(c). Yield and ultimate tensile strengths as a function of elongation are given in Figs. 54 and 55. For 316 and 304 stainless steel alloys made by DED, a general trend of yield strength decreasing with increased elongation is observed, but no clear trend is present between ultimate tensile strength and elongation (Fig. 54(b)). Conversely, in the same alloys made by PBF, yield strength and ultimate tensile strength increase with elongation (Fig. 55), which may be due to high porosity in samples that exhibit 20% elongation or less, as this would limit ductility and therefore strength in strain-hardening alloys.

**Table 12**

Mechanical properties of austenitic stainless steels parts fabricated by AM compared to those of their traditionally processed counterparts.

SS alloy	P (W)	v (mm/s)	H (J/mm)	$\rho$ (%)	Orientation	E (GPa)	$\sigma_y$ (MPa)	$\sigma_{uts}$ (MPa)	Elongation (%)	HV	Refs.
<i>Directed energy deposition – powder feedstock</i>											
304	–	–	–	100	Long.	–	448	710	59	–	[541]
					Transv.	–	324	655	70	–	
304L	2300	8.5	271	>99.9	Long.	–	337 ± 29	609 ± 18	48.2 ± 2.5	–	[357]
	4000	10.6	371		Transv.	–	314 ± 6	606 ± 13	56.4 ± 5.8	–	
					Long.	–	277 ± 27	581 ± 20	41.8 ± 3.5	–	
					Transv.	–	274 ± 7	560 ± 12	50.5 ± 6.7	–	
316	–	–	–	100	Long.	–	593	807	33	–	[541,675]
					Transv.	–	448	793	36–66	–	
316	–	–	–	93.2–97.4	Long.	192–199	363–487	648–970	20–44	–	[676]
316	600–1400	2–10	76–500	–	Long.	–	558	639	21	310–350	[472]
					Transv.	–	352	536	46		
316L	570	13	45	99.6	Long.	–	490 ± 8	685 ± 5	51 ± 2	164–215	[677]
					Transv.	–	280 ± 6	580 ± 10	62 ± 5	–	
316L	1000	6	167	–	Long.	–	–	812–901	9–15	305	[482]
316L	400	15	27	100	Long.	–	576	776	33	272 ± 35	[473]
					Transv.	–	479	703	46	289 ± 16	
316L	1650	23.3	71	97.6	Transv.	–	450	510	20	270	[474]
	1450	20	73	96.7	Transv.	–	440	470	18	240	
	1150	16.7	69	96.8	Transv.	–	410	460	22	215	
	1000	13.3	75	96.3	Transv.	–	420	440	15	220	
	800	10	80	96.2	Transv.	–	405	430	14	220	
<i>Powder bed fusion</i>											
304	200	25	8	100	Long.	–	520	710	38	–	[478]
					Transv.	–	450	580	58	–	
304L	95	70	1.36	–	Long.	–	182	393	25.9	217	[660]
	90	1.06	–	–	–	–	156	389	22.1	209	
316L	200	Up to 1000	>0.2	99.9	Long.	–	602 ± 47	664 ± 7	30 ± 0	235	[479]
					Transv.	–	557 ± 14	591 ± 12	42 ± 2	–	
316L	100	400	0.25	97.2 ± 1.2	Long.	165	438 ± 28	528 ± 23	10 ± 2	–	[480]
					Transv.	–	435 ± 2	504 ± 12	16 ± 3	–	
	591	0.17	98.5 ± 1.4		Long.	166	379 ± 17	489 ± 28	23 ± 6	–	
					Transv.	–	287 ± 6	317 ± 11	7 ± 4	–	
	600	0.17	98 ± 1.0		Long.	164	399 ± 29	486 ± 40	9 ± 3	–	
					Transv.	–	316 ± 6	367 ± 6	7 ± 1	–	
316L	175	700	0.25	97.5 ± 1	Long.	–	534 ± 5.7	653 ± 3.4	16.2 ± 0.8	–	[475,476]
				93.8 ± 2.6	Transv.	–	444 ± 26.5	567 ± 18.6	8 ± 2.9	–	
316L	380	635–3000	0.13–0.60	>99	–	–	–	–	–	220–213	[469]
316L	100	300	0.33	98.6	–	151.5 ± 13.1	–	501.1 ± 8.3	–	–	[678]
316L	103	425	0.24	–	Transv.	–	640	760	30	–	[481]
<i>Traditionally processed</i>											
304L	Annealed				–	–	168	556	61	136	[679]
304L	Annealed				–	–	265 ± 9	722 ± 14	62.3 ± 2.6	–	[357]
316L	Cast				–	200	365 ± 22	596 ± 16	69 ± 9	–	[480]
316L	Annealed				–	–	241	586	50	215–225	[473]

P = Laser power, v = Scanning speed, H = Linear heat input,  $\rho$  = Density, E = Elastic modulus,  $\sigma_y$  = Yield strength,  $\sigma_{uts}$  = Ultimate tensile strength, HV = Vickers hardness.

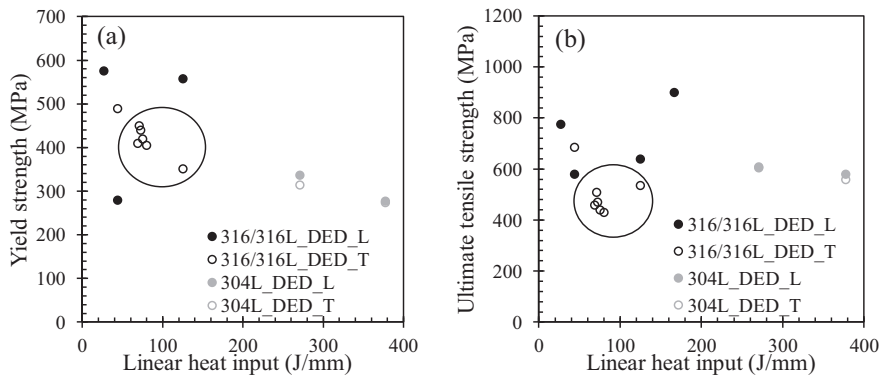


**Fig. 51.** (a) Yield strength and (b) ultimate tensile strength as a function of linear heat input in austenitic stainless steels made by DED AM. Data enclosed in the circles are from specimens made using CO<sub>2</sub> laser, while other data are either from specimens made using Nd:YAG lasers, or the laser used was not mentioned. “L” denotes samples whose tensile axis was along the longitudinal direction, while “T” denotes those in which tension was applied in the transverse direction. Data from Table 12.

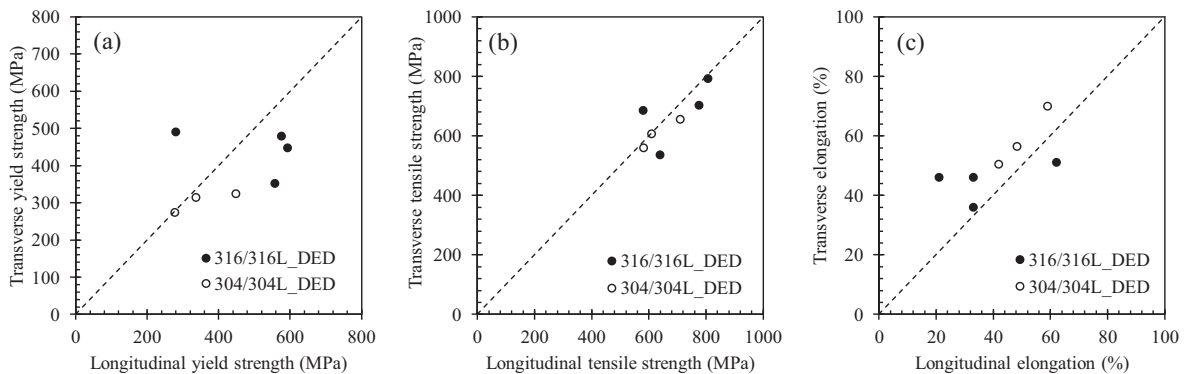


**Fig. 52.** (a) Yield strength (b), ultimate tensile strength, and (c) elongation along the transverse direction versus that along that in the longitudinal direction in austenitic stainless steels made by DED AM. Data from Table 12.

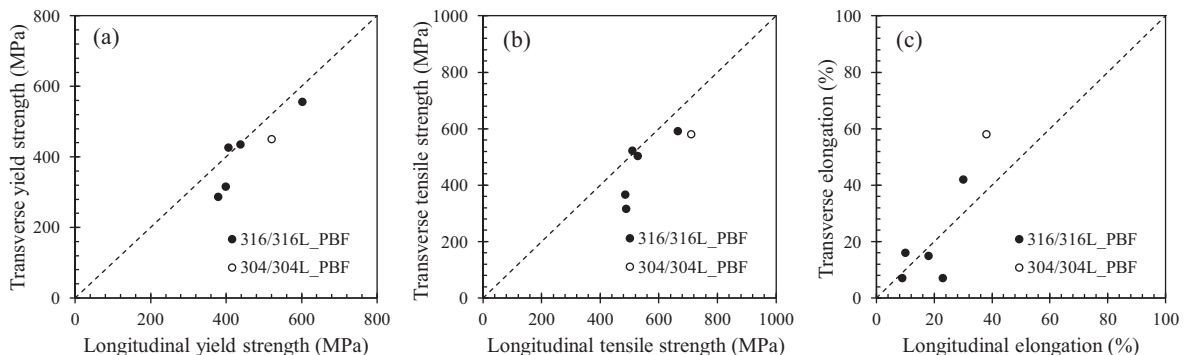


**Fig. 53.** (a) Yield strength, (b) ultimate tensile strength, and (c) elongation along the transverse direction versus that along the longitudinal direction in austenitic stainless steels made by PBF AM. Data from Table 12.

#### 4.1.2. Precipitation hardening (PH) stainless steel

The most commonly studied precipitation hardening (PH) stainless steels made by AM include AISI type 630 martensitic precipitation hardening stainless steel or 17-4 PH stainless steel (17-4 PH) and AISI type S15500 martensitic precipitation hardening stainless steel or 15-5 PH stainless steel (15-5 PH). As-built components consist of a mixture of austenite (50–75 vol%) and martensite (25–50 vol%) built in nitrogen, and mostly martensite (92 vol%) built in argon [483,484]. Heat treatment results in the desired precipitation of Cu-rich particles in a martensitic matrix [483–487].

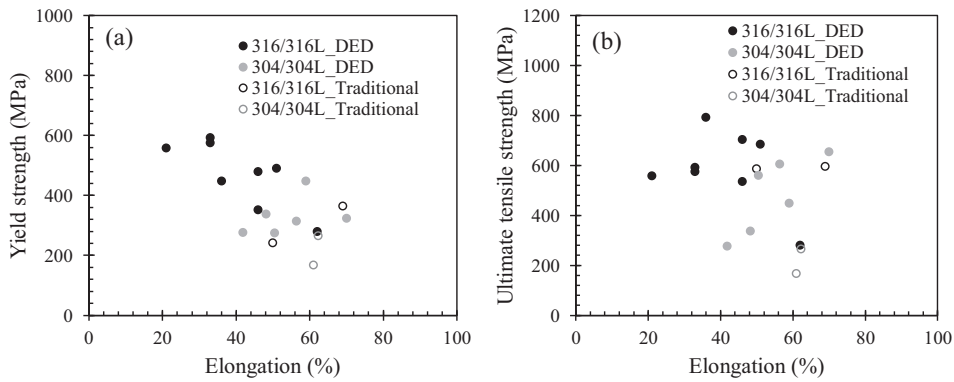


**Fig. 54.** (a) Yield strength and (b) ultimate tensile strength as a function of elongation in austenitic stainless steels made by DED AM compared with their traditionally processed counterparts. Data from Table 12.

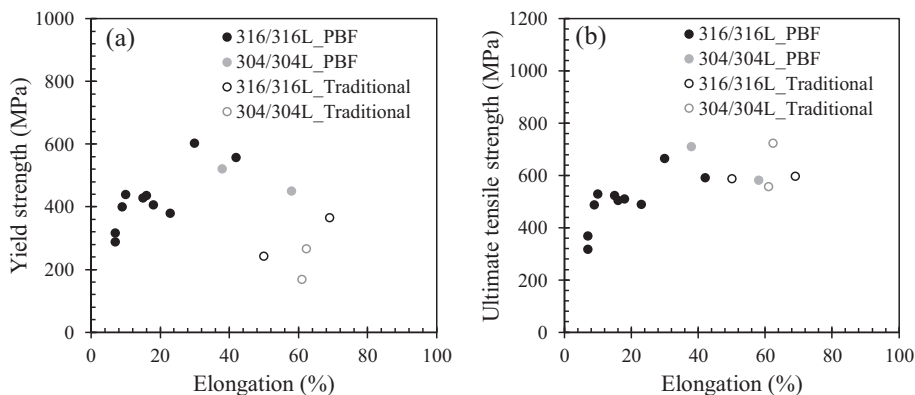


**Fig. 55.** (a) Yield strength and (b) ultimate tensile strength as a function of elongation in austenitic stainless steels made by PBF AM. Data from Table 12.

**Table 13**

Summary of mechanical properties of as-built precipitation hardening stainless steels fabricated by additive manufacturing and traditional methods in literature.

SS alloy	P (W)	v (mm/s)	H (J/mm)	$\rho$ (%)	Orientation	E (GPa)	$\sigma_y$ (MPa)	$\sigma_{uts}$ (MPa)	Elongation (%)	HV	Ref.
<i>Directed energy deposition – powder feedstock</i>											
17-4 PH	350	8.3	36.1	–	–	$40 \pm 10$	$400 \pm 100$	$900 \pm 200$	$5 \pm 3$	441	[488]
<i>Powder bed fusion</i>											
17-4 PH	190	787	0.24	98.7	Long.	–	$661 \pm 24$	$1255 \pm 3$	$16.2 \pm 2.5$	$333 \pm 2$	[485]
17-4 PH	195	800	0.24	–	Transv.	–	$570 \pm 13$	$944 \pm 35$	$50 \pm 1$	–	[483]
17-4 PH	95	350	0.27	–	Long.	–	$610 \pm 10$	$1050 \pm 20$	$11 \pm 0$	–	[487]
					Transv.	–	$610 \pm 10$	$910 \pm 10$	$3.5 \pm 1.5$	–	
<i>Traditionally processed</i>											
17-4 PH	Wrought, solution annealed and aged				–	–	199	992	1018	13.4	430
											[680]

P = Laser power, v = Scanning speed, H = Linear heat input,  $\rho$  = Density, E = Elastic modulus,  $\sigma_y$  = Yield strength,  $\sigma_{uts}$  = Ultimate tensile strength, HV = Vickers hardness.

Table 13 shows that as-built AM components generally have lower yield strength and hardness than their heat treated wrought counterparts, which is most likely due to the relative soft retained austenite in the AM components. A strain-induced phase transformation from austenite to martensite occurs during plastic deformation of the AM materials, which results in a high level of strain hardening. The transformation can lead to superior elongations and comparable ultimate tensile strengths in as-built AM parts compared to heat treated AM parts and their heat treated wrought counterparts [483,487,488].

There are not enough published studies with the necessary parameters presented to draw conclusions from the data of yield and ultimate tensile strengths as a function of linear heat input in as-built 17-4 PH stainless steel. The yield and ultimate tensile strengths of as-built 17-4 stainless steel subject to aging improved slightly compared to the strengths of as-built 17-4 stainless steel, but the strengths did not reach those of as-built materials subject to solution annealing followed

by peak aging (H900), as shown in [Table 14](#) and [Fig. 56](#). Aged 17-4 PH stainless steel contains martensite and retained austenite which likely explains this observation. Austenite has a high solubility of Cu, which inhibits the precipitation of Cu-rich particles and suppresses precipitation hardening. Solution annealing transforms austenite to martensite, which increases the amounts of Cu-rich precipitates, resulting in an increase in yield and ultimate tensile strengths [[483](#)]. However, solution annealing followed by over aging (H1025 and H1150) coarsens the precipitates, resulting in a decrease in yield and ultimate tensile strengths [[483,485](#)], as shown in [Table 14](#).

Defects such as lack-of-fusion pores, partially melted powder and secondary phase particles act as crack nucleation sites under tensile loading, which decrease the ductility of pH stainless steels made by AM [[487](#)].

#### 4.2. Nickel base alloys

Ni-base alloys used in AM include Inconel 625, Inconel 718 and Invar 36. Ni-base superalloys Inconel 718 and Inconel 625 are widely used in the aerospace industry due to their high strengths at elevated temperatures [[489](#)]. The mechanical properties reported in literature for Ni-base alloys fabricated using AM are reported in [Table 15](#). While a tradeoff between strength and ductility is typically observed in metals, [Fig. 57](#) shows no clear trend between ultimate tensile strength and ductility data for Ni-base alloys processed via AM, which can be attributed to varying AM techniques compared. The different types of processes include PBF-L, PBF-EB, DED-L, and DED-PA [[399,490–496](#)].

To investigate anisotropy in parts made by AM, the longitudinal tensile strength versus transverse tensile strength is plotted in [Fig. 58\(a\)](#), and longitudinal ductility versus transverse ductility is plotted in [Fig. 58\(b\)](#) [[399,491–493,496,497](#)]. These plots indicate that there is no clear trend in anisotropy, despite columnar grains oriented along the build direction in AM parts. Insufficient data exist to compare strength or ductility as a function of linear or volumetric heat input in Ni-base alloys. Thus, more data is needed to link processing, structure, and properties in these alloys made by AM.

**Table 14**

Summary of mechanical properties of post heat treated precipitation hardening stainless steels fabricated by additive manufacturing and traditional methods in literature.

SS alloy	Post heat treatment	Orientation	$\sigma_y$ (MPa)	$\sigma_{uts}$ (MPa)	Elongation (%)	HV	Ref.
17-4 PH	H900 (480 °C for 1 h)	Long.	945 ± 12	1417 ± 6	15.5 ± 1.3	375 ± 3	[485]
	H1025 (550 °C for 4 h)		870 ± 25	1358 ± 8	13.3 ± 1.5	399 ± 8	
	H1150 (620 °C for 4 h)		1005 ± 15	1319 ± 2	11.1 ± 0.4	381 ± 3	
	CA (solution annealed, 1040 °C for 30 min)		939 ± 9	1188 ± 6	9 ± 1.5	330 ± 3	
	CA + H900		1352 ± 18	1444 ± 2	4.6 ± 0.4	417 ± 5	
	CA + H1025		1121 ± 9	1172 ± 2	9.6 ± 1.7	350 ± 4	
17-4 PH	CA + H1150		859 ± 11	1017 ± 15	16.6 ± 1.2	317 ± 3	
	650 °C for 2 h	Transv.	619 ± 1	915 ± 38	12 ± 1	–	[483]
	788 °C for 2 h		857 ± 14	1487 ± 10	7 ± 1	–	
17-4 PH	788 °C for 2 h + H900		1126 ± 14	1457 ± 3	12 ± 3	–	
	CA+H900	Long.	910	1210 ± 10	8 ± 1	–	[487]
			700 ± 10	1050 ± 20	3.2 ± 1.5	–	
15-5 PH	H900	Long.	1297 ± 1.0	1450 ± 2.1	12.5 ± 1.1	–	[486]
17-4 PH	Wrought, solution annealed and aged		992	1018	13.4	430	[680]

$\sigma_y$  = Yield strength,  $\sigma_{uts}$  = Ultimate tensile strength, HV = Vickers hardness.

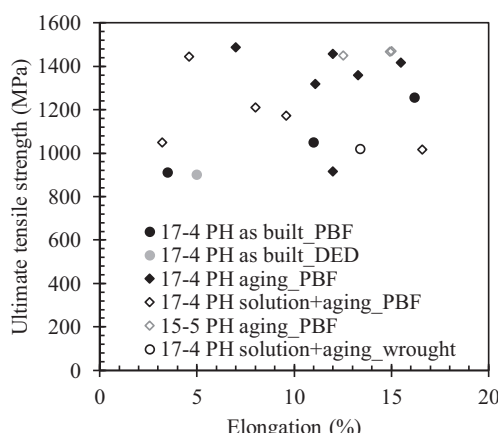


**Fig. 56.** Ultimate tensile strength as a function of elongation in as-built and heat treated PH stainless steels. Data from [Tables 13 and 14](#).

The dependence of Vickers hardness (HV) on chemical composition is shown in Fig. 59. A form of the nickel equivalent ( $Ni_{EQ}$ ) [498] was combined with a constrained multivariate linear regression analysis to elements that are not included in the  $Ni_{EQ}$  expression [499] using independent experimental data [180,305,326,378,382,412,454,494,500–509]. The final expression, coined as  $\varphi$ , was shown to be:

$$\begin{aligned} \varphi = & Ni + 0.65Cr + 0.98Mo + 1.05Mn + 0.35Si + 12.6C - 6.36Al + 3.80B + 0.01Co + 0.26Fe + 7.06Hf \\ & + 1.20Nb + 4.95Ta + 5.78Ti + 2.88W \end{aligned} \quad (31)$$

with each element expressed in weight percentage. The expression was shown to be valid in the following maximum concentration of elements: 6.5 wt% Al, 3.75 wt% B, 0.5 wt% C, 19.2 wt% Co, 21.8 wt% Cr, 24.7 wt% Fe, 1.5 wt% Hf, 0.48 wt% Mn, 9.75 wt% Mo, 5.1 wt% Nb, 4.25 wt% Si, 6.35 wt% Ta, 4.7 wt% Ti and 4.9 wt% W. It is interesting to note that when the effects of cooling rates and resulting microstructures are neglected, an approximate relationship between composition and hardness can still be obtained and used with a reasonable degree of accuracy. This finding highlights the importance of chemical composition and its influence on a commonly measured mechanical property. Similar analyses have also been established for steels and aluminum alloys [499].

#### 4.3. Titanium alloys

Titanium alloys have been widely studied in the field of AM due to their attractiveness for aerospace applications. More specifically, Ti-6Al-4V has received the most attention of any other alloy due to its high strength-to-weight ratio. Many investigations of Ti-6Al-4V focus on the direct relations between mechanical properties and either processing parameters or microstructure. The most important parameters in determining microstructure and resulting properties are those that influence the thermal history and cooling rates. For Ti-6Al-4V, even the smallest changes in cooling rates can have significant effects on mechanical properties [510]. Important factors include process parameters, build geometry and size and surrounding conditions. For example, Zhao et al. [511] showed that component size had a significant effect on the mechanical properties in PBF-EB of Ti-6Al-4V. In particular, small samples (on the order of 1.7 mm in diameter), had approximately 20% higher strength and 80% lower ductility compared to larger samples (on the order of 7 mm in diameter). This difference was attributed to thinner ductile  $\alpha$ -laths (0.4  $\mu$ m in the small components compared to 1.4  $\mu$ m in the large components) due to faster cooling rates and a larger relative pore size compared to the cross-sectional area in the small samples compared to the larger samples [511].

Regarding variations in processing parameters in PBF-EB, Hrabe et al. [512] found that increased energy input led to larger melt pool size, which resulted in a lower temperature gradient and therefore increased  $\alpha$  lath thickness and prior- $\beta$  grain size. The increases in microstructural features with these processing parameter variations led to decreased yield strength, ultimate tensile strength and hardness.

AM process related factors such as defects, build location and scanning strategies can also directly impact mechanical properties. For example, Galarraga et al. [513] found that the internal porosity of samples fabricated by PBF-L was dependent on location of the sample in the build platform. The porosity of samples in the middle of the build plate (0.25 vol%) was more than twice as high as that in samples on the edge of the build plate (0.09 vol%). Additionally, it was found that non-spherical lack-of-fusion pores, which often contain partially melted particles, were more detrimental to mechanical properties in the as-built, transverse direction than in the longitudinal direction, due to the fact that the long axis of these pores is oriented in the longitudinal direction, so the sharp edges of these flat pores act as stress risers when tension is applied in the transverse direction, but not when tension is applied along the long axis of the pores. As a result, vertical, or transverse samples had 28% lower elongation than horizontal, or longitudinal, samples [513].

Monotonic mechanical properties of as-deposited AM Ti-6Al-4V are given in Table 16, with post-treated Ti-6Al-4V properties given in Table 17. The tensile strength versus ductility in as-deposited and heat-treated Ti-6Al-4V is given in Fig. 60 [17,150,213,359,394,435,442,475,486,511,513–545]. The lack of a negative trend in this data may be partially attributed to the low strain hardening behavior of Ti-6Al-4V, which means that large variations in ductility do not correspond to significant changes in strength. Additional scatter can be attributed to differences between processes, various parameters used, efficiency of heat sources and build geometry from which samples were extracted.

To examine potential anisotropy of mechanical properties, a plot of tensile strength along the transverse direction versus that along the longitudinal direction is given in Fig. 61(a) [17,150,435,442,511,513,515,516,521,524,534,535,538,539,544,546]. A strong trend in neither anisotropy nor isotropy can be observed, which can again be attributed to the low strain hardening behavior of Ti-6Al-4V. The ductility along the transverse direction versus longitudinal direction is given in Fig. 61(b) [17,150,435,442,511,513,514,516,521,524,534,535,538,539,544,545], which highlights the scatter in ductility. While some scatter in ductility is expected on conventionally processed alloys, scatter in AM materials can be amplified by the processing conditions and the presence of porosity, internal defects and residual stresses that can result in micro-crack formation.

Finally, to examine processing-property relationships, the tensile strength and ductility are plotted versus linear heat input in Fig. 62(a) and (b), respectively. The data shows a weak trend in which increasing linear heat input results in a slight decrease of tensile strength. However, there is no notable trend between linear heat input and ductility [17,150,378,442,475,511,515,516,518–523,528,544–547].

**Table 15**

Summary of mechanical properties of Ni-base alloys fabricated by AM in literature, compared to traditionally processed counterparts, where HT=heat treated.

Alloy	P (W)	$v$ (mm/s)	H (J/mm)	Orientation	E (GPa)	$\sigma_y$ (MPa)	$\sigma_{uts}$ (MPa)	Elongation (%)	HV	Ref.	
<i>Powder bed fusion – laser heat source</i>											
Invar 36	400	1800–4300	0.22	As-deposited	Long. Transv.	400 340	535 455	14 30		[492]	
				HT	Long.	311	447	32			
Inconel 625	200	800–1200	0.25	HIP	Long. Transv.	380 360	900 880	58 58	347 296	[491]	
Inconel 625	50	130	0.38	As-deposited	Long. Transv.	$202.24 \pm 4.12$ $140.66 \pm 8.67$	$800 \pm 20$ $1070 \pm 60$	$1030 \pm 50$ $720 \pm 30$	8–10 8–10		[496]
Haynes 230	200	450–1200	0.44	As-deposited	Long. Transv.	$205 \pm 4$ $152 \pm 1$	$798 \pm 5$ $656 \pm 4$	$1102 \pm 6$ $941 \pm 2$	28 ± 1 32 ± 3		[493]
<i>Powder bed fusion – electron beam heat source</i>											
Inconel 625	1800	$10^4$	0.18	As-deposited HIP	Transv. Transv.	410 330	750 770	44 69	224	[491]	
<i>Directed energy deposition – powder feedstock</i>											
Inconel 718	–	–	–	As-deposited	Long.	650	1000	38% (Reduction in area)		[497]	
				HT	Long.	1257	1436	13% (Reduction in area)			
				HT+ HIP	Long.	1155	1380	20.4% (Reduction in area)			
Inconel 718	2350	8	294	As-deposited	Long.	590	845	11		[490]	
				HT	Long.	1133	1240	9			
					Long.	1170	1360	18			
<i>Directed energy deposition – wire feedstock</i>											
Inconel 625		5		As-deposited	Long. Transv.	180		$722 \pm 17$ $684 \pm 23$	$42.27 \pm 2.4$ $40.13 \pm 3.7$	240–270	[399]
Inconel 718		5		As-deposited	Long.	$154 \pm 1$	$473 \pm 6$	$828 \pm 8$	28 ± 2		[494]
Inconel 718				As-deposited	Long.	163	666	1022	26.1		[495]
				HT	Long.	24.1	947	1242	23.5		
				HT	Long.	25.8	932	942	22.2		
<i>Traditionally processed</i>											
Inconel 718	Cast - typical					915	1090	11	266 (max)	[681–683]	
	Annealed and Aged - minimum					862	1034	20	318		
Inconel 625	Cast - typical					350	710	48	266 (max)	[386,682–684]	
	Annealed - typical					430	940	51.5	145 (min)		
Invar 36	Cast - typical					265	483	44	–	[497,685]	
	Annealed - typical					260	470	37	131		

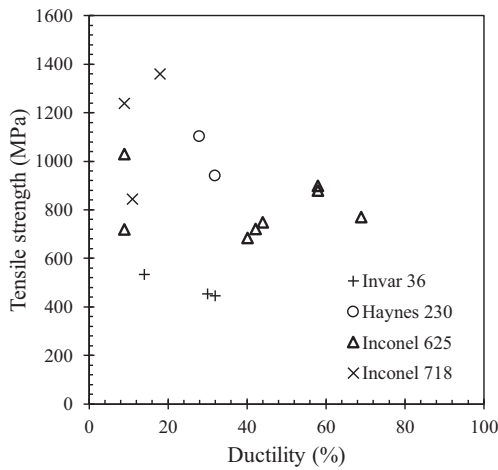


**Fig. 57.** Tensile strength versus uniaxial tension ductility for Ni-base alloys fabricated via AM. Data from Table 15.

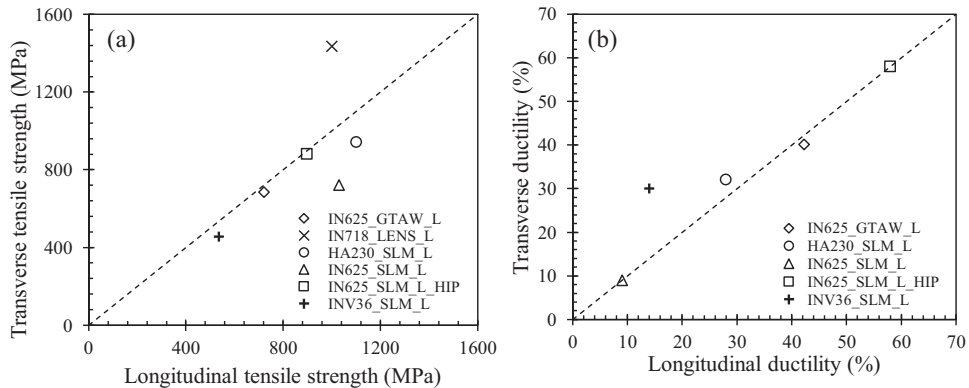


**Fig. 58.** Determination of the presence of mechanical anisotropy in additively manufactured Ni-base alloys with (a) transverse versus longitudinal tensile strength and (b) transverse versus longitudinal ductility. Data from Table 15.

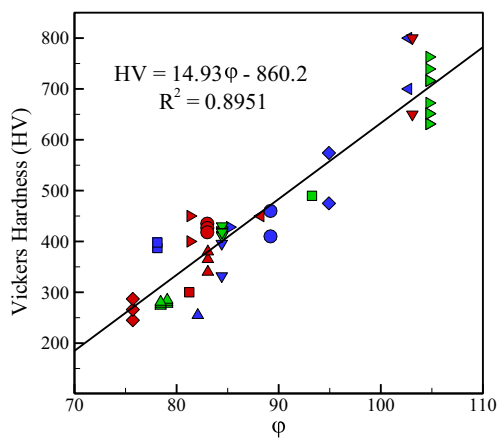


**Fig. 59.** As-deposited HV [180,305,326,378,382,412,454,494,500–509] as a function of  $\phi$ , which depends on the chemical composition of nickel-based AM alloys.

**Table 16**

Mechanical properties of as-deposited Ti-6Al-4V parts fabricated by AM compared to cast and annealed Ti-6Al-4V.

AM System	P (W)	v (mm/s)	H (J/mm)	Orientation	E (GPa)	$\sigma_y$ (MPa)	$\sigma_{uts}$ (MPa)	Ductility (%)	HV	Ref.
<i>Powder bed fusion – laser heat source</i>										
Realizer PBF-L	200	1000	0.20	Long. Transv.	1220 1200	1150 1300	6 6 ± 1			[511]
Renishaw AM250	157	225	0.70	Long. Transv.	115 ± 6 119 ± 7	978 ± 5 967 ± 10	1143 ± 6 1117 ± 3	11.8 ± 0.5 8.9 ± 0.4		[442]
<i>Powder bed fusion – electron beam heat source</i>										
Arcam A1	50– 3500	3000	0.02	Long. Transv.	783 ± 15 812 ± 12	833 ± 22 851 ± 19	2.7 ± 0.4 3.6 ± 0.9			[515]
Arcam A2	7000	1000	7.0	Long. Transv.	890 ± 5 880 ± 10	970 950 ± 5	12 ± 1.2 14 ± 1.2			[544]
Arcam S12	–	–	–	Long. Transv.	982.9 ± 5.7 984.1 ± 8.5	1029.7 ± 7.0 1032.9 ± 12.9	12.2 ± 0.8 9.0 ± 0.26	372.0 ± 7.2 367.6 ± 8.3		[513]
Arcam A2				Long. Transv.	1006 1001	1066 1073	15 11			[516]
Arcam Q10				Long. Transv.	973 1051	1032 1116	15 12			[516]
<i>Directed energy deposition – powder feedstock</i>										
Custom	2000	10.6	189	Long. Transv.	115 ± 5 113 ± 5	961 ± 40 916 ± 34	1072 ± 33 1032 ± 31	17 ± 4 19 ± 4		[17]
<i>Directed energy deposition – wire feedstock</i>										
Custom	3500			Long. Transv.	980 ± 70 860 ± 10	1060 ± 70 935 ± 15	4 ± 0.8 9.6 ± 1.2			[544]
Custom	2625	7.5	350	Long. Transv.	818 ± 30 792 ± 15	895 ± 40 870 ± 20	4 ± 1 11 ± 3.5	355 ± 28		[545]
Custom	2192.3	10	438	Long. Transv.	890 ± 30 860 ± 10	965 ± 15 935 ± 20	8 ± 2 17 ± 3.5	341 ± 15		[545]
EOS DMLS	170	1250	0.14	Long. Transv.	1099 1162	1186 1260	8.47 8.07			[518]
<i>Traditionally fabricated</i>										
Cast – typical					896	1000	8	200		[510,686]
Annealed – typical					855	930	12	202		[686,687]

P = Laser power, v = Scanning speed, H = Linear heat input,  $\rho$  = Density, E = Elastic modulus,  $\sigma_y$  = Yield strength,  $\sigma_{uts}$  = Ultimate tensile strength, HV = Vickers hardness.

**Table 17**

Mechanical properties of post-processed Ti-6Al-4V parts fabricated by AM.

Heat treatment	Orientation	E (GPa)	$\sigma_y$ (MPa)	$\sigma_{uts}$ (MPa)	Ductility (%)	Ref.
<i>Powder bed fusion – laser and electron heat sources</i>						
750 °C heat treatment in vacuum furnace, furnace cool	Long. Transv.	113 109	964 1058	1041 1114	7 3 ± 2	[514]
1203 K, 130 MPa, 3hr	Transv.	–	850	900	12	[511]
650 °C, 4 h. in Ar; furnace cool to room temperature	Long. Transv.	–	1195 ± 19.89 1143 ± 38.34	1269 ± 9.57 1219 ± 20.15	5 ± 0.52 4.89 ± 0.65	[486]
730 °C, 2 h in N <sub>2</sub>	Long. Transv.	113 ± 9 117 ± 6	958 ± 6 937 ± 9	1057 ± 8 1052 ± 11	12.4 ± 0.7 9.6 ± 0.9	[442]
843 °C, 2 h, furnace cool	Long. Transv.	–	845 810 ± 40	920 860 ± 60	17.5 ± 0.5 15.5 ± 1.5	[544]
1203 K, 130 MPa, 3 h	Transv.	–	890	980	17	[511]
<i>Directed energy deposition – wire feedstock</i>						
843 °C, 2 h, furnace cool	Long. Transv.	–	920 ± 20 870 ± 40	990 ± 15 940 ± 40	9.75 ± 2 11.25 ± 2	[544]
600 °C, 4 h, furnace cool	Long. Transv.	–	875 ± 45 846 ± 5	940 ± 40 927 ± 5	7.5 ± 1.8 11 ± 3.2	[545]
843 °C, 2 h, furnace cool	Long. Transv.	–	822 ± 42 812 ± 12	897 ± 43 884 ± 14	12.5 ± 1 10.6 ± 4	[545]
704 °C furnace cool to below 538 °C	Long. Transv.	–	805 ± 10 790 ± 10	920 ± 20 890 ± 20	12 ± 2 16 ± 2	[517]

E = Elastic modulus,  $\sigma_y$  = Yield strength,  $\sigma_{uts}$  = Ultimate tensile strength.

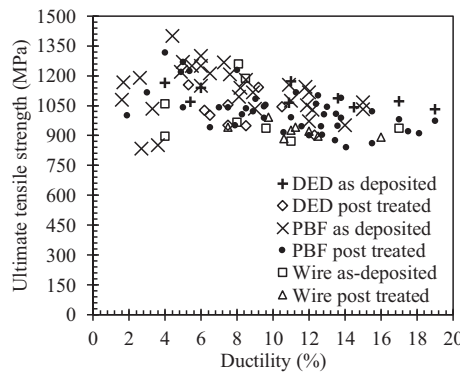


**Fig. 60.** Tensile strength versus ductility in powder and wire DED and PBF of Ti-6Al-4V in as-deposited and heat-treated conditions. All orientations are considered for each technique. Data from [698], Tables 16 and 17.

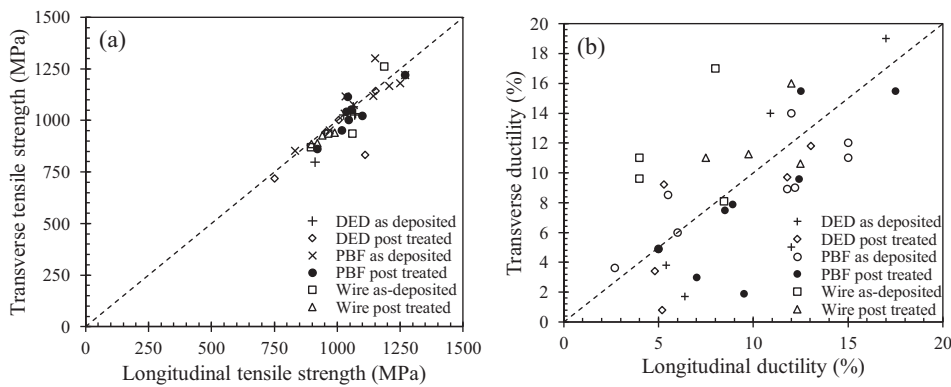


**Fig. 61.** Measure of anisotropy in additively manufactured Ti-6Al-4V with (a) transverse versus longitudinal tensile strength [17,150,435,442,511,513, 515,516,521,524,534,535,538,539,544,546] and (b) transverse versus longitudinal ductility) [17,150,435,442,511,513,514,516,521,524,534,535,538,539, 544,545].

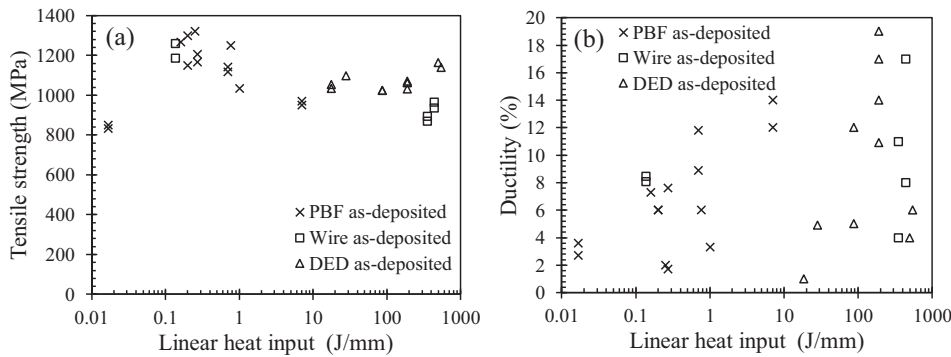


**Fig. 62.** (a) Tensile strength and (b) ductility of Ti-6Al-4V as a function of linear heat input [17,150,378,442,475,511,515,516,518–523,528,544–547].

#### 4.4. Lightweight alloys

##### 4.4.1. Aluminum alloys

The most commonly studied Al alloy in AM is AlSi10Mg. Table 18 shows the ultimate tensile strength and ductility values in additively manufactured AlSi10Mg are generally higher than or equal to as-cast and high pressure die cast (HPDC) AlSi10Mg, which can be attributed to the fine microstructures seen in AM samples [386,548–550]. As shown in Fig. 63(a), there is no notable anisotropy in the tensile strength in the additively manufactured AlSi10Mg; however, Fig. 63(b) shows

**Table 18**

Processing parameters and mechanical properties of Al alloys fabricated by AM compared to their traditionally processed counterparts.

Alloy	P (W)	v (mm/s)	H (J/mm)	Post Treatment	Orient.	E (GPa)	$\sigma_y$ (MPa)	$\sigma_{uts}$ (MPa)	Ductility (%)	HV	Ref.
<i>Powder bed fusion</i>											
AlSi10Mg	250	500	0.50	As-built	Long. Transv.	250 240	350 280	2.5 1.2	145	[688]	
				T6 <sup>a</sup>	Long. Transv.	285 290	340 330	4.5 2.2	116		
AlSi10Mg	250	500	0.50	As-built	Long. Transv.	125 140	250 270	6.6 4.6	75	[688]	
				T6 <sup>a</sup>	Long. Transv.	295 285	350 340	6.5 4.9	118		
AlSi10Mg				As-built	Long. Transv.	75 ± 10 70 ± 10	270 ± 10 240 ± 10	460 ± 20 460 ± 20	9 ± 2 6 ± 2	119 ± 5	[689]
					2 h/300 °C	Long. Transv.	70 ± 10 60 ± 10	230 ± 15 230 ± 15	345 ± 10 350 ± 10	12 ± 2 11 ± 2	
AlSi10Mg	200	1400	0.14	As-built	Long. Transv.	68 ± 3 396 ± 8	391 ± 6 396 ± 8	5.55 ± 0.4 3.47 ± 0.6	127	[548]	
AlSi10Mg	200	1400	0.14	As-built	Long. 6h/175°C	68 ± 3 66 ± 5	396 ± 8 399 ± 7	3.5 ± 0.6 3.3 ± 0.4	136 ± 9 152 ± 5	[690]	
AlSi10Mg	195	800	0.24	2 h/300 °C	Long. Transv.	252 ± 11 240 ± 5	348 ± 5 347 ± 6	6.6 ± 0.3 5.1 ± 0.3	105 ± 2 108 ± 1	[691]	
AlSi10Mg	195	800	0.24	2 h/300 °C	Long. Transv.	73 ± 1 72 ± 1	243 ± 7 231 ± 3	330 ± 3 329 ± 2	6.2 ± 0.3 4.1 ± 0.2	105 ± 2 108 ± 3	[643]
AlSi10Mg	200	571	0.35	As-built	Transv. 6 h/160 °C	330 ± 10 292 ± 4	1.4 ± 0.3 3.9 ± 0.5			[563]	
AlSi10Mg	175	1025	0.17	As-built	Long. Transv.	250 225	340 320	1.2		[550]	
AlSi10Mg	400	1000	0.40	2 h/300 °C	Long. Transv.	182 ± 5 184 ± 5	282 ± 5 288 ± 5	25.2 ± 1 18.3 ± 1		[692]	
AlSi10Mg		1000		2 h/300 °C	Long. Transv.	70.2 70.7	169 169	267 273	9.1 8.2	94 ± 5	[693]
AlSi10Mg	370	1300	0.28	2 h/300 °C	Long. Transv.	181 177	284 285	18		[549]	
AlSi10Mg	370	1300	0.28	2 h/300 °C	Long. Transv.	182 180	285 287	18			
AlSi10Mg	370	1300	0.28	2 h/300 °C	Long. Transv.	182 180	284 287	16			
AlSi12	320	1455	0.22	As-built	Transv. 6 h/200 °C	260 260	375 340	2.8 2.4		[645]	
					6 h/300 °C 6 h/350 °C 6 h/400 °C 6 h/500 °C	170 120 100 95	275 190 155 140	5 9.2 15 13			
AlSi12	350	930	0.38	As-built	Transv. 240 °C	369.3 ± 3.4 361.1 ± 4.5	202.2 ± 4.3 201.5 ± 3.7	4.38 ± 0.16 4.05 ± 0.15		[562]	
AlSi12	350	930	0.38	As-built	Transv. 240 °C	418.9 ± 9.6 372.3 ± 7.2	220.5 ± 9.4 218.0 ± 6.9	3.91 ± 0.27 3.41 ± 0.29			
AlSi12	350	930	0.38	As-built	Transv. 200 °C	78.7 ± 2.3 76.5 ± 1.8	220.5 ± 9.5 218.0 ± 3.9	3.91 ± 0.27 3.41 ± 0.16		[694]	
Al-Sc-Mg	195			4 h/325 °C	Long. Transv.	515 500	530 525	15 13	177	[646]	
Al-Cu-Mg	200	83.3	2.40		Transv.	276.2 ± 41	402.4 ± 9.5	6 ± 1.4	111	[650]	
<i>Wire-fed</i>											
ER2319					Long. Transv.	114 106	263 258	18.3 15.6	68.3	[695]	
<i>Traditionally processed</i>											
AlSi10Mg				HPDC	71	160–185	300–350	3–5	95–105	[696]	
				HPDC-T6	71	285–330	330–365	3.5	130–133		
AlSi12				Die Cast	71	131	290	3.5		[697]	

P = Laser power, v = Scanning speed, H = Linear heat input,  $\rho$  = Density, E = Elastic modulus,  $\sigma_y$  = Yield strength,  $\sigma_{uts}$  = Ultimate tensile strength, HV = Vickers hardness.

<sup>a</sup> Refers to solution treatment at 525 °C for 6 h, water quenching and subsequent aging at 165 °C for 7 h.

the elongation to failure is higher in the longitudinal direction than the transverse direction. Another commonly used Al alloy used in AM in which mechanical properties have been widely reported is AlSi12. A comparison between the reported strength and ductility measurements between the alloys is shown in Fig. 64.

As discussed in previous sections, AM-induced defects have a great impact of mechanical properties. Regarding the formation of defects, Aboulkhair et al. [189] studied the link between pore shape and scanning speed in AlSi10Mg deposited using PBF-L. It was shown that at speeds higher than 500 mm/s with a laser power of 100 W, lack of fusion porosity and

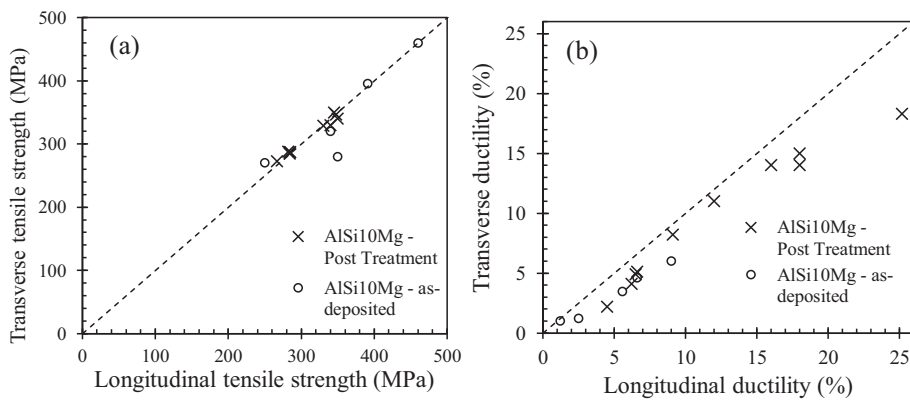


**Fig. 63.** (a) Transverse versus longitudinal tensile strength, and (b) transverse versus longitudinal ductility in additively manufactured AlSi10Mg. Data from Table 18.

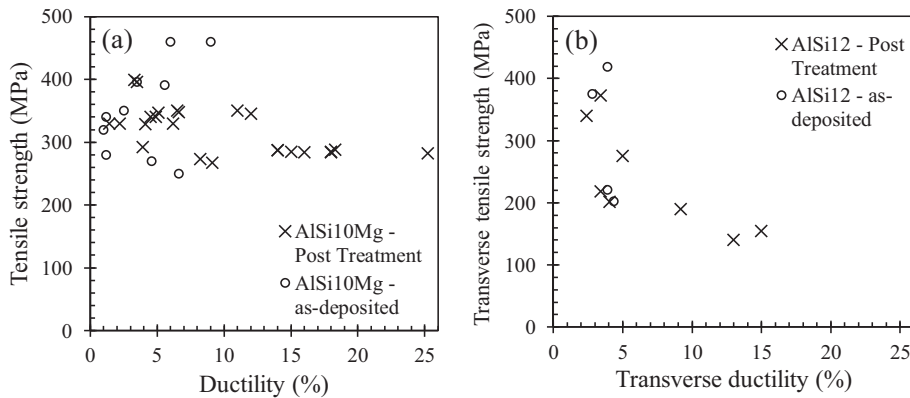


**Fig. 64.** Tensile strength versus ductility in (a) AlSi10Mg and (b) AlSi12 in as-deposited and heat-treated conditions. All orientations are considered for AlSi10Mg, while all data reported for AlSi12 is in transverse orientation. Data from Table 18.

unmelted particles were present, while below this speed spherical porosity was more prominent. A relative density of 99.77 ± 0.08% was achieved with a laser scanning speed of 500 mm/s, a hatch spacing of 50 µm, laser power of 100 W, a layer thickness of 40 µm, and a pre-sinter scan strategy [189].

Due to the strong interactions between aluminum and oxygen at relatively low temperatures, surrounding environment conditions can become especially important when processing aluminum alloys to achieve target properties. Although there are few studies, Bauer et al. [551] investigated the effect of oxygen on AlSi10Mg deposited via PBF AM and aged for 6 h at 170 °C. Samples deposited in a build chamber with controlled oxygen content of 30 ppm O<sub>2</sub> resulted in different properties depending on the initial oxygen content of the powder. Powder with less oxygen (0.027 wt%) and 40 vol% spherical particles resulted in a yield strength of 335 MPa, while powder with more oxygen (0.095 wt%) and only 10 vol% spherical particles had a yield strength of 311 MPa. However, the tensile elongation to failure was approximately 7% for both materials. When processing in an uncontrolled O<sub>2</sub> environment (>1000 ppm), the yield strength of the low oxygen content powder was 326 MPa and 291 MPa for the high oxygen powder, however the ductility was greater in the high oxygen content powder (6.7%) than in the low oxygen powder (6.1%) [551].

Attempts have been made to deposit Al 6061, which is a precipitation hardened alloy containing magnesium and silicon. Fulcher et al. [552] used direct metal laser sintering (DMLS) to fabricate Al 6061, but found large intergranular cracks formed during deposition due to anisotropic contraction in the solidified material. Due to both the elongated grains that grew through build layers and the corresponding locations of intergranular cracks, the mechanical behavior was anisotropic in that the ultimate tensile strength was significantly lower in the longitudinal direction (42 MPa) compared to that in the transverse direction (230 MPa).

#### 4.4.2. Magnesium alloys

Conventional welding and joining techniques require low heat inputs within a narrow range to successfully process Mg alloys. Thus far, there has been minimal research on magnesium and its alloys made by AM due to the difficulty in process-

ing. However, there have been studies on optimizing AM processing parameters for the fabrication of Mg via AM. Ng et al. [553] performed optimization of the deposition of magnesium using PBF-L by studying the behavior of 20 mm long single tracks. They studied the impact of varying energy density (from 1.27 to  $7.84 \times 10^9$  J/m<sup>2</sup>) as well as the impact of using a continuous versus a pulsed laser heat input. For both continuous and pulsed laser, the grain size grew from 2.3 to 4.9 μm with increasing energy density. However, the hardness decreased from 88.7 to 66.2 HV when using a continuous laser, and 96.9–68.3 HV when using a pulsed laser input, with increasing energy density. Zhang et al. [554] used PBF-L to manufacture Mg-9wt%Al, whose as-deposited microstructure contained Mg, Mg<sub>17</sub>Al<sub>12</sub> and MgO. They achieved relative densities of up to 82% using a laser power of 15 W and scan speed of 20 mm/s. Hardness values reached 75 HV compared to 60 HV of as-cast AZ91 alloy. Hu et al. [555] investigated PBF-L of pure magnesium achieving an as-deposited sample density of 95%. They varied scanning speed (optimal 0.1 m/s), laser beam energy (optimal 90 W), hatch spacing (optimal 0.1 mm), laser spot diameter (optimal 0.1 mm), and powder layer thickness (optimal 0.03 mm). Powder size was also varied from 400 mesh to 250 mesh, where the coarser powder (average particle diameter of 43.3 μm) increased the relative density over that of the finer powder (95.28–96.13%) and microhardness (44.75–52.43 HV). These property improvements were attributed to better flowability of the coarse powder, resulting in a more consistent layer thickness, and less powder being blown away from gas flow during processing.

#### 4.5. Fatigue in AM

While monotonic tensile properties are most commonly examined in additively manufactured components, there have been studies on fatigue behavior of some alloys made by AM. Due to its potential to be used in biomedical and aerospace applications, the fatigue properties of additively manufactured Ti-6Al-4V are of critical importance and have been examined most thoroughly. Fatigue properties inherently have much scatter in experimental data regardless of the type of processing. In AM, this scatter can be amplified due to the presence of common defects or intentionally introduced geometrical nonuniformities. The areas of research regarding fatigue properties in AM can generally be broken down into investigations on surface related defects, internal defects and the effects of post processing on fatigue life.

Fatigue behavior concerns the mechanical response of a material that is subjected to cyclic loading. Applied stresses are usually tensile or a combination of tension and compression. In a material completely free of porosity or surface related defects, fatigue failure occurs in a catastrophic manner when voids form due to the pile up of dislocations and propagate outward until complete fracture. When stress concentrators such as surface or internal defects are introduced, the number of cycles required for fracture of a specimen can be greatly reduced, thus decreasing fatigue life.

Surface roughness is currently a major drawback of AM, as it provides stress concentrations that serve as crack nucleation sites, thus limiting fatigue performance. Greitemeier et al. [556] compared the high cycle fatigue properties of Ti-6Al-4V manufactured via PBF-EB and direct metal laser sintering (DMLS) and found that reducing surface roughness increased fatigue performance for both (DMLS reached  $10^7$  cycles at 550 MPa, EBM at 260 MPa). Similarly, Spierings et al. [481], studied the fatigue performance of two stainless steels, 316L and 15-5PH, manufactured via PBF-L. The fatigue limit of 316L in the as-built condition was 200 MPa, while machining the surfaces increased the fatigue limit to 250 MPa. Machining and polishing the samples further increased the fatigue limit to 260 MPa, which is greater than the fatigue limit of wrought 316L (141–207 MPa). Additively manufactured and machined 15-5PH reached a fatigue limit of 850 MPa, which was superior to the fatigue limit of wrought 15-5PH of 270–372 MPa. In almost all cases, it can be concluded that a smoother surface yields better fatigue performance than the as-built rough surfaces.

Similar to surface roughness, internal defects have a significant impact on the fatigue life of AM components. As discussed previously, lack of fusion defects and porosity are the two most common internal defects seen in parts built by AM. The morphology, location, size and volume fraction of internal defects are the primary variables that affect fatigue performance. Elongated voids with sharp corners, like those seen in lack of fusion, are the most detrimental type of internal defects as the stresses at the crack tips can be many times higher than the applied stress. Johnson et al. [557] studied DED-L of IN 718, and showed that samples with observable lack of fusion porosity exhibited fatigue lives two to three times shorter than wrought counterparts at comparable strain amplitudes. Sterling et al. [558], who studied the DED-L of Ti-6Al-4V, concluded that large pores close to the surface and with irregular or sharpe features had the most negative impact on fatigue performance. Although Amsterdam and Kool [539] found that IN 718 deposited by AM and subsequently heat treated compared to annealed and aged IN 718 had similar fatigue strength (480 MPa and 500 MPa, respectively) at  $2 \times 10^7$  cycles [559], it is important to note that crack initiation was found to occur near the sample surface in areas with greater amount of porosity, where both gas pores and lack of fusion pores were observed on the fracture surfaces. In a study on multiaxial fatigue behavior of PBF-L Ti-6Al-4V, Fatemi et al. found that pores near the surfaces of samples were the most dominant factor in shortening the fatigue lives of specimens under all loading conditions examined [560]. A review by Yadollahi and Shamsaei on the primary challenges for AM of increased fatigue resistant materials indicates that large, irregular voids, especially those near the surface, are the major life limiting factor for the fatigue lives of AM components [561].

Siddique et al. [562] studied the as-built fatigue performance of PBF-L AISI12 samples built with different build plate temperatures and found that samples built without an elevated build plate temperature had the best fatigue properties ( $1.8 \pm 0.9 \times 10^5$  cycles at 120 MPa); however, they also had the largest scatter in the fatigue data. This finding was attributed to the increase in lack of fusion porosity (>50 μm) at the edges (within 250 μm of the samples surface) of samples fabricated

with the elevated build plate temperature. While internal gas pores do not have as drastic of an effect as lack of fusion pores, large amounts of gas porosity can still have a negative effect on fatigue performance. The reason gas pores are less detrimental is due to their spherical morphology and small size.

Other internal features of AM parts besides lack of fusion defects and gas porosity can also influence fatigue performance. Brittle secondary phases such as intermetallic compounds and oxides can nucleate cracks that easily propagate into the larger matrix phases, especially when these phases are irregular shaped. For example, it was found that two sizes of oxides were most prevalent, larger oxides (microns long) and small, sub-micron oxides in AlSi10Mg made by PBF-L [549]. The large oxides were formed via oxidized vapor or spatter during fabrication while the smaller inclusions were pre-existing oxides in the powder. When the larger oxides were observed, more pores ranging from several microns to tens of microns in size were present.

Significant efforts have been made to study the effect of post processing heat treatments and HIP for improving fatigue properties. Heat treatments have the ability to coarsen microstructural features (e.g.,  $\alpha$ -lath widths and prior- $\beta$  grains in Ti-6Al-4V) and relieve the residual stresses incorporated during deposition. Maskery et al. [563] studied as-built PBF-L AlSi10Mg samples which were post heat treated with a solution treatment to coarsen the microstructure and soften the as-built material. In fatigue loading, the as-built and heat-treated samples were failed after  $10^6$  cycles at 85 MPa and 134 MPa, respectively, indicating that heat treatment improved fatigue strength.

HIP treatments both coarsen the microstructure and close internal pores, such as gas porosity and small lack of fusion defects. Leuders and co-workers [532] studied the fatigue crack growth in Ti-6Al-4V, showing the effect of heat treatment and hot isostatic pressing (HIP) on the fatigue threshold and the rate of crack growth. They found that heat treatment and HIP resulted in similar increases in the fatigue performance of Ti-6Al-4V made by AM. Since both general heat treatment and HIP coarsen the microstructural features and relieve residual stresses, but only HIP closes pores, they concluded that the closing of pores was of secondary importance to coarsening the microstructure and relieving residual stresses.

In a similar study [556], the effect of HIP alone was found to not have a significant effect on fatigue properties on samples with as-built surface finishes. However, milled and HIPed specimens showed improved fatigue properties for both EBM and DMLS. Additionally, in the HIPed/milled samples, because the internal defects were successfully closed, fracture occurred at locations of microstructural inhomogeneity rather than at defects, similar to what is observed in annealed/milled samples [556]. Similarly, Riemer et al. [564] found that the combination of reducing surface roughness while closing internal pores had the largest impact on fatigue performance of SS316L processed by PBF-L. The fatigue limit in the as-built condition was found to be 108 MPa, which was increased to 267 MPa with surface machining, and further increased to 294 MPa with machining followed by annealing at 650 °C, or to 317 MPa when the sample was machined and subjected to HIP. The surface finish increased fatigue performance as reducing the roughness reduced the number of notches that could lead to crack initiation, while the heat treatments reduced residual stresses and HIP closed pores in the sample.

Data on the anisotropy of fatigue properties is lacking, however Brandl et al. [565] studied the high cycle fatigue performance of AlSi10Mg made by PBF-L in the longitudinal and transverse direction, showing that the fatigue properties were superior in the longitudinal direction (reached  $10^6$  cycles at 210 MPa) than in the transverse direction (reached  $10^6$  cycles at 118 MPa).

A comprehensive review of fatigue in additively manufactured Ti-6Al-4V is given in [566]. In this review, fatigue life curves for conventionally-processed Ti-6Al-4V and that made by different AM methods, including PFB-L, PBF-EB, and DED with powder were compared. The comparisons showed that the largest impact on fatigue life was the surface roughness. In particular, in every case, by machining the rough as-built surface, which comes from both the stepped layers in AM and un-melted powder on the surface, improved the fatigue life curves by reducing the number of crack nucleation sites. Additionally, heat treatment and hot isostatic pressing (HIP) improved fatigue life. It is noted that among the studies, and within single studies, there was significant scatter in the fatigue life data, which can be attributed to variations in processing conditions (e.g., laser power, laser scanning speed, hatch spacing, layer height) and variations in internal porosity, including the overall volume fraction of pores, their shape, and their size distribution.

Fatemi et al., examined the effects of loading condition, surface roughness, and defects on the fatigue properties of PBF-L Ti-6Al-4V specimens (see Fig. 65). They found that compared to wrought counterparts, AM samples had significantly shorter fatigue lives in multiaxial loading conditions regardless of surface finish [560]. The exception was in low cycle fatigue (LCF) torsion tests, where PBF-L samples had longer lives than wrought material due to greater softening of the wrought material. Furthermore, machined AM surfaces had greater fatigue lives than as-built samples for all loading conditions, although the effect was not as important as the effect of internal and near surface defects. Specimens with the largest pores and overall porosity had the shortest fatigue lives. This study highlights the complexity of the factors that dictate the fatigue properties of AM components.

Yadollahi and Shamsaei identified additional challenges for determining fatigue properties of AM materials, including the variation in thermal histories from test coupons compared to complex in-service part geometries, which makes predicting full part performance based on the results of fatigue testing of simple coupons difficult [561]. Also, achieving homogenous microstructures and defect distributions in AM is difficult, resulting in highly anisotropic fatigue behavior. The authors suggested developing AM specific post-processing approaches such as adopting HIP and surface machining methods, as well as factoring in build part orientations, to leverage favorable microstructural and loading axes with respect to defect directions.

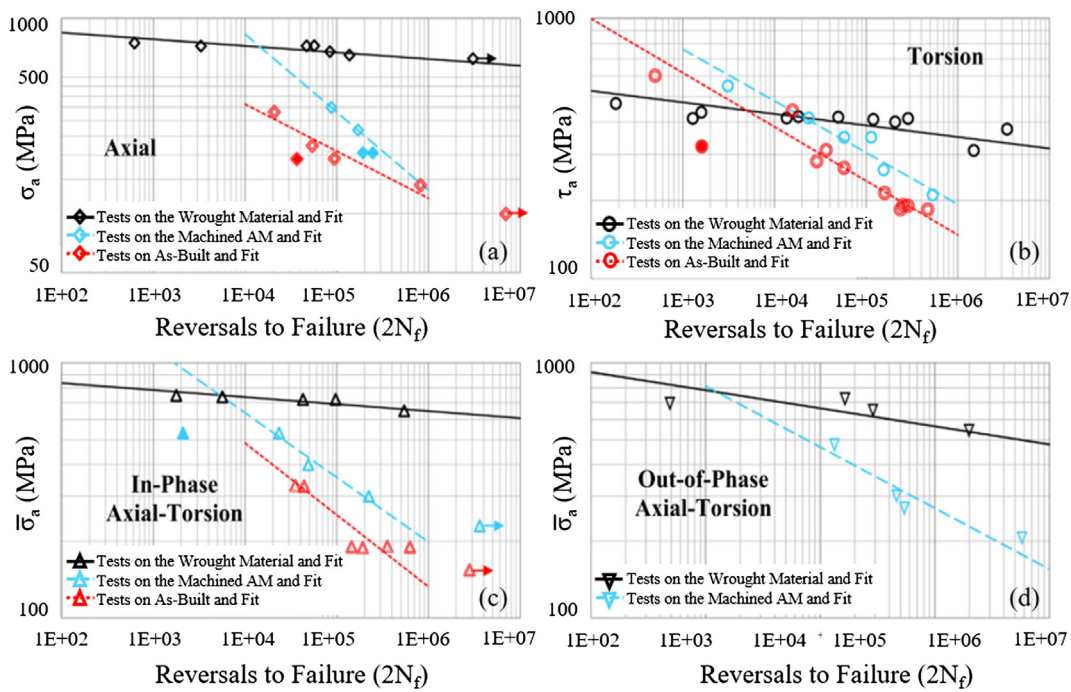


**Fig. 65.** Superimposed results of fatigue tests on wrought and AM materials under (a) axial loading, (b) torsion loading, (c) in-phase axial-torsion loading, and (d) 90° out-of-phase axial-torsion loading. von Mises equivalent stress is used for the combined tests. Excluded data points from line fittings are shown with solid symbols [560].

#### 4.6. Creep in AM

Similar to fatigue, the difference between creep properties of AM and conventionally processed parts is due to the presence of defects and fine microstructural features. However, due to complexities in creep testing, including the range of potential heat treatments, applied stresses, and test temperatures, as well as the paucity of studies available in the literature, no consistent trends can yet be derived for the creep behavior of additively manufactured metals.

Kuo et al. [567] found striking differences in the rupture life of IN718 processed by direct metal laser sintering in the as deposited (270 h), solution treated and aged (100 h) and directly aged (550 h). All mentioned conditions of IN 718 fell well below the rupture life of wrought IN 718 (1200 h). The varying times to rupture in additively manufactured Inconel 718 were attributed to the varying microstructures in each condition, namely the distribution and morphology of  $\delta$ -precipitates. The  $\delta$ -precipitates have an acicular needle-like shape in the solution treated and aged condition, which act as nucleation sites for damage accumulation and a decrease in creep life, whereas in the directly aged condition, the  $\delta$  precipitates remain round particles.

However, the creep behavior of IN 718 fabricated by PBF-L and subsequently heat treated has been found to be superior to that of conventionally cast and wrought IN 718 [568,569]. This improvement in properties is due to fact that a higher volume of uniformly-dispersed fine  $\gamma''$  and  $\gamma'$  precipitates formed in the additively manufactured material compared to the conventionally processed IN 718. This formation of precipitates in AM suppressed the formation of the  $\delta$  phase. It has been found in IN 718 that when  $\delta$  phase is less than 45% phase fraction at grain boundaries the creep mechanism is due to wedge cracks and void formation, while above this percentage void growth and grain boundary sliding is the primary mechanism of creep [570]. Additionally, 0.50–0.65  $\mu\text{m}$  subgrains formed in the PBF-L process, which also improved the creep response [568]. The improvement in creep resistance in AM over cast or wrought IN 718 was independent of initial build orientation [569].

Creep of IN 738LC, another precipitation-strengthened nickel-base superalloy, manufactured via PBF-L has been found to be anisotropic [571,572]. Specimens manufactured in the transverse orientation with elongated grains aligned with the build direction were shown to perform as well as the lower bound of cast material [571], while those in the longitudinal orientation were noticeably inferior. The anisotropy was partly attributed to the anisotropic elastic properties due to the strong texture in the fine columnar grains [572]. The inferior creep behavior of the PBF-L material compared to its cast counterpart was mainly due to the fine grains, and variation in  $\gamma'$  precipitate size, morphology, and location in the former.

A study on a Co–28Cr–6Mo–0.23C–0.17N (CCM) alloy manufactured via PBF-EB was conducted by Sun et al. [573]. This CCM alloy consists of metastable  $\gamma$ -fcc (columnar morphology) and stable  $\varepsilon$ -hcp (equiaxed morphology) phases in the as-built condition. The material was transformed to completely  $\varepsilon$ -hcp prior to creep testing to avoid transformation during tests. Evaluation of creep was conducted in a temperature range of 650–800 °C and a stress range of 240–330 MPa. The creep

curves of the AM material exhibited all the typical stages of creep behavior, and fracture of the samples occurred in regions of finer grains. During the PBF-EB process the grains near the baseplate grow larger than those near the top due to the fact that the build chamber is kept at an elevated temperature (700 °C). It was found that  $\epsilon$ -grains in the as-built, bottom portion of the parts were larger than those produced by the post-processing transformation heat treatment. The study suggested that the creep mechanism of grain boundary sliding promoted initiation and propagation of voids at grain boundaries; therefore, that finer grains are detrimental to creep resistance. A two-step heat treatment that replicates the thermal history of the PBF-EB process was proposed as a method for enlarging grain size throughout the builds and avoiding failure in fine grained regions.

#### 4.7. Discussion

It is challenging to directly compare the microstructures and mechanical properties of components fabricated by AM due to the many variables involved in this fabrication technique. For example, if samples are made using the same powder bed fusion system, the thermal history of the part, and therefore structure and properties, will vary with laser power, laser scanning speed, layer height, hatch spacing, and laser spot size. Even if these parameters are kept consistent between builds, the thermal history is influenced by the laser scan strategy, which can often not be dictated by the user in commercial systems. The scan strategy depends on the placement of the components onto the substrate, but also what other components are being built in the same powder bed fusion build.

Additionally, the field lacks a standard for mechanical test methodology for comparing properties among studies. Therefore, even if processing parameters are held constant among studies or reported, the thermal history within a part will depend on the geometry of the part as well as potentially the geometry of the extracted test specimen. This means when one group extracts samples from flat coupons near the baseplate while another group extracts samples from vertical walls, the thermal history, microstructure, and mechanical properties will vary in these components. Finally, the size and shape of the extracted test specimen can be a key factor in disparate mechanical properties, since in additively manufactured materials, the grain sizes vary widely, such that sometimes they can be on the same order as the dimension of the test specimen. Therefore, the relative grain sizes with respect to sample dimensions must be considered and reported. In order for a full scientific understanding of processing, microstructure, and mechanical property relationships in AM to be obtained, it is imperative that future studies report the processing parameters and AM geometries, and extracted sample geometries when reporting mechanical properties. Ideally, the thermal history would also be monitored and reported to quantitatively link processing to structure.

### 5. AM of special materials

AM has a wide application to fabricate intricate components such as jewelry, dental crowns and electric connectors with precious metals like gold, silver, palladium and platinum. AM also has unique features to produce components of high melting point refractory alloys that are difficult to process using conventional methods. Recently, powder based AM processes are also employed to manufacture products with varying compositions in order to obtain better structure and properties. In this section, AM of these refractory alloys, precious metals and compositionally graded alloys are described.

#### 5.1. Refractory alloys

Refractory metal alloys such as tungsten, tantalum, niobium, molybdenum, vanadium, chromium and rhenium are the highest melting point metals and have BCC or HCP crystal structures. These metals and alloys have unique properties and applications that include high temperature strength, biocompatibility, low thermal expansion, superconductivity, high density and used in structural applications in high radiation environments. Refractory metals are reactive at elevated temperatures and can lose ductility when processed with insufficient shielding from atmospheric contamination. These alloys are often welded in vacuum using the PBF-EB. Development efforts for building of complex structures with these alloys suitable for use in extreme environments [574] in the aerospace and nuclear industries dates back to the 1960s. Limitations in applying these materials more widely include their high cost, a limited supply of commercial shapes, and difficulties in fabrication using conventional metal process technology. As a result, AM is a candidate technology to expand the use of these materials as it can reduce the need for conventional processing steps, produce commercial shapes and use significantly smaller quantities of expensive materials. Early work in the laser powder fusing of metals into complex shapes using computer models and control demonstrated the potential of the technology to refractory metal components [575,576]. Because of this work, subsequent technology advances focused on the development of high purity of spherical metal powders better suited for additive applications [577].

Tungsten alloys provide low thermal expansion and high strength at high temperatures and have found applications in furnace applications and components experiencing high heat flux. Due to its high density it has found application in radiation shielding, energy beam collimation and balance weight applications. While conventional processing often relies on high temperature sintering, high purity environments in AM enable the formation of complex shapes. Binder jet AM technology

may also be employed to form complex tungsten shapes. Tungsten displays brittle behavior at ambient temperatures limiting the use of conventional processing methods. Melting and solidification can result in large grain heterogeneity further contributing to its brittle behavior. A study performed using PBF-L processing of W powder mixed with 2.5% TiC, created a solid solution of Ti and C in a W matrix in an attempt to refine grain growth in the as-deposited material. Although micro cracking was observed in the as-deposited material, the report provides important details on parameter selection of the PBF-L process used to achieve wetting and prevent balling defects allowing deposition of bulk material [578]. The role of oxide contamination and consolidation of tungsten PBF-L processing was also studied in efforts to improve the density [579].

Tantalum, with a melting point of 2996 °C, is a ductile refractory metal offering biocompatibility and chemical resistance. Tantalum is used for medical applications such as scaffolds and coatings and is also suitable for high temperature heat shield and furnace applications. Tantalum can be applied over titanium substrates using the LENS process [580] to produce porous surfaces for bone implants. It has also been studied as a porous coating for CoCr alloys [581] using PBF-L. In another study, tantalum was deposited using the PBF-L process to determine the microstructure and crystallographic texture of the deposit as a function of scan strategy in bulk samples produced using 0° rotation of the scan pattern (no rotation between layers), 60° and 90° rotations between build layers. All deposits were nearly fully dense (99.6%). The 0° rotation sample featured large columnar grains oriented in the ⟨1 1 1⟩ crystal direction, preferentially oriented along the growth direction and direction of heat flow as predicted by the model. Rotation between layers was shown to increase competitive growth as determined by SEM and EBSD examination. Compression testing in three orientations with respect to the build direction and the planar deposition process contributed to anisotropy in the yield strength. Powder size ranged from 13 to 26 µm and PBF-L parameters were not given [313]. In another study [582] PBF-L of pure tantalum was demonstrated to produce highly porous (80% open structure) tantalum implants featuring a dodecahedron lattice with a 150-µm strut size and a 500-µm pores size. Spherical powder of 10–25 µm size range was fused into shape for both mechanical testing and implantation into rats. Mechanical tests showed properties close to that of human bone. Bone re-generation and ingrowth performance showed a strong functional implant bone interface after twelve weeks. Furthermore, cytotoxicity tests show non-cytotoxicity as per ISO-10993-5, making PBF-L of tantalum cytocompatible.

Niobium, with a melting point of 2495 °C, has the highest superconducting transition temperature of all elements at 7.5 K, and because of this, is the material choice for superconducting radiofrequency (SRF) cavities for linear accelerators. Difficulties in forming, inconsistent grain structure or pickup of impurities when employing conventional deep drawing and EB welded fabrication can contribute to non-uniform Lorentz forces and create mechanical deformation that degrades performance.

A feasibility study was performed to investigate the microstructure of PBF-EB deposition of pure niobium [583]. A parameter study was performed for two sizes of spherical powder, 130 µm powder and a bi-modal mix of 43 µm and 86 µm sizes. Heating and cooling cycles between a build plate temperature of 720 °C and a temperature of 580 °C for raking (powder layer spreading to prevent agglomeration), required significant exploration of the parameter space. Acceptable deposits were produced for each powder batch with the bimodal powder displaying no observable porosity and the 130-µm powder displaying some observable porosity. A detailed analysis using SEM, XRD and TEM showed oblong columnar grain extending along the build direction and a high dislocation density as compared with annealed Nb sheet. These results indicated the feasibility of depositing pure Nb using PBF-EB.

A further study investigated the fabrication and characterization of next-generation SRF cavities, utilizing complex free-form design. The design featuring varying wall thicknesses and external lattice support structures, was demonstrated using PBF-EB to build a high-purity Nb SRF structure and analyze the deposit [584]. A parametric study was performed to optimize deposit density by varying beam focus current, travel speed and electron beam current. The report describes chamber cleaning and the use of residual gas monitoring to characterize purity within the processing environment. In addition, the report describes the chemical composition of the high purity Nb, characterized at every point along the processes chain from ingot to wire drawing, to powder atomization, to the finished part. This material characterization identified the constituent impurity element pickup along the entire process chain while confirming the purity of the EBM AM processing environment. Results of the parameter study showed a 99.7% relative density achieved in an environment with negligible elemental pressures or contaminant pickup. The as-fabricated microstructure displayed preferred orientation and texture evidence by elongated columnar grains oriented along the fabrication direction (Z-axis) and corresponding variations in hardness indicating anisotropy as a function of the planar deposition. The observed ductile fracture was expected based on measured values of percent elongation and reduction in area. The mechanical properties were found to be in agreement with reactor grade niobium. These results are relevant in the application of PBF-EB to all Nb and high conductivity materials used in these applications.

Molybdenum has a melting point of 2620 °C, and is a potential material for use in high temperature applications such as the inner wall of a fusion reactor experiment using an PBF-L method [585]. Mo, like W, is a difficult material to weld due to its brittle properties and crack sensitivity although Mo alloys such as TZM (Ti-Zr-Mo) are weldable using the electron beam process and strict process conditions. A PBF-L parameter study [585] was performed by varying laser power, layer thickness and scan track overlap conditions to determine the degree of melting and density of the deposit. A nitrogen atmosphere, no preheat conditions of the build stage or powder bed and a maximum laser power of 200 W contributed to limiting melting, discoloration, a high degree of porosity, and in certain cases cracking and distortion [586].

## 5.2. Precious metals

Precious metal alloys such as gold, silver and platinum and palladium find wide application in jewelry due to luster, value, corrosion resistance and ease of fabrication [574]. They are also used in electronics and electrical contacts due to conductivity [587] and orthodontic crowns, with palladium being more affordable than platinum.

Gold jewelry commands a large market of the global gold market estimated to be US \$100B in 2014 by the World Gold Council. In a preliminary study [588] performed an optimization of PBF-L parameters to avoid surface defects, achieve smooth surfaces and obtain fully dense deposits of gold alloys containing Si, Ge and Ga. Practical design considerations such as support structures were developed.

A follow up study [589] determined the dimensional accuracy and structural strength for red-gold (Au, Si, Ge) and platinum (95% Pt, Co) alloys. The semiconductor elements of Si and Ge are added to Red-Gold to increase laser coupling, to smooth surfaces and reduce porosity, while the nearly pure platinum readily couples with laser radiation. Powder morphology was spherical with grain size ranges of 1–53 µm for each. The as-deposited gold alloy deposited by PBF-L are harder and more brittle than investment cast alloy but can be furnace annealed to increase ductility by 34%. The as-deposited PBF-L Pt alloy had a grain size of 30 µm compared to the cast Pt alloy grain size of 300 µm. Annealing the PBF-L Pt samples at 920 °C for 25 min increased ductility by 16%. Tensile test specimens were produced for as-deposited and annealed Au and Pt alloy samples and the results are shown in Table 19.

Palladium, rhodium, ruthenium, iridium offer high temperature chemically resistant coatings. While iridium has been deposited into a free form structure using DED-L [575], most applications have been associated with coatings of refractory metal components. Palladium and rhodium can be deposited through apertures, layer-by-layer into free form shapes at the micro scale using a photo resist pattern using a sub-micron resolution photomask, in a method used by the semi-conductor industry. The process is capable of millimeter scale parts with micron scale resolution as compared to PBF-L stainless steel deposits [590].

## 5.3. Compositinally graded alloys

Functionally graded materials (FGMs) are a class of materials in which the chemistry or structure vary as a function of position. When made by AM, the primary method of fabrication is DED with powder. However, PBF systems [591] and a system combining wire and powder DED [592] have also been used. In compositionally graded FGMs made by AM, both abrupt [591,593–597] and smooth [598–604] gradients have been fabricated. In smoothly graded FGMs, the composition is graded over multiple layers in increments generally on the order of 3 vol% [598,599,602], while in abruptly graded FGMs, the composition changes directly from one alloy/element to another across a single interface similar to that in dissimilar fusion welding.

Different trends are seen in FGMs in which the crystal structure of the two base alloys is the same or different. In FGMs that change from one element or alloy to another with the same crystal structure, the hardness has been found to follow a rule of mixtures from the hardness of the first constituent element/alloy to the last [601–604]. One exception was seen in an FGM graded from 304L SS to Invar 36, both of which have FCC crystal structures [599]. In that FGM, the hardness dipped below that of the constituent alloys due to the formation of softer secondary phases in the gradient zone. The hardness decrease was purposefully designed into the gradient path in order to avoid brittle intermetallic phases that could cause cracking. In FGMs that grade between metals or alloys with different crystal structures, the hardness has been found to fluctuate and not follow a rule of mixtures. Sometimes the fluctuations in hardness exceed, or fall below, that of the two constituent alloys/elements. For example, in an FGM graded from commercially pure Ti to TiC [600], the hardness increased suddenly at a location where carbides formed. In a FGM graded from Ti-6Al-4V to V, the hardness was found to initially increase at the beginning of the gradient zone when V was added to the  $\alpha$ -hexagonal close-packed (hcp) Ti phase. As more V was added the hardness dropped and reached a plateau as the  $\alpha$ -hcp phase transitioned completely to the softer  $\beta$ -body-centered cubic (bcc) phase, since V stabilizes the bcc phase in titanium alloys. At the very end of the gradient, the hardness dropped to that of pure V [599].

Hardness trends in abrupt gradient FGMs are not as clearly defined as the transition zone between the two terminal alloys/elements that includes the interface itself and the layers surrounding the interface. In this transition zone, a FGM of Ti-6Al-4V to Fe - 82 wt% V exhibited a sharp increase and subsequent decrease in hardness due to the dilution of the

**Table 19**  
Ultimate tensile strength and elongation of the additively manufactured precious metal components.

Alloy	UTS (MPa)	RA (%)
PBF-L, Au, as-deposited	455	29.4
PBF-L, Au, annealed	420	39.4
PBF-L, Pt, as-deposited	511	4.11
PBF-L, Pt, annealed	441	4.77

two constituent alloys [597]. Another abrupt gradient FGM of Ti-6Al-4V to Ti-6.5Al-3.5Mo-1.5Zr-0.3Si exhibited a rule of mixture change in hardness the first two layers past the interface before plateauing [593].

As to be expected, abrupt gradient FGMs incorporate stark changes in microstructure at the interface between the two constituent metals/alloys, including changes in grain size and orientation, and the phase volume fractions (e.g.,  $\alpha$  vs.  $\beta$  phase in a Ti-6Al-4V to Ti-6.5Al-3.5Mo-1.5Zr-0.3Si FGM) [591,593,598]. Conversely, smooth gradient FGM tend to show more gradual transitions in microstructural features, for example in grain size [598], within the gradient zone [600,602]. Fessler et al. [601] directly compared smooth and abrupt gradients of Invar to 316L stainless steel. While no quantitative data was provided, the team qualitatively analyzed the two FGMs. In the abrupt gradient sample, there was a distinct change in both microstructure and composition at the interface. In comparison, the 50% Invar and 50% 316L stainless steel of the smooth gradient sample showed a very uniform microstructure, indicating that a complete alloying of the two constituent alloys.

FGMs may present a feasible alternative to abrupt changes in composition, structure and properties in dissimilar metal welds. Gradual change in properties seen in FGMs between two alloys reduces stress across the transition joints compared to that in traditional friction stir welding. Hofmann et al. [605] created finite element models of an automobile valve stem that combines 304L stainless steel and Inconel 625 to show that by grading between alloys, the thermal stresses due to thermal expansion mismatch can be reduced by a factor of 10 when comparing friction stir weld joints to functionally graded joints due to smooth variations in the coefficient of thermal expansion in the latter. Additionally, the sharp joint in welding provides a location in which intermetallic phases can form, further weakening the component. For example, it is challenging to join Ti and its alloys to stainless steels due to the formation of brittle Fe-Ti intermetallic phases at the weld joint [606–608], which results in cracking or a weak location in the joint. Reichardt et al. [598] attempted to circumvent this issue by studying an FGM graded from Ti-6Al-4V to 304L stainless steel, using V as an intermediate alloy to mitigate the effects of the formation of the intermetallic phases. In general, FGMs can potentially mitigate both the issue of localized stress concentrations due to disparate elastic and thermal properties as well as the introduction of undesirable phases due to the gradual change of composition and therefore properties across a much wider gradient zone.

When fabricating FGMs, secondary phases like intermetallics and carbides commonly form, which can lead to cracking in the samples. Both microcracks [602,604] spanning no more than a layer and macrocracks spanning the entire sample [597,598,600] have been observed. The latter has been observed primarily in FGMs grading between metals/alloys with different crystal structures, such as hcp to fcc [597] or fcc to bcc [598].

There are several inherent challenges in using AM to fabricate FGMs. It has been found that the cooling rate decreases and melts pool size increases as more layers are deposited during the AM process for a monolithic sample [79]. When blending different materials in an FGM, these base alloys or elements are likely to have different melting temperatures, which will impact the effectiveness of the heat input on sufficiently melting the constituent alloys/elements, and may also result in preferential vaporization of some elements [152]. Additionally, differences in melting temperatures, coefficients of thermal expansion, and liquid surface tension, between the constituent metals can result in unmelted powder [598] or porosity [604]. These are intrinsic properties that cannot be changed; however, it is possible that by altering processing parameters like power or scanning speed, the resulting effects can be mitigated [244]. Additionally, differences in elastic modulus, coefficient of thermal expansion, and crystal structure or lattice parameters, can lead to significant residual stresses that lead to component cracking.

## 6. Welding vs AM

The most popular metal AM methods use traditional welding heat sources (arc, plasma, lasers and electron beams) to locally melt and fuse powder or wire consumables into 3D parts, without the necessity of a die or mold. Although the technologies used in welding and AM are oftentimes identical, AM has greatly benefited from advanced computer control technology, allowing for fabrication of components with higher resolution than ever before. However, many of the physical processes in AM variants are nearly identical to those in welding. This section discusses similarities and differences between the two in an attempt to bring some perspective on how the experience developed in welding science and technology over the past century can be integrated into the rapidly expanding field of metal AM.

### 6.1. Processes and applications

The American Welding Society, AWS, was established in 1919 [609] at a time when electrical power was readily available but welding technology was in its infancy. Rapid developments in the following decade led to the understanding of modern methods for improving the metallurgical quality of welds, along with great advances in production rates through developments in shielding gasses, high quality consumables, and integrated wire arc welding technologies. High power electron beams for welding were advanced in the 1960s, while high power lasers for welding were advanced in the 1980s [73]. Along with other heat sources, AWS defines over 50 joining methods in its “Master Chart of Welding and Allied Processes” [610], but only five of these techniques have found their way into mainstream AM processes: laser (LBW), electron beam (EBW), gas metal arc (GMAW), gas tungsten arc (GTAW) and plasma arc (PAW), with one additional process, ultrasonic (USW) being developed for sheet or foil type consumables. These processes represent a good selection of powers, power densities, and deposition rates for AM, but it is likely that more of the recognized welding processes will be used for AM in the future.

From an application standpoint there is a difference between welding and AM, relating to their relative positions in the manufacturing field. Welding “is a joining process that produces coalescence of materials by heating them to a suitable temperature, with or without the application of pressure, and with or without the use of filler metal” per AWS terms and definitions [610]. In essence, welding takes two or more semi-finished parts and joins them together to fabricate a more complex component. AM, on the other hand, is not used to join semi-finished components, but rather fabricates a single component usually in a layer by layer fashion [12]. AM parts may be joined together, or joined to other parts, at a later stage by traditional welding methods. Welding can be performed autogenously (without added filler metal) or with filler metal that is principally wire, occasionally strip, and sometimes powders as additions to welding electrodes. AM however must have a feedstock to build a part, and uses fine powders (~50 µm mean size) in the powder bed processes, powder additions in the DED process (~100 µm mean size) [2], or wire consumables in the higher deposition rate process using lasers, electron beams, or arcs as the power source [2,26]. Note that most wires used for welding or AM are on the order of 1.0 mm in diameter or larger, so the amount of material that can be deposited per unit time is much larger than can be accomplished with fine powder processes. Wires also come at a reduced price per gram, and have lower surface area per unit volume which reduces contamination in the deposit.

## 6.2. Deposition rates and surface finish

The physical size of welds and the size of AM builds vary considerably depending on the welding or AM method and the specific parameters. Smaller physical dimensions of the parts require highly focused low power (<400 W) heat sources with small spot sizes and computer controlled motion systems to provide the appropriate spatial resolution. In PBF processes, smaller part dimensions of <200 µm features for example, typically use <50 µm powders and low power beams with spot sizes on the order of 100 µm or less. These beams must be moved very rapidly, on the order of 1 m/s, to avoid keyhole modes and associated porosity [182,295]. The physical size of the largest part that can be made is limited by the size of the powder bed. Finer powders cost more to produce than larger powders and can be more difficult to work with and feed, so the per-gram cost of deposited metal increases as the feature size reduces [2]. DED processes on the other hand use multi kW lasers with spot sizes of several mm in order to deposit as much material per unit time as possible for cladding and surfacing applications [2]. The largest AM metal components are produced using the DED-EB process. Large spherical titanium alloy propulsion tanks have been produced as demonstration hardware for space applications at meter scale while titanium ballast tanks have been demonstrated for unmanned drone submarines [1]. DED-L systems, such as those offered by RPM Innovations, are capable of depositing complex shapes of over a meter in the 5' × 5' × 7' build chamber. Scaling of PBF systems will limit part dimensions due to the challenges of handling and recycling of large volumes of metal powder. Large AM parts are also fabricated by wire based processes, again with multi-kW power level capabilities using arcs, lasers or electron beams as the heat sources, and continuously fed wires with deposition rates on the order of 5 kg/h for arc based processes [26], and 18 kg/h for electron beam based processes [1]. These wire-based processes are CNC or robot controlled, and is not constrained to the size of a powder bed, allowing parts of any size to be created. This can be a significant advantage over powder bed processes that are typically limited in size to about a 0.4 m footprint, with some systems approaching a 1 m footprint [1]. The wire based methods have already been used to fabricate high value added aerospace structural components up to meters in length [26]. Scaling to even larger sizes is not a problem as robots can be attached to large gantry systems to be moved over large distances, or can construct their own support tracks as the structure is built and can be used to fabricate components many meters long for example [26].

Welds follow similar patterns from joining very small parts used in the microelectronics and MEMS industries [611], to large structures such as ships, nuclear pressure vessels, and bridge construction [612]. Low power laser beams with spot sizes less than 50 µm have traditionally been used to make the smallest size welds. However, recent advances in electron beam welding technology produce 50 µm sized beams for micro-joining using scanning electron microscope type technology [436]. Higher power electron beams with spot sizes on the order of 200 µm [613] are more common, and are used to produce some of the deepest welds, reaching six inches or more in steel in a single pass [614] and produce high quality welds due to the fact that they are made in vacuum. Multi-pass arc welding methods are used for larger components of many inches thick with no size restrictions on the structures being joined, and have been used over the past century with many applications [612,615].

As the deposition rate of any process increases, so does the surface flatness and roughness, which tend to scale with the layer height in AM or bead height in welding [26]. For many welding applications, this is not a concern as welds can be designed to accommodate rough surfaces, or can be post machined if needed. However, for many AM components final surface roughness is important since they are intended to be used in the as fabricated condition for net shape applications. Powder beds have a special condition, different from welding and wire based processes, whereby satellite particles create an unavoidable roughness on a similar scale to the powder, as shown in one example for a 316L lattice structure in Fig. 66. For complex powder bed builds, and for parts with internal surface features, post processing is either expensive or impossible. For comparison, Fig. 67 shows a photograph and cross section through a small keyhole electron beam weld in 21-6-9 stainless steel. The photograph of the weld shows a semi-regular pattern of ripples on the top surface of the weld, created by the effects of melt pool motion on the solidifying portion of the melt pool. The cross section shows an overlapping cosmetic pass that smooths the surface of the keyhole weld.

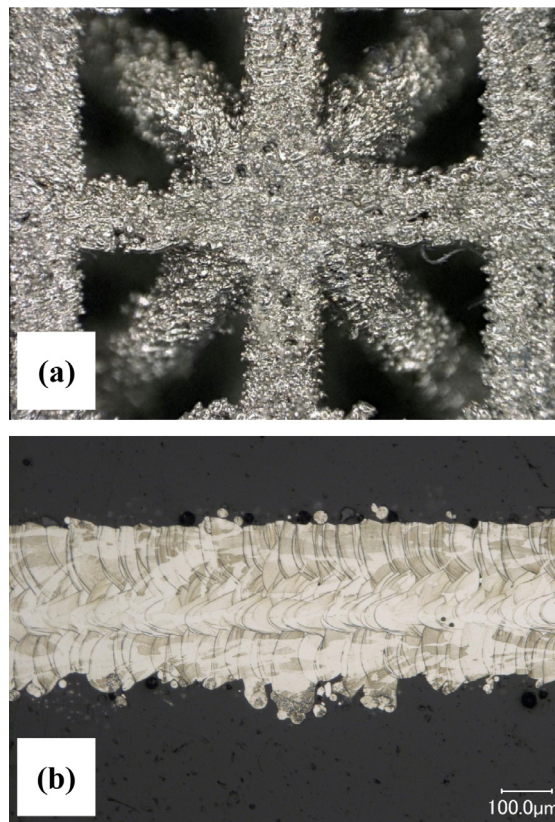


**Fig. 66.** Laser powder bed fabricated 316L stainless steel lattice with sub mm features, and powder particles bonded to the surface, referred to as satellites, create a micro-rough surface. (A) Magnified photograph of the as deposited structure. (B) Metallographic cross section through a truss member [626].

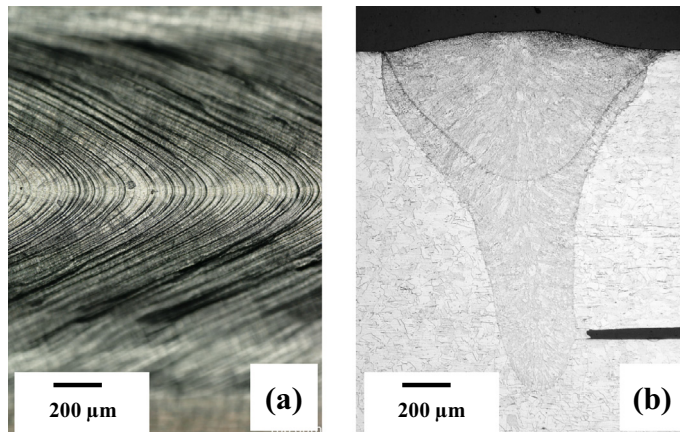


**Fig. 67.** (a) Photograph of the top surface of an electron beam weld in 21-6-9 stainless steel and (b) cross section of this weld showing a smaller cosmetic pass that smooths the top surface [626].

### 6.3. Localized heat sources

When comparing the fundamental behavior of AM and welding, there is one common concept that links them together in that they both require, or utilize, a localized heat source to create the small melt pool for the process to take place. Fig. 68 shows illustration of a localized melt pool used for welding. Melting takes place on the front side of the pool, while solidification and solid state cooling transformations take place on the back side of the weld pool to create a fusion zone (FZ) and heat affected zone (HAZ) around unaffected base metal. The melt pool reaches temperatures in excess of the liquidus tem-

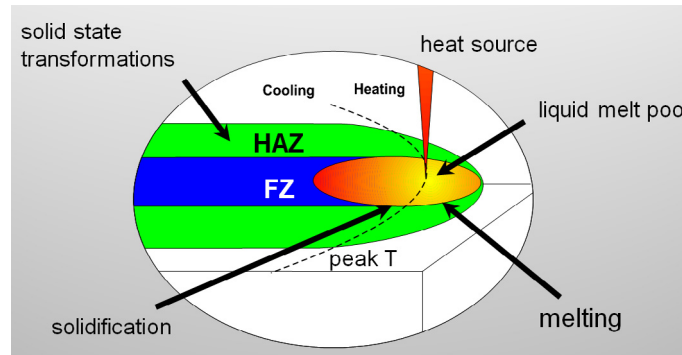


**Fig. 68.** Illustration of a localized melt pool used for welding. Melting takes place on the front side of the pool, while solidification and solid state cooling transformations take place on the back side of the weld pool to create a fusion zone (FZ) and heat affected zone (HAZ) around unaffected base metal.

perature of the alloy, resulting in steep thermal gradients between it and the base metal that surrounds it [210,216]. The same mechanisms take place during metal AM except that powder or wire is added to the melt pool to build up the necessary layers.

All of the thermophysical properties and process parameters affect the development of the localized fusion zone in welding and AM processes. Heat deposition, dissipation, conduction, and convection; surface tension gradients, buoyancy; thermal expansion, and metal vaporization all contribute to the formation of the localized fusion zone. Non-dimensional parameters are often used to describe the effects of a group of variables and are discussed in Section 2.7 of this paper. High deposition rate AM processes such as DED-L and wire-additive methods share identical physical processes to welds and the non-dimensional numbers applied to welding work well for these processes. However, some differences occur between welding and laser powder bed for example, where much higher scanning speeds are employed, lower thermal conductivity powder bed surround the fusion track and heat transfer conditions change with layers and hatching. A good example is Peclet number (Eq. (8)) which compares the relative magnitudes of heat transported by convection and conduction. As the fusion zone size reduces with higher scan speed, the thermal diffusivity of the liquid metal does not change and the characteristic velocity depends on spatial gradient of temperature because of the Marangoni effect. Because of these changes, the Peclet number does not scale linearly with scan speed.

The local thermal conditions around the melt pool control the cooling rate of the weld and create the conditions that ultimately form the microstructures and macrostructure of the resulting weld or AM deposit. The size and shape of the melt pool are strongly affected by its scan speed, which can be orders of magnitude higher in some AM processes than in typical welds. Fig. 69 shows the calculated effect of scan speed on arc welds, where the melt pool length relative to its width and depth increases with increasing scan speed, and the melt pool reduces in size [699]. There are many analytic, numeric and experimental studies of this effect, including the influence of welding heat input and different materials on weld pool geometry and cooling rate [616,617]. Intense laser and electron beams can create keyhole welds, due to vaporization of the metal, that require numerical heat transfer and fluid flow models to adequately analyze laser [295] and electron beam welding [618]. Although the keyhole mode is often beneficial for welding to produce deep narrow welds, it is often avoided in AM processing due to the creation of porosity. All of these above-mentioned models are generally applicable to metal AM processing, and provide good starting points for estimating melt pool size and cooling rates.

The localized heat source and associated temperature gradients create a situation where plastic deformation occurs around the melt pool due to constrained thermal expansion and soft metals at high temperatures. Fig. 70 shows this effect schematically, where temperature gradients and residual stress build up as the melt pool passes over a given point [616]. The residual stress that builds up is tensile near the weld centerline, and compressive in the base metal once the weld has cooled. The tensile stresses that build up near the weld can be a source of solidification and HAZ cracking [210,216] in addition to distortion. Fig. 71 shows six typical distortion profiles that occur in welding, and the same effects can occur in AM builds. It is important to note that AM parts always start on a substrate, or build plate, that provides some degree of mechanical restraint. The stiffer the build plate, the less distortion will occur, however, the residual stresses increase as the restraint increases, and can reach the yield stress of the deposited metal [615]. Some AM processes, particularly powder bed, have the ability to build isolated islands that can be linked together to form a continuous part, and they also change the deposition pattern from layer to layer [188]. Different scan strategies can influence both the residual stress and distortion that develop in AM builds. Similar strategies are routinely followed in arc welding to mitigate residual stress and distortions. However, if the build direction is always the same direction, i.e. vertically up, distortion and residual stress cannot be totally eliminated. Some non-powder bed processes can develop build strategies whereby mirror imaged parts are built on opposing sides of the build plate to balance out distortion. This same strategy is often used in welding where deliberate sequences are developed to balance out distortion effects, and computational efforts have been developed for optimizing welding schedules [619,620]. Additional details about residual stress and distortion of AM components are discussed in Section 2.10 of this article.

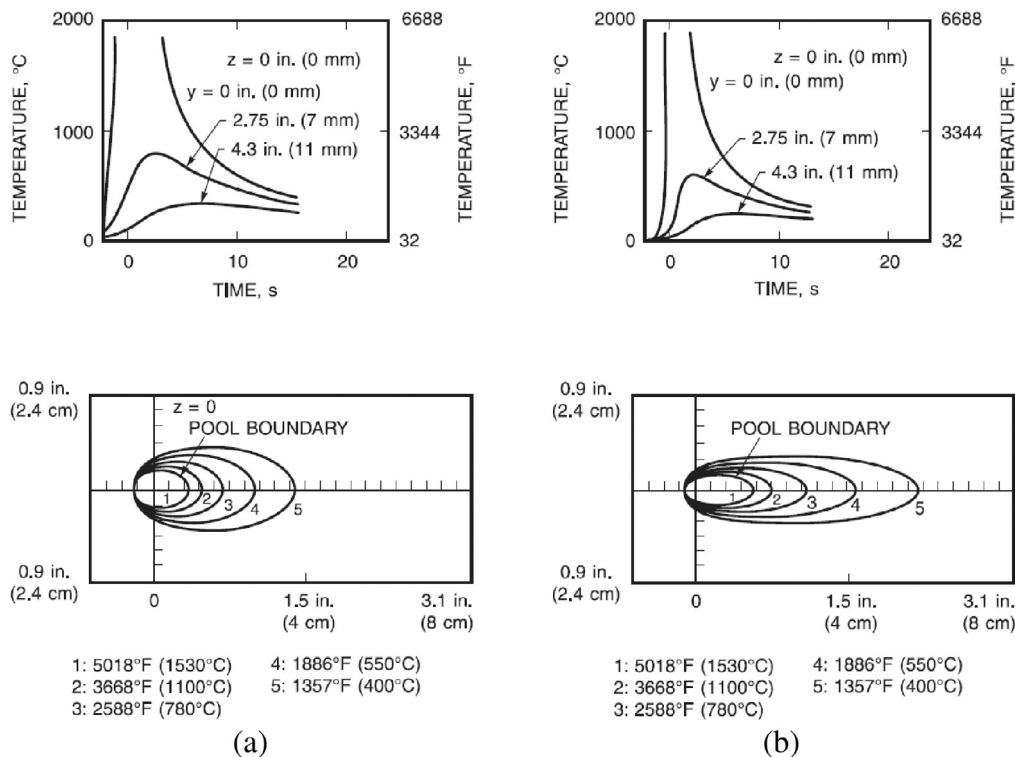


**Fig. 69.** Calculations showing the effect of increasing weld speed (1, 5, 8 mm/s) on weld pool shape of a low carbon steel, where the melt pool becomes smaller and more elongated in the welding direction as the speed increases [699].

#### 6.4. Microstructure and macrostructure

Ultimately, the mechanical properties of an AM build or a weld depend on their microstructural and macrostructural features in addition to any defects that are formed. For a given alloy, the microstructure is related to the specific processing parameters, and how they affect the local solidification rate, R, and the temperature gradient, G, in the solidifying melt pool [319]. G and R are further related to the geometric shape of the weld pool, in a way that produces local variations of these parameters, and the cooling rate, GR, throughout the cross section of the weld [297,298]. Preferred crystallographic growth directions in welds and AM tend to align the grains forming in the FZ parallel to the temperature gradient. This creates a columnar grain structure within the FZ [297,298,319]. Since the columnar grains align with the temperature gradient, they grow normal to the melt pool solidification surface, and curve towards the top center of the melt pool as it travels, as indicated in Fig. 72 [621]. It is clear that the visual appearance of the columnar grains will vary considerably depending on the angle that the cross section is made to the growth direction [298,315]. AM melt pools behave essentially the same way as welds, particularly for the high deposition rate AM wire and DED processes. However, DED processes can alter scan directions from layer to layer, creating more complex microstructures than typically seen in welds. A herringbone effect that has been observed in the microstructures of Inconel 718 is shown in Fig. 73, formed by parallel DED-L passes that are alternated in direction from layer to layer. PBF uses very fast moving beams that produce long and shallow melt pools. This change in geometric shape of the melt pool creates a condition whereby the solidifying AM powder bed grains grow more upright, and curve less towards the centerline of the melt pool than typical welds [315].

Macroscopic texture arises in both multipass welds and in AM parts when the grains formed in one layer continue to grow into the next layer and so on. Fig. 74 shows one such part in a wire arc AM process in Ti-6Al-4V [622]. The large columnar grains running vertically are created by epitaxial growth from a previous layer and preferred dendrite or cell solidification directions that align with the temperature gradient. In the case of vertical AM builds, where heat flow is largely through the base metal substrate, the temperature gradient is substantially downward, creating the macroscopic textures such as the one shown in Fig. 74. Welds will follow this same general pattern, but since they have different configurations for heat to flow out of the weld region, the columnar textured grains don't always follow vertical upward paths as is common in layer-by-layer AM processing. EBSD is useful for interpreting texture, and Fig. 75 compares a single pass electron beam weld in a stainless steel alloy [296] with an DED fabricated AM multilayer part [623]. Looking at just one of the passes in the AM part, and comparing it to the single pass EB weld shows similarities in that grains are columnar in shape, growing from the base metal towards the top center, and that many different grain orientations are present as indicated by the different colors.

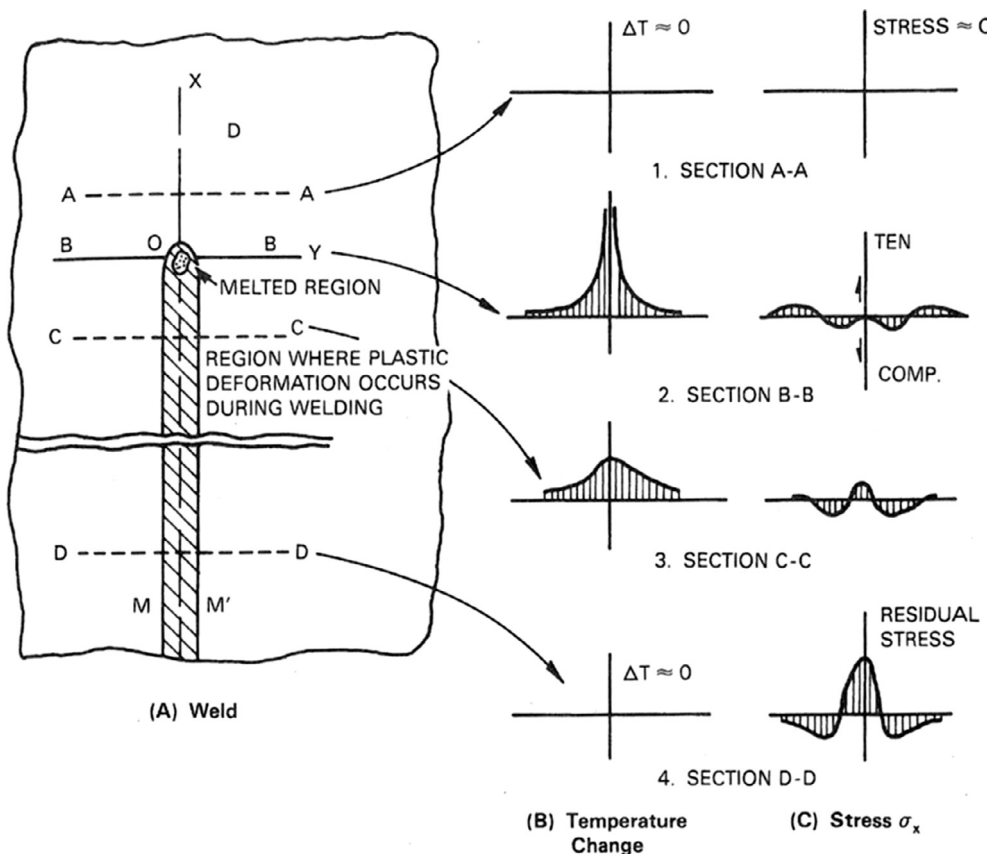


**Fig. 70.** Localized heat sources create temperature gradients and non-uniform plastic deformation that ultimately results in tensile forces acting near the weld region [216,700].

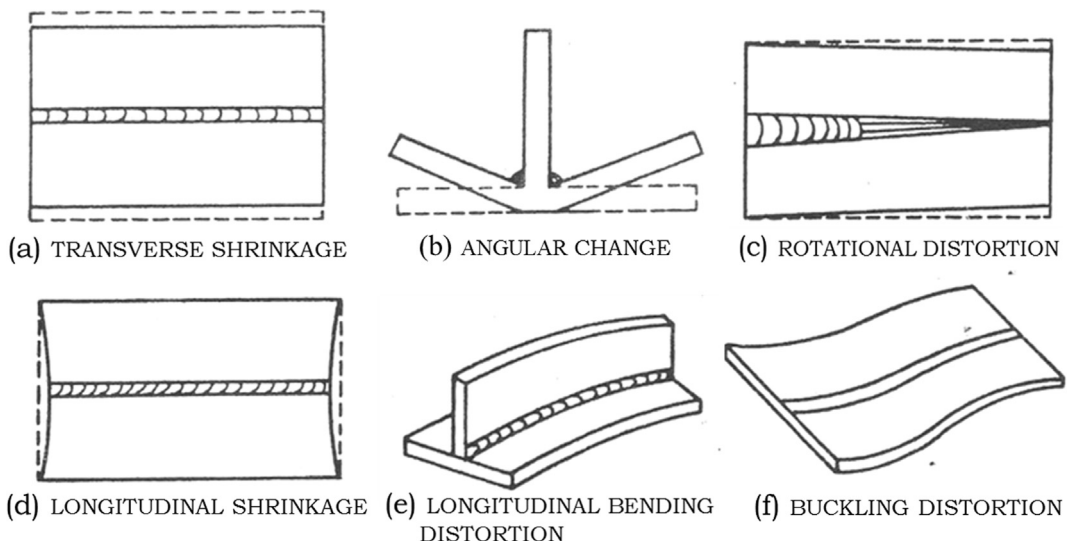


**Fig. 71.** Six types of distortion that occur during welding as a result of the localized heat. Source [216].

The principal differences are that the AM part has grains growing off of previously solidified layers, whereas the EB weld has grains growing off of the equiaxed grains in the base metal. Even so, the majority of the solidified cross sections in both cases look similar, when comparing a single AM melt pool to a single pass weld.

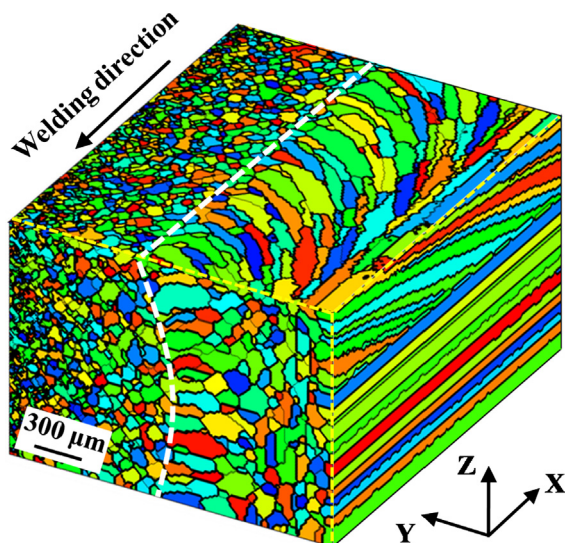


**Fig. 72.** Coupled thermal fluid calculated grain structure in the FZ and HAZ for a laser weld in copper from the centerline of the weld (RHS) into the base metal (LHS) [621].

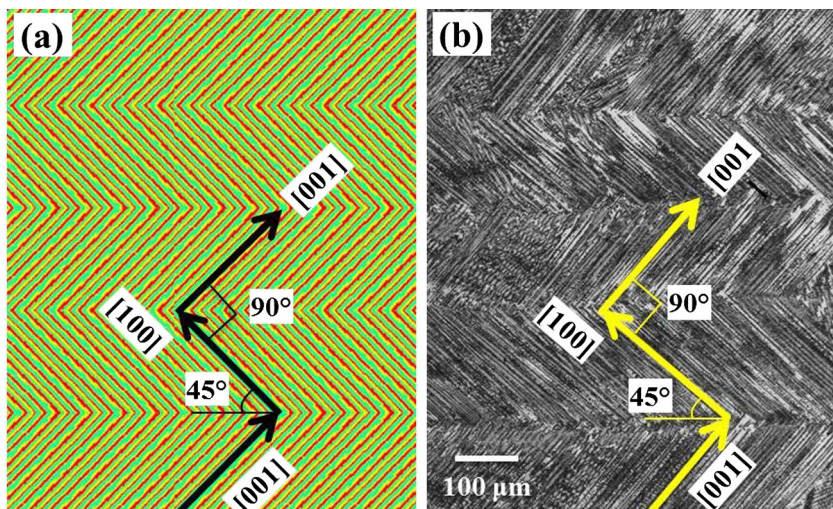


**Fig. 73.** Solidification texture produced by DED-L of Inconel 718. (a) calculated pattern for dendrites or cells growing along the [0 0 1] direction, and (b) optical micrograph of the cross section [315].

Although the fundamental connection of metal AM and welding occurs as the result of localized melt pools, one distinction between AM and welding is the dominant use of powders in some of the AM processes. PBF and DED powder fed processes both use powders but in different ways, while welding uses much less. PBF processes are discussed in detail throughout this article, and are used to build components entirely out of one alloy, or a homogenous mixture of powders. The DED process is different whereby the heat source, most often a laser, is used to melt a substrate and dissimilar metal powder particles are fed into this liquid pool. The result is often a composite mixture, useful for cladding for wear or temperature resistant surfaces, repair of surface defects, or building up gradual transitions from one alloy to another as functionally graded composite [624,625]. Fig. 76 shows one such example where a thin layer of tungsten powder particles is deposited on an aluminum alloy surface [626]. The density and melting point differences between these two materials make them difficult to produce by any other way, including welding.

### 6.5. Mechanical properties

Welds can be either stronger or weaker than the base metals that they join, depending on many metallurgical factors that are influenced by the welding process. Oftentimes, when welding non-heat treatable alloys in the annealed condition, the

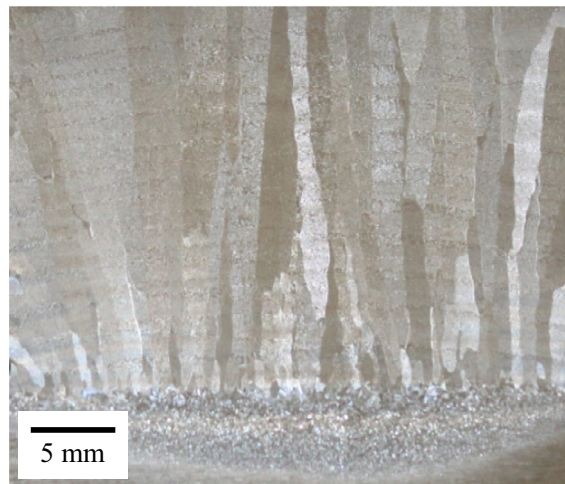


**Fig. 74.** Macroscopic texture in a Ti-6Al-4V wire arc AM build shows the continuation of prior  $\beta$ -Ti grains growing vertically through the horizontal build layers [622].

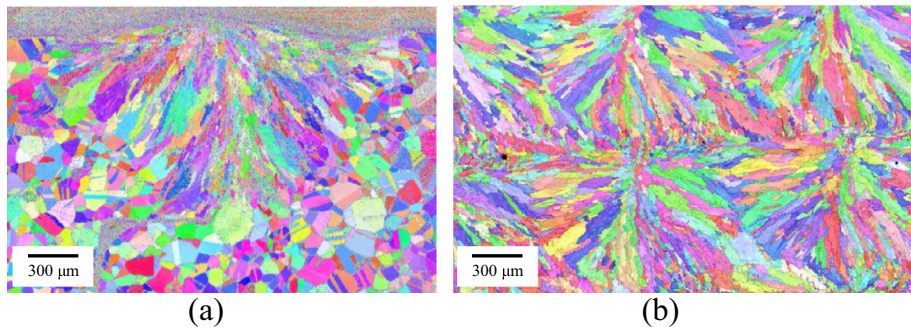


**Fig. 75.** Comparison of grain structure formed in (a) a single pass electron beam weld in 21-6-9 stainless steel [296], with (b) a DED multilayer AM build in 304L stainless steel [623].

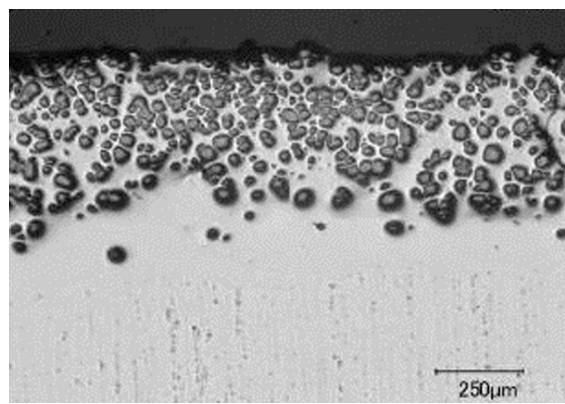


**Fig. 76.** Micrograph of an aluminum alloy with a DED layer of tungsten particles and pure aluminum deposited on the surface [626].

weld region is stronger than the base metal due to a combination of factors, including a refinement of the microstructure, and/or second phases that form in the weld. Fig. 77(a) shows the results of a cross weld tensile test in a 21-6-9 SS electron beam weld, indicating that the FZ has a higher hardness than the base metal, and when pulled in tension, the failure occurs outside the weld zone [296]. Fig. 77(b) shows a micrograph taken near the fusion boundary where the single phase large grained base metal on the left transitions to a fine two phase microstructure in the weld FZ [296]. Fig. 77(c) shows that

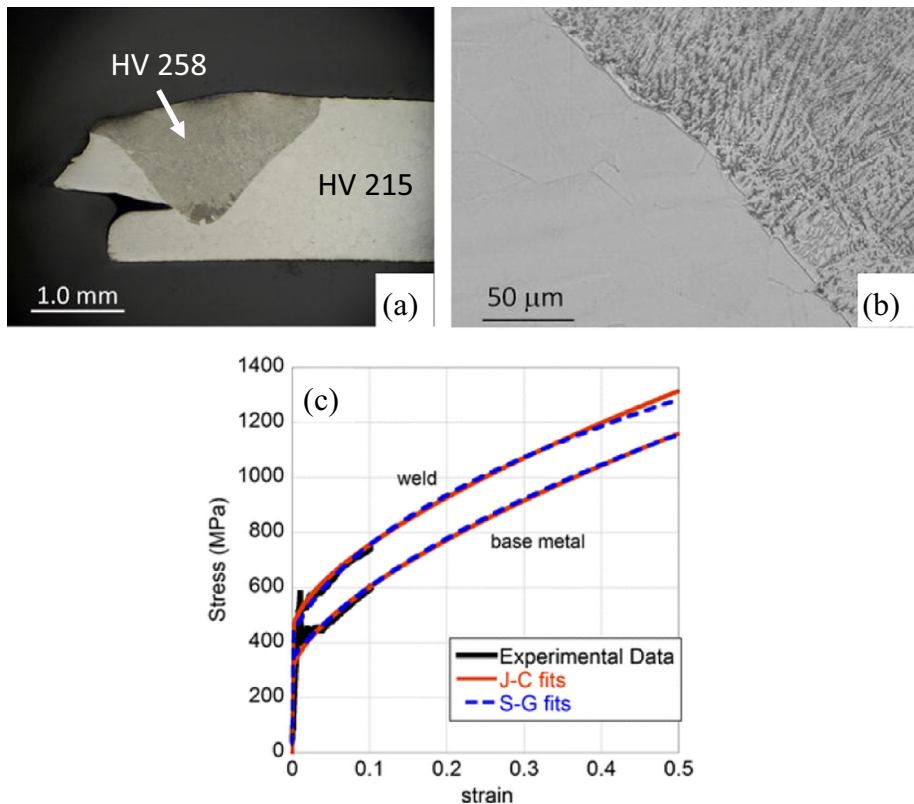


**Fig. 77.** (a) Tensile test specimen pulled across a weld, showing failure in the base metal [296]. (b) Micrograph showing the transition from the annealed single phase base metal to the fine two-phase microstructure of the weld. (c) Modeled stress strain behavior based on nanoindentation methods, showing that the weld is stronger than the base metal [296].

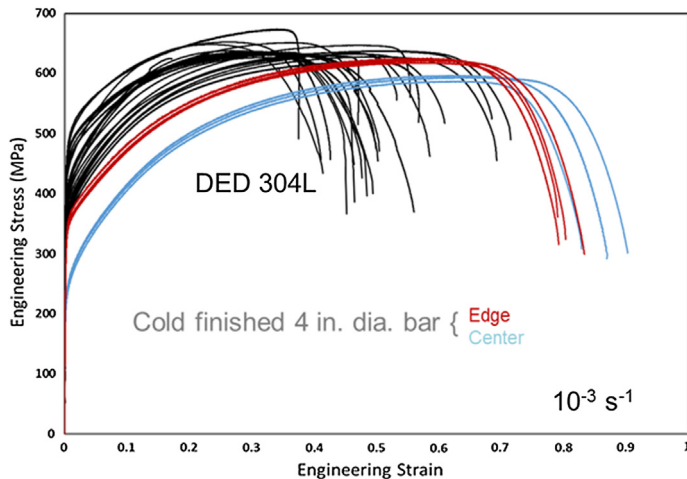


**Fig. 78.** Comparison of stress-strain behavior of DED fabricated metal (black lines) with cold finished 304L bar on the edge (red lines) and center (blue lines) [623].

the predicted stress-strain curve for the weld metal, based on nanoindentation methods, has a yield strength 26% higher than the base metal, with similar work hardening characteristics [296].

AM built components also often show higher yield strengths than the base metals that they are formed from, but ductility is almost always reduced due to a combination of factors including porosity, build defects, contamination, residual stress, and poor surface finish [2]. One example of this is shown in Fig. 78, which compares the tensile properties of 304L SS made using a DED process to cold worked stainless steel [623]. In this plot, the blue and red lines show the base metal properties

for the center of the bar (low cold work) to the edge of the bar (high cold work) respectively. Yield strength and ultimate strength increase with cold work, and all have elongations to failure of 80% or higher. The AM part on the other hand, shown by the black lines, has similar yield strength to the edge of the bar with high amounts of cold work, and even higher ultimate strengths. The elongation to failure is severely reduced however, to values less than 40% in some cases with a very large variability that severely impacts its applicability. Defects that form during layer by layer AM processes can be particularly detrimental to the mechanical properties of the components since they are can link together in plane more easily then randomly formed defects. Fig. 79 shows one example of this, where *in-situ* synchrotron based observations of defect growth during mechanical testing of a stainless steel 316L PBF-L part were made and compared to wrought material [181]. Low porosity and high porosity AM builds are shown, and indicate that the pores occur with a periodic spacing related to the layer spacing of the build, and that failure initiates at these defects.

### 6.6. Summary

In summary, metal AM and welding are similar in many respects as related to the effects that a localized heat source has on materials. Melting, solidification, solid state phase transformations, residual stress, and distortion occur in both AM and

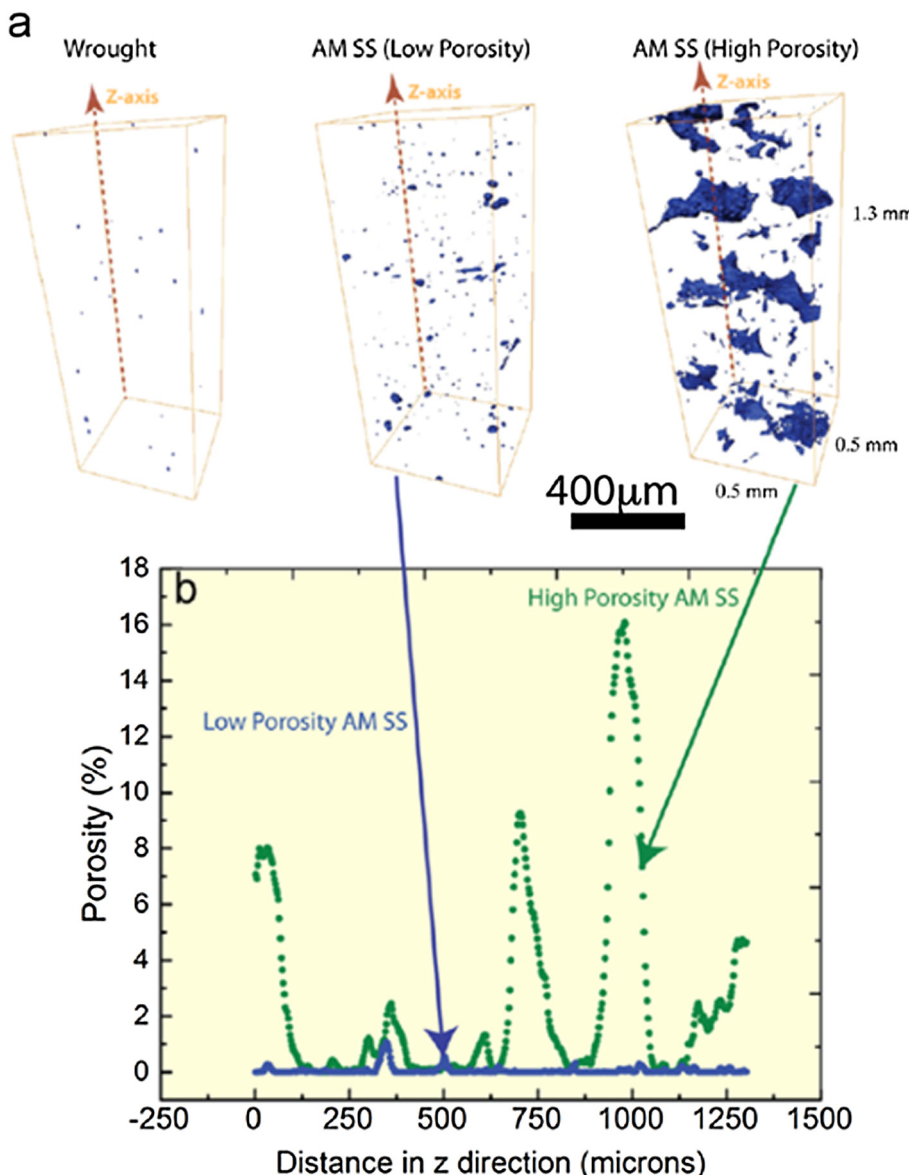


**Fig. 79.** *In-situ* synchrotron based measurement of porosity in laser powder bed fabricated 316L SS AM component, compared to wrought material. High and low porosity AM builds are shown, and indicate periodic spacing of the defects related to the layer height [181].

welding processes, and the fundamental mechanisms for each of these effects are the same. One major distinction between the two is that welding joins two semi-finished parts together to make a more complex part, whereas AM fabricates a single component that may be later welded or joined to other components. Other differences between welding and AM components tend to be process related. High deposition wire based AM and welding processes use the same heat sources and methods and can often be treated as identical processes from metallurgical point of view, whereas high speed powder bed processes may obtain higher cooling rates than typical welds. From the processing perspective, AM is always computer controlled but welding may be manual or computer controlled depending on the application, which has an effect on regularity of the deposits, precision, and control of melt pool shape. Surface finish is different for AM and welding processes, and in general, the surface quality decreases with the layer thickness and/or deposition rate. It is important to note that the powder bed AM processes never produce a surface finish better than the mean powder particle size of the feed stock due to satellite particles attached to the surface.

Where the major differences between AM and welding lie, are principally related to the powder based AM processes. High speeds, on the order of 1 m/s, and small spot sizes, on the order of 50 µm, associated with PBF allows parts to be fabricated with dimensions on the order of 100 µm. At this scale, AM has a great advantage in producing intricate parts that are not easily attainable by any other methods. Such high scan speeds are required in powder bed AM to create the desired spatial resolution while avoiding keyhole mode interactions that can produce excessive porosity. Laser and electron beam welds, on the other hand, often benefit from the keyhole mode by producing deep narrow welds with minimal heat effect on the surrounding base metals. AM components are subject to the same metallurgical effects as welds and are subject to different cooling rates produced by different processing speeds. Even though the mechanical properties of welds and AM parts do not always follow the same trends, the mechanical properties of both are almost always different than the native base metals that they are made from. In addition, solidification texture and inherent defects, such as porosity and lack of fusion seem to be unavoidable in layer by layer AM processes. These defects can create undesired variability in the mechanical response of AM parts that presents challenges and opportunities for future work in the AM field.

## 7. Printability of alloys

Printability, as a term used in the context of AM metal processing, rates the ability of a feedstock material to be successfully deposited as bulk material meeting the mechanical, metallurgical, and functional performance requirements of a specific application. It depends on both the alloy and the process because of the significant differences in the alloy properties and the unique thermal and other conditions of the individual AM processes. These differences require considerable attention to understand the susceptibility of alloys to forming common defects in order to produce sound, reliable parts. In the welding literature, the concept of weldability recognizes the fact that some alloys are easier to weld than others. However, in the AM literature there is no formally agreed upon definition of printability of alloys.

Printability is most often determined by experiments. Trial and error is used to explore a parameter space holding all but a few parameters constant and systematically applying parametric changes and observing the response to each change. The goal is to identify a region within the experimental parameter space where successful material deposition is obtained. The results effectively represent the pathways to produce the desired deposit without knowing explicitly the complex relationship between the thermal, mechanical and chemical/metallurgical processes. With experience and knowledge gained, a heuristic approach may be developed to narrow the process parameter range and reduce the number of experiments needed to optimize deposit quality for various alloys. However, this approach is time consuming and expensive and inhibits wide adoption of the approach.

Given the wide range of alloys and AM processes it is helpful to try to classify alloy-process combinations in a qualitative way according to their outcomes: A-easily printed, quality deposit, B-acceptable print quality at specified parameters, C-restricted or poor quality, limited parameter space and D-not printable. Table 20 shows the printability of several widely used alloys deposited by different AM processes based on these outcomes. Although the data are very valuable to obtain sound deposits, experimental determination of optimum process conditions to obtain these results require considerable effort.

An alternative approach is to use phenomenological modeling of AM calibrated and validated by experimental data. Here the goal is to theoretically examine the sensitivity of the process variables to the formation of several common defects. The outcome is a ranking of alloys and AM processes based on their susceptibility to common defects. The modeling results not only provide a detailed description of many of the simultaneously occurring physical processes that take place during AM, they reveal conditions needed to achieve an acceptable deposit by preventing defect formation. The methods are limited by the availability of both well tested numerical models and reliable thermo-mechanical material properties over a wide range of temperature. An additional challenge is the computational cost of models with sufficient spatial and temporal resolution to accurately capture the details of these complex processes. In the following two sections, both the experimental and theoretical approaches of defining printability are examined.

### 7.1. Printability of PBF AM processes

In the case of PBF-L and PBF-EB, experience, experimentation and characterization are often used to obtain a quantitative or qualitative assessment of the deposit quality. [627]. Fig. 80 shows the effects of power and scanning speed on the quality

**Table 20**

Experimentally determined printability of different alloy-process combinations.

Alloy Type	PBF-L	PBF-EB	DED-L	DED-EB	DED-PA
Aluminum	–	–	A	2319, 4043	A
AlSi10Mg	A	–	–	–	–
Copper-base alloys	–	–	A	Cu70-Ni30 Ni30-Cu70	C
Magnesium	–	–	–	–	B, A
Nickel-base alloys	–	–	A	–	A
IN625	A	–	–	625	–
IN718	A	A	–	718	–
HX	A	–	–	–	–
Cobalt-Chrome alloys	A	A	A	–	–
Precious metals	A	–	–	–	–
Steels	–	–	A	4043	–
Maraging Steel	A	–	–	–	–
Stainless Steel	–	–	A	300 Series	–
316L	A	–	–	–	–
17-4 PH	A	–	–	–	–
PH-1 (EOS)	A	–	–	–	–
GP1 (EOS)	A	–	–	–	–
CX (EOS)	A	–	–	–	–
Titanium	–	–	A	Ti alloys	A
Ti-6-4	A	A	–	–	–
Ti-6-4 ELI	A	A	–	–	–
Grade 2	A	A	–	–	–
Refractory Metals	–	–	–	Ta, W, Nb, Zr	–
Intermetallic alloys	B-TiAl	–	–	–	–

A - easily printed, quality deposit, B - acceptable print quality at specified parameters, C - restricted or poor quality, limited parameter space and D - not printable.

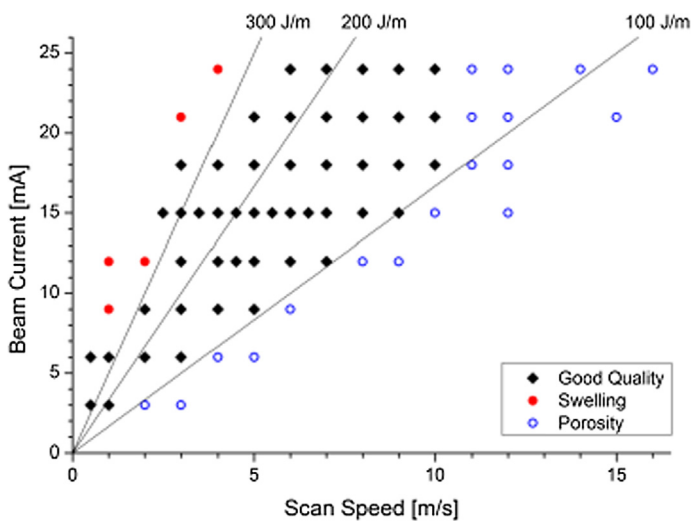


**Fig. 80.** Process map for the PBF-EB of Ti-6Al-4V for achieving optimal build quality [628].

of the PBF-EB Ti-6AL-4V deposits [628]. A parametric study was conducted to determine the effects of porosity and density on tensile strength and ductility. At lower linear heat inputs, specimens contained more than 1% porosity and showed lower tensile strength and greatly reduced ductility. Linear heat inputs in excess of 200 J/m caused noticeable loss of aluminum, while even higher values resulted in pronounced swelling of the specimen top surface. The results showed that good quality deposits could be obtained between 100 and 200 J/m.

Fig. 81 shows the extreme differences in porosity of AlSi10Mg deposited by PBF-L for different power densities and scanning speeds [629]. It was found that the levels of spherical porosity could be altered by drying the powder with the laser beam and also by the selection of process parameters. The different levels of porosity affected the corresponding deposit density. However, in cases where a number of parameters are varied over a wide range of the parameter space, it is possible that competing or additive effects take place affecting the generation or entrapment of pores. For example, one may spec-

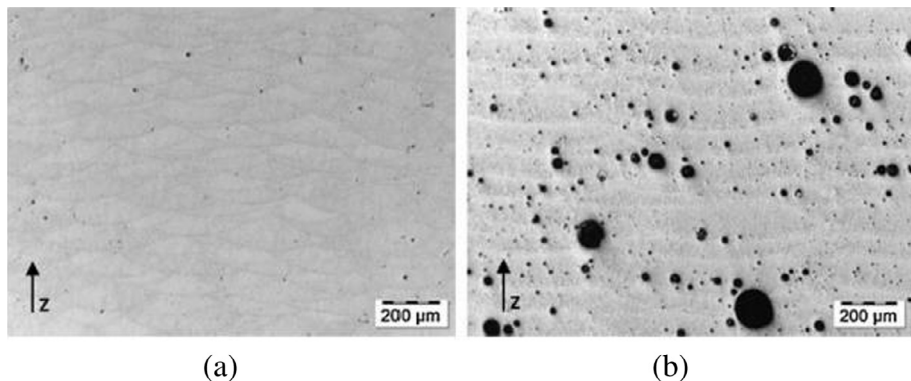


**Fig. 81.** AlSi10Mg deposited by the PBF-L with laser beam diameter = 0.3 mm, velocity 2250 mm/s resulting in a deposit pore density of 0.4% (left) and laser beam diameter = 1 mm, velocity 250 mm/s resulting in a deposit pore density of 9.2% [629].

ulate the relationship between porosity and the causative effects such as moisture, pore coalescence, keyhole instability and how they are affected by the subsequent layer remelting.

In another example [630], solidification cracking in a nickel-based alloy IN 625, deposited by PBF-L, was mitigated by altering the powder bed preheat from 150 °C to 300 °C. The improvement was attributed to a reduction in the temperature gradients and stresses associated with the cracking. Examples such as these point to the utility of applying thermal-mechanical models to the selection of processing conditions such as preheat to optimize printability.

A final example is presented in Fig. 82 [631] where the balling behavior of stainless steel and nickel powders was analyzed during PBF-L. The effects of oxygen level, thickness of powder layer, laser scanning speed and laser power were examined. In each case, the printability of the material could be called into question as a result of a poorly developed process or losing control of one or more process parameters.

All of the above examples highlight both the utility and the difficulties associated with process development and process mapping, the time and cost associated with running experiments, and the limitation of varying the few primary parameters under the control of the operator. A listing of a few primary processing parameters is presented in Table 21. It is important to note these parameters vary as a function of time and position and can interact with each other in a highly coupled and com-

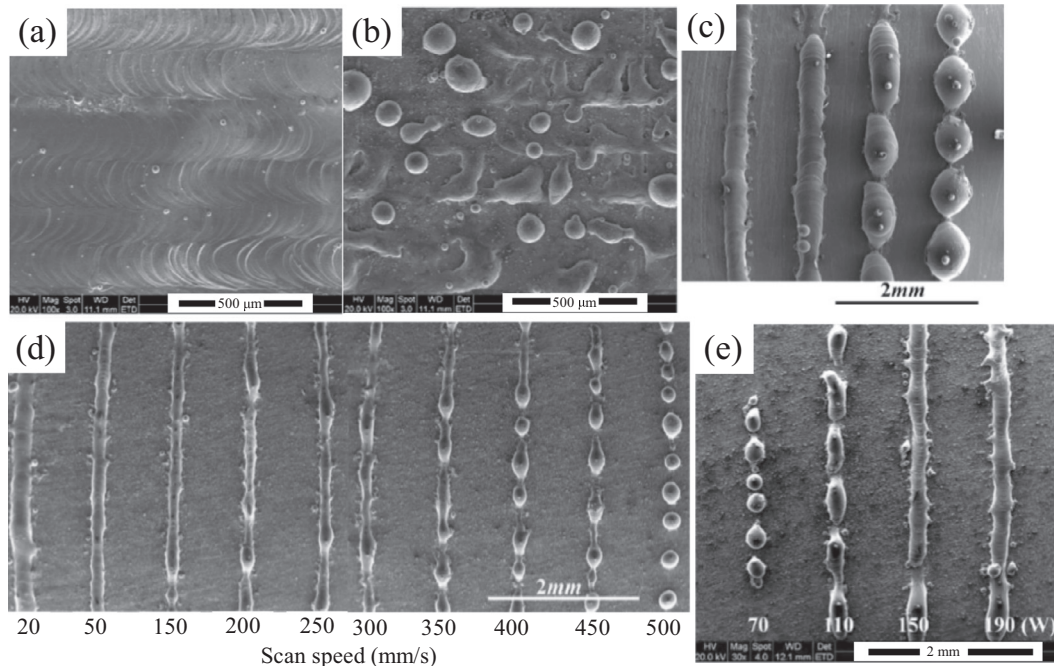


**Fig. 82.** Balling phenomenon in PBF-L resulting from different mechanisms due to process related variables including (a-1, a-2) differing oxygen contents (b) layer thickness (c) scanning speed and (d) laser power [631].

**Table 21**

Primary processing parameters of PBF and DED.

PBF-L	DED-L	
Beam power, W	Beam power, W	
Energy Density, J/mm <sup>2</sup>	Energy Density, J/mm <sup>2</sup>	
Beam focal offset, spot size	Beam focal offset, spot size	
Hatch spacing (line offset), μm	Hatch spacing (line offset), μm	
Scan speed, m/s	Travel speed, cm/s	
Scan strategy	Powder flow rate	
Powder, PSD, morphology	Powder, PSD, morphology	
Powder layer thickness, μm	Powder layer thickness, μm	
Powder moisture level	Powder moisture level	
Deposit layer, Z step, μm	Deposit layer, Z step, μm	
Build plate preheat, °C	Inert gas flow	
Powder bed preheat, °C		
Chamber gas, ppm O <sub>2</sub> , H <sub>2</sub> O		
<b>Additional PBF-EB parameters</b>		
Chamber vacuum	<b>Additional DED-EB, DED-PA parameters</b>	
Sinter pass parameters	Volts, Amps, wire feed rate	

plex manner. Few of these parameters are under direct control of the operator. The extent to which expert knowledge, experience and process mapping may be used to determine the printability of a new material, given the many degree of freedom of these processes is limited.

### 7.2. Printability of DED AM processes

In the case of DED-L and DED-PA, where processing conditions are similar to conventional arc or laser welding, a comparison may be made with the determination of weldability of ferrous and nonferrous alloys [294]. Simple weldability tests are available for the ranking of base metals and weld metals. The circular patch test for steels and Houldcroft fishbone test for aluminum are two such tests to rank susceptibility to hot cracking. This data shows the weldability for arc based processes only and does not consider the high cooling rates or strain localization of materials processed by laser or electron beam heat sources. The various levels of weldability are given as: A-recommended or easily weldable, B-acceptable or not best selection or weldable with precautions, C-possibly usable but not popular or restricted use or difficult to weld, or No-not recommended or not weldable [632]. This classification undoubtedly inspired the classification of printability discussed before. In addition, AM metal designs can feature a wide range of thermal and mechanical conditions due to widely varying wall thicknesses or process parameter ranges within a single build invalidating comparisons with all but DED-PA.

While a wide range of alloys can be processed into spherical powder with a morphology suitable for use in commercial original equipment manufacturer (OEM) AM systems, a limited selection of common engineering alloys are offered by machine vendors with corresponding parameter sets suitable for acceptable printability. In principle, an adaptation of a weldability chart may be made for the printability of alloys using data provided from OEM manufacturers of AM equipment, the producers of AM powders, and those processes using filler wire feedstock or references to printability taken from the open literature. However, several problems occur when trying to populate the chart with data from OEM manufacturers that may list materials with a recommended parameter set. Powder producers list materials and alloy types available in forms suitable for printing but with no reference to printability as it relates to the suitability of the deposited material to achieve the properties required to perform in-service of a specific application.

The determination of printability as derived from references in the open literature must take into account the relative lack of reported powder characterization, the suitability of the procedures and parameters used to produce the deposit and the methods used in characterizing the deposit itself. A listing of OEM printable materials combined with an understanding of the weldability of these alloys can provide an initial framework for understanding the printability of common engineering alloys. The problem with such a listing is the rapid evolution of the technology with respect to powder technology, AM machine technology and differences between the processes of various vendors. However, the rapid increase in AM metal machine sales will surely expand this list as applications reach technology readiness production levels providing a powerful incentive for the inclusion of a wider range of alloys.

### 7.3. Theoretical calculations of printability

Process simulation using phenomenological models may be used to better understand the thermal, mechanical and chemical response and define regions of the processing space that are likely to produce quality results. Such examples could be lack of fusion, keyhole instability, cracking, residual stress accumulation and depletion of a volatile alloying element. Knowledge derived from a limited volume of empirical observations of the processes and materials is insufficient due to the complexity of AM material-process parameter interactions.

Although many researchers mainly focus their studies on one specific alloy, a recent study [152] examined the printability of some common engineering alloys in terms of thermal distortion, vaporization of alloying elements and lack of fusion voids by utilizing a well-tested numerical heat transfer and fluid flow model. It was stated that certain alloys are more susceptible to considerable amounts of thermal strain and distortion due to the differences in thermo-physical properties and the highly transient, non-uniform heating and cooling of the AM process. Dimensional analysis was used to study the susceptibility of different alloys to thermal distortion by developing a thermal strain parameter given by Eq. (12). Coupling Eq. (12) with multi-layer heat transfer and fluid flow simulations, the maximum thermal strain during deposition was compared for Ti-6Al-4V, SS 316 and IN 625. Fig. 83 shows that for the same processing conditions, Ti-6Al-4V will exhibit higher thermal strain when compared to SS 316 and IN 625. This result can be attributed to the significantly different thermophysical properties of Ti-6Al-4V. The work was extended recently [244] where the thermal strain parameter of Eq. (12) was used to evaluate the role of process parameters and non-dimensional numbers. It was shown that thermal strain has a strong dependence on the Fourier number, Marangoni number and non-dimensional temperature, which can be used as back-of-the-envelope calculations to examine printability. Further computational studies [141] developed a thermo-mechanical model to compare the residual stresses during multi-layer deposition of Ti-6Al-4V and IN 718. It was found that Ti-6Al-4V exhibited higher residual stress than IN 718 under the same process conditions. However, the normalized residual stress, defined as the ratio of residual stress to yield strength, of Ti-6Al-4V was actually lower due to its high strength.

Many engineering alloys contain significant amounts of volatile elements that can selectively vaporize during high temperature melting processes such as AM. However, certain alloys are more vulnerable to vaporization than others which can lead to changes in chemical composition. Recently, an investigation [152] into alloying element vaporization was undertaken by coupling heat transfer and fluid flow calculations with the kinetics of vaporization to examine the relative susceptibilities of various alloys to changes in chemical compositions. As summarized in Fig. 84, it was found that Ti-6Al-4V was most susceptible to composition change due to the large amounts of aluminum, which has a relatively high vapor pressure at elevated temperatures when compared to Ti and V. To understand which alloys are likely to exhibit susceptibility to significant composition change, it is often useful to first look at vapor pressure data. Fig. 85 shows the equilibrium vapor pressures of pure elements that make up the common AM alloys [633]. It can be seen that elements such as Al, Mg, Mn and Zn are much more volatile than heavier elements such as Mo, Nb and W. Therefore, it can be expected that when large amounts of volatile elements are present in an alloy, noticeable composition change will occur. This phenomenon has been reported experimentally

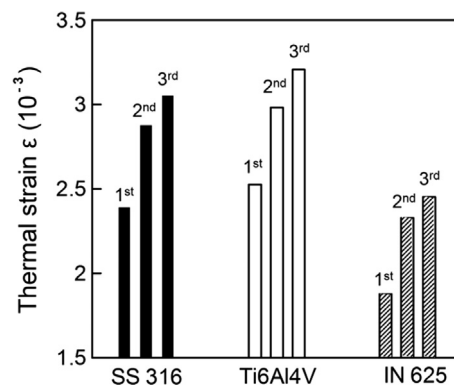


**Fig. 83.** Comparison of the maximum thermal strain between three common AM alloys [152].

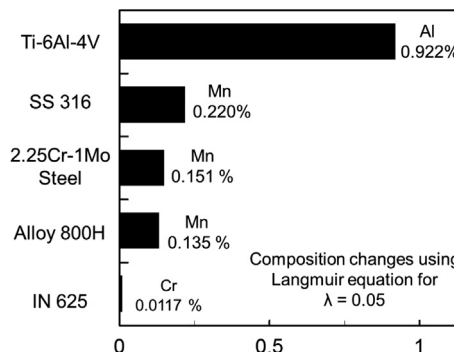


**Fig. 84.** Composition change of the most volatile alloying elements for various engineering alloys calculated from the Langmuir equation [152].

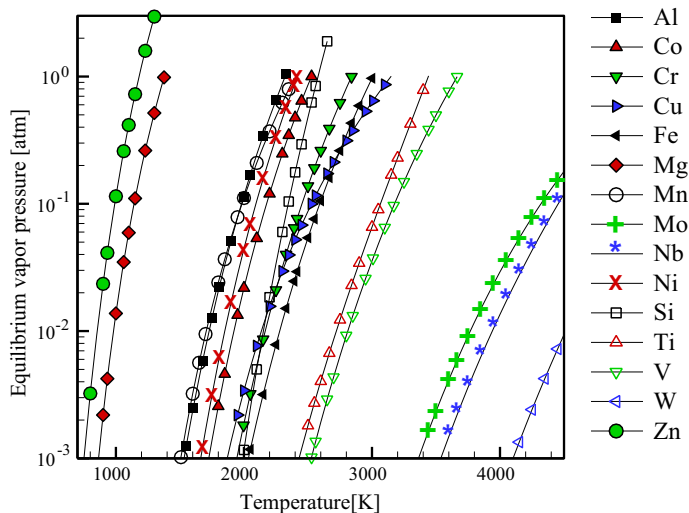


**Fig. 85.** Equilibrium vapor pressure [633] data as a function of temperature for the most common elements found in AM alloys.

for Ti-6Al-4V [164,166] and AA2039 [165]. On the other hand, when an alloy contains multiple volatile alloying elements, such as in Fe-Ni-Cr alloys, the composition change depends on various process parameters that affect the temperature distribution on the vaporizing surfaces and the volume of liquid pool from which the vapors originate and the duration during which the deposit remains liquid.

Lack of fusion defects are commonly seen in AM and result from the inadequate penetration of a deposited layer into the previous layer or improper hatch spacing between two successive passes. The susceptibility of different alloys to lack of fusion was examined through the ratio of melt pool height to layer thickness defined as a lack of fusion index, LF [152]. A value of LF sufficiently greater than one signified adequate penetration into the previously deposited layer and therefore adequate bonding. Heat transfer and fluid flow calculations for identical process parameters for various alloys indicated that Ti-6Al-4V was the most printable of the alloys for avoiding lack of fusion as shown in Fig. 15(d). In addition to inadequate penetration, experimental observations of lack of fusion due to improper hatch spacing have been widely reported for multiple alloy systems [634]. There exists an optimal hatch spacing for each deposition to ensure proper bonding without excessive overlapping. To date, this optimal spacing is usually achieved by trial and error through multiple pass depositions [188]. Although this takes time and material, it appears to be a reasonable approach. However, it should be noted that this method may not be sufficient for the special case of multiple material systems. Directed energy deposition AM has proven itself to be a promising technique for fabricating compositionally gradient parts as multiple alloy gradients such as Ti-6Al-4V to Invar [635], Ti-6Al-4V to pure V [599], SS 304L to IN 625 [602], pure Fe to Fe-50 at.% Al [636], SS 316L to Stellite 6 [637], 2.25Cr-1Mo Steel to Alloy 800H [638] and Ti-6Al-4V to IN 718 [639] have already been investigated. When a material system differs greatly in thermo-physical properties, significant differences in melt pool dimensions can occur within a build as it changes compositions. Fig. 86(a) shows a macrograph displaying a large bulge in the transition region of a Ti-6Al-4V to Invar 36 compositionally graded specimen [635]. Fig. 86(b) shows that although the composition change is linear, the solidus and liquidus temperatures do not change in a clear trend as a function of composition. This leads one to believe that in some cases, functionally graded alloys may require non-uniform processing conditions to achieve sound builds free of lack of fusion defects.

It should be noted that the concept of printability is not limited to only the defects discussed in this section. For example, porosity is perhaps the most commonly observed defect in AM. There is an abundance of literature reporting densities lower than theoretical densities owing to porosity for aluminum alloys [35,148,179,189,270,548,555,640–650], steels [651–657], nickel base alloys [180,368,378,401,494,503,507,509,658,659], stainless steels [33,205,267,312,357,468,469,485,660,661] and titanium alloys [188,429,521,529,531,532,662]. However, porosity is often much more prevalent in aluminum alloys, making them difficult to print with AM when compared to nickel based superalloys or titanium alloys.

Modeling and simulation of the printability of AM alloys based on big data analytics [663] relies on the examination of large data sets to train and optimize algorithms to correlate input conditions to output conditions. Such correlations reveal patterns useful for optimization and the identification of trends within the data range. In general, these methods require very large volume of data with considerable processing and storage requirements. The application of this approach to AM is currently in its infancy. Limitations exist in the sensing of input variables and in the characterization and determination of the output conditions, in this case, the “quality” of the deposit or the “success” of the printing process.

In short, standardized testing for the printability of AM alloys needs to be developed similar to those developed to rate the weldability of commercial engineering alloys and filler wires. Access to models that can rank the printability of alloys considering both chemistry and the local thermal and mechanical conditions for a wide range of potential build conditions would be useful. Part design freedom and the wide range of processing conditions and parameter selection may offer suitable

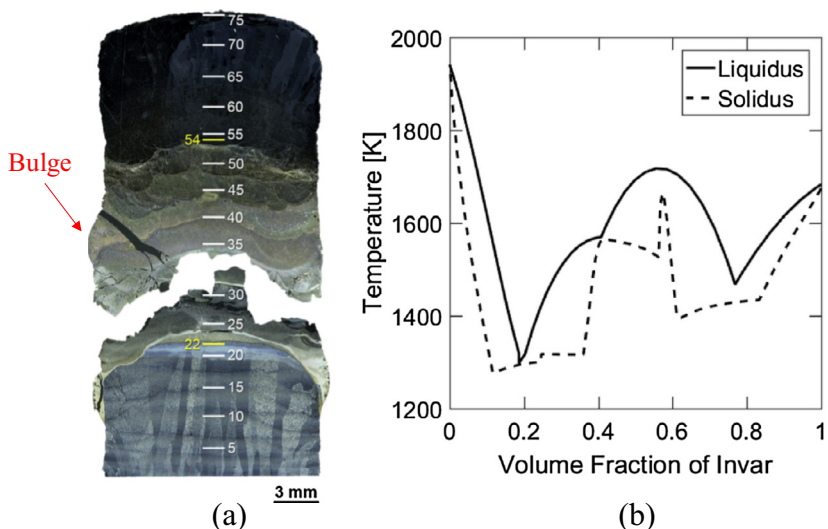


**Fig. 86.** A compositionally graded build between Ti-6Al-4V and Invar 36 showing (a) a macrograph displaying a bulged and cracked region and (b) the change from solidus and liquidus temperatures as a function of volume fraction Invar [635].

printability to alloys otherwise considered to have poor weldability. Specialty hybrid AM metal systems designed specifically for the determination of material-process-structure-property relationships are needed as the observability of commercial systems hinders real time in-situ interrogation and characterization over a wide range of process conditions and parameters. Automated data collection from AM machines is required to rapidly collect large volumes of data to build process maps and test simulations.

## 8. Concluding remarks

AM processes are now increasingly used in aerospace, automotive and medical industries because of many unique attributes, particularly for producing value added components that could not be made easily by conventional processing. The growing volume of sales of commercial AM equipment points toward a deeper market penetration in the future. There are several synergistic factors for its growth. These include the continuing improvements of computational hardware and software, more affordable equipment such as lasers, improvements in automation, the valuable knowledge base of both metallurgy and fusion welding and the creativity of a young, technologically-skilled, global workforce. However, several scientific and technological issues now affect AM product quality and cost, including prevalence of defects in parts such as porosity, lack of fusion voids, poor surface finish, distortion and residual stresses. The issues need to be addressed to enable wider commercial adaptation of AM.

Although mechanical properties of parts produced by AM are in many cases comparable with their conventionally processed counterparts, properties can vary with process parameters and locally within a part. Controlling mechanical properties of parts will require greater understanding of both the AM process and the evolution of microstructure under complex thermal cycles. Progress in better understanding the AM processes will be important to avoid common defects and to ultimately tailor composition, structure and properties of AM parts based on scientific principles. Furthermore, greater market penetration of AM will require an increased level of standardization and control to attain repeatable processes to produce parts with consistent properties.

Improved process sensing and adaptive control would be critical to regulate the AM processes to achieve high productivity and avoid common defects [664]. An important component of process control is the availability of well-tested, real time models that serve as a bridge for relating process variables with target properties of the parts. When adequately standardized, phenomenological modeling can be a powerful tool to assess the role of AM process variables on product quality prior to production. These models can compute the most important factors that affect the metallurgical product quality such as temperature and velocity fields, cooling rates and solidification parameters. Development and testing of phenomenological models can provide a sound basis for the eventual construction of digital twins of physical AM machines [665,666]. When integrated with genetic algorithms and other global search algorithms, these digital twins of AM machines can be made bi-directional, greatly expanding their utility by switching traditional input and output variables to tailor product attributes, optimize production variables, reduce defects and improve product quality. However, the development of the digital twins will require considerable time, effort and resources.

So far, phenomenological models have been of limited use to practicing engineers because of their computationally intensive nature, complexity, lack of standardization, high cost of development and testing, and limited access. A practical way to

bridge the gaps between the attributes of the phenomenological models and the needs in the shop floor is the development of reliable but simpler models that are useful for selecting process variables and avoiding common defects in parts. The comprehensive models can be used to calibrate simpler and faster reduced models that can be used in real time.

Efforts are underway for improved understanding of the interrelation between process, structure, properties and performance of AM parts. Developing a better metallurgical knowledge base of AM parts will require sustained research and development in AM processes, and the structure and properties of AM components over the coming decades. As the preceding sections of this review show, compositional, microstructural and stress gradients are common to AM parts. The approach of treating structure and properties as homogeneous is clearly not appropriate for understanding the behavior of AM components. There are opportunities to develop new theory and methodology to evaluate microstructure, properties and performance of AM parts in the presence of various gradients.

Challenges also remain in improving productivity of AM processes, enhancing performance of AM produced components, lowering the high cost of producing quality metal powders and making the equipment more affordable. Large parts are difficult to produce in the commercially available equipment of many processes such as PBF-L. A more comprehensive understanding of the AM processes and innovations in these areas are needed for greater technological adaptation of the AM processes.

Currently much of the software necessary for the operation of AM are proprietary. Greater availability of open source computer codes for the operation of AM processes would be helpful for their continuing development by taking advantage of talents of a larger pool of scientists and engineers. Finally, the existing brute force methods of certifying a part, process and material for each component is time consuming and expensive. A faster and smarter method of certifying parts would facilitate adoption of AM to more widespread commercial use.

Many unique technical capabilities such as tool-less, design-driven, on-site manufacturing of customized parts and building highly complex components in one step soon after conceptualization provide unprecedented business advantages for AM. As a result, there has been a growing recognition of its importance in the engineering research community and governmental funding agencies. This review shows that significant progress is being made in achieving better scientific understanding of AM processes and the structure, properties and fitness for service of manufactured parts. The growing knowledge base is critical for producing defect free, reproducible parts for many new applications. Making high quality parts, rapidly and reproducibly in a cost effective manner remains an important goal. Attainment of this important milestone, although within the reach of engineering research community, will require sustained research and development over several decades due to the highly complex nature of AM.

## Acknowledgements

We acknowledge the support from the U.S. Department of Energy NEUP under Grant No. DE-NE0008280. T.M. acknowledges the support from the American Welding Society research fellowship under Grant No. 179466. J.W.E. acknowledges the auspices of the U.S. Department of Energy by Lawrence Livermore National Laboratory under Contract DE-AC52-07NA27344. A.M.B. acknowledges support from the National Science Foundation through award number CMMI-1402978. Finally, W.Z. acknowledges the support from the U.S. Office of Naval Research under award number N00014-14-1-0688. We sincerely thank the reviewers for their comments. They were genuinely helpful in improving the manuscript.

## References

- [1] Milewski JO. Additive manufacturing of metals. Springer series in materials science, vol. 258. Springer: 2017.
- [2] Sames WJ, List FA, Pannala S, Dehoff RR, Babu SS. The metallurgy and processing science of metal additive manufacturing. *Int Mater Rev* 2016;61(5):315–60.
- [3] Korner C. Additive manufacturing of metallic components by selective electron beam melting - a review. *Int Mater Rev* 2016;61(5):361–77.
- [4] Herzog D, Seyda V, Wycisk E, Emmelmann C. Additive manufacturing of metals. *Acta Mater* 2016;117:371–92.
- [5] Bourell DL. Perspectives on additive manufacturing. *Ann Rev Mater Res* 2016;46:1–18.
- [6] King WE, Anderson AT, Ferencz RM, Hodge NE, Kamath C, Khairallah SA, et al. Laser powder bed fusion additive manufacturing of metals: physics, computational, and materials challenges. *Appl Phys Rev* 2015;2(4):041304.
- [7] Gu DD, Meiners W, Wissenbach K, Poprawe R. Laser additive manufacturing of metallic components: materials, processes and mechanisms. *Int Mater Rev* 2012;57(3):133–64.
- [8] Collins PC, Brice DA, Samimi P, Ghamarian I, Fraser HL. Microstructural control of additively manufactured metallic materials. *Ann Rev Mater Res* 2016;46:63–91.
- [9] Lewandowski JJ, Seifi M. Metal additive manufacturing: a review of mechanical properties. *Ann Rev Mater Res* 2016;46:151–86.
- [10] Olakunmi EO, Cochrane RF, Dalgarno KW. A review on selective laser sintering/melting (SLS/SLM) of aluminium alloy powders: processing, microstructure, and properties. *Prog Mater Sci* 2015;74:401–77.
- [11] Yap CY, Chua CK, Dong ZL, Liu ZH, Zhang DQ, Loh LE, et al. Review of selective laser melting: Materials and applications. *Appl Phys Rev* 2015;2(4).
- [12] Standard terminology for additive manufacturing technologies. *ASTM Int* 2013;F2792–12a.
- [13] Frazier WE. Metal additive manufacturing: a review. *J Mater Eng Perform* 2014;23(6):1917–28.
- [14] Herderick E. Additive manufacturing of metals: a review. *Mater Sci Tech* 2011;1413–25.
- [15] Tapia G, Elwany A. A review on process monitoring and control in metal-based additive manufacturing. *J Manuf Sci Eng* 2014;136(6):060801.
- [16] Imran MK, Masood SH, Brandt M, Bhattacharya S, Mazumder J. Direct metal deposition (DMD) of H13 tool steel on copper alloy substrate: evaluation of mechanical properties. *Mater Sci Eng A* 2011;528(9):3342–9.
- [17] Keist JS, Palmer TA. Role of geometry on properties of additively manufactured Ti-6Al-4V structures fabricated using laser based directed energy deposition. *Mater Des* 2016;106:482–94.
- [18] Ma MM, Wang ZM, Zeng XY. Effect of energy input on microstructural evolution of direct laser fabricated IN718 alloy. *Mater Charact* 2015;106:420–7.

- [19] Malukhin K, Ehmann K. Material characterization of NiTi based memory alloys fabricated by the laser direct metal deposition process. *J Manuf Sci Eng* 2006;128(3):691–6.
- [20] Riza SH, Masood SH, Wen CE, Ruan D, Xu SQ. Dynamic behaviour of high strength steel parts developed through laser assisted direct metal deposition. *Mater Des* 2014;64:650–9.
- [21] Shah K, Pinkerton AJ, Salman A, Li L. Effects of melt pool variables and process parameters in laser direct metal deposition of aerospace alloys. *Mater Manuf Process* 2010;25(12):1372–80.
- [22] Baufeld B, Brandl E, van der Biest O. Wire based additive layer manufacturing: comparison of microstructure and mechanical properties of Ti-6Al-4V components fabricated by laser-beam deposition and shaped metal deposition. *J Mater Process Technol* 2011;211(6):1146–58.
- [23] Brandl E, Palm F, Michailov V, Viehweger B, Leyens C. Mechanical properties of additive manufactured titanium (Ti-6Al-4V) blocks deposited by a solid-state laser and wire. *Mater Des* 2011;32(10):4665–75.
- [24] Brandl E, Schobert A, Leyens C. Morphology, microstructure, and hardness of titanium (Ti-6Al-4V) blocks deposited by wire-feed additive layer manufacturing (ALM). *Mater Sci Eng A* 2012;532:295–307.
- [25] Wang T, Zhu YY, Zhang SQ, Tang HB, Wang HM. Grain morphology evolution behavior of titanium alloy components during laser melting deposition additive manufacturing. *J Alloy Comp* 2015;632:505–13.
- [26] Ding DH, Pan ZX, Cuiuri D, Li HJ. Wire-feed additive manufacturing of metal components: technologies, developments and future interests. *Int J Adv Manuf Technol* 2015;81(1–4):465–81.
- [27] Ding J, Colegrove P, Mehnert J, Ganguly S, Almeida PMS, Wang F, et al. Thermo-mechanical analysis of wire and arc additive layer manufacturing process on large multi-layer parts. *Comp Mater Sci* 2011;50(12):3315–22.
- [28] Williams SW, Martina F, Addison AC, Ding J, Pardal G, Colegrove P. Wire plus arc additive manufacturing. *Mater Sci Tech* 2016;32(7):641–7.
- [29] Xiong J, Lei YY, Chen H, Zhang GJ. Fabrication of inclined thin-walled parts in multi-layer single-pass GMAW-based additive manufacturing with flat position deposition. *J Mater Process Technol* 2017;240:397–403.
- [30] Hildreth OJ, Nassar AR, Chasse KR, Simpson TW. Dissolvable metal supports for 3D direct metal printing. *3d Print Addit Manuf* 2016;3(2):90–7.
- [31] Bhavar V, Kattire P, Patil V, Khot S, Gujar K, Singh R. A review on powder bed fusion technology of metal additive manufacturing. In: 4th International conference and exhibition on additive manufacturing technologies; 2014. p. 1–2.
- [32] Jamshidinia M, Sadek A, Wang W, Kelly S. Additive manufacturing of steel alloys using laser powder-bed fusion. *Adv Mater Process* 2015;173(1):20–4.
- [33] Kamath C, El-dasher B, Gallegos GF, King WE, Sisto A. Density of additively-manufactured, 316L SS parts using laser powder-bed fusion at powers up to 400 W. *Int J Adv Manuf Technol* 2014;74(1–4):65–78.
- [34] Khairallah SA, Anderson AT, Rubenchik A, King WE. Laser powder-bed fusion additive manufacturing: physics of complex melt flow and formation mechanisms of pores, spatter, and denudation zones. *Acta Mater* 2016;108:36–45.
- [35] Mower TM, Long MJ. Mechanical behavior of additive manufactured, powder-bed laser-fused materials. *Mater Sci Eng A* 2016;651:198–213.
- [36] Dehoff RR, Babu SS. Characterization of interfacial microstructures in 3003 aluminum alloy blocks fabricated by ultrasonic additive manufacturing. *Acta Mater* 2010;58(13):4305–15.
- [37] Ram GDJ, Robinson C, Yang Y, Stucker BE. Use of ultrasonic consolidation for fabrication of multi-material structures. *Rapid Prototyp J* 2007;13(4):226–35.
- [38] Ultrasonic additive manufacturing <<http://www.insidemetalladditivemanufacturing.com/blog/ultrasonic-additive-manufacturing>> [browsed November 2016].
- [39] Meteyer S, Xu X, Perry N, Zhao YF. Energy and material flow analysis of binder-jetting additive manufacturing processes. In: 21st CIRP conference on life cycle engineering; 2014. p. 19–25.
- [40] Thompson DA. Binder jet additive manufacturing <<http://www.lboro.ac.uk/research/amrg/about/the7categoriesofadditivemanufacturing/binderjetting/>> [browsed January 2017].
- [41] Karlsson J, Snis A, Engqvist H, Lausmaa J. Characterization and comparison of materials produced by Electron Beam Melting (EBM) of two different Ti-6Al-4V powder fractions. *J Mater Process Technol* 2013;213(12):2109–18.
- [42] Zhao XM, Chen J, Lin X, Huang WD. Study on microstructure and mechanical properties of laser rapid forming Inconel 718. *Mater Sci Eng A* 2008;478(1–2):119–24.
- [43] Slotwinski JA, Garboczi EJ, Stutzman PE, Ferraris CF, Watson SS, Peltz MA. Characterization of metal powders used for additive manufacturing. *J Res Natl Inst Stan* 2014;119:460–93.
- [44] Santomaso A, Lazzaro P, Canu P. Powder flowability and density ratios: the impact of granules packing. *Chem Eng Sci* 2003;58(13):2857–74.
- [45] Anderson IE, Figliola RS, Morton H. Flow mechanisms in high-pressure gas atomization. *Mater Sci Eng A* 1991;148(1):101–14.
- [46] Bourdeau RG. Rotary atomizing process. US Patent 1983; No. 4415511.
- [47] Champagne B, Angers R. REP (Rotating Electrode Process) atomization mechanisms. *Powder Metall Int* 1984;16(3):125–8.
- [48] Ozols A, Sirkin HR, Vicente EE. Segregation in Stellite powders produced by the plasma rotating electrode process. *Mater Sci Eng A* 1999;262(1–2):64–9.
- [49] Seki Y, Okamoto S, Takigawa H, Kawai N. Effect of atomization variables on powder characteristics in the high-pressured water atomization process. *Met Powder Rep* 1990;45(1):38–40.
- [50] Pinkerton AJ, Li L. Direct additive laser manufacturing using gas- and water-atomised H13 tool steel powders. *Int J Adv Manuf Technol* 2005;25(5–6):471–9.
- [51] Schade CT, Murphy TF, Walton C. Development of atomized powders for additive manufacturing. In: Powder metallurgy word congress; 2014.
- [52] Sames W, Medina F, Peter W, Babu S, Dehoff R. Effect of process control and powder quality on Inconel 718 produced using electron beam melting. In: Proceedings of the 8th international symposium on superalloy 718 and derivatives; 2014. p. 409.
- [53] Liu B, Wildman R, Tuck C, Ashcroft I, Hague R. Investigation the effect of particle size distribution on processing parameters optimisation in selective laser melting process. In: International solid freeform fabrication symposium: an additive manufacturing conference. University of Texas at Austin; 2011. p. 227–38.
- [54] Qi H, Azer M, Ritter A. Studies of standard heat treatment effects on microstructure and mechanical properties of laser net shape manufactured Inconel 718. *Metall Mater Trans A* 2009;40a(10):2410–22.
- [55] Tang HP, Qian M, Liu N, Zhang XZ, Yang GY, Wang J. Effect of powder reuse times on additive manufacturing of Ti-6Al-4V by selective electron beam melting. *JOM* 2015;67(3):555–63.
- [56] Stecker S, Lachenberg K, Wang H, Salo R. Advanced electron beam free form fabrication methods & technology. In: AWS welding show. Atlanta (GA); 2006. p. 35–46.
- [57] Syed WUH, Pinkerton AJ, Li L. Combining wire and coaxial powder feeding in laser direct metal deposition for rapid prototyping. *Appl Surf Sci* 2006;252(13):4803–8.
- [58] Zhou J, Zhang Y, Chen J. Numerical simulation of random packing of spherical particles for powder-based additive manufacturing. *J Manuf Sci Eng* 2009;131(3):031004.
- [59] Klassen A, Scharowsky T, Korner C. Evaporation model for beam based additive manufacturing using free surface lattice Boltzmann methods. *J Phys D Appl Phys* 2014;47(27):275303.
- [60] Kovaleva I, Kovalev O, Smurov I. Model of heat and mass transfer in random packing layer of powder particles in selective laser melting. *Phys Proc* 2014;56:400–10.
- [61] Lee Y, Zhang W. Modeling of heat transfer, fluid flow and solidification microstructure of nickel-base superalloy fabricated by laser powder bed fusion. *Addit Manuf* 2016;12:178–88.

- [62] Beving DE, McDonnell AMP, Yang WS, Yan YS. Corrosion resistant high-silica-zeolite MFI coating - One general solution formulation for aluminum alloy AA-2024-T3, AA-5052-H32, AA-6061-T4, and AA-7075-T6. *J Electrochem Soc* 2006;153(8):B325–9.
- [63] Cormier D, Harrysson A, West H. Characterization of H13 steel produced via electron beam melting. *Rapid Prototyp J* 2004;10(1):35–41.
- [64] Rahman M, Seah WKH, Teo TT. The machinability of Inconel 718. *J Mater Process Technol* 1997;63(1–3):199–204.
- [65] Seshacharyulu T, Medeiros SC, Frazier WG, Prasad YVRK. Microstructural mechanisms during hot working of commercial grade Ti-6Al-4V with lamellar starting structure. *Mater Sci Eng A* 2002;325(1–2):112–25.
- [66] Wendt J, Chin D. The ac corrosion of stainless steel—II. The polarization of ss304 and ss316 in acid sulfate solutions. *Corros Sci* 1985;25(10):901–15.
- [67] Yun HM, Ennis PJ, Nickel H, Schuster H. The effect of high-temperature reactor primary circuit helium on the formation and propagation of surface cracks in Alloy 800-H and Inconel-617. *J Nucl Mater* 1984;125(3):258–72.
- [68] Farahmand P, Kovacevic R. An experimental-numerical investigation of heat distribution and stress field in single- and multi-track laser cladding by a high-power direct diode laser. *Opt Laser Technol* 2014;63:154–68.
- [69] Martukanitz R, Michaleris P, Palmer T, DebRoy T, Liu Z-K, Otis R, et al. Toward an integrated computational system for describing the additive manufacturing process for metallic materials. *Addit Manuf* 2014;1:52–63.
- [70] Peyre P, Aubry P, Fabbro R, Neveu R, Longuet A. Analytical and numerical modelling of the direct metal deposition laser process. *J Phys D Appl Phys* 2008;41(2):025403.
- [71] Lim GC, Steen WM. Measurement of the temporal and spatial power distribution of a high-power CO<sub>2</sub>-laser beam. *Opt Laser Technol* 1982;14(3):149–53.
- [72] Lasers and laser-related equipment-Test methods for laser beam widths, divergence angles and beam propagation ratios. ISO Standard. 2005;11146–2.
- [73] Elmer JW, Hochanadel P, Lachenberg K, Webber T. Introduction to high energy density electron and laser beam welding. In: *Joining: welding fundamentals and processes*; 2009.
- [74] LaFlamme G, Powers D. Diagnostic device quantifies, defines geometric characteristics of electron-beams. *Weld J* 1991;70(10):33–40.
- [75] Elmer JW, Teruya A, O'Brien D. Tomographic imaging of noncircular and irregular electron beam current density distributions. *Weld J* 1993;72(11).
- [76] Elmer JW, Teruya AT. An enhanced faraday cup for rapid determination of power density distribution in electron beams. *Weld J* 2001;80(12):288s–95s.
- [77] Palmer TA, Elmer JW. Characterisation of electron beams at different focus settings and work distances in multiple welders using the enhanced modified Faraday cup. *Sci Technol Weld Join* 2007;12(2):161–74.
- [78] Lu M, Kou S. Power and current distributions in gas tungsten arcs. *Weld J* 1988;67(2):S29–34.
- [79] Manvatkar V, De A, DebRoy T. Heat transfer and material flow during laser assisted multi-layer additive manufacturing. *J Appl Phys* 2014;116(12): Article No. 124905.
- [80] Wang XC, Laoui T, Bonse J, Kruth JP, Lauwers B, Froyen L. Direct selective laser sintering of hard metal powders: experimental study and simulation. *Int J Adv Manuf Technol* 2002;19(5):351–7.
- [81] Miranda RM, Lopes G, Quintino L, Rodrigues JP, Williams S. Rapid prototyping with high power fiber lasers. *Mater Des* 2008;29(10):2072–5.
- [82] Lv SX, Tian XB, Wang HT, Yang SQ. Arc heating hot wire assisted arc welding technique for low resistance welding wire. *Sci Technol Weld Join* 2007;12(5):431–5.
- [83] He X, Norris JT, Fuerschbach PW, DebRoy T. Liquid metal expulsion during laser spot welding of 304 stainless steel. *J Phys D Appl Phys* 2006;39(3):525–34.
- [84] Mumtaz KA, Hopkinson N. Selective laser melting of thin wall parts using pulse shaping. *J Mater Process Technol* 2010;210(2):279–87.
- [85] Eschey C, Lutzmann S, Zaeh M. Examination of the powder spreading effect in Electron Beam Melting (EBM). In: *Solid freeform fabrication*. Austin (TX); 2009. p. 3–5.
- [86] Kahnert M, Lutzmann S, Zaeh M. Layer formations in electron beam sintering. In: *Solid freeform fabrication symposium*; 2007. p. 88–99.
- [87] Mughal MP, Fawad H, Mufti RA, Siddique M. Deformation modelling in layered manufacturing of metallic parts using gas metal arc welding: effect of process parameters. *Model Simul Mater Sc* 2005;13(7):1187–204.
- [88] Vasinonta A, Beuth JL, Griffith M. Process maps for predicting residual stress and melt pool size in the laser-based fabrication of thin-walled structures. *J Manuf Sci Eng* 2007;129(1):101–9.
- [89] Goldak J, Chakravarti A, Bibby M. A new finite-element model for welding heat-sources. *Metall Trans B* 1984;15(2):299–305.
- [90] Svensson LE, Gretoft B, Bhadeshia HKDH. An analysis of cooling curves from the fusion zone of steel weld deposits. *Scand J Metall* 1986;15(2):97–103.
- [91] Markl M, Korner C. Multiscale modeling of powder bed-based additive manufacturing. *Ann Rev Mater Res* 2016;46:93–123.
- [92] Manvatkar V, De A, DebRoy T. Spatial variation of melt pool geometry, peak temperature and solidification parameters during laser assisted additive manufacturing process. *Mater Sci Tech* 2015;31(8):924–30.
- [93] Raghavan A, Wei HL, Palmer TA, DebRoy T. Heat transfer and fluid flow in additive manufacturing. *J Laser Appl* 2013;25(5): Article No. 052006.
- [94] Patankar S. Numerical heat transfer and fluid flow. CRC Press; 1980.
- [95] David SA, DebRoy T. Current issues and problems in welding science. *Science* 1992;257(5069):497–502.
- [96] DebRoy T, David SA. Physical processes in fusion welding. *Rev Mod Phys* 1995;67(1):85–112.
- [97] Mcnallan MJ, DebRoy T. Effect of temperature and composition on surface-tension in Fe-Ni-Cr alloys containing sulfur. *Metall Trans B* 1991;22(4):557–60.
- [98] Sahoo P, DebRoy T, Mcnallan MJ. Surface-tension of binary metal - surface-active solute systems under conditions relevant to welding metallurgy. *Metall Trans B* 1988;19(3):483–91.
- [99] Mishra S, Lienert TJ, Johnson MQ, DebRoy T. An experimental and theoretical study of gas tungsten arc welding of stainless steel plates with different sulfur concentrations. *Acta Mater* 2008;56(9):2133–46.
- [100] Pitschner W, DebRoy T, Mundra K, Ebner R. Role of sulfur and processing variables on the temporal evolution of weld pool geometry during multikilowatt laser beam welding of steels. *Weld J* 1996;75(3):S71–80.
- [101] Michaleris P. Modeling metal deposition in heat transfer analyses of additive manufacturing processes. *Finite Elem Anal Des* 2014;86:51–60.
- [102] Mills KC. Recommended values of thermophysical properties for selected commercial alloys. Woodhead Publishing; 2002.
- [103] Nandan R, DebRoy T, Bhadeshia HKDH. Recent advances in friction-stir welding - process, weldment structure and properties. *Prog Mater Sci* 2008;53(6):980–1023.
- [104] Fathi A, Toyserkani E, Khajepour A, Durali M. Prediction of melt pool depth and dilution in laser powder deposition. *J Phys D Appl Phys* 2006;39(12):2613–23.
- [105] Huang Y, Khamesee MB, Toyserkani E. A comprehensive analytical model for laser powder-fed additive manufacturing. *Addit Manuf* 2016;12:90–9.
- [106] Picasso M, Marsden CF, Wagniere JD, Frenk A, Rappaz M. A simple but realistic model for laser cladding. *Metall Mater Trans B* 1994;25(2):281–91.
- [107] Cheng B, Chou K. Melt pool geometry simulations for powder-based electron beam additive manufacturing. In: *24th Annual international solid freeform fabrication symposium-an additive manufacturing conference*. Austin (TX, USA); 2013.
- [108] Contuzzi N, Campanelli S, Ludovico A. 3D finite element analysis in the selective laser melting process. *Int J Simul Model* 2011;10(3):113–21.
- [109] Hodge NE, Ferencz RM, Solberg JM. Implementation of a thermomechanical model for the simulation of selective laser melting. *Comput Mech* 2014;54(1):33–51.
- [110] Ilin A, Logvinov R, Kulikov A, Prihodovsky A, Xu H, Ploshikhin V, et al. Computer aided optimisation of the thermal management during laser beam melting process. *Phys Proc* 2014;56:390–9.
- [111] Jamshidinia M, Kovacevic R. The influence of heat accumulation on the surface roughness in powder-bed additive manufacturing. *Surf Topogr Metrol Prop* 2015;3(1):014003.

- [112] Prabhakar P, Sames W, Dehoff R, Babu S. Computational modeling of residual stress formation during the electron beam melting process for Inconel 718. *Addit Manuf* 2015;7:83–91.
- [113] Riedlbauer D, Steinmann P, Mergheim J. Thermomechanical finite element simulations of selective electron beam melting processes: performance considerations. *Comput Mech* 2014;54(1):109–22.
- [114] Soylemez E, Beuth JL, Taminger K. Controlling melt pool dimensions over a wide range of material deposition rates in electron beam additive manufacturing. In: Proceedings of 21st solid freeform fabrication symposium. Austin (TX); 2010. p. 9–11.
- [115] Verhaeghe F, Craeghs T, Heulens J, Pandelaers L. A pragmatic model for selective laser melting with evaporation. *Acta Mater* 2009;57(20):6006–12.
- [116] Zeng K, Pal D, Gong HJ, Patil N, Stucker B. Comparison of 3DSIM thermal modelling of selective laser melting using new dynamic meshing method to ANSYS. *Mater Sci Tech* 2015;31(8):945–56.
- [117] Jamshidinia M, Kong F, Kovacevic R. Numerical modeling of heat distribution in the electron beam melting<sup>®</sup> of Ti-6Al-4V. *J Manuf Sci Eng* 2013;135(6):061010.
- [118] Yuan PP, Gu DD. Molten pool behaviour and its physical mechanism during selective laser melting of TiC/AlSi10Mg nanocomposites: simulation and experiments. *J Phys D Appl Phys* 2015;48(3):035303.
- [119] Gusarov A, Smurov I. Modeling the interaction of laser radiation with powder bed at selective laser melting. *Phys Proc* 2010;5:381–94.
- [120] He X, Mazumder J. Transport phenomena during direct metal deposition. *J Appl Phys* 2007;101(5): Article No. 053113.
- [121] Morville S, Carin M, Peyre P, Gharbi M, Carron D, Le Masson P, et al. 2D longitudinal modeling of heat transfer and fluid flow during multilayered direct laser metal deposition process. *J Laser Appl* 2012;24(3):032008.
- [122] Qi H, Mazumder J, Ki H. Numerical simulation of heat transfer and fluid flow in coaxial laser cladding process for direct metal deposition. *J Appl Phys* 2006;100(2): Article No. 024903.
- [123] Wen SY, Shin YC. Modeling of transport phenomena during the coaxial laser direct deposition process. *J Appl Phys* 2010;108(4): Article No. 044908.
- [124] Lee Y, Nordin M, Babu SS, Farson DF. Effect of fluid convection on dendrite arm spacing in laser deposition. *Metall Mater Trans B* 2014;45(4):1520–9.
- [125] Lee Y, Zhang W. Mesoscopic simulation of heat transfer and fluid flow in laser powder bed additive manufacturing. In: International solid free form fabrication symposium. Austin; 2015. p. 1154–65.
- [126] Khairallah SA, Anderson A. Mesoscopic simulation model of selective laser melting of stainless steel powder. *J Mater Process Technol* 2014;214(11):2627–36.
- [127] King W, Anderson AT, Ferencz RM, Hodge NE, Kamath C, Khairallah SA. Overview of modelling and simulation of metal powder bed fusion process at Lawrence Livermore National Laboratory. *Mater Sci Tech* 2015;31(8):957–68.
- [128] Korner C, Attar E, Heinl P. Mesoscopic simulation of selective beam melting processes. *J Mater Process Technol* 2011;211(6):978–87.
- [129] Korner C, Bauereiss A, Attar E. Fundamental consolidation mechanisms during selective beam melting of powders. *Model Simul Mater Sci* 2013;21(8):085011.
- [130] Moser D, Pannala S, Murthy J. Computation of effective thermal conductivity of powders for selective laser sintering simulations. *J Heat Transf* 2016;138(8):082002.
- [131] Roberts IA, Wang CJ, Esterlein R, Stanford M, Mynors DJ. A three-dimensional finite element analysis of the temperature field during laser melting of metal powders in additive layer manufacturing. *Int J Mach Tool Manuf* 2009;49(12–13):916–23.
- [132] Zhang L, Michaleris P. Investigation of Lagrangian and Eulerian finite element methods for modeling the laser forming process. *Finite Elem Anal Des* 2004;40(4):383–405.
- [133] Amine T, Newkirk JW, Liou F. Investigation of effect of process parameters on multilayer builds by direct metal deposition. *Appl Therm Eng* 2014;73(1):500–11.
- [134] Hu YP, Chen CW, Mukherjee K. Measurement of temperature distributions during laser cladding process. *J Laser Appl* 2000;12(3):126–30.
- [135] Shishkovsky IV, Scherbakov VI, Morozov YG, Kuznetsov MV, Parkin IP. Surface laser sintering of exothermic powder compositions. *J Therm Anal Calorim* 2008;91(2):427–36.
- [136] Benda J. Temperature controlled selective laser sintering. In: Proceedings of the solid freeform fabrication symposium; 1994. p. 277–284.
- [137] Doubenskaia M, Pavlov M, Chivel Y. Optical system for on-line monitoring and temperature control in selective laser melting technology. In: Key engineering materials; 2010. p. 458–61.
- [138] Hu DM, Kovacevic R. Sensing, modeling and control for laser-based additive manufacturing. *Int J Mach Tool Manu* 2003;43(1):51–60.
- [139] Jian X, Jinghua S, Yiqing G. Novel measurement method for selective laser sintering transient temperature field. In: 3rd International symposium on advanced optical manufacturing and testing technologies: optical test and measurement technology and equipment; 2007. p. 67234N–67234N.
- [140] Price S, Cooper K, Chou K. Evaluations of temperature measurements by near-infrared thermography in powder-based electron-beam additive manufacturing. In: Proceedings of the solid freeform fabrication symposium. Austin (TX): University of Texas; 2012. p. 761–73.
- [141] Mukherjee T, Zhang W, DebRoy T. An improved prediction of residual stresses and distortion in additive manufacturing. *Comp Mater Sci* 2017;126:360–72.
- [142] Elmer JW, Allen SM, Eagar TW. Microstructural development during solidification of stainless-steel alloys. *Metall Trans A* 1989;20(10):2117–31.
- [143] Mukherjee T, Manvatkar V, De A, DebRoy T. Dimensionless numbers in additive manufacturing. *J Appl Phys* 2017;121: Article No. 064904.
- [144] Kistler NA, Nassar AR, Reutzel EW, Corbin DJ, Beese AM. Effect of directed energy deposition processing parameters on laser deposited Inconel<sup>®</sup> 718: microstructure, fusion zone morphology, and hardness. *J Laser Appl* 2017;29(2):022005.
- [145] Antonysamy AA. Microstructure, texture and mechanical property evolution during additive manufacturing of Ti6Al4V alloy for aerospace applications. Manchester (UK): The University of Manchester; 2012.
- [146] Sames WJ, Unocic KA, Dehoff RR, Lolla T, Babu SS. Thermal effects on microstructural heterogeneity of Inconel 718 materials fabricated by electron beam melting. *J Mater Res* 2014;29(17):1920–30.
- [147] Shen N, Chou Y. Numerical thermal analysis in electron beam additive manufacturing with preheating effects. In: Proceedings of the 23rd solid freeform fabrication symposium. Austin (TX); 2012. p. 774–84.
- [148] Li YL, Gu DD. Parametric analysis of thermal behavior during selective laser melting additive manufacturing of aluminum alloy powder. *Mater Des* 2014;63:856–67.
- [149] Yin H, Felicelli SD. Dendrite growth simulation during solidification in the LENS process. *Acta Mater* 2010;58(4):1455–65.
- [150] Carroll BE, Palmer TA, Beese AM. Anisotropic tensile behavior of Ti-6Al-4V components fabricated with directed energy deposition additive manufacturing. *Acta Mater* 2015;87:309–20.
- [151] van Elsen M, Al-Bender F, Kruth JP. Application of dimensional analysis to selective laser melting. *Rapid Prototyp J* 2008;14(1):15–22.
- [152] Mukherjee T, Zuback JS, De A, DebRoy T. Printability of alloys for additive manufacturing. *Sci Rep* 2016;6: Article No. 9717.
- [153] Wei P. The physics of weld bead defects. INTECH Open Access Publisher; 2012.
- [154] Soderstrom E, Mendez P. Humping mechanisms present in high speed welding. *Sci Technol Weld Join* 2006;11(5):572–9.
- [155] Kumar A, DebRoy T. Toward a unified model to prevent humping defects in gas tungsten arc welding. *Weld J* 2006;85(12):292s–304s.
- [156] Kazanas P, Deherkar P, Almeida P, Lockett H, Williams S. Fabrication of geometrical features using wire and arc additive manufacture. *Proc Inst Mech Eng Part B-J Eng Manuf* 2012;226(B6):1042–51.
- [157] Adebayo A, Mehnen J, Tonnelier X. Limiting travel speed in additive layer manufacturing. In: 9th International conference on trends in welding research. Chicago (IL, USA); 2013.
- [158] Martina F, Mehnen J, Williams SW, Colegrove P, Wang F. Investigation of the benefits of plasma deposition for the additive layer manufacture of Ti-6Al-4V. *J Mater Process Technol* 2012;212(6):1377–86.
- [159] Wang FD, Williams S, Rush M. Morphology investigation on direct current pulsed gas tungsten arc welded additive layer manufactured Ti6Al4V alloy. *Int J Adv Manuf Technol* 2011;57(5–8):597–603.

- [160] Lopes G, Miranda R, Quintino L, Rodrigues J. Additive manufacturing of Ti-6Al-4V based components with high power fiber lasers. London: Tailor & Francis Group; 2007.
- [161] Gusarov AV, Yadroitsev I, Bertrand P, Smurov I. Heat transfer modelling and stability analysis of selective laser melting. *Appl Surf Sci* 2007;254(4):975–9.
- [162] Khan PAA, DebRoy T. Alloying element vaporization and weld pool temperature during laser-welding of AISI 202 stainless steel. *Metall Trans B* 1984;15(4):641–4.
- [163] Borisov OV, Mao XL, Fernandez A, Caetano M, Russo RE. Inductively coupled plasma mass spectrometric study of non-linear calibration behavior during laser ablation of binary Cu-Zn Alloys. *Spectrochim Acta B* 1999;54(9):1351–65.
- [164] Brice CA, Rosenberger BT, Sankaran SN, Taminger KM, Woods B, Nasserafi R. Chemistry control in electron beam deposited titanium alloys. *Mater Sci Forum* 2009;155–8.
- [165] Brice C, Shenoy R, Kral M, Buchanan K. Precipitation behavior of aluminum alloy 2139 fabricated using additive manufacturing. *Mater Sci Eng A* 2015;648:9–14.
- [166] Gaytan SM, Murr LE, Medina F, Martinez E, Lopez MI, Wicker RB. Advanced metal powder based manufacturing of complex components by electron beam melting. *Mater Technol* 2009;24(3):180–90.
- [167] Taminger K. Electron beam additive manufacturing: state-of-the-technology, challenges & opportunities. In: Direct digital manufacturing workshop. Solomons (MD); 2010.
- [168] He X, DebRoy T, Fuerschbach PW. Alloying element vaporization during laser spot welding of stainless steel. *J Phys D Appl Phys* 2003;36(23):3079–88.
- [169] Mundra K, DebRoy T. Toward understanding alloying element vaporization during laser-beam welding of stainless steel. *Weld J* 1993;72(1):S1–9.
- [170] Semiatin SL, Ivanchenko VG, Akhonin SV, Ivasishin OM. Diffusion models for evaporation losses during electron-beam melting of alpha/beta-titanium alloys. *Metall Mater Trans B* 2004;35(2):235–45.
- [171] He X, DebRoy T, Fuerschbach PW. Composition change of stainless steel during microjoining with short laser pulse. *J Appl Phys* 2004;96(8):4547–55.
- [172] Zhao H, DebRoy T. Weld metal composition change during conduction mode laser welding of aluminum alloy 5182. *Metall Mater Trans B* 2001;32(1):163–72.
- [173] Mundra K, DebRoy T. Calculation of weld metal composition change in high-power conduction mode carbon-dioxide laser-welded stainless steels. *Metall Trans B* 1993;24(1):145–55.
- [174] Khan PAA, DebRoy T, David SA. Laser-beam welding of high-manganese stainless steels - examination of alloying element loss and microstructural changes. *Weld J* 1988;67(1):S1–7.
- [175] Collur MM, Paul A, DebRoy T. Mechanism of alloying element vaporization during laser-welding. *Metall Trans B* 1987;18(4):733–40.
- [176] Matthews MJ, Guss G, Khairallah SA, Rubenchik AM, Depond PJ, King WE. Denudation of metal powder layers in laser powder bed fusion processes. *Acta Mater* 2016;114:33–42.
- [177] Barclay RC. Parameter optimization for controlling aluminum loss when laser depositing Ti-6Al-4V. Missouri University of Science and Technology; 2013.
- [178] Morgan R, Sutcliffe CJ, O'Neill W. Density analysis of direct metal laser re-melted 316L stainless steel cubic primitives. *J Mater Sci* 2004;39(4):1195–205.
- [179] Olakanmi EO, Cochrane RF, Dalgarno KW. Densification mechanism and microstructural evolution in selective laser sintering of Al-12Si powders. *J Mater Process Technol* 2011;211(1):113–21.
- [180] Jia QB, Gu DD. Selective laser melting additive manufacturing of Inconel 718 superalloy parts: densification, microstructure and properties. *J Alloy Comp* 2014;585:713–21.
- [181] Carlton HD, Haboub A, Gallegos GF, Parkinson DY, MacDowell AA. Damage evolution and failure mechanisms in additively manufactured stainless steel. *Mater Sci Eng A* 2016;651:406–14.
- [182] King WE, Barth HD, Castillo VM, Gallegos GF, Gibbs JW, Hahn DE, et al. Observation of keyhole-mode laser melting in laser powder-bed fusion additive manufacturing. *J Mater Process Technol* 2014;214(12):2915–25.
- [183] Kaplan A. A model of deep penetration laser-welding based on calculation of the keyhole profile. *J Phys D Appl Phys* 1994;27(9):1805–14.
- [184] Svensson M, Acklid U, Ab A. Titanium alloys manufactured with electron beam melting mechanical and chemical properties. In: Proceedings of the materials and processes for medical devices conference; 2010. p. 189–94.
- [185] Darvish K, Chen ZW, Pasang T. Reducing lack of fusion during selective laser melting of CoCrMo alloy: effect of laser power on geometrical features of tracks. *Mater Des* 2016;112:357–66.
- [186] Elmer JW, Vaja J, Carlton H, Pong R. The effect of Ar and N<sub>2</sub> shielding gas on laser weld porosity in steel, stainless steels, and nickel. *Weld J* 2015;94(10).
- [187] Elmer JW, Vaja J, Carlton H. The effect of reduced pressure on laser keyhole weld porosity and weld geometry in commercially pure titanium and nickel. *Weld J* 2016;95(11):419S–30S.
- [188] Thijssen L, Verhaeghe F, Craeghs T, Van Humbeeck J, Kruth JP. A study of the micro structural evolution during selective laser melting of Ti-6Al-4V. *Acta Mater* 2010;58(9):3303–12.
- [189] Aboulkhair NT, Everitt NM, Ashcroft I, Tuck C. Reducing porosity in AlSi10Mg parts processed by selective laser melting. *Addit Manuf* 2014;1:77–86.
- [190] Bauereiss A, Scharowsky T, Korner C. Defect generation and propagation mechanism during additive manufacturing by selective beam melting. *J Mater Process Technol* 2014;214(11):2522–8.
- [191] Slotwinski JA, Garboczi EJ, Hebenstreit KM. Porosity measurements and analysis for metal additive manufacturing process control. *J Res Natl Inst Stan* 2014;119:494–528.
- [192] Girardin E, Renghini C, Dyson J, Calabucci V, Moroncini F, Albertini G. Characterization of porosity in a laser sintered MMCp using X-ray synchrotron phase contrast microtomography. *Mater Sci Appl* 2011;2(09):1322.
- [193] Gong X, Anderson T, Chou K. Review on powder-based electron beam additive manufacturing technology. In: ASME/ISCIE 2012 international symposium on flexible automation; 2012. p. 507–15.
- [194] Strano G, Hao L, Everson RM, Evans KE. Surface roughness analysis, modelling and prediction in selective laser melting. *J Mater Process Technol* 2013;213(4):589–97.
- [195] Mumtaz K, Hopkinson N. Top surface and side roughness of Inconel 625 parts processed using selective laser melting. *Rapid Prototyp J* 2009;15(2):96–103.
- [196] Lyczkowska E, Szymczyk P, Dybala B, Chlebus E. Chemical polishing of scaffolds made of Ti-6Al-7Nb alloy by additive manufacturing. *Arch Civ Mech Eng* 2014;14(4):586–94.
- [197] Dehoff R, Duty C, Peter W, Yamamoto Y, Chen W, Blue C, et al. Case study: additive manufacturing of aerospace brackets. *Adv Mater Process* 2013;171(3):19–22.
- [198] Mumtaz K, Hopkinson N. Selective laser melting of Inconel 625 using pulse shaping. *Rapid Prototyp J* 2010;16(4):248–57.
- [199] Rahmati S, Vahabli E. Evaluation of analytical modeling for improvement of surface roughness of FDM test part using measurement results. *Int J Adv Manuf Technol* 2015;79(5–8):823–9.
- [200] Qiu CL, Panwisawas C, Ward M, Basoalto HC, Brooks JW, Attallah MM. On the role of melt flow into the surface structure and porosity development during selective laser melting. *Acta Mater* 2015;96:72–9.
- [201] Kruth JP, Froyen L, Van Vaerenbergh J, Mercelis P, Rombouts M, Lauwers B. Selective laser melting of iron-based powder. *J Mater Process Technol* 2004;149(1–3):616–22.
- [202] Niu HJ, Chang ITH. Instability of scan tracks of selective laser sintering of high speed steel powder. *Scripta Mater* 1999;41(11):1229–34.

- [203] Gu DD, Shen YF. Balling phenomena in direct laser sintering of stainless steel powder: metallurgical mechanisms and control methods. *Mater Des* 2009;30(8):2903–10.
- [204] Kruth JP, Levy G, Klocke F, Childs THC. Consolidation phenomena in laser and powder-bed based layered manufacturing. *CIRP Ann Manuf Techn* 2007;56(2):730–59.
- [205] Yasa E, Deckers J, Kruth JP. The investigation of the influence of laser re-melting on density, surface quality and microstructure of selective laser melting parts. *Rapid Prototyp J* 2011;17(5):312–27.
- [206] Calignano F, Manfredi D, Ambrosio EP, Iuliano L, Fino P. Influence of process parameters on surface roughness of aluminum parts produced by DMLS. *Int J Adv Manuf Technol* 2013;67(9–12):2743–51.
- [207] Spierings AB, Herres N, Levy G. Influence of the particle size distribution on surface quality and mechanical properties in AM steel parts. *Rapid Prototyp J* 2011;17(3):195–202.
- [208] Kempen K, Thijss L, Vrancken B, Buls S, Van Humbeeck J, Kruth J. Producing crack-free, high density M2 Hss parts by selective laser melting: pre-heating the baseplate. In: Proceedings of the 24th international solid freeform fabrication symposium. Austin (TX): Laboratory for freeform fabrication; 2013. p. 131–9.
- [209] Carter LN, Attallah MM, Reed RC. Laser powder bed fabrication of nickel-base superalloys: Influence of parameters; characterisation, quantification and mitigation of cracking. *Superalloys 2012;2012:577–86*.
- [210] Kou S. Welding metallurgy. 2nd ed. Hoboken, NJ: John Wiley & Sons; 2003.
- [211] Carter LN, Wang X, Read N, Khan R, Aristizabal M, Essa K, et al. Process optimisation of selective laser melting using energy density model for nickel based superalloys. *Mater Sci Tech* 2016;32(7):657–61.
- [212] Zhao XM, Lin X, Chen J, Xue L, Huang WD. The effect of hot isostatic pressing on crack healing, microstructure, mechanical properties of Rene88DT superalloy prepared by laser solid forming. *Mater Sci Eng A* 2009;504(1–2):129–34.
- [213] Lewis GK, Schlienger E. Practical considerations and capabilities for laser assisted direct metal deposition. *Mater Des* 2000;21(4):417–23.
- [214] Mercelis P, Kruth JP. Residual stresses in selective laser sintering and selective laser melting. *Rapid Prototyp J* 2006;12(5):254–65.
- [215] Goldak JA, Akhlaghi M. Computational welding mechanics. 1st ed. US: Springer; 2006.
- [216] Masubuchi K. Analysis of welded structures: residual stresses, distortion, and their consequences. 1st ed. Elmsford (New York): Pergamon Press Inc.; 1980.
- [217] Rathbun HJ, Fredette LF, Scott PM, Csontos AA, Rudland DL. NRC welding residual stress validation program international round robin program and findings. In: ASME 2011 Pressure vessels and piping conference; 2011. p. 1539–45.
- [218] Qiao DX, Feng ZL, Zhang W, Wang YL, Crooker P. Modeling of weld residual plastic strain and stress in dissimilar metal butt weld in nuclear reactors. Proceedings of the ASME pressure vessels and piping conference - 2013, Vol 6b: Materials and Fabrication; 2014.
- [219] Pellereau B, Hurrell P, Gill C, Francis J, Bate S. Phase transformation properties sensitivity study in a ferritic groove weld. In: Proceedings of the ASME pressure vessels and piping conference - 2013, Vol 6b: Materials and Fabrication; 2014.
- [220] Labudovic M, Hu D, Kovacevic R. A three dimensional model for direct laser metal powder deposition and rapid prototyping. *J Mater Sci* 2003;38(1):35–49.
- [221] Smith J, Xiong W, Yan W, Lin S, Cheng P, Kafka OL, et al. Linking process, structure, property, and performance for metal-based additive manufacturing: computational approaches with experimental support. *Comput Mech* 2016;57(4):583–610.
- [222] Lindgren L-E. Finite element modeling and simulation of welding part 1: increased complexity. *J Therm Stresses* 2001;24(2):141–92.
- [223] Lindgren L-E. Finite element modeling and simulation of welding. Part 2: improved material modeling. *J Therm Stress* 2001;24(3):195–231.
- [224] Lindgren L-E. Finite element modeling and simulation of welding. Part 3: efficiency and integration. *J Therm Stress* 2001;24(4):305–34.
- [225] De A, DebRoy T. A perspective on residual stresses in welding. *Sci Technol Weld Join* 2011;16(3):204–8.
- [226] Denlinger ER, Michaleris P. Effect of stress relaxation on distortion in additive manufacturing process modeling. *Addit Manuf* 2016;12:51–9.
- [227] Song X, Xie M, Hofmann F, Illston T, Connolley T, Reinhard C, et al. Residual stresses and microstructure in Powder Bed Direct Laser Deposition (PB DLD) samples. *Int J Mater Form* 2015;8(2):245–54.
- [228] Fergani O, Berto F, Welo T, Liang SY. Analytical modelling of residual stress in additive manufacturing. *Fatigue Fract Eng M* 2017;40(6):971–8.
- [229] Alimardani M, Toyserkani E, Huissoon JP. A 3D dynamic numerical approach for temperature and thermal stress distributions in multilayer laser solid freeform fabrication process. *Opt Laser Eng* 2007;45(12):1115–30.
- [230] Beuth J, Klingbeil N. The role of process variables in laser-based direct metal solid freeform fabrication. *JOM* 2001;53(9):36–9.
- [231] Kahlen FJ, Kar A. Residual stresses in laser-deposited metal parts. *J Laser Appl* 2001;13(2):60–9.
- [232] Wang L, Felicelli SD, Craig JE. Experimental and numerical study of the LENS rapid fabrication process. *J Manuf Sci Eng* 2009;131(4):041019.
- [233] Wang L, Felicelli SD, Pratt P. Residual stresses in LENS-deposited AISI 410 stainless steel plates. *Mater Sci Eng A* 2008;496(1–2):234–41.
- [234] Chew Y, Pang JHL, Bi G, Song B. Thermo-mechanical model for simulating laser cladding induced residual stresses with single and multiple clad beads. *J Mater Process Technol* 2015;224:89–101.
- [235] Dai K, Shaw L. Thermal and stress modeling of multi-material laser processing. *Acta Mater* 2001;49(20):4171–81.
- [236] Ghosh S, Choi J. Three-dimensional transient finite element analysis for residual stresses in the laser aided direct metal/material deposition process. *J Laser Appl* 2005;17(3):144–58.
- [237] Ghosh S, Choi J. Modeling and experimental verification of transient/residual stresses and microstructure formation in multi-layer laser aided DMD process. *J Heat Trans* 2006;128(7):662–79.
- [238] Ghosh S, Choi J. Deposition pattern based thermal stresses in single-layer laser aided direct material deposition process. *J Manuf Sci Eng* 2007;129(2):319–32.
- [239] Nie ZG, Wang G, McGuffin-Cawley JD, Narayanan B, Zhang SJ, Schwam D, et al. Experimental study and modeling of H13 steel deposition using laser hot-wire additive manufacturing. *J Mater Process Technol* 2016;235:171–86.
- [240] Chiumenti M, Cervera M, Salmi A, de Saracibar CA, Dialami N, Matsui K. Finite element modeling of multi-pass welding and shaped metal deposition processes. *Comput Method Appl Mech Eng* 2010;199(37–40):2343–59.
- [241] Denlinger ER, Irwin J, Michaleris P. Thermomechanical modeling of additive manufacturing large parts. *J Manuf Sci Eng* 2014;136(6):061007.
- [242] Kamara AM, Marimuthu S, Li L. A numerical investigation into residual stress characteristics in laser deposited multiple layer Waspaloy parts. *J Manuf Sci Eng* 2011;133(3):031013.
- [243] Marimuthu S, Clark D, Allen J, Kamara A, Mativenga P, Li L, et al. Finite element modelling of substrate thermal distortion in direct laser additive manufacture of an aero-engine component. *Proc Inst Mech Eng, Part C: J Mech Eng Sci* 2013;1987–99.
- [244] Mukherjee T, Manvatkar V, De A, DebRoy T. Mitigation of thermal distortion during additive manufacturing. *Scripta Mater* 2017;127:79–83.
- [245] Denlinger ER, Heigel JC, Michaleris P. Residual stress and distortion modeling of electron beam direct manufacturing Ti-6Al-4V. *Proc Inst Mech Eng Part B-J Eng Manuf* 2015;229(10):1803–13.
- [246] Ding J, Colegrove P, Mehnert J, Williams S, Wang F, Almeida PS. A computationally efficient finite element model of wire and arc additive manufacture. *Int J Adv Manuf Technol* 2014;70(1–4):227–36.
- [247] Li C, Fu C, Guo Y, Fang F. A multiscale modeling approach for fast prediction of part distortion in selective laser melting. *J Mater Process Technol* 2016;229:703–12.
- [248] Yuan MG, Ueda Y. Prediction of residual stresses in welded T- and I-joints using inherent strains. *J Eng Mater* 1996;118(2):229–34.
- [249] Withers PJ, Bhadeshia HKDH. Residual stress. Part 1 – Measurement techniques. *Mater Sci Tech* 2001;17(4):355–65.
- [250] Attallah MM, Jennings R, Wang X, Carter LN. Additive manufacturing of Ni-based superalloys: the outstanding issues. *MRS Bull* 2016;41(10):758–64.
- [251] Withers PJ, Turksi M, Edwards L, Bouchard PJ, Buttle DJ. Recent advances in residual stress measurement. *Int J Pres Ves Pip* 2008;85(3):118–27.

- [252] Liu FC, Lin X, Yang GL, Song MH, Chen J, Huang WD. Microstructure and residual stress of laser rapid formed Inconel 718 nickel-base superalloy. *Opt Laser Technol* 2011;43(1):208–13.
- [253] Lu YJ, Wu SQ, Gan YL, Huang TT, Yang CG, Lin JJ, et al. Study on the microstructure, mechanical property and residual stress of SLM Inconel-718 alloy manufactured by differing island scanning strategy. *Opt Laser Technol* 2015;75:197–206.
- [254] Griffith ML, Schlienger ME, Harwell LD, Oliver MS, Baldwin MD, Ensz MT, et al. Understanding thermal behavior in the LENS process. *Mater Des* 1999;20(2–3):107–13.
- [255] Casavola C, Carnpanelli SL, Pappalettere C. Preliminary investigation on distribution of residual stress generated by the selective laser melting process. *J Strain Anal Eng* 2009;44(1):93–104.
- [256] Lai YB, Liu WJ, Kong Y, Wang FY, Zhao YH. Influencing factors of residual stress of Ti-6.5Al-1Mo-1V-2Zr alloy by laser rapid forming process. *Rare Metal Mat Eng* 2013;42(7):1526–30.
- [257] Zhang SY, Lin X, Chen J, Huang WD. Influence of heat treatment on residual stress of Ti-6Al-4V alloy by laser solid forming. *Rare Metal Mat Eng* 2009;38(5):774–8.
- [258] Liu Y, Yang YQ, Wang D. A study on the residual stress during selective laser melting (SLM) of metallic powder. *Int J Adv Manuf Technol* 2016;87(1–4):647–56.
- [259] Yadroitsev I, Yadroitseva I. Evaluation of residual stress in stainless steel 316L and Ti6Al4V samples produced by selective laser melting. *Virtual Phys Prototyp* 2015;10(2):67–76.
- [260] Brice CA, Hofmeister WH. Determination of bulk residual stresses in electron beam additive-manufactured aluminum. *Metall Mater Trans A* 2013;44a(11):5147–53.
- [261] Cottam R, Wang J, Luzin V. Characterization of microstructure and residual stress in a 3D H13 tool steel component produced by additive manufacturing. *J Mater Res* 2014;29(17):1978–86.
- [262] Moat RJ, Pinkerton AJ, Li L, Withers PJ, Preuss M. Residual stresses in laser direct metal deposited Waspaloy. *Mater Sci Eng A* 2011;528(6):2288–98.
- [263] Pratt P, Felicelli SD, Wang L, Hubbard CR. Residual stress measurement of laser-engineered net shaping AISI 410 thin plates using neutron diffraction. *Metall Mater Trans A* 2008;39a(13):3155–63.
- [264] Rangaswamy P, Griffith ML, Prime MB, Holden TM, Rogge RB, Edwards JM, et al. Residual stresses in LENS (R) components using neutron diffraction and contour method. *Mater Sci Eng A* 2005;399(1–2):72–83.
- [265] Rangaswamy P, Holden TM, Rogge RB, Griffith ML. Residual stresses in components formed by the laser-engineered net shaping (LENS (R)) process. *J Strain Anal Eng* 2003;38(6):519–27.
- [266] Vrancken B, Cain V, Knutsen R, Van Humbeeck J. Residual stress via the contour method in compact tension specimens produced via selective laser melting. *Scripta Mater* 2014;87:29–32.
- [267] Wu AS, Brown DW, Kumar M, Gallegos GF, King WE. An experimental investigation into additive manufacturing-induced residual stresses in 316L stainless steel. *Metall Mater Trans A* 2014;45a(13):6260–70.
- [268] Zhang W, Feng Z, Crooker P. Improved procedure for computing residual stresses from neutron diffraction data and its application to multipass dissimilar welds. *Sci Technol Weld Joi* 2011;16(3):254–60.
- [269] Tammas-Williams S, Todd I. Design for additive manufacturing with site-specific properties in metals and alloys. *Scripta Mater* 2017;135:105–10.
- [270] Buchbinder D, Meiners W, Pirch N, Wissenbach K, Schrage J. Investigation on reducing distortion by preheating during manufacture of aluminum components using selective laser melting. *J Laser Appl* 2014;26(1):012004.
- [271] Dunbar A, Denlinger E, Heigel J, Michaleris P, Guerrier P, Martukanitz R, et al. Development of experimental method for in situ distortion and temperature measurements during the laser powder bed fusion additive manufacturing process. *Addit Manuf* 2016;12:25–30.
- [272] Salvati E, Lunt A, Ying S, Sui T, Zhang H, Heason C, et al. Eigenstrain reconstruction of residual strains in an additively manufactured and shot peened nickel superalloy compressor blade. *Comput Method Appl Mech Eng* 2017;320:335–51.
- [273] Gao M, Wang ZM, Li XY, Zeng XY. The effect of deposition patterns on the deformation of substrates during direct laser fabrication. *Comput Method Appl Mech Eng* 2013;135(3):034502.
- [274] Colegrove PA, Coules HE, Fairman J, Martina F, Kashoob T, Mamash H, et al. Microstructure and residual stress improvement in wire and arc additively manufactured parts through high-pressure rolling. *J Mater Process Technol* 2013;213(10):1782–91.
- [275] Martina F, Roy MJ, Szost BA, Terzi S, Colegrove PA, Williams SW, et al. Residual stress of as-deposited and rolled wire plus arc additive manufacturing Ti-6Al-4V components. *Mater Sci Tech* 2016;32(14):1439–48.
- [276] Szost BA, Terzi S, Martina F, Boisselier D, Prytuliak A, Pining T, et al. A comparative study of additive manufacturing techniques: Residual stress and microstructural analysis of CLAD and WAAM printed Ti-6Al-4V components. *Mater Des* 2016;89:559–67.
- [277] Mani M, Lane B, Dommez A, Feng S, Moylan S, Fesperm R. Measurement science needs for real-time control of additive manufacturing powder bed fusion processes. Gaithersburg (MD): National Institute of Standards and Technology [Standard No NISTIR 2015;8036].
- [278] Fathi A, Khajepour A, Durali M, Toyserkani E. Geometry control of the deposited layer in a nonplanar laser cladding process using a variable structure controller. *J Manuf Sci Eng* 2008;130(3):031003.
- [279] Salehi D, Brandt M. Melt pool temperature control using LabVIEW in Nd: YAG laser blown powder cladding process. *Int J Adv Manuf Technol* 2006;29(3–4):273–8.
- [280] Davis TA, Shin YC. Vision-based clad height measurement. *Mach Vision Appl* 2011;22(1):129–36.
- [281] Rodriguez E, Mireles J, Terrazas CA, Espalin D, Perez MA, Wicker RB. Approximation of absolute surface temperature measurements of powder bed fusion additive manufacturing technology using in situ infrared thermography. *Addit Manuf* 2015;5:31–9.
- [282] Bi G, Sun C, Gasser A. Study on influential factors for process monitoring and control in laser aided additive manufacturing. *J Mater Process Technol* 2013;213(3):463–8.
- [283] Islam M, Purtonen T, Piili H, Salminen A, Nyrhilä O. Temperature profile and imaging analysis of laser additive manufacturing of stainless steel. *Phys Proc* 2013;41:835–42.
- [284] Denlinger ER, Heigel JC, Michaleris P, Palmer TA. Effect of inter-layer dwell time on distortion and residual stress in additive manufacturing of titanium and nickel alloys. *J Mater Process Technol* 2015;215:123–31.
- [285] Heigel J, Michaleris P, Reutzel E. Thermo-mechanical model development and validation of directed energy deposition additive manufacturing of Ti-6Al-4V. *Addit Manuf* 2015;5:9–19.
- [286] Barua S, Liou F, Newkirk J, Sparks T. Vision-based defect detection in laser metal deposition process. *Rapid Prototyp J* 2014;20(1):77–85.
- [287] Tang L, Landers RG. Melt pool temperature control for laser metal deposition processes-Part I: online temperature control. *J Manuf Sci Eng* 2010;132(1):011010.
- [288] Tang L, Landers RG. Melt pool temperature control for laser metal deposition processes-Part II: layer-to-layer temperature control. *J Manuf Sci Eng* 2010;132(1):011011.
- [289] Zeinali M, Khajepour A. Height control in laser cladding using adaptive sliding mode technique: theory and experiment. *J Manuf Sci Eng* 2010;132(4):041016.
- [290] Popova E, Rodgers TM, Gong X, Cecen A, Madison JD, Kalidindi SR. Process-structure linkages using a data science approach: application to simulated additive manufacturing data. *Integ Mater Manuf Innov* 2017;1–15.
- [291] Farshidianfar MH, Khajepour A, Gerlich A. Real-time control of microstructure in laser additive manufacturing. *Int J Adv Manuf Technol* 2016;82(5–8):1173–86.
- [292] Nassar AR, Keist JS, Reutzel EW, Spurgeon TJ. Intra-layer closed-loop control of build plan during directed energy additive manufacturing of Ti-6Al-4V. *Addit Manuf* 2015;6:39–52.
- [293] Lippold JC. *Welding metallurgy and weldability*. Hoboken, NJ: John Wiley and Sons; 2014.

- [294] ASM Handbook. Welding fundamentals and processes. ASM International; 2011.
- [295] Rai R, Elmer JW, Palmer TA, DebRoy T. Heat transfer and fluid flow during keyhole mode laser welding of tantalum, Ti-6Al-4V, 304L stainless steel and vanadium. *J Phys D Appl Phys* 2007;40(18):5753–66.
- [296] Elmer JW, Ellsworth GF, Florando JN, Golosker IV, Mulay RP. Microstructure and mechanical properties of 21-6-9 stainless steel electron beam welds. *Metall Mater Trans A* 2017;48(4):1771–87.
- [297] Wei HL, Elmer JW, DebRoy T. Origin of grain orientation during solidification of an aluminum alloy. *Acta Mater* 2016;115:123–31.
- [298] Wei HL, Elmer JW, DebRoy T. Three-dimensional modeling of grain structure evolution during welding of an aluminum alloy. *Acta Mater* 2017;126:413–25.
- [299] Vilar R, Santos EC, Ferreira PN, Franco N, da Silva RC. Structure of NiCrAlY coatings deposited on single-crystal alloy turbine blade material by laser cladding. *Acta Mater* 2009;57(18):5292–302.
- [300] Ocelík V, Furár I, De Hosson JTM. Microstructure and properties of laser clad coatings studied by orientation imaging microscopy. *Acta Mater* 2010;58(20):6763–72.
- [301] Sun S, Durandet Y, Brandt M. Parametric investigation of pulsed Nd: YAG laser cladding of stellite 6 on stainless steel. *Surf Coat Technol* 2005;19(2):225–31.
- [302] Thivillon L, Bertrand P, Laget B, Smurov I. Potential of direct metal deposition technology for manufacturing thick functionally graded coatings and parts for reactors components. *J Nucl Mater* 2009;385(2):236–41.
- [303] Pei Y, De Hosson JTM. Functionally graded materials produced by laser cladding. *Acta Mater* 2000;48(10):2617–24.
- [304] Dinda GP, Dasgupta AK, Mazumder J. Laser aided direct metal deposition of Inconel 625 superalloy: microstructural evolution and thermal stability. *Mater Sci Eng A* 2009;509(1–2):98–104.
- [305] Dinda GP, Dasgupta AK, Mazumder J. Texture control during laser deposition of nickel-based superalloy. *Scripta Mater* 2012;67(5):503–6.
- [306] Basak A, Das S. Epitaxy and microstructure evolution in metal additive manufacturing. *Ann Rev Mater Res* 2016;46(1):125–49.
- [307] Das S. Physical aspects of process control in selective laser sintering of metals. *Adv Eng Mater* 2003;5(10):701–11.
- [308] Rappaz M, Gandin CA. Probabilistic modeling of microstructure formation in solidification processes. *Acta Metall Mater* 1993;41(2):345–60.
- [309] David SA, Vitek JM. Correlation between solidification parameters and weld microstructures. *Int Mater Rev* 1989;34(5):213–45.
- [310] Dinda GP, Dasgupta AK, Mazumder J. Evolution of microstructure in laser deposited Al-11.28%Si alloy. *Surf Coat Technol* 2012;206(8–9):2152–60.
- [311] Garibaldi M, Ashcroft I, Simonelli M, Hague R. Metallurgy of high-silicon steel parts produced using Selective Laser Melting. *Acta Mater* 2016;110:207–16.
- [312] Yadollahi A, Shamsaei N, Thompson SM, Seely DW. Effects of process time interval and heat treatment on the mechanical and microstructural properties of direct laser deposited 316L stainless steel. *Mater Sci Eng A* 2015;644:171–83.
- [313] Thijss L, Sistiaga MLM, Wauthle R, Xie QG, Kruth JP, Van Humbeeck J. Strong morphological and crystallographic texture and resulting yield strength anisotropy in selective laser melted tantalum. *Acta Mater* 2013;61(12):4657–68.
- [314] Liu Z, Qi H. Effects of processing parameters on crystal growth and microstructure formation in laser powder deposition of single-crystal superalloy. *J Mater Process Technol* 2015;216:19–27.
- [315] Wei HL, Mazumder J, DebRoy T. Evolution of solidification texture during additive manufacturing. *Sci Rep* 2015;5: Article No. 16446.
- [316] Liu Z, Qi H. Effects of substrate crystallographic orientations on crystal growth and microstructure formation in laser powder deposition of nickel-based superalloy. *Acta Mater* 2015;87:248–58.
- [317] Liu W, DuPont JN. Effects of melt-pool geometry on crystal growth and microstructure development in laser surface-melted superalloy single crystals. *Acta Mater* 2004;52(16):4833–47.
- [318] Carter LN, Martin C, Withers PJ, Attallah MM. The influence of the laser scan strategy on grain structure and cracking behaviour in SLM powder-bed fabricated nickel superalloy. *J Alloy Comp* 2014;615:338–47.
- [319] Kurz W, Giovanola B, Trivedi R. Theory of microstructural development during rapid solidification. *Acta Metall* 1986;34(5):823–30.
- [320] Kobryn PA, Semiatin SL. Microstructure and texture evolution during solidification processing of Ti-6Al-4V. *J Mater Process Technol* 2003;135(2–3):330–9.
- [321] Blecher JJ, Palmer TA, DebRoy T. Solidification map of a nickel-base alloy. *Metall Mater Trans A* 2014;45A(4):2142–51.
- [322] Nastac L, El-Kaddah N. Experimental and stochastic modeling of the globular microstructure and the microsegregation evolution during the solidification of magnesium alloys cast at low superheat via containerless melting. *J Manuf Sci Prod* 2015;15(1):3–12.
- [323] Liu W, Dupont J. Effects of substrate crystallographic orientations on crystal growth and microstructure development in laser surface-melted superalloy single crystals. Mathematical modeling of single-crystal growth in a melt pool (Part II). *Acta Mater* 2005;53(5):1545–58.
- [324] Wang L, Wang N. Effect of substrate orientation on the formation of equiaxed stray grains in laser surface remelted single crystal superalloys: experimental investigation. *Acta Mater* 2016;104:250–8.
- [325] Wang L, Wang N, Yao WJ, Zheng YP. Effect of substrate orientation on the columnar-to-equiaxed transition in laser surface remelted single crystal superalloys. *Acta Mater* 2015;88:283–92.
- [326] Acharya R, Bansal R, Gambone JJ, Kaplan MA, Fuchs GE, Rudawski NG, et al. Additive manufacturing and characterization of René 80 superalloy processed through scanning laser epitaxy for turbine engine hot-section component repair. *Adv Eng Mater* 2015;17(7):942–50.
- [327] Y-j Xie, M-c Wang, D-w Huang. Comparative study of microstructural characteristics of electrospark and Nd:YAG laser epitaxially growing coatings. *Appl Surf Sci* 2007;253(14):6149–56.
- [328] Do X, Li D, Zhang A, He B, Zhang H, Doan T. Investigation on multi-track multi-layer epitaxial growth of columnar crystal in direct laser forming. *J Laser Appl* 2013;25(1):012007.
- [329] Vilar R, Almeida A. Repair and manufacturing of single crystal Ni-based superalloys components by laser powder deposition—a review. *J Laser Appl* 2015;27(S1):S17004.
- [330] Zhang C, Li L, Deceuster A. Thermomechanical analysis of multi-bead pulsed laser powder deposition of a nickel-based superalloy. *J Mater Process Technol* 2011;211(9):1478–87.
- [331] Liang Y-J, Wang H-M. Origin of stray-grain formation and epitaxy loss at substrate during laser surface remelting of single-crystal nickel-base superalloys. *Mater Des* 2016;102:297–302.
- [332] Joseph J, Jarvis T, Wu X, Stanford N, Hodgson P, Fabijanic DM. Comparative study of the microstructures and mechanical properties of direct laser fabricated and arc-melted Al<sub>x</sub>CoCrFeNi high entropy alloys. *Mater Sci Eng A* 2015;633:184–93.
- [333] Acharya R, Das S. Additive manufacturing of IN100 superalloy through scanning laser epitaxy for turbine engine hot-section component repair: process development, modeling, microstructural characterization, and process control. *Metall Mater Trans A* 2015;46(9):3864–75.
- [334] Basak A, Acharya R, Das S. Additive manufacturing of single-crystal superalloy CMSX-4 through scanning laser epitaxy: computational modeling, experimental process development, and process parameter optimization. *Metall Mater Trans A* 2016;47(8):3845–59.
- [335] Liu Z, Qi H. Numerical simulation of transport phenomena for a double-layer laser powder deposition of single-crystal superalloy. *Metall Mater Trans A* 2014;45(4):1903–15.
- [336] Ramsperger M, Singer RF, Körner C. Microstructure of the nickel-base superalloy CMSX-4 fabricated by selective electron beam melting. *Metall Mater Trans A* 2016;47(3):1469–80.
- [337] Liu WP, DuPont JN. Direct laser deposition of a single-crystal Ni<sub>3</sub>Al-based IC221W alloy. *Metall Mater Trans A* 2005;36A(12):3397–406.
- [338] Acharya R, Bansal R, Gambone JJ, Das S. A coupled thermal, fluid flow, and solidification model for the processing of single-crystal alloy CMSX-4 through scanning laser epitaxy for turbine engine hot-section component repair (Part I). *Metall Mater Trans B* 2014;45(6):2247–61.
- [339] Acharya R, Bansal R, Gambone JJ, Das S. A microstructure evolution model for the processing of single-crystal alloy CMSX-4 through scanning laser epitaxy for turbine engine hot-section component repair (part II). *Metall Mater Trans B* 2014;45(6):2279–90.

- [340] Anderson TD, DuPont JN, DebRoy T. Origin of stray grain formation in single-crystal superalloy weld pools from heat transfer and fluid flow modeling. *Acta Mater* 2010;58(4):1441–54.
- [341] Anderson TD, DuPont JN, DebRoy T. Stray grain formation in welds of single-crystal Ni-base superalloy CMSX-4. *Metall Mater Trans A* 2009;41(1):181–93.
- [342] Das S, Bourell DL, Babu SS. Metallic materials for 3D printing. *MRS Bull* 2016;41(10):729–41.
- [343] Gaumann M, Bezencon C, Canalis P, Kurz W. Single-crystal laser deposition of superalloys: processing-microstructure maps. *Acta Mater* 2001;49(6):1051–62.
- [344] Gaumann M, Henry S, Cleton F, Wagniere JD, Kurz W. Epitaxial laser metal forming: analysis of microstructure formation. *Mater Sci Eng A* 1999;271(1–2):232–41.
- [345] Flemings MC. Solidification processing. New York: McGraw-Hill; 1974.
- [346] Hunt JD. Steady-state columnar and equiaxed growth of dendrites and eutectic. *Mater Sci Eng* 1984;65(1):75–83.
- [347] Hunziker O, Dye D, Reed RC. On the formation of a centrelne grain boundary during fusion welding. *Acta Mater* 2000;48(17):4191–201.
- [348] Tian Y, McAllister D, Colijn H, Mills M, Farson D, Nordin M, et al. Rationalization of microstructure heterogeneity in Inconel 718 builds made by the direct laser additive manufacturing process. *Metall Mater Trans A* 2014;45(10):4470–83.
- [349] Nie P, Ojo OA, Li Z. Numerical modeling of microstructure evolution during laser additive manufacturing of a nickel-based superalloy. *Acta Mater* 2014;77:85–95.
- [350] Liu F, Lin X, Leng H, Cao J, Liu Q, Huang C, et al. Microstructural changes in a laser solid forming Inconel 718 superalloy thin wall in the deposition direction. *Opt Laser Technol* 2013;45:330–5.
- [351] Parimi LL, A RG, Clark D, Attallah MM. Microstructural and texture development in direct laser fabricated IN718. *Mater Charact* 2014;89:102–11.
- [352] Birmingham MJ, Kent D, Zhan H, StJohn DH, Dargusch MS. Controlling the microstructure and properties of wire arc additive manufactured Ti-6Al-4V with trace boron additions. *Acta Mater* 2015;91:289–303.
- [353] Lu SL, Qian M, Tang HP, Yan M, Wang J, StJohn DH. Massive transformation in Ti-6Al-4V additively manufactured by selective electron beam melting. *Acta Mater* 2016;104:303–11.
- [354] Raghavan N, Dehoff R, Pannala S, Simunovic S, Kirka M, Turner J, et al. Numerical modeling of heat-transfer and the influence of process parameters on tailoring the grain morphology of IN718 in electron beam additive manufacturing. *Acta Mater* 2016;112:303–14.
- [355] Sridharan N, Gussev M, Seibert R, Parish C, Norfolk M, Terrani K, et al. Rationalization of anisotropic mechanical properties of Al-6061 fabricated using ultrasonic additive manufacturing. *Acta Mater* 2016;117:228–37.
- [356] Tan X, Kok YJ, Descoins M, Mangelinck D, Tor SB, et al. Graded microstructure and mechanical properties of additive manufactured Ti-6Al-4V via electron beam melting. *Acta Mater* 2015;97:1–16.
- [357] Wang Z, Palmer TA, Beese AM. Effect of processing parameters on microstructure and tensile properties of austenitic stainless steel 304L made by directed energy deposition additive manufacturing. *Acta Mater* 2016;110:226–35.
- [358] Wu J, Wang XQ, Wang W, Attallah MM, Loretto MH. Microstructure and strength of selectively laser melted AlSi10Mg. *Acta Mater* 2016;117:311–20.
- [359] Xu W, Brandt M, Sun S, Elambasseril J, Liu Q, Latham K, et al. Additive manufacturing of strong and ductile Ti-6Al-4V by selective laser melting via in situ martensite decomposition. *Acta Mater* 2015;85:74–84.
- [360] Rai A, Markl M, Körner C. A coupled cellular automaton-Lattice Boltzmann model for grain structure simulation during additive manufacturing. *Comp Mater Sci* 2016;124:37–48.
- [361] Yan J, Gao M, Li G, Zhang C, Zeng X, Jiang M. Microstructure and mechanical properties of laser-MIG hybrid welding of 1420 Al-Li alloy. *Int J Adv Manuf Technol* 2012;66(9–12):1467–73.
- [362] Chen Y, Lu F, Zhang K, Nie P, Elm Hosseini SR, Feng K, et al. Dendritic microstructure and hot cracking of laser additive manufactured Inconel 718 under improved base cooling. *J Alloy Comp* 2016;670:312–21.
- [363] Book TA, Sangid MD. Evaluation of select surface processing techniques for in situ application during the additive manufacturing build process. *JOM* 2016;68(7):1780–92.
- [364] Gong X, Chou K. Phase-field modeling of microstructure evolution in electron beam additive manufacturing. *JOM* 2015;67(5):1176–82.
- [365] Wu SQ, Lu YJ, Gan YL, Huang TT, Zhao CQ, Lin JJ, et al. Microstructural evolution and microhardness of a selective-laser-melted Ti-6Al-4V alloy after post heat treatments. *J Alloy Comp* 2016;672:643–52.
- [366] Liu Z, Qi H, Jiang L. Control of crystal orientation and continuous growth through inclination of coaxial nozzle in laser powder deposition of single-crystal superalloy. *J Mater Process Technol* 2016;230:177–86.
- [367] Montero Sistiaga ML, Mertens R, Vrancken B, Wang X, Van Hooreweder B, Kruth J-P, et al. Changing the alloy composition of Al7075 for better processability by selective laser melting. *J Mater Process Technol* 2016;238:437–45.
- [368] Helmer HE, Körner C, Singer RF. Additive manufacturing of nickel-based superalloy Inconel 718 by selective electron beam melting: processing window and microstructure. *J Mater Res* 2014;29(17):1987–96.
- [369] Bi G, Sun C-N, Chen H-c, Ng FL, Ma CCK. Microstructure and tensile properties of superalloy IN100 fabricated by micro-laser aided additive manufacturing. *Mater Des* 2014;60:401–8.
- [370] Chen Y, Zhang K, Huang J, Hosseini SRE, Li Z. Characterization of heat affected zone liquation cracking in laser additive manufacturing of Inconel 718. *Mater Des* 2016;90:586–94.
- [371] Liu W, Lu F, Wei Y, Ding Y, Wang P, Tang X. Special zone in multi-layer and multi-pass welded metal and its role in the creep behavior of 9Cr1Mo welded joint. *Mater Des* 2016;108:195–206.
- [372] Zinoviev A, Zinovieva O, Plosikhin V, Romanova V, Balokhonov R. Evolution of grain structure during laser additive manufacturing. Simulation by a cellular automata method. *Mater Des* 2016;106:321–9.
- [373] Antonysamy AA, Meyer J, Prangnell PB. Effect of build geometry on the  $\beta$ -grain structure and texture in additive manufacture of Ti6Al4V by selective electron beam melting. *Mater Charact* 2013;84:153–68.
- [374] Donoghue J, Antonysamy AA, Martina F, Colegrave PA, Williams SW, Prangnell PB. The effectiveness of combining rolling deformation with Wire-Arc Additive Manufacture on beta-grain refinement and texture modification in Ti-6Al-4V. *Mater Charact* 2016;114:103–14.
- [375] de Formanoir C, Michotte S, Rigo O, Germain L, Godet S. Electron beam melted Ti-6Al-4V: microstructure, texture and mechanical behavior of the as-built and heat-treated material. *Mater Sci Eng A* 2016;652:105–19.
- [376] Helmer H, Bauereiß A, Singer RF, Körner C. Grain structure evolution in Inconel 718 during selective electron beam melting. *Mater Sci Eng A* 2016;668:180–7.
- [377] Ma Y, Cuiuri D, Hoye N, Li H, Pan Z. The effect of location on the microstructure and mechanical properties of titanium aluminides produced by additive layer manufacturing using in-situ alloying and gas tungsten arc welding. *Mater Sci Eng A* 2015;631:230–40.
- [378] Vilaro T, Colin C, Bartout JD, Nazé L, Sennour M. Microstructural and mechanical approaches of the selective laser melting process applied to a nickel-base superalloy. *Mater Sci Eng A* 2012;534:446–51.
- [379] Dehoff RR, Kirka MM, Sames WJ, Bilheux H, Tremsin AS, Lowe LE, et al. Site specific control of crystallographic grain orientation through electron beam additive manufacturing. *Mater Sci Tech* 2015;31(8):931–8.
- [380] Wang X, Deng D, Qi M, Zhang H. Influences of deposition strategies and oblique angle on properties of AISI316L stainless steel oblique thin-walled part by direct laser fabrication. *Opt Laser Technol* 2016;80:138–44.
- [381] Niendorf T, Leuders S, Riener A, Richard HA, Tröster T, Schwarze D. Highly anisotropic steel processed by selective laser melting. *Metall Mater Trans B* 2013;44(4):794–6.
- [382] Kanagarajah P, Brenne F, Niendorf T, Maier HJ. Inconel 939 processed by selective laser melting: effect of microstructure and temperature on the mechanical properties under static and cyclic loading. *Mater Sci Eng A* 2013;588:188–95.

- [383] Kunze K, Etter T, Grässlin J, Shklover V. Texture, anisotropy in microstructure and mechanical properties of IN738LC alloy processed by selective laser melting (SLM). *Mater Sci Eng A* 2015;620:213–22.
- [384] Dinda GP, Dasgupta AK, Bhattacharya S, Natu H, Dutta B, Mazumder J. Microstructural characterization of laser-deposited Al 4047 alloy. *Metall Mater Trans A* 2012;44(5):2233–42.
- [385] Bhattacharya S, Dinda GP, Dasgupta AK, Natu H, Dutta B, Mazumder J. Microstructural evolution and mechanical, and corrosion property evaluation of Cu–30Ni alloy formed by Direct Metal Deposition process. *J Alloy Comp* 2011;509(22):6364–73.
- [386] Thijss L, Kempen K, Kruth JP, Van Humbeeck J. Fine-structured aluminium products with controllable texture by selective laser melting of pre-alloyed AlSi10Mg powder. *Acta Mater* 2013;61(5):1809–19.
- [387] Holesinger T, Carpenter J, Lienert T, Patterson B, Papin P, Swenson H, et al. Characterization of an aluminum alloy hemispherical shell fabricated via direct metal laser melting. *JOM* 2016;68(3):1000–11.
- [388] Boehm-Courjault E, Gonzales F, Jacot A, Kohler F, Mariaux A, Niederberger C, et al. EBSD: a powerful microstructure analysis technique in the field of solidification. *J Microsc-oxford* 2009;233(1):160–9.
- [389] Al-Bermani SS, Blackmore ML, Zhang W, Todd I. The origin of microstructural diversity, texture, and mechanical properties in electron beam melted Ti–6Al–4V. *Metall Mater Trans A* 2010;41(13):3422–34.
- [390] Chen S, Guillemot G, Gandin C-A. Three-dimensional cellular automaton-finite element modeling of solidification grain structures for arc-welding processes. *Acta Mater* 2016;115:448–67.
- [391] Murr LE, Gaytan SM, Ceylan A, Martinez E, Martinez JL, Hernandez DH, et al. Characterization of titanium aluminide alloy components fabricated by additive manufacturing using electron beam melting. *Acta Mater* 2010;58(5):1887–94.
- [392] Cong B, Ding J, Williams S. Effect of arc mode in cold metal transfer process on porosity of additively manufactured Al-6.3%Cu alloy. *Int J Adv Manuf Technol* 2014;76(9–12):1593–606.
- [393] Sing SL, Yeong WY, Wiria FE. Selective laser melting of titanium alloy with 50 wt% tantalum: microstructure and mechanical properties. *J Alloy Comp* 2016;660:461–70.
- [394] Vrancken B, Thijss L, Kruth JP, Van Humbeeck J. Heat treatment of Ti6Al4V produced by selective laser melting: microstructure and mechanical properties. *J Alloy Comp* 2012;541:177–85.
- [395] Zhang Q, Chen J, Tan H, Lin X, Huang WD. Influence of solution treatment on microstructure evolution of TC21 titanium alloy with near equiaxed  $\beta$  grains fabricated by laser additive manufacture. *J Alloy Comp* 2016;666:380–6.
- [396] Zhang Q, Chen J, Lin X, Tan H, Huang WD. Grain morphology control and texture characterization of laser solid formed Ti6Al2Sn2Zr3Mo1.5Cr2Nb titanium alloy. *J Mater Process Technol* 2016;238:202–11.
- [397] Gong X, Lydon J, Cooper K, Chou K. Beam speed effects on Ti–6Al–4V microstructures in electron beam additive manufacturing. *J Mater Res* 2014;29(17):1951–9.
- [398] Zhu Y, Tian X, Li J, Wang H. The anisotropy of laser melting deposition additive manufacturing Ti–6.5Al–3.5Mo–1.5Zr–0.3Si titanium alloy. *Mater Des* 2015;67:538–42.
- [399] Wang JF, Sun QJ, Wang H, Liu JP, Feng JC. Effect of location on microstructure and mechanical properties of additive layer manufactured Inconel 625 using gas tungsten arc welding. *Mater Sci Eng A* 2016;676:395–405.
- [400] Dehoff RR, Kirk MM, List FA, Unocic KA, Sames WJ. Crystallographic texture engineering through novel melt strategies via electron beam melting: Inconel 718. *Mater Sci Tech* 2015;31(8):939–44.
- [401] Murr LE, Martinez E, Gaytan SM, Ramirez BI, Machado BI, Shindo PW, et al. Microstructural architecture, microstructures, and mechanical properties for a nickel-base superalloy fabricated by electron beam melting. *Metall Mater Trans A* 2011;42(11):3491–508.
- [402] Prabhu AW, Vincent T, Chaudhary A, Zhang W, Babu SS. Effect of microstructure and defects on fatigue behaviour of directed energy deposited Ti–6Al–4V. *Sci Technol Weld Join* 2015;20(8):659–69.
- [403] Schempf P, Rethmeier M. Understanding grain refinement in aluminium welding. *Weld World* 2015;59(6):767–84.
- [404] Vrancken B, Thijss L, Kruth JP, Van Humbeeck J. Microstructure and mechanical properties of a novel  $\beta$  titanium metallic composite by selective laser melting. *Acta Mater* 2014;68:150–8.
- [405] Birmingham MJ, McDonald SD, Dargusch MS, StJohn DH. Grain-refinement mechanisms in titanium alloys. *J Mater Res* 2008;23(1):97–104.
- [406] Sistla H, Newkirk JW, Liou FF, Tms. Microstructural characterization and mechanical properties of laser deposited high entropy alloys. In: Tms 2014 supplemental proceedings; 2014. p. 1087–92.
- [407] Wu Z, David SA, Feng Z, Bei H. Weldability of a high entropy CrMnFeCoNi alloy. *Scripta Mater* 2016;124:81–5.
- [408] Martina F, Colegrave PA, Williams SW, Meyer J. Microstructure of interpass rolled wire + arc additive manufacturing Ti-6Al-4V components. *Metall Mater Trans A* 2015;46(12):6103–18.
- [409] Rutter B, Ramsperger M, Mujica Ronceny L, Lopez-Galilea I, Körner C, Theisen W. Impact of hot isostatic pressing on microstructures of CMSX-4 Ni-base superalloy fabricated by selective electron beam melting. *Mater Des* 2016;110:720–7.
- [410] Song B, Dong S, Liu Q, Liao H, Coddet C. Vacuum heat treatment of iron parts produced by selective laser melting: microstructure, residual stress and tensile behavior. *Mater Des* 2014;54:727–33.
- [411] Brandl E, Greitemeier D. Microstructure of additive layer manufactured Ti–6Al–4V after exceptional post heat treatments. *Mater Lett* 2012;81:84–7.
- [412] Amato KN, Gaytan SM, Murr LE, Martinez E, Shindo PW, Hernandez J, et al. Microstructures and mechanical behavior of Inconel 718 fabricated by selective laser melting. *Acta Mater* 2012;60(5):2299–39.
- [413] Cao J, Liu F, Lin X, Huang C, Chen J, Huang W. Effect of overlap rate on recrystallization behaviors of Laser Solid Formed Inconel 718 superalloy. *Opt Laser Technol* 2013;45:228–35.
- [414] Strößner J, Terock M, Glatzel U. Mechanical and microstructural investigation of nickel-based superalloy IN718 manufactured by selective laser melting (SLM). *Adv Eng Mater* 2015;17(8):1099–105.
- [415] Li W, Liu J, Zhou Y, Li S, Wen S, Wei Q, et al. Effect of laser scanning speed on a Ti-45Al-2Cr-5Nb alloy processed by selective laser melting: Microstructure, phase and mechanical properties. *J Alloy Comp* 2016;688:626–36.
- [416] Vastola G, Zhang G, Pei QX, Zhang YW. Modeling the microstructure evolution during additive manufacturing of Ti6Al4V: a comparison between electron beam melting and selective laser melting. *JOM* 2016;68(5):1370–5.
- [417] Guo C, Ge W, Lin F. Effects of scanning parameters on material deposition during electron beam selective melting of Ti-6Al-4V powder. *J Mater Process Technol* 2015;217:148–57.
- [418] Simonelli M, Tse YY, Tuck C. The formation of  $\alpha$  +  $\beta$  microstructure in as-fabricated selective laser melting of Ti–6Al–4V. *J Mater Res* 2014;29(17):2028–35.
- [419] Fischer M, Joguet D, Robin G, Peltier L, Laheurte P. In situ elaboration of a binary Ti-26Nb alloy by selective laser melting of elemental titanium and niobium mixed powders. *Mater Sci Eng C* 2016;62:852–9.
- [420] Kang N, Yuan H, Coddet P, Ren Z, Bernage C, Liao H, et al. On the texture, phase and tensile properties of commercially pure Ti produced via selective laser melting assisted by static magnetic field. *Mater Sci Eng C* 2017;70(Pt 1):405–7.
- [421] Cloots M, Uggowitzer PJ, Wegener K. Investigations on the microstructure and crack formation of IN738LC samples processed by selective laser melting using Gaussian and doughnut profiles. *Mater Des* 2016;89:770–84.
- [422] Guo Y, Jia L, Sun S, Kong B, Liu J, Zhang H. Rapid fabrication of Nb-Si based alloy by selective laser melting: microstructure, hardness and initial oxidation behavior. *Mater Des* 2016;109:37–46.
- [423] Song B, Dong S, Coddet P, Liao H, Coddet C. Fabrication of NiCr alloy parts by selective laser melting: columnar microstructure and anisotropic mechanical behavior. *Mater Des* 2014;53:1–7.

- [424] Tradowsky U, White J, Ward RM, Read N, Reimers W, Attallah MM. Selective laser melting of AlSi10Mg: influence of post-processing on the microstructural and tensile properties development. *Mater Des* 2016;105:212–22.
- [425] Yang J, Yu H, Yin J, Gao M, Wang Z, Zeng X. Formation and control of martensite in Ti-6Al-4V alloy produced by selective laser melting. *Mater Des* 2016;108:308–18.
- [426] Bormann T, Müller B, Schinhammer M, Kessler A, Thalmann P, de Wild M. Microstructure of selective laser melted nickel-titanium. *Mater Charact* 2014;94:189–202.
- [427] Divya VD, Muñoz-Moreno R, Messé OMDM, Barnard JS, Baker S, Illston T, et al. Microstructure of selective laser melted CM247LC nickel-based superalloy and its evolution through heat treatment. *Mater Charact* 2016;114:62–74.
- [428] Li W, Liu J, Wen S, Wei Q, Yan C, Shi Y. Crystal orientation, crystallographic texture and phase evolution in the Ti-45Al-2Cr-5Nb alloy processed by selective laser melting. *Mater Charact* 2016;113:125–33.
- [429] Tammas-Williams S, Zhao H, Léonard F, Derguti F, Todd I, Prangnell PB. XCT analysis of the influence of melt strategies on defect population in Ti-6Al-4V components manufactured by Selective Electron Beam Melting. *Mater Charact* 2015;102:47–61.
- [430] Chlebus E, Gruber K, Kuźnicka B, Kurzak J, Kurzynowski T. Effect of heat treatment on the microstructure and mechanical properties of Inconel 718 processed by selective laser melting. *Mater Sci Eng A* 2015;639:647–55.
- [431] Cloots M, Kunze K, Uggowitzer PJ, Wegener K. Microstructural characteristics of the nickel-based alloy IN738LC and the cobalt-based alloy Mar-M509 produced by selective laser melting. *Mater Sci Eng A* 2016;658:68–76.
- [432] Dadbakhsh S, Vrancken B, Kruth JP, Luyten J, Van Humbeeck J. Texture and anisotropy in selective laser melting of NiTi alloy. *Mater Sci Eng A* 2016;650:225–32.
- [433] Muñoz-Moreno R, Divya VD, Driver SL, Messé OMDM, Illston T, Baker S, et al. Effect of heat treatment on the microstructure, texture and elastic anisotropy of the nickel-based superalloy CM247LC processed by selective laser melting. *Mater Sci Eng A* 2016;674:529–39.
- [434] Simonelli M, Tse YY, Tuck C. On the texture formation of selective laser melted Ti-6Al-4V. *Metall Mater Trans A* 2014;45(6):2863–72.
- [435] Vilardo T, Colin C, Bartout JD. As-fabricated and heat-treated microstructures of the Ti-6Al-4V alloy processed by selective laser melting. *Metall Mater Trans A* 2011;42(10):3190–9.
- [436] Buchbinder D, Meiners W, Wissenbach K, Poprawe R. Selective laser melting of aluminum die-cast alloy—correlations between process parameters, solidification conditions, and resulting mechanical properties. *J Laser Appl* 2015;27(S2):S29205.
- [437] Townsend A, Senin N, Blunt L, Leach RK, Taylor JS. Surface texture metrology for metal additive manufacturing: a review. *Precis Eng* 2016;46:34–47.
- [438] Moat RJ, Pinkerton AJ, Li L, Withers PJ, Preuss M. Crystallographic texture and microstructure of pulsed diode laser-deposited Waspaloy. *Acta Mater* 2009;57(4):1220–9.
- [439] Bhattacharya S, Dinda GP, Dasgupta AK, Mazumder J. A comparative study of microstructure and mechanical behavior of CO<sub>2</sub> and diode laser deposited Cu-38Ni alloy. *J Mater Sci* 2014;49(6):2415–29.
- [440] Ding Y, Muñiz-Lerma JA, Trask M, Chou S, Walker A, Brochu M. Microstructure and mechanical property considerations in additive manufacturing of aluminum alloys. *MRS Bull* 2016;41(10):745–51.
- [441] Bartkowiak K, Ullrich S, Frick T, Schmidt M. New developments of laser processing aluminium alloys via additive manufacturing technique. *Phys Proc* 2011;12:393–401.
- [442] Simonelli M, Tse YY, Tuck C. Effect of the build orientation on the mechanical properties and fracture modes of SLM Ti-6Al-4V. *Mater Sci Eng A* 2014;616:1–11.
- [443] Jägle EA, Choi P-P, Van Humbeeck J, Raabe D. Precipitation and austenite reversion behavior of a maraging steel produced by selective laser melting. *J Mater Res* 2014;29(17):2072–9.
- [444] Murr LE, Gaytan SM, Ramirez DA, Martinez E, Hernandez J, Amato KN, et al. Metal fabrication by additive manufacturing using laser and electron beam melting technologies. *J Mater Sci Technol* 2012;28(1):1–14.
- [445] Mazumder J, Choi J, Nagarathnam K, Koch J, Hetzer D. The direct metal deposition of H13 tool steel for 3-D components. *JOM* 1997;49(5):55–60.
- [446] Elmer JW. A new path forward for understanding microstructural evolution during welding. *Weld J* 2008;87:149s–66s.
- [447] Elmer JW, Palmer T, Zhang W, DebRoy T. Time resolved X-ray diffraction observations of phase transformations in transient arc welds. *Sci Technol Weld Join* 2008;13(3):265–77.
- [448] Elmer JW, Palmer T. In-situ phase mapping and direct observations of phase transformations during arc welding of 1045 steel. *Metall Mater Trans A* 2006;37(7):2171–82.
- [449] Babu S, Elmer JW, David S, Quintana M. In situ observations of non-equilibrium austenite formation during weld solidification of an Fe-C-Al-Mn low-alloy steel. *Proc R Soc Lond A: Math, Phys Eng Sci* 2002;458(2020):811–21.
- [450] Mayr P, Palmer T, Elmer JW, Specht ED, Allen S. Formation of delta ferrite in 9 Wt pct Cr steel investigated by in-situ X-ray diffraction using synchrotron radiation. *Metall Mater Trans A* 2010;41(10):2462–5.
- [451] Kenel C, Schloth P, Van Petegem S, Fife JL, Grolimund D, Menzel A, et al. In situ synchrotron X-ray diffraction and small angle X-ray scattering studies on rapidly heated and cooled Ti-Al and Al-Cu-Mg alloys using laser-based heating. *JOM* 2016;68(3):978–84.
- [452] Kenel C, Grolimund D, Fife JL, Samson VA, Van Petegem S, Van Swyngedouw H, et al. Combined in situ synchrotron micro X-ray diffraction and high-speed imaging on rapidly heated and solidified Ti-48Al under additive manufacturing conditions. *Scripta Mater* 2016;114:117–20.
- [453] Cakmak E, Kirk MM, Watkins TR, Cooper RC, An K, Choo H, et al. Microstructural and micromechanical characterization of IN718 theta shaped specimens built with electron beam melting. *Acta Mater* 2016;108:161–75.
- [454] Murr LE, Martinez E, Pan XM, Gaytan SM, Castro JA, Terrazas CA, et al. Microstructures of Rene 142 nickel-based superalloy fabricated by electron beam melting. *Acta Mater* 2013;61(11):4289–96.
- [455] Li J, Wang HM. Microstructure and mechanical properties of rapid directionally solidified Ni-base superalloy Rene'41 by laser melting deposition manufacturing. *Mater Sci Eng A* 2010;527(18–19):4823–9.
- [456] Zhang YN, Cao X, Wanjara P, Medraj M. Oxide films in laser additive manufactured Inconel 718. *Acta Mater* 2013;61(17):6562–76.
- [457] Clark D, Bache MR, Whittaker MT. Shaped metal deposition of a nickel alloy for aero engine applications. *J Mater Process Technol* 2008;203(1–3):439–48.
- [458] Xiao H, Li SM, Xiao WJ, Li YQ, Cha LM, Mazumder J, et al. Effects of laser modes on Nb segregation and Laves phase formation during laser additive manufacturing of nickel-based superalloy. *Mater Lett* 2017;188:260–2.
- [459] Manikandan SGK, Sivakumar D, Rao KP, Kamaraj M. Effect of weld cooling rate on Laves phase formation in Inconel 718 fusion zone. *J Mater Process Technol* 2014;214(2):358–64.
- [460] Rombouts M, Maes G, Mertens M, Hendrix W. Laser metal deposition of Inconel 625: microstructure and mechanical properties. *J Laser Appl* 2012;24(5):052007.
- [461] Song H. Multi-scale microstructure characterization for improved understanding of microstructure-property relationship in additive manufacturing [PhD Thesis]. The Ohio State University; 2016.
- [462] Sridharan N, Chaudhary A, Nandwana P, Babu SS. Texture evolution during laser direct metal deposition of Ti-6Al-4V. *JOM* 2016;68(3):772–7.
- [463] Aboulkhair NT, Tuck C, Ashcroft I, Maskery I, Everitt NM. On the precipitation hardening of selective laser melted AlSi10Mg. *Metall Mater Trans A* 2015;46(8):3337–41.
- [464] Trelewicz JR, Halada GP, Donaldson OK, Manogharan G. Microstructure and corrosion resistance of laser additively manufactured 316L stainless steel. *JOM* 2016;68(3):850–9.
- [465] Manvatkar VD, Gokhale AA, Jagan Reddy G, Venkataramana A, De A. Estimation of melt pool dimensions, thermal cycle, and hardness distribution in the laser-engineered net shaping process of austenitic stainless steel. *Metall Mater Trans A* 2011;42(13):4080–7.

- [466] Zheng B, Zhou Y, Smugeresky JE, Schoenung JM, Lavernia EJ. Thermal behavior and microstructure evolution during laser deposition with laser-engineered net shaping: Part II. Experimental investigation and discussion. *Metall Mater Trans A* 2008;39(9):2237–45.
- [467] Lin X, Cao Y, Wu X, Yang H, Chen J, Huang W. Microstructure and mechanical properties of laser forming repaired 17–4PH stainless steel. *Mater Sci Eng A* 2012;553:80–8.
- [468] Cherry JA, Davies HM, Mehmood S, Lavery NP, Brown SGR, Sienz J. Investigation into the effect of process parameters on microstructural and physical properties of 316L stainless steel parts by selective laser melting. *Int J Adv Manuf Technol* 2014;76(5–8):869–79.
- [469] Sun Z, Tan X, Tor SB, Yeong WY. Selective laser melting of stainless steel 316L with low porosity and high build rates. *Mater Des* 2016;104:197–204.
- [470] 304/304L stainless steel product data bulletin. AK Steel Corporation; 2013 <[http://www.aksteel.com/pdf/markets\\_products/stainless/austenitic/304\\_304L\\_data\\_bulletin.pdf](http://www.aksteel.com/pdf/markets_products/stainless/austenitic/304_304L_data_bulletin.pdf)>.
- [471] Stainless steel 316/316L product data bulletin. AK Steel Corporation; 2013 <[http://www.aksteel.com/pdf/markets\\_products/stainless/austenitic/316\\_316L\\_Stainless\\_Steel\\_PDB\\_201512.pdf](http://www.aksteel.com/pdf/markets_products/stainless/austenitic/316_316L_Stainless_Steel_PDB_201512.pdf)>.
- [472] Zhang K, Wang S, Liu W, Shang X. Characterization of stainless steel parts by laser metal deposition shaping. *Mater Des* 2014;55:104–19.
- [473] Zielińska M, Durejko T, Polański M, Kuncie I, Płociński T, Zieliński W, et al. The microstructure, mechanical properties and corrosion resistance of 316L stainless steel fabricated using laser engineered net shaping. *Mater Sci Eng A* 2016;677:1–10.
- [474] Ma M, Wang Z, Wang D, Zeng X. Control of shape and performance for direct laser fabrication of precision large-scale metal parts with 316L stainless steel. *Opt Laser Technol* 2013;45:209–16.
- [475] Mertens A, Reginster S, Paydas H, Contrepois Q, Dormal T, Lemaire O, et al. Mechanical properties of alloy Ti-6Al-4V and of stainless steel 316L processed by selective laser melting: influence of out-of-equilibrium microstructures. *Powder Metall* 2014;57(3):184–9.
- [476] Mertens A, Reginster S, Contrepois Q, Dormal T, Lemaire O, Leconte-Beckers J. Microstructures and mechanical properties of stainless steel AISI 316L processed by selective laser melting. *Mater Sci Forum* 2014;898:903.
- [477] Modest M, Ready J, Farson D. *Handbook of laser materials processing*. Orlando, USA: Magnolia Publishing Inc; 2001.
- [478] Guan K, Wang ZM, Gao M, Li XY, Zeng XY. Effects of processing parameters on tensile properties of selective laser melted 304 stainless steel. *Mater Des* 2013;50:581–6.
- [479] Tolosa I, Garciandía F, Zubiri F, Zapirain F, Esnaola A. Study of mechanical properties of AISI 316 stainless steel processed by “selective laser melting”, following different manufacturing strategies. *Int J Adv Manuf Technol* 2010;51(5–8):639–47.
- [480] Rottger A, Geenen K, Windmann M, Binner F, Theisen W. Comparison of microstructure and mechanical properties of 316 L austenitic steel processed by selective laser melting with hot-isostatic pressed and cast material. *Mater Sci Eng A* 2016;678:365–76.
- [481] Spierings AB, Starr TL, Wegener K. Fatigue performance of additive manufactured metallic parts. *Rapid Prototyp J* 2013;19(2):88–94.
- [482] Li J, Deng D, Hou X, Wang X, Ma G, Wu D, et al. Microstructure and performance optimisation of stainless steel formed by laser additive manufacturing. *Mater Sci Tech* 2016;32(12):1223–30.
- [483] Rafi HK, Pal D, Patil N, Starr TL, Stucker BE. Microstructure and mechanical behavior of 17–4 precipitation hardenable steel processed by selective laser melting. *J Mater Eng Perform* 2014;23(12):4421–8.
- [484] Murr LE, Martinez E, Hernandez J, Collins S, Amato KN, Gaytan SM, et al. Microstructures and properties of 17–4 PH stainless steel fabricated by selective laser melting. *J Mater Res Technol* 2012;1(3):167–77.
- [485] LeBrun T, Nakamoto T, Horikawa K, Kobayashi H. Effect of retained austenite on subsequent thermal processing and resultant mechanical properties of selective laser melted 17–4 PH stainless steel. *Mater Des* 2015;81:44–53.
- [486] Rafi HK, Starr TL, Stucker BE. A comparison of the tensile, fatigue, and fracture behavior of Ti-6Al-4V and 15–5 PH stainless steel parts made by selective laser melting. *Int J Adv Manuf Technol* 2013;69(5–8):1299–309.
- [487] Yadollahi A, Shamsaei N, Thompson SM, Elwany A, Bian LK, Asme. Mechanical and microstructural properties of selective laser melted 17–4 PH stainless steel. In: Proceedings of the ASME international mechanical engineering congress and exposition. New York; 2015.
- [488] Ning FD, Cong WL. Microstructures and mechanical properties of Fe-Cr stainless steel parts fabricated by ultrasonic vibration-assisted laser engineered net shaping process. *Mater Lett* 2016;179:61–4.
- [489] Donachie MJ, Donachie SJ. *Superalloys: a technical guide*. Materials Park (OH): ASM International; 2002.
- [490] Zhao X, Chen J, Lin X, Huang W. Study on microstructure and mechanical properties of laser rapid forming Inconel 718. *Mater Sci Eng A* 2008;478(1–2):119–24.
- [491] Amato K. Comparison of microstructures and properties for a Ni-base superalloy (Alloy 625) fabricated by electron beam melting. *J Mater Sci Res* 2012;1(2):3.
- [492] Qiu CL, Adkins NJE, Attallah MM. Selective laser melting of Invar 36: microstructure and properties. *Acta Mater* 2016;103:382–95.
- [493] Bauer T, Dawson K, Spierings A, Wegener K. Microstructure and mechanical characterisation of SLM processed Haynes® 230®. In: Solid freeform symposium; 2015.
- [494] Baufeld B. Mechanical properties of Inconel 718 parts manufactured by shaped metal deposition (SMD). *J Mater Eng Perform* 2012;21(7):1416–21.
- [495] Bird RK, Hibberd J. Tensile properties and microstructure of Inconel 718 fabricated with electron beam freeform fabrication (EBF3). Hampton (VA, USA); 2009.
- [496] Yadroitsev I, Thivillon L, Bertrand P, Smurov I. Strategy of manufacturing components with designed internal structure by selective laser melting of metallic powder. *Appl Surf Sci* 2007;254(4):980–3.
- [497] Blackwell PL. The mechanical and microstructural characteristics of laser-deposited IN718. *J Mater Process Technol* 2005;170(1–2):240–6.
- [498] Zhang L, Wen M, Imade M, Fukuyama S, Yokogawa K. Effect of nickel equivalent on hydrogen gas embrittlement of austenitic stainless steels based on type 316 at low temperatures. *Acta Mater* 2008;56(14):3414–21.
- [499] Zuback JS, DebRoy T. Unpublished research; 2017.
- [500] Paul CP, Jain A, Ganesh P, Negi J, Nath AK. Laser rapid manufacturing of Colmonoy-6 components. *Opt Laser Eng* 2006;44(10):1096–109.
- [501] Paul CP, Ganesh P, Mishra SK, Bhargava P, Negi J, Nath AK. Investigating laser rapid manufacturing for Inconel-625 components. *Opt Laser Technol* 2007;39(4):800–5.
- [502] Sexton L, Lavin S, Byrne G, Kennedy A. Laser cladding of aerospace materials. *J Mater Process Technol* 2002;122(1):63–8.
- [503] Wang Z, Guan K, Gao M, Li X, Chen X, Zeng X. The microstructure and mechanical properties of deposited-IN718 by selective laser melting. *J Alloy Compd* 2012;513:518–23.
- [504] Abe F, Osakada K, Shiomi M, Uematsu K, Matsumoto M. The manufacturing of hard tools from metallic powders by selective laser melting. *J Mater Process Technol* 2001;111(1):210–3.
- [505] Zhong M, Yang L, Liu W, Huang T, He J. Laser rapid manufacturing of special pattern Inco 718 nickel-based alloy component. In: Photonics Asia 2004; 2005. p. 59–66.
- [506] Li J, Wang HM, Tang HB. Effect of heat treatment on microstructure and mechanical properties of laser melting deposited Ni-base superalloy Rene'41. *Mater Sci Eng A* 2012;550:97–102.
- [507] Harrison NJ, Todd I, Mumtaz K. Reduction of micro-cracking in nickel superalloys processed by selective laser melting: a fundamental alloy design approach. *Acta Mater* 2015;94:59–68.
- [508] Wang X, Chou YK. A method to estimate residual stress in metal parts made by Selective Laser Melting. In: ASME 2015 international mechanical engineering congress and exposition; 2015. p. V02AT02A015–V02AT02A015.
- [509] Zhang K, Liu WJ, Shang XF. Characteristics of laser aided direct metal powder deposition process for nickel-based superalloy. *Mater Sci Forum* 2007;534–536:457–60.
- [510] Donachie MJ. *Titanium: a technical guide* ASM international; 2000.

- [511] Zhao XL, Li SJ, Zhang M, Liu YD, Sercombe TB, Wang SG, et al. Comparison of the microstructures and mechanical properties of Ti-6Al-4V fabricated by selective laser melting and electron beam melting. *Mater Des* 2016;95:21–31.
- [512] Hrabe N, Quinn T. Effects of processing on microstructure and mechanical properties of a titanium alloy (Ti-6Al-4V) fabricated using electron beam melting (EBM). Part 2: energy input, orientation, and location. *Mater Sci Eng A* 2013;573:271–7.
- [513] Galarraga H, Lados DA, Dehoff RR, Kirka MM, Nandwana P. Effects of the microstructure and porosity on properties of Ti-6Al-4V ELI alloy fabricated by electron beam melting (EBM). *Addit Manuf* 2016;10:47–57.
- [514] Shunmugavel M, Polishetty A, Littlefair G. Microstructure and mechanical properties of wrought and additive manufactured Ti-6Al-4V cylindrical bars. *Proc Technol* 2015;20:231–6.
- [515] Edwards P, O'Conner A, Ramulu M. Electron beam additive manufacturing of titanium components: properties and performance. *J Manuf Sci Eng* 2013;135(6):061016.
- [516] Zhai YW, Galarraga H, Lados DA. Microstructure evolution, tensile properties, and fatigue damage mechanisms in Ti-6Al-4V alloys fabricated by two additive manufacturing techniques. *Proc Eng* 2015;114:658–66.
- [517] Akerfeldt P, Antti ML, Pederson R. Influence of microstructure on mechanical properties of laser metal wire-deposited Ti-6Al-4V. *Mater Sci Eng A* 2016;674:428–37.
- [518] Palanivel S, Dutt AK, Faierson EJ, Mishra RS. Spatially dependent properties in a laser additive manufactured Ti-6Al-4V component. *Mater Sci Eng A* 2016;654:39–52.
- [519] Zhang XD, Zhang H, Grylls RJ, Lienert TJ, Brice C, Fraser HL, et al. Laser-deposited advanced materials. *J Adv Mater* 2001;33(1):17–23.
- [520] Yu J, Rombouts M, Maes G, Motmans F. Material properties of Ti6Al4V parts produced by laser metal deposition. *Phys Proc* 2012;39:416–24.
- [521] Qiu CL, Ravi GA, Dance C, Ranson A, Dilworth S, Attallah MM. Fabrication of large Ti-6Al-4V structures by direct laser deposition. *J Alloy Comp* 2015;629:351–61.
- [522] Zhang SY, Lin X, Chen J, Huang WD. Heat-treated microstructure and mechanical properties of laser solid forming Ti-6Al-4V alloy. *Rare Met* 2009;28(6):537–44.
- [523] Dinda GP, Song L, Mazumder J. Fabrication of Ti-6Al-4V scaffolds by direct metal deposition. *Metall Mater Trans A* 2008;39A(12):2914–22.
- [524] Alcristo J, Enriquez A, Garcia H, Hinkson S, Steelman T, Silverman E, et al. Tensile properties and microstructures of laser-formed Ti-6Al-4V. *J Mater Eng Perform* 2011;20(2):203–12.
- [525] Keicher DM, Miller WD. LENSTM moves beyond RP to direct fabrication. *Met Powder Rep* 1998;12(53):26–8.
- [526] Optomec LENS materials. Optomec, Inc.; 2016 <<http://www.optomec.com/3d-printed-metals/lens-materials/>>.
- [527] Edwards P, Ramulu M. Fatigue performance evaluation of selective laser melted Ti-6Al-4V. *Mater Sci Eng A* 2014;598:327–37.
- [528] Vandebroucke B, Kruth JP. Selective laser melting of biocompatible metals for rapid manufacturing of medical parts. *Rapid Prototyp J* 2007;13(4):196–203.
- [529] Facchini L, Magalini E, Robotti P, Molinari A, Hoges S, Wissenbach K. Ductility of a Ti-6Al-4V alloy produced by selective laser melting of prealloyed powders. *Rapid Prototyp J* 2010;16(6):450–9.
- [530] Hollander DA, von Walter M, Wirtz T, Sellei R, Schmidt-Rohlfing B, Paar O, et al. Structural, mechanical and in vitro characterization of individually structured Ti-6Al-4V produced by direct laser forming. *Biomaterials* 2006;27(7):955–63.
- [531] Kasperovich G, Hausmann J. Improvement of fatigue resistance and ductility of TiAl6V4 processed by selective laser melting. *J Mater Process Technol* 2015;220:202–14.
- [532] Leuders S, Thöne M, Riemer A, Niendorf T, Tröster T, Richard H, et al. On the mechanical behaviour of titanium alloy TiAl6V4 manufactured by selective laser melting: Fatigue resistance and crack growth performance. *Int J Fatigue* 2013;48:300–7.
- [533] Murr L, Quinones S, Gaytan S, Lopez M, Rodela A, Martinez E, et al. Microstructure and mechanical behavior of Ti-6Al-4V produced by rapid-layer manufacturing, for biomedical applications. *J Mech Behav Biomed* 2009;2(1):20–32.
- [534] Qiu C, Adkins NJ, Attallah MM. Microstructure and tensile properties of selectively laser-melted and of HIPed laser-melted Ti-6Al-4V. *Mater Sci Eng A* 2013;578:230–9.
- [535] Rafi H, Karthik N, Gong H, Starr TL, Stucker BE. Microstructures and mechanical properties of Ti6Al4V parts fabricated by selective laser melting and electron beam melting. *J Mater Eng Perform* 2013;22(12):3872–83.
- [536] Ramosoeu M, Booyesen G, Ngonda T, Chikwanda H. Mechanical properties of direct laser sintered Ti-6Al-V4. In: Materials science and technology conference (MS&T), Columbus (OH); 2011. p. 1460–8.
- [537] Systems EG-EO. Material data sheet - EOS Titanium Ti64. EOS: München (Germany); 2011.
- [538] Kobryn P, Semiatin S. Mechanical properties of laser-deposited Ti-6Al-4V. In: Solid freeform fabrication proceedings; 2001. p. 6–8.
- [539] Amsterdam E, Kool G. High cycle fatigue of laser beam deposited Ti-6Al-4V and Inconel 718. In: ICAF 2009, Bridging the gap between theory and operational practice. Rotterdam (The Netherlands); 2009. p. 1261–74.
- [540] Arcella FG, Froes F. Producing titanium aerospace components from powder using laser forming. *JOM* 2000;52(5):28–30.
- [541] Griffith ML, Ensz MT, Puskar JD, Robino CV, Brooks JA, Phillipier JA, et al. Understanding the microstructure and properties of components fabricated by laser engineered net shaping (LENS). In: MRS proceedings; 2000. p. 9.
- [542] Leuders S, Lieneke T, Lammers S, Tröster T, Niendorf T. On the fatigue properties of metals manufactured by selective laser melting—the role of ductility. *J Mater Res* 2014;29(17):1911–9.
- [543] Koike M, Greer P, Owen K, Lilly G, Murr LE, Gaytan SM, et al. Evaluation of titanium alloys fabricated using rapid prototyping technologies—electron beam melting and laser beam melting. *Materials* 2011;4(10):1776–92.
- [544] Brandl E, Leyens C, Palm F. Mechanical properties of additive manufactured Ti-6Al-4V using wire and powder based processes. In: IOP conference series: materials science and engineering; 2011. p. 012004.
- [545] Brandl E, Baufeld B, Leyens C, Gault R. Additive manufactured Ti-6Al-4V using welding wire: Comparison of laser and arc beam deposition and evaluation with respect to aerospace material specifications. *Phys Proc* 2010;5:595–606.
- [546] Yao B, Ma X-L, Lin F, Ge W-J. Microstructure and mechanical properties of Ti-6Al-4V components fabricated by laser micro cladding deposition. *Rare Met* 2015;34(7):445–51.
- [547] Edwards P, Ramulu M. Effect of build direction on the fracture toughness and fatigue crack growth in selective laser melted Ti-6Al-4V. *Fatigue Fract Eng M* 2015;38(10):1228–36.
- [548] Kempen K, Thijss L, Van Humbeeck J, Kruth J-P. Mechanical properties of AlSi10Mg produced by selective laser melting. *Phys Proc* 2012;39:439–46.
- [549] Tang M, Pistorius PC. Oxides, porosity and fatigue performance of AlSi10Mg parts produced by selective laser melting. *Int J Fatigue* 2017;94:192–201.
- [550] Read N, Wang W, Essa K, Attallah MM. Selective laser melting of AlSi10Mg alloy: process optimisation and mechanical properties development. *Mater Des* 2015;65:417–24.
- [551] Bauer DM, Dietrich K, Walter M, Foret P, Palm F, Witt G. Effect of process gas and powder quality on aluminum alloys processed by laser based powder bed melting process. In: Proceedings of international solid freeform fabrication symposium; 2016. p. 419–25.
- [552] Fulcher BA, Leigh DK, Watt TJ. Comparison of AlSi10Mg and Al 6061 processed through DMLS. In: Proceedings of the solid freeform fabrication (SFF) symposium. Austin (TX, USA); 2014.
- [553] Ng CC, Savalani MM, Lau ML, Man HC. Microstructure and mechanical properties of selective laser melted magnesium. *Appl Surf Sci* 2011;257(17):7447–54.
- [554] Zhang BC, Liao HL, Coddet C. Effects of processing parameters on properties of selective laser melting Mg-9%Al powder mixture. *Mater Des* 2012;34:753–8.
- [555] Sing SL, Lam LP, Zhang DQ, Liu ZH, Chua CK. Interfacial characterization of SLM parts in multi-material processing: Intermetallic phase formation between AlSi10Mg and C18400 copper alloy. *Mater Charact* 2015;107:220–7.

- [556] Greitemeier D, Palm F, Syassen F, Melz T. Fatigue performance of additive manufactured TiAl6V4 using electron and laser beam melting. *Int J Fatigue* 2017;94:211–7.
- [557] Johnson AS, Shuai S, Shamsaei N, Thompson SM, Bian L. Fatigue behavior and failure mechanisms of direct laser deposited Inconel 718. In: Solid freeform fabrication 2016: proceedings of the 26th annual international solid freeform fabrication symposium—an additive manufacturing conference; 2016. p. 499–511.
- [558] Sterling AJ, Torrie B, Shamsaei N, Thompson SM, Seely DW. Fatigue behavior and failure mechanisms of direct laser deposited Ti-6Al-4V. *Mater Sci Eng A* 2016;655:100–12.
- [559] Ma XF, Duan Z, Shi HJ, Murai R, Yanagisawa E. Fatigue and fracture behavior of nickel-based superalloy Inconel 718 up to the very high cycle regime. *J Zhejiang Univ-Sci A* 2010;11(10):727–37.
- [560] Fatemi A, Molaei R, Sharifimehr S, Phan N, Shamsaei N. Multiaxial fatigue behavior of wrought and additive manufactured Ti-6Al-4V including surface finish effect. *Int J Fatigue* 2017;100:347–66.
- [561] Yadollahi A, Shamsaei N. Additive manufacturing of fatigue resistant materials: challenges and opportunities. *Int J Fatigue* 2017;98:14–31.
- [562] Siddique S, Imran M, Wycisk E, Emmelmann C, Walther F. Influence of process-induced microstructure and imperfections on mechanical properties of AlSi12 processed by selective laser melting. *J Mater Process Technol* 2015;221:205–13.
- [563] Maskery I, Aboulkhair N, Tuck C, Wildman R, Ashcroft I, Everitt N, et al. Fatigue performance enhancement of selectively laser melted aluminium alloy by heat treatment. In: 26th Annual international solid freeform fabrication symposium. Austin (TX, USA); 2015. p. 1017–25.
- [564] Riemer A, Leuders S, Thone M, Richard HA, Troster T, Niendorf T. On the fatigue crack growth behavior in 316L stainless steel manufactured by selective laser melting. *Eng Fract Mech* 2014;120:15–25.
- [565] Brandl E, Heckenberger U, Holzinger V, Buchbinder D. Additive manufactured AlSi10Mg samples using Selective Laser Melting (SLM): Microstructure, high cycle fatigue, and fracture behavior. *Mater Des* 2012;34:159–69.
- [566] Li P, Warner D, Fatemi A, Phan ND. On the fatigue performance of additively manufactured Ti-6Al-4V to enable rapid qualification for aerospace applications. In: 57th AIAA/ASCE/AHS/ASC structures, structural dynamics, and materials conference; 2016. p. 1656.
- [567] Kuo YL, Horikawa S, Kakehi K. Effects of build direction and heat treatment on creep properties of Ni-base superalloy built up by additive manufacturing. *Scripta Mater* 2017;129:74–8.
- [568] Pröbstle M, Neumeier S, Hopfenmüller J, Freund LP, Niendorf T, Schwarze D, et al. Superior creep strength of a nickel-based superalloy produced by selective laser melting. *Mater Sci Eng A* 2016;674:299–307.
- [569] Song H. Multi-scale microstructure characterization for improved understanding of microstructure-property relationship in additive manufacturing. The Ohio State University; 2016.
- [570] Chen W, Chaturvedi MC. Dependence of creep fracture of Inconel 718 on grain boundary precipitates. *Acta Mater* 1997;45(7):2735–46.
- [571] Rickenbacher L, Etter T, Hövel S, Wegener K. High temperature material properties of IN738LC processed by selective laser melting (SLM) technology. *Rapid Prototyp J* 2013;19(4):282–90.
- [572] Kunze K, Etter T, Grasslin J, Shklover V. Texture, anisotropy in microstructure and mechanical properties of IN738LC alloy processed by selective laser melting (SLM). *Mater Sci Eng A-Struct Mater Prop Microstruct Process* 2015;620:213–22.
- [573] Sun S-H, Koizumi Y, Kurosu S, Li Y-P, Chiba A. Phase and grain size inhomogeneity and their influences on creep behavior of Co-Cr-Mo alloy additive manufactured by electron beam melting. *Acta Mater* 2015;86:305–18.
- [574] Cooper F. Sintering and additive manufacturing: the new paradigm for the jewellery manufacturer. *Johnson Matthey Technol Rev* 2015;59(3):233–42.
- [575] Milewski JO, Dan JT, Gary KL. Directed light fabrication of rhenium components. In: International symposium on rhenium and rhenium alloys. Orlando (FL): TMS; 1997.
- [576] Lewis G, Thoma D, Nemec R, Milewski J. Directed light fabrication of refractory metals. In: International conference on powder metallurgy and particulate materials. Chicago (IL, USA); 1997.
- [577] Leonhardt TA. Spherical rhenium powder. US Patent 2003; No. 6551377.
- [578] Gu DD, Dai DH, Chen WH, Chen HY. Selective laser melting additive manufacturing of hard-to-process tungsten-based alloy parts with novel crystalline growth morphology and enhanced performance. *J Manuf Sci Eng* 2016;138(8):081003.
- [579] Zhou X, Liu XH, Zhang DD, Shen ZJ, Liu W. Balling phenomena in selective laser melted tungsten. *J Mater Process Technol* 2015;222:33–42.
- [580] Balla VK, Bodhak S, Bose S, Bandyopadhyay A. Porous tantalum structures for bone implants: fabrication, mechanical and in vitro biological properties. *Acta Biomater* 2010;6(8):3349–59.
- [581] Fox P, Pogson S, Sutcliffe C, Jones E. Interface interactions between porous titanium/tantalum coatings, produced by Selective Laser Melting (SLM), on a cobalt-chromium alloy. *Surf Coat Technol* 2008;202(20):5001–7.
- [582] Wauthle R, van der Stok J, Yavari SA, Van Humbeeck J, Kruth JP, Zadpoor AA, et al. Additively manufactured porous tantalum implants. *Acta Biomater* 2015;14:217–25.
- [583] Martinez E, Murr LE, Hernandez J, Pan X, Amato K, Frigola P, et al. Microstructures of niobium components fabricated by electron beam melting. *Metall Microstruct Anal* 2013;2(3):183–9.
- [584] Terrazas CA, Mireles J, Gaytan SM, Morton PA, Hinojos A, Frigola P, et al. Fabrication and characterization of high-purity niobium using electron beam melting additive manufacturing technology. *Int J Adv Manuf Technol* 2016;84(5–8):1115–26.
- [585] Faidel D, Jonas D, Natour G, Behr W. Investigation of the selective laser melting process with molybdenum powder. *Addit Manuf* 2015;8:88–94.
- [586] Wadsworth J, Morse GR, Chewey PM. The microstructure and mechanical properties of a welded molybdenum alloy. *Mater Sci Eng* 1983;59(2):257–73.
- [587] Khan M, Dickens P. Processing parameters for Selective Laser Melting (SLM) of gold. In: Proceedings of solid freeform fabrication symposium; 2008. p. 278–89.
- [588] Zito D, Carlotto A, Loggi A, Sbornicchia P, Maggiani D, SpA P, et al. Optimization of SLM technology main parameters in the production of gold and platinum jewelry. In: The Santa Fe symposium on jewelry manufacturing technology; 2014. p. 439–70.
- [589] Zito D, Carlotto A, Loggi A, Sbornicchia P, Bruttomesso D, Rappo S, et al. Definition and solidity of gold and platinum jewelry produced using selective laser melting (SLM<sup>TM</sup>) technology. In: The Santa Fe symposium on jewelry manufacturing technology; 2015. p. 455–92.
- [590] Cohen A. MICA freeform vs selective laser melting. Microfabrica; 2016 <<http://www.microfabrica.com/downloads/MIC-WhitePaper-2014.pdf>>.
- [591] Ge W, Lin F, Guo C. Functional gradient material of Ti-6Al-4V and (alpha)-TiAl fabricated by electron beam selective melting. In: Solid freeform fabrication symposium; 2015. p. 12.
- [592] Wang F, Mei J, Jiang H, Wu XH. Production of functionally-graded samples using simultaneous powder and wire-feed. In: Materials science forum, 539. Trans Tech Publications; 2007. p. 3631–6.
- [593] Ren HS, Liu D, Tang HB, Tian XJ, Zhu YY, Wang HM. Microstructure and mechanical properties of a graded structural material. *Mater Sci Eng A* 2014;611:362–9.
- [594] Akinlabi ET, Akinlabi SA. Characterization of functionally graded commercially pure titanium (CPTI) and titanium carbide (TiC) powders. In: Proceedings of the world congress on engineering; 2015. p. 1–3.
- [595] Liang YJ, Liu D, Wang HM. Microstructure and mechanical behavior of commercial purity Ti/Ti-6Al-2Zr-1Mo-1V structurally graded material fabricated by laser additive manufacturing. *Scripta Mater* 2014;74:80–3.
- [596] Järvinen J-P, Matilainen V, Li X, Piili H, Salminen A, Mäkelä I, et al. Characterization of effect of support structures in laser additive manufacturing of stainless steel. *Phys Proc* 2014;56:72–81.
- [597] Pulugurtha SR, Newkirk J, Liou F, Chou H-N. Functionally graded materials by laser metal deposition (reprint). Missouri University of Science and Technology Rolla; 2010. p. 1–31.

- [598] Reichardt A, Dillon RP, Borgonia JP, Shapiro AA, McEnerney BW, Momose T, et al. Development and characterization of Ti-6Al-4V to 304L stainless steel gradient components fabricated with laser deposition additive manufacturing. *Mater Des* 2016;104:404–13.
- [599] Hofmann DC, Roberts S, Otis R, Kolodziejska J, Dillon RP, Suh JO, et al. Developing gradient metal alloys through radial deposition additive manufacturing. *Sci Rep* 2014;4: Article No. 5357.
- [600] Liu WP, DuPont JN. Fabrication of functionally graded TiC/Ti composites by Laser Engineered Net Shaping. *Scripta Mater* 2003;48(9):1337–42.
- [601] Fessler J, Nickel A, Link G, Prinz F, Fussell P. Functional gradient metallic prototypes through shape deposition manufacturing. In: Proceedings of the solid freeform fabrication symposium. Austin (TX): University of Texas at Austin; 1997. p. 521–8.
- [602] Carroll BE, Otis RA, Borgonia JP, Suh JO, Dillon RP, Shapiro AA, et al. Functionally graded material of 304L stainless steel and inconel 625 fabricated by directed energy deposition: characterization and thermodynamic modeling. *Acta Mater* 2016;108:46–54.
- [603] Kahlen FJ, von Klitzing A, Kar A. Hardness, chemical, and microstructural studies for laser-fabricated metal parts of graded materials. *J Laser Appl* 2000;12(5):205–9.
- [604] Articek U, Milfelner M, Anzel I. Synthesis of functionally graded material H13/Cu by LENS technology. *Adv Product Eng Manage* 2013;8(3):169–76.
- [605] Hofmann DC, Kolodziejska J, Roberts S, Otis R, Dillon RP, Suh JO, et al. Compositationally graded metals: a new frontier of additive manufacturing. *J Mater Res* 2014;29(17):1899–910.
- [606] Gao Y, Tsumura T, Nakata K. Dissimilar welding of titanium alloys to steels. *Trans JWRI* 2012;41(2):7–12.
- [607] Kundu S, Sam S, Chatterjee S. Evaluation of interface microstructure and mechanical properties of the diffusion bonded joints of Ti-6Al-4V alloy to micro-duplex stainless steel. *Mater Sci Eng A* 2011;528(15):4910–6.
- [608] Dey HC, Ashfaq M, Bhaduri AK, Rao KP. Joining of titanium to 304L stainless steel by friction welding. *J Mater Process Technol* 2009;209(18–19):5862–70.
- [609] American welding society. AWS <<http://www.aws.org/about>> [browsed January 2017].
- [610] Standard welding terms and definitions, AWS 3.0:89. American Welding Society; 1989.
- [611] Zhou YN. Microjoining and nanojoining. Elsevier; 2008.
- [612] Welding Handbook. Materials and applications, part 1, 9th ed. Miami (FL): American Welding Society; 2010.
- [613] Elmer JW, Teruya A. An enhanced Faraday cup for rapid determination of power density distribution in electron beams. *Weld J* 2001;80(12):288-s.
- [614] Arata Y. *Plasma, electron and laser beam technology: development and use in materials processing*. Metals Park (OH, USA): American Society for Metals; 1986.
- [615] Dong P, Brust FW. Welding residual stresses and effects on fracture in pressure vessel and piping components: a millennium review and beyond. *J Press Vess* 2000;122(3):329–38.
- [616] ASM Handbook. Welding, brazing and soldering. ASM International; 1993.
- [617] Eagar T, Tsai N. Temperature fields produced by traveling distributed heat sources. *Weld J* 1983;62(12):346–55.
- [618] Rai R, Palmer T, Elmer JW, DebRoy T. Heat transfer and fluid flow during electron beam welding of 304L stainless steel alloy. *Weld J* 2009;88(3):54S–61S.
- [619] Goldak J, Asadi M. Computational weld mechanics and optimization of welding procedures, welds and welded structures. *Trans JWRI*, Special Issue on WSE2011 2011;55–60.
- [620] Goldak JA, Akhlaghi M. Computer simulation of welding processes. *Comput Weld Mech* 2005;16–69.
- [621] Wei HL, Elmer JW, DebRoy T. Crystal growth during keyhole mode laser welding. *Acta Mater* 2017;133:10–20.
- [622] Williams S. Unpublished work. Cranfield University; 2016.
- [623] Maguire M. Unpublished work. Sandia National Laboratory; 2016.
- [624] Wu X. A review of laser fabrication of metallic engineering components and of materials. *Mater Sci Tech* 2007;23(6):631–40.
- [625] Yadroitsev I, Bertrand P, Laget B, Smurov I. Application of laser assisted technologies for fabrication of functionally graded coatings and objects for the international thermonuclear experimental reactor components. *J Nucl Mater* 2007;362(2):189–96.
- [626] Elmer JW. Private contribution. Lawrence Livermore National Laboratory.
- [627] Seifi M, Christiansen D, Beuth J, Harrysson O, Lewandowski JJ. Process mapping, fracture and fatigue behavior of Ti-6Al-4V produced by EBM additive manufacturing. In: Proceedings of world conference on titanium, 13th. Wiley Warrendale (PA), Hoboken (NJ): TMS; 2016. p. 1373–7.
- [628] Kirchner A, Klöden B, Luft J, Weißgärtner B, Kieback B. Process window for electron beam melting of Ti-6Al-4V. *Powder Metall* 2015;58(4):246–9.
- [629] Weingarten C, Buchbinder D, Pirch N, Meiners W, Wissenbach K, Poprawe R. Formation and reduction of hydrogen porosity during selective laser melting of AlSi10Mg. *J Mater Process Technol* 2015;221:112–20.
- [630] Shuai L, Wei Q, Shi Y, Zhang J, Wei L. Micro-crack formation and controlling of Inconel 625 parts. In: Solid freeform fabrication symposium. Austin (TX); 2016. p. 520–9.
- [631] Li R, Liu J, Shi Y, Wang L, Jiang W. Balling behavior of stainless steel and nickel powder during selective laser melting process. *Int J Adv Manuf Technol* 2012;59(9–12):1025–35.
- [632] Budinski KG. Engineering materials: properties and selection, 4th ed. Prentic Hall; 1992.
- [633] Yaws CL. Handbook of vapor pressure: volume 4: inorganic compounds and elements. Gulf Professional Publishing; 1995.
- [634] Gong H, Rafi K, Gu H, Stark T, Stucker B. Analysis of defect generation in Ti-6Al-4V parts made using powder bed fusion additive manufacturing processes. *Addit Manuf* 2014;1:87–98.
- [635] Bobbio LD, Otis RA, Borgonia JP, Dillon RP, Shapiro AA, Liu Z-K, et al. Additive manufacturing of a functionally graded material from Ti-6Al-4V to Invar: experimental characterization and thermodynamic calculations. *Acta Mater* 2017;127:133–42.
- [636] Shen C, Pan Z, Cuiuri D, Roberts J, Li H. Fabrication of Fe-FeAl functionally graded material using the wire-arc additive manufacturing process. *Metall Mater Trans B* 2015;47(1):763–72.
- [637] Muller P, Mognol P, Hascoet JY. Modeling and control of a direct laser powder deposition process for functionally graded materials (FGM) parts manufacturing. *J Mater Process Technol* 2013;213(5):685–92.
- [638] Brentrup GJ, DuPont JN. Fabrication and characterization of graded transition joints for welding dissimilar alloys. *Weld J* 2013;92(3):72s–9s.
- [639] Domack MS, Baughman JM. Development of nickel-titanium graded composition components. *Rapid Prototyp J* 2005;11(1):41–51.
- [640] Aboulkhair NT, Maskery I, Tuck C, Ashcroft I, Everitt NM. On the formation of AlSi10Mg single tracks and layers in selective laser melting: microstructure and nano-mechanical properties. *J Mater Process Technol* 2016;230:88–98.
- [641] Buchbinder D, Schleifenzbaum H, Heidrich S, Meiners W, Bultmann J. High power selective laser melting (HP SLM) of aluminum parts. *Phys Proc* 2011;12:271–8.
- [642] Chou R, Milligan J, Paliwal M, Brochu M. Additive manufacturing of Al-12Si alloy via pulsed selective laser melting. *JOM* 2015;67(3):590–6.
- [643] Manfredi D, Calignano F, Krishnan M, Canali R, Ambrosio EP, Atzeni E. From powders to dense metal parts: characterization of a commercial AlSiMg alloy processed through direct metal laser sintering. *Materials* 2013;6(3):856–69.
- [644] Maskery I, Aboulkhair NT, Corfield MR, Tuck C, Clare AT, Leach RK, et al. Quantification and characterisation of porosity in selectively laser melted Al-Si10-Mg using X-ray computed tomography. *Mater Charact* 2016;111:193–204.
- [645] Prashanth KG, Scudino S, Klauss HJ, Surreddi KB, Lober L, Wang Z, et al. Microstructure and mechanical properties of Al-12Si produced by selective laser melting: effect of heat treatment. *Mater Sci Eng A* 2014;590:153–60.
- [646] Schmidtke K, Palm F, Hawkins A, Emmelmann C. Process and mechanical properties: applicability of a scandium modified Al-alloy for laser additive manufacturing. *Phys Proc* 2011;12:369–74.
- [647] Taminger KM, Hafley RA, Domack MS. Evolution and control of 2219 aluminum microstructural features through electron beam freeform fabrication. *Mater Sci Forum* 2006;519–521:1297–302.

- [648] Wang XJ, Zhang LC, Fang MH, Sercombe TB. The effect of atmosphere on the structure and properties of a selective laser melted Al-12Si alloy. *Mater Sci Eng A* 2014;597:370–5.
- [649] Yan C, Hao L, Hussein A, Young P, Huang J, Zhu W. Microstructure and mechanical properties of aluminium alloy cellular lattice structures manufactured by direct metal laser sintering. *Mater Sci Eng A* 2015;628:238–46.
- [650] Zhang H, Zhu HH, Qi T, Hu ZH, Zeng XY. Selective laser melting of high strength Al-Cu-Mg alloys: processing, microstructure and mechanical properties. *Mater Sci Eng A* 2016;656:47–54.
- [651] Bhattacharya S, Dinda GP, Dasgupta AK, Mazumder J. Microstructural evolution of AISI 4340 steel during Direct Metal Deposition process. *Mater Sci Eng A* 2011;528(6):2309–18.
- [652] Casalino G, Campanelli SL, Contuzzi N, Ludovico AD. Experimental investigation and statistical optimisation of the selective laser melting process of a maraging steel. *Opt Laser Technol* 2015;65:151–8.
- [653] Choi J, Chang Y. Characteristics of laser aided direct metal/material deposition process for tool steel. *Int J Mach Tool Manu* 2005;45(4–5):597–607.
- [654] Haselhuhn AS, Wijnen B, Anzalone GC, Sanders PG, Pearce JM. In situ formation of substrate release mechanisms for gas metal arc weld metal 3-D printing. *J Mater Process Technol* 2015;226:50–9.
- [655] Kempen K, Yasa E, Thijssen L, Kruth JP, Van Humbeeck J. Microstructure and mechanical properties of Selective Laser Melted 18Ni-300 steel. In: Lasers in manufacturing 2011: proceedings of the sixth international wlt conference on lasers in manufacturing; 2011. p. 255–63.
- [656] Sander J, Hufenbach J, Giebelner L, Wendrock H, Kuhn U, Eckert J. Microstructure and properties of FeCrMoVC tool steel produced by selective laser melting. *Mater Des* 2016;89:335–41.
- [657] Xie JW, Fox P, O'Neill W, Sutcliffe C. Effect of direct laser re-melting processing parameters and scanning strategies on the densification of tool steels. *J Mater Process Technol* 2005;170(3):516–23.
- [658] Bi GJ, Gary KLN, Teh KM, Jarfors AEW. Feasibility study on the laser aided additive manufacturing of die inserts for liquid forging. *Mater Des* 2010;31: S112–6.
- [659] Zhang K, Liu W, Shang X. Research on the processing experiments of laser metal deposition shaping. *Opt Laser Technol* 2007;39(3):549–57.
- [660] Abd-Elghany K, Bourell DL. Property evaluation of 304L stainless steel fabricated by selective laser melting. *Rapid Prototyp J* 2012;18(5):420–8.
- [661] Yadroitsev I, Yadroitseva I, Bertrand P, Smurov I. Factor analysis of selective laser melting process parameters and geometrical characteristics of synthesized single tracks. *Rapid Prototyp J* 2012;18(3):201–8.
- [662] Kobryn PA, Moore EH, Semiatin SL. The effect of laser power and traverse speed on microstructure, porosity, and build height in laser-deposited Ti-6Al-4V. *Scripta Mater* 2000;43(4):299–305.
- [663] Lee J, Lapira E, Bagheri B, Kao H-A. Recent advances and trends in predictive manufacturing systems in big data environment. *Manuf Lett* 2013;1(1):38–41.
- [664] Huang Y, Leu MC, Mazumder J, Donmez A. Additive manufacturing: current state, future potential, gaps and needs, and recommendations. *J Manuf Sci Eng* 2015;137(1): Article No. 014001.
- [665] DebRoy T, Zhang W, Turner J, Babu S. Building digital twins of 3D printing machines. *Scripta Mater* 2017;135:119–24.
- [666] Knapp GL, Mukherjee T, Zuback JS, Wei HL, Palmer TA, De A, et al. Building blocks for a digital twin of additive manufacturing. *Acta Mater* 2017;135:390–9.
- [667] Amon CH, Beuth JL, Weiss LE, Merz R, Prinz FB. Shape deposition manufacturing with microcasting: processing, thermal and mechanical issues. *J Manuf Sci Eng* 1998;120(3):656–65.
- [668] Chin RK, Beuth JL, Amon CH. Thermomechanical modeling of molten metal droplet solidification applied to layered manufacturing. *Mech Mater* 1996;24(4):257–71.
- [669] Chin RK, Beuth JL, Amon CH. Successive deposition of metals in solid freeform fabrication processes, part 1: thermomechanical models of layers and droplet columns. *J Manuf Sci Eng* 2001;123(4):623–31.
- [670] Chin RK, Beuth JL, Amon CH. Successive deposition of metals in solid freeform fabrication processes, part 2: thermomechanical models of adjacent droplets. *J Manuf Sci Eng* 2001;123(4):632–8.
- [671] Klingbeil NW, Beuth JL, Chin RK, Amon CH. Residual stress-induced warping in direct metal solid freeform fabrication. *Int J Mech Sci* 2002;44(1):57–77.
- [672] Foroozmehr E, Kovacevic R. Effect of path planning on the laser powder deposition process: thermal and structural evaluation. *Int J Adv Manuf Technol* 2010;51(5–8):659–69.
- [673] Sochalski-Kolbus LM, Payzant EA, Cornwell PA, Watkins TR, Babu SS, Dehoff RR, et al. Comparison of residual stresses in Inconel 718 simple parts made by electron beam melting and direct laser metal sintering. *Metall Mater Trans A* 2015;46a(3):1419–32.
- [674] Zhong M, Sun H, Liu W, Zhu X, He J. Boundary liquation and interface cracking characterization in laser deposition of Inconel 738 on directionally solidified Ni-based superalloy. *Scripta Mater* 2005;53(2):159–64.
- [675] Griffith ML, Keicher DM, Atwood CL, Romero JA, Smugeresky JE, Harwell LD, et al. Free form fabrication of metallic components using Laser Engineered Net Shaping (LENS(TM)). In: Solid freeform fabrication proceedings, September 1996; 1996. p. 125–31.
- [676] Xue Y, Pascu A, Horstemeyer MF, Wang L, Wang PT. Microporosity effects on cyclic plasticity and fatigue of LENS (TM)-processed steel. *Acta Mater* 2010;58(11):4029–38.
- [677] Yu J, Rombouts M, Maes G. Cracking behavior and mechanical properties of austenitic stainless steel parts produced by laser metal deposition. *Mater Des* 2013;45:228–35.
- [678] Zhang BC, Dembinski L, Coddet C. The study of the laser parameters and environment variables effect on mechanical properties of high compact parts elaborated by selective laser melting 316L powder. *Mater Sci Eng A* 2013;584:21–31.
- [679] Qu S, Huang CX, Gao YL, Yang G, Wu SD, Zang QS, et al. Tensile and compressive properties of AISI 304L stainless steel subjected to equal channel angular pressing. *Mater Sci Eng A* 2008;475(1–2):207–16.
- [680] Wu JH, Lin CK. Influence of high temperature exposure on the mechanical behavior and microstructure of 17–4 PH stainless steel. *J Mater Sci* 2003;38(5):965–71.
- [681] Nickel alloy 718-properties, composition, heat treatments and specifications. AZO Materials; 2008 <<http://www.azom.com/article.aspx?ArticleID=4188>>.
- [682] Donachie MJ. Superalloys-source book. American Society for Metals: Metals Park (OH); 1984, [424 p.]
- [683] Materials-alloys poured. American Casting Company; 2014 <<http://americancastingco.com/materials/>>.
- [684] Nickel-based super alloy Inconel 625-properties and applications by united performance alloys. AZO Materials; 2008 <<http://www.azom.com/article.aspx?ArticleID=4461>>.
- [685] Frantz EL. Nonferrous alloys and special purpose materials. ASM International; 1990.
- [686] Rocha SSD, Adabo GL, Henriques GEP, Nóbilo MAdA. Vickers hardness of cast commercially pure titanium and Ti-6Al-4V alloy submitted to heat treatments. *Braz Dent J* 2006;17(2):126–9.
- [687] Kobryn PA. Casting of titanium alloys. OH: Wright-Patterson AFB; 1996. p. 112.
- [688] Buchbinder D. Generative fertigung von aluminiumbauteilen für die serienproduktion. AluGenerativ Abschlussbericht BMBF 01RIO639A-D; 2010.
- [689] Material data sheet: EOS aluminium AlSi10Mg for EOSINT M 270. EOS; 2014 <<https://www.anubis3d.com/documents/dm3s/datasheets/Aluminum-AlSi10Mg.pdf>>.
- [690] Kempen K, Thijssen L, Van Humbeeck J, Kruth J-P. Processing AlSi10Mg by selective laser melting: parameter optimisation and material characterisation. *Mater Sci Tech* 2015;31(8):917–23.
- [691] Manfredi D, Calignano F, Ambrosio EP, Krishnan M, Canali R, Bihammo S, et al. Direct metal laser sintering: an additive manufacturing technology ready to produce lightweight structural parts for robotic applications. *Metall Ital* 2013;10:15–24.

- [692] Rosenthal I, Stern A, Frage N. Strain rate sensitivity and fracture mechanism of AlSi10Mg parts produced by selective laser melting. *Mater Sci Eng A* 2017;682:509–17.
- [693] Rosenthal I, Stern A, Frage N. Microstructure and mechanical properties of AlSi10Mg parts produced by the laser beam additive manufacturing (AM) technology. *Metall Microstruct Anal* 2014;3(6):448–53.
- [694] Siddique S, Wycisk E, Frieling G, Emmelmann C, Walther F. Microstructural and mechanical properties of selective laser melted Al 4047. *Appl Mech Mater* 2015.
- [695] Gu J, Cong B, Ding J, Williams SW, Zhai Y. Wire+arc additive manufacturing of aluminium. In: Solid freeform fabrication proceedings; 2014. p. 451–8.
- [696] Lumley R. Technical data sheets for heat treated aluminium high pressure die castings. CSIRO Light Metals Flagship; 2008 <[http://mastersonics.com/documents/mmm\\_applications/ultrasonic\\_metallurgy/pio2-hpdc-aluminum.pdf](http://mastersonics.com/documents/mmm_applications/ultrasonic_metallurgy/pio2-hpdc-aluminum.pdf)>.
- [697] Aluminum A413.0-F die casting alloy. MatWeb <<http://www.matweb.com/search/datasheet.aspx?matguid=641c7123204a4c6bb81190f8685cf60d&ckck=1>> [browsed March 2017].
- [698] Beese AM, Carroll BE. Review of mechanical properties of Ti-6Al-4V made by laser-based additive manufacturing using powder feedstock. *JOM* 2016;68(3):724–34.
- [699] Welding Handbook. 9th ed. Miami (FL): American Welding Society; 2001.
- [700] Welding Handbook. Welding technology, 8th ed. Miami (FL): American Welding Society; 1987.